MESOPOROUS MATERIALS

by Yu-May TAN

THESIS SUBMITTED FOR THE DEGREE OF
DOCTOR OF PHILOSOPHY

July 2001

Department of Chemistry
University of Southampton
Highfield
Southampton SO17 1BJ,
UK.

UNIVERSITY OF SOUTHAMPTON

ABSTRACT

FACULTY OF SCIENCE
CHEMISTRY

Doctor of Philosophy

MESOPOROUS MATERIALS

by **Yu-May TAN**

Recently, mesoporous metal films containing high surface areas have been produced electrochemically by using lyotropic liquid crystalline phases as templating agents. The main advantage is the versatility of this method, where other materials can be prepared. This thesis describes three areas with the common theme of the electrodeposition of materials in the presence of lyotropic liquid crystals.

The first area looks at the attempts to polymerise aniline in the hexagonal phase of $C_{16}EO_8$ and to characterise the films made. Although aniline could electropolymerise in a lyotropic liquid crystalline system, no evidence for nanostructure could be obtained.

The next area studies the diffusion of the ferricyanide redox couple in the presence of Brij® 56, which may give a clearer picture of carrying out electrochemistry in the regular structured lyotropic liquid crystalline phases of a surfactant. Ferricyanide chemistry appeared more reversible in the surfactant system, and a timescale appeared to exist for the organisation of the liquid crystalline phase of Brij® 56 into equilibrium.

The third area studies the electrodeposition of mesoporous palladium (Pd). Mesoporous Pd prepared electrochemically from the hexagonal phase of $C_{16}EO_8$ at room temperature has already been shown by Guerin to improve the performance of pellistors. Our work sets out to recreate and extend the experimental conditions when using a cheaper alternative surfactant, i.e. Brij® 56. The main purpose is to find the conditions suitable to deposit Pd on pellistors for comparison with the data obtained by Guerin. Electrodeposition of Pd in the hexagonal phase of Brij® 56 was possible on SRL 136a pellistors, and exposing them to methane showed evidence of sensitivity.

Most importantly, the combination of the three areas show the different facets to electrodeposition in the lyotropic liquid crystalline phases of a surfactant, and that a cheap and widely available surfactant, i.e. Brij® 56, can be used to construct a gas sensor.

Acknowledgements

I want to thank Professor Phil Bartlett for his kind and invaluable supervision during my PhD.

I would like to thank Southampton Innovations Ltd. and City Technology Ltd. for funding, particularly Dr. M. Willett and Dr. S. LeClerc from City Technology Ltd. for their discussions and assistance with gas testing experiments. I also would like to thank Professor Julian Gardner and Siu Man Lee from Warwick University for their discussions and supply of sensors.

I would like to thank Alastair Clarke and Dr. B. Cressey for their assistance with SEM and TEM experiments, and the group of Prof. M. Weller for assistance with X-ray experiments.

Many many thanks to Dr. Paul Wilde, Fabrice Birembaut, Jun Yao, Anne de Paepe, Ron Haaksman, Dr. Evelyne Simon, Dr. Guy Denuault and his group, especially Stuart Abercrombie and Stuart Evans for their warm friendship and wicked sense of humour, including all the jokes! I like to also thank my best friends, Dr. Diana Boaventura, Sophie Wu and Carmen Lopez Falcon.

Most of all, I am indebted to my family.

Chapter One

1 Nanostructured or Mesoporous Materials

In the last decade, there has been considerable interest in materials developed with pore sizes in the *mesoporous* domain (2 – 50 nm) due to their potential applications in, for example, catalysis.[1, 2, 3, 4] In the review carried out on *ordered mesoporous materials (OMMs)* by Seddon *et al.*[5], the explosion in the number of publications over the last decade can be seen in their plot, Figure 1.

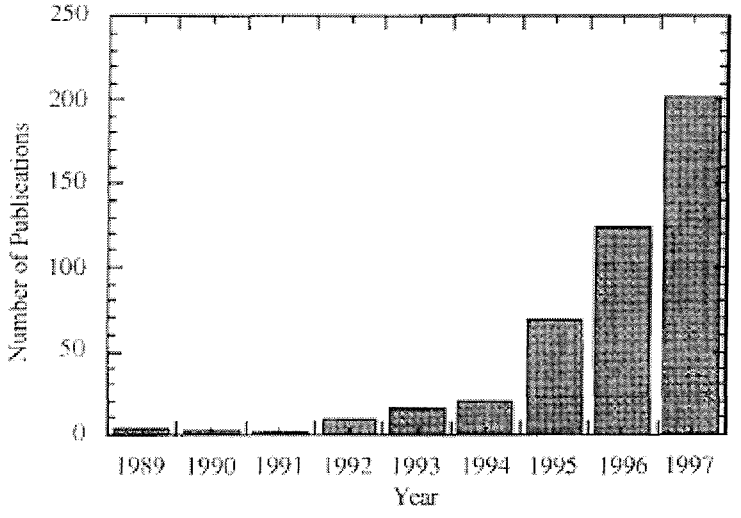

Figure 1 Recent plot of the number of papers published in the field of mesoporous materials between 1989 and 1997.[5]

Despite the considerable research into their syntheses and applications, their structures and mechanisms of formation remain the subject of vigorous debate.

Recently, Attard *et al.*[1, 2, 6] introduced a new approach to synthesising and characterising OMMs where they were produced chemically and electrochemically in the presence of lyotropic liquid crystals. In addition, the electrochemical techniques were found to produce reproducible results on relatively short experimental timescales. The high porosity and structural order of nanometer dimensions were confirmed by commonly used techniques such as transmission electron microscopy (TEM) and powder x-ray diffraction (XRD). Most interestingly, the nanostructure of the materials was found

effectively to be a cast of the structure of the liquid crystalline phase used in the synthesis.

This electrochemical approach is further analysed in this thesis. Divided into several topics, the effect of deposition conditions on the properties of films deposited in a lyotropic liquid crystalline phase is the main theme.

The implications are significant, strengthening the appeal of electrochemistry as a simple and versatile tool for tailoring the film properties for desired applications. For example, in the manufacture of pellistors, palladium (Pd) metal is the catalyst layer covering the alumina bead of a pellistor, being an effective catalyst for methane oxidation.[7, 8] A nanoporous and nanostructured form of Pd could enhance its catalytic activity on pellistors.

Therefore, structure on a nanoscale, hence *nanostructure*, is made possible by the transfer of the physical arrangement of lyotropic liquid crystals onto metals and ceramics by chemical synthesis and electrochemistry.

1.1 Introduction

1.1.1 Background

Materials with large surface areas are useful in catalysis. Microporous and mesoporous inorganic solids are good examples with pore diameters of ≤ 20 Å and about 20 - 500 Å respectively.[3]

Porous solids whose pore width is below 2 nm are classified by IUPAC as microporous. While some zeolites[9] tend to be naturally occuring microporous solids, others are also artificial zeolites. Another example are aluminophosphates, which contain similar structures. The original interest in these materials started in the field of mineralogy, and 24 naturally occuring zeolite compounds were discovered before 1900.[10] By 1948, the first synthetic zeolite was produced, and the development of the technique of x-ray diffraction has helped characterise many more zeolites.

Zeolites consist of a crystalline 3-d aluminosilicate framework, containing ordered channel systems with narrow pore size distributions. In the 1960s, the addition

of tetra-alkylammonium ions as templates in inorganic synthesis produced new structures such as the ZSM-5 family of zeolites. "Template Theory" was developed to explain the structure-directing effect of these ions where charge distribution, size and geometric shape of the template ion were believed to be the main factors. With their very high surface area and small pore size distribution, zeolites are valuable in catalytic applications and feature commonly in daily household products like washing powders.

However, the small pore sizes obtained are similar to those of very small molecules, and this limits the size of species which can enter into the pores and thus limits their catalytic applications. For instance, the cracking of the heavier fractions of crude oil needs larger channels than those possessed by zeolites.[11] In catalysis, larger sized species are often required, and the requirements can be met in a recently developed family of materials, known as *ordered mesoporous materials (OMMs)*, containing larger sized pores.

Therefore, porous solids whose pore width is extended into the mesoporous domain (classified by IUPAC as between 2 and 50 nm), have attracted an explosion of interest over the last decade. In 1992, Mobil scientists used low concentrations of ionic surfactants as templating agents for the first time for the synthesis of mesoporous silicas, naming the family as M41S.[3, 12] They obtained highly ordered porous structures with channels greater than 2 nm combined with narrow pore size distributions. These silica materials are different from the zeolites, as they are amorphous instead of crystalline.

This Mobil surfactant-mediated synthesis has already been applied to other materials, resulting in a variety of inorganic mesoporous materials.[13] Considerable interest has seen the application of these materials with channel-like mesopores of uniform size as hosts or templates for the synthesis of nanowires which can be useful in nanoelectronics,[14] and as model porous solids for studies of the behaviour of matter in confined space such as capillary condensation/evaporation.[15]

Therefore, the availability of these mesoporous materials with pore sizes tunable in as wide range as possible, is useful in many fields of nanotechnology. Despite the considerable research into their syntheses and applications, their structures and mechanisms of formations remain the subject of vigorous debate.

So far, the Mobil scientists had used low concentrations of ionic surfactants as templating agents for the first time for the synthesis of mesoporous silicas. A new dimension to the surfactant-templating approach of synthesising OMMs was provided by Attard *et al.*[2, 4] at the University of Southampton, who used much higher concentrations of surfactants as templating agents. At these high concentrations, the surfactants form lyotropic liquid crystalline phases. Attard and coworkers showed that OMMs could thus be produced chemically and electrochemically in the presence of lyotropic liquid crystals.

Besides the synthesis of mesoporous silica, Attard *et al.* have produced mesoporous metals such as platinum (Pt). The pore diameters of the metals can be chosen within a range, i.e. 1.7 and 15 nm, with the help of surfactants containing different chain lengths, hydrophobic additives like *n*-alkanes, or polymeric surfactants; these metals tend to have very high volumetric surface areas (300 – 1500 m^2 per cm^3 of material).[5] Therefore, structure on a nanoscale, hence *nanostructure*, is made possible by the transfer of the physical arrangement of lyotropic liquid crystals onto metals and ceramics by chemical synthesis and electrochemistry. These metal structures are unique and cannot be made (as yet) by any other methods.

More detailed comparisons, including advantages, between the Mobil and the Southampton research are discussed later in this chapter.

1.1.2 Applications

Materials with pores in the mesoporous domains, i.e. 20 - 500 Å, do attract interest in a wide range of fields, such as applications in catalysis, batteries, sensor and fuel cell technologies.[16] Several well-known applications of such materials, particularly metals, are introduced here to show their wide-ranging appeal.

1.1.2.1 Catalysis

One important application is the catalytic application of OMMs. In this thesis, Pd metal was studied, and being in the same group as platinum in the periodic table, the most common applications of this metal group are included here.

The uses of this metal group in catalysis include the hydrogenation of olefins, oxidation of ammonia for the production of nitric acid, and the reduction of nitrogen oxides in the control of car exhaust emissions.[17]

A catalyst can be broadly defined as a substance that increases the rate of chemical reactions without undergoing net chemical change itself.[18] It lowers the potential energy barrier between reactants and products by stabilising the transition state and activates the reactants. One example is the heterogeneous catalyst, whose surface contains specific properties, and whose activity is present at its interface where the reactant must be adsorbed.

For the reduction of many organic compounds, catalytic hydrogenation is one of the most convenient methods because mixing the catalyst in a solvent with the substrate in a hydrogen atmosphere easily affects the reaction, and the catalyst can be separated from the end product by filtration.[19] Besides metallic oxides and sulfides, the most common catalysts for catalytic hydrogenation are the platinum metals, i.e. Pt, Pd, Rh and Ru. These metals are excellent catalysts, encouraging the reduction of most functional groups under mild conditions, except the amide, carboxyl and carboxylic esters groups.[20] Used as finely divided metal particles, they can also be used supported on a carrier eg. alumina or activated carbon. However, the latter form tends to be more active due to greater surface area, although the activity depends on the support type and the method of preparation.

Pd metal as a heterogeneous catalyst is commonly used industrially, and it is often used supported on a carrier like carbon, having high surface areas, generally 120 $m^2 g^{-1}$. Of the platinum metal group, it is frequently used as the mildest reducing agent in the metal form; for example, unlike Pt and Ru, Pd cannot reduce aldehydes to alcohols, so this property can be utilised to produce more selective catalysts.[21] For the hydrogenation of olefins and acetylene, it is mostly used supported on a carrier. Other reactions catalysed by Pd include the decarbonylation of aldehydes and the reduction of aromatic and nitrogen-containing compounds.[22] Pd is also known to be one of the best catalysts for methane oxidation.[23]

It can be seen in this section that surface adsorption and catalyst surface area can have a great deal of influence on the reactions discussed. Thus, producing OMMs with very high surface areas can be attractive in catalytic applications.

1.1.2.2 Fuel Cell Catalysis

Another example of catalytic application is fuel cell catalysis. One of the driving forces for research into this area is the search for alternative energy sources for the purpose of energy conservation. Fuel cell systems are believed to incur low running costs and give greater fuel efficiencies than the current power plant by producing minimum waste heat. One future application is the replacement of the automobile internal combustion engine.

Commonly characterised by the electrolyte used, a fuel cell is essentially an electrochemical cell into which there is a continuous supply of reactants from the outside; the electron flow from the reactions occuring at the working electrode generate an electrical current.[24] For instance, in the proton exchange membrane fuel cell, PEMFC, a polymer membrane is sandwiched between two electrodes coated with a Pt-based catalyst; when supplied with fuel and air, electric power can be generated at cell voltages up to 1 V and power densities of up to 1 W cm^{-2}. In the direct methanol fuel cell DMFC, the anode needs a very effective methanol oxidation catalyst. Therefore, the efficiency of fuel cell technology is known to be connected to the development of electrocatalyst technology, and Pt or Pt containing catalysts have been found to be the most effective for both anode and cathode reactions.[24] The alteration of electrocatalytic properties of Pt through alloying with other metals, and through using dopants such as tin oxide, has already been studied for both anodic and cathodic applications.[25] Another common requirement in selecting suitable catalysts for fuel cell systems is the identification of electroactive catalysts that are stable for long periods in a corrosive environment.

In PEMFCs, the Pt-based catalysts used are supported on carbon, where the loading of the metal is high, e.g. up to 40 wt% Pt supported, giving very high surface areas greater than 75 m^2 g^{-1}. These catalysts are made by precipitation, and even at this loading, typical particle size is less than 4 nm.[24]

1.1.2.3 Pollution Control

Another example of catalytic application regards the control of automotive pollutants over the last three decades. The internal combustion engine of an automobile contributes significantly to atmospheric pollution through emission of carbon monoxide, nitric oxide and unburnt hydrocarbons;[26] besides their toxicity, these chemicals are recognised to be responsible for the smog covering many cities. Besides the requirement to withstand high temperatures, a "three-way catalyst" has been developed to convert these chemicals simultaneously into harmless products, i.e. carbon dioxide, water and nitrogen.[27] For example, in a Pt/Rh catalyst, Pt catalyses the oxidation of hydrocarbons and CO, and Rh catalyses the reduction of NO;[28] these noble metals are dispersed on porous support of metal oxide, i.e. Al_2O_3, ZrO_2 and CeO_2, containing surface areas as high as 100 m^2 g^{-1}.[28] The inclusion of Pd metal in these catalysts is currently studied because of lower noble metal cost reduction and improvements to durability.[29]

1.1.2.4 Other Applications

The examples given above summarise the use of high surface area catalysts where they are mainly supported small particles, but these materials are not the same as OMMs. For the applications of actual ordered mesoporous metals (synthesised from the lyotropic liquid crystalline phases), there is very little literature except that from the Southampton University researchers.[2, 4]

However, for ordered mesoporous silicas, there is considerable interest currently in the modification of the surfaces of the pores with metal ions to make catalysts, which is mainly directed towards the development of selective catalysts.[30]

The Mobil surfactant-mediated synthesis of mesoporous silica has already been applied to other materials, resulting in a variety of inorganic mesoporous materials.[13] Considerable interest has seen the application of these materials with channel-like mesopores of uniform size as hosts or templates for the synthesis of nanowires which can be useful in nanoelectronics,[14] and as model porous solids for studies of the behaviour of matter in confined space such as capillary condensation/evaporation.[15]

Therefore, the availability of these mesoporous materials with pore sizes tunable in as wide range as possible, is useful in many fields of nanotechnology.

1.2 Brief Introduction to Liquid Crystals

As mentioned previously, OMMs may be produced from *lyotropic liquid crystalline* mixtures, either chemically or electrochemically. Nanostructure is made possible by the transfer of the physical arrangement of lyotropic liquid crystals onto a material. The following paragraphs introduce the field of liquid crystals.

Many subtances can exist in more than one state of matter for example as solids, liquids and gases. They differ in terms of the amount of order they possess; in a solid molecules are in fixed positions and oriented in a fixed way; at the other extreme, in a gas molecules are free to move.

Temperature can be defined as a measure of the random motion of molecules. Molecules move and vibrate more the greater the temperature. Because the attractive forces between the molecules in a particular state of matter do not alter with temperature but the random motion does increase, the attractive forces will keep the molecules less ordered as the temperature rises.

Therefore, all substances contain some form of intermolecular forces and exist in a specific state of matter at any temperature. This specific state of matter is known as the *phase* stable at that temperature. When the temperature changes causing the phase to be no longer stable, the substance changes phase. This takes place at a precise temperature, i.e. a *phase transition* takes place at this temperature.

There is another phase known as the liquid crystal phase[31] which is different from the solid and liquid phases. Behaving like a liquid, a liquid crystal can flow and take the shape of its container. However, it is cloudy in appearance, suggesting that it could differ from liquids in a basic manner.

As mentioned before, the solid phase contains positional and orientational types of order. However, melting the solid to a liquid will remove both completely and the molecules move and tumble randomly.

On the other hand, when melting the solid to a *liquid crystal*, the positional order may disappear but not all the orientational order; the molecules may be free to move but will orient in a specific direction. Moreover, this orientational order will not be perfect like in a solid, with the molecules of a liquid crystal tending to point more along the direction of orientation than another. This partial alignment is therefore not present in a

liquid and is the basic difference between a liquid and a liquid crystal. Thus, a liquid crystal phase is recognised as a new phase, or state, of matter.

This is further confirmed by the amount of energy required to cause a phase transition, known as the *latent heat* of the transition. It is a useful gauge of how different the phases are. In the case of cholesteryl myristate, which consists mainly of carbon and hydrogen atoms and can commonly be found in our cell membranes, the latent heat of the solid to liquid crystal transition is 272 J per gram while the latent heat for the liquid crystal to liquid transition is 29 J per gram. This indicates that liquid crystals are more like liquids than solids. When the solid melts to a liquid crystal, most of its order disappears but there is a little more order than in a liquid. This order further disappears at the phase transition of liquid crystal to liquid.

It is possible to predict which type of molecule becomes liquid crystalline at a certain temperature. Firstly, the molecular shape tends to be elongated. Secondly, some rigidity must be present in the middle region, and lastly, having flexible ends seem beneficial. When oriented parallel to one another, elongated molecules tend to contain stronger attractive forces and collide less as they point in one direction. Flexible ends position the molecule more easily in between other molecules as they move.

The field of liquid crystals is enormous and really cannot be described in only a few paragraphs. In purely general terms, it can be divided into two classes: *thermotropics* and *lyotropics*. The first concerns only pure substances which display specific liquid-crystalline phases according to temperature changes. The latter class concerns mixtures of at least two different substances that exhibit different liquid-crystalline phases not only according to changes in temperature but also according to changes in the ratio of the concentrations of the components in the mixture.

1.3 Lyotropic Liquid Crystals

Lyotropic liquid crystals form an integral part of our work on OMMs. As mentioned previously, molecules in liquid crystals self assemble into phases in which orientational order and/or positional order (in one, two or three dimensions) continue over macroscopic ($\geq$ 50 nm) distances.

Molecules with end groups containing different properties make up a lyotropic liquid crystalline mixture. One end may have an affinity for water (i.e. hydrophilic) because it is polar, unlike the other end (i.e. hydrophobic) because it consists mainly of carbon and hydrogen. Placed in water, the similar ends will tend to arrange together, with the hydrophilic ends in contact with water for instance. As a result, different structures of various shapes form, such as spheres and cylinders, and they may order in a specific arrangement, hence forming liquid crystalline phases. These molecules are therefore also known as *amphiphilic* molecules (loving both kinds) or as *surfactants*.

Such molecules tend to migrate to the liquid surface. This property is important to technology and science. For instance, the crude oil industry is researching into amphiphile / water / oil system; much oil is trapped in porous rocks and if the oil fields could be flooded with a cheap amphiphile / water mixture, the oil may combine into the micelles, thereby enabling oil recovery.

Another very important property of surfactants is their liquid crystalline structures, i.e. the polar and non-polar end groups. One key example is soap molecules and their ability to dissolve oil and dirt. The second example is phospholipids, which exist widely in biological systems.

Last but not least, their structures could be transferred chemically or electrochemically onto materials, as shown by Attard *et al.*[1, 2]

1.3.1 Lyotropic Liquid Crystalline Structures

When drawing such structures, it is common to depict the hydrophilic group as a circle and the hydrophobic group as a tail. Figure 2 illustrates the assembly of these end groups into two of the lyotropic liquid crystalline structures that exist, hexagonal and lamellar.

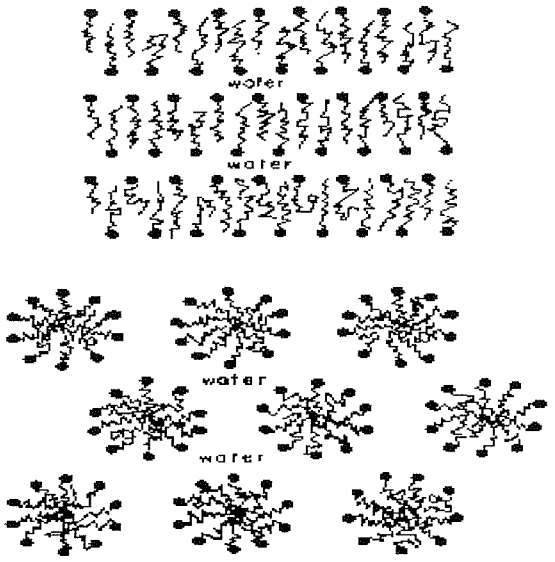

Figure 2 Cross-section diagrams of the lamellar (top) and the hexagonal (bottom) lyotropic liquid crystal phases. The circles represent hydrophilic groups and the zig-zag lines represent hydrophobic groups.[31]

When water is present, the amphiphilic molecules enter the solution, and with increasing amphiphilic concentration, several structures will start to form.

Firstly, *micelles* form spherically with polar head groups on the outside and the hydrocarbon end chains towards the centre. This type of structure is stable if the concentration is greater than the *critical micelle concentration* (cmc). Typically the cmc value is less than 1 wt% of surfactant with respect to the total water content. The hydrophilic groups on the outside are in contact with the water molecules, shielding the hydrophobic end chains from the water. Increasing the amount of surfactant in solution forms more micelles until eventually a point is reached where the micelles combine to form even larger structures.

Increasing the concentration generally up to 50 wt % forms the *hexagonal phase* The hydrophilic groups of the micellar structures remain in contact with water, shielding the hydrophobic end chains, and these micellar structures come together as long cylindrical rods in an hexagonal array.

At much higher concentrations, flat bilayers of amphiphiles form with water separating them, forming the *lamellar phase*. Sometimes, another phase called the *cubic*

phase forms between the concentrations of hexagonal and lamellar phases, forming *Ia3d* cubic structures.

These phases are some of the most commonly studied structures. For these phases to form, the temperature must be high enough. The temperature at which solid crystals melt forming the liquid crystalline phases, is known as the *Kraft temperature.*

1.3.2 Polarised-Light Optical Microscopy

Polarised-light optical microscopy is often used to identify a lyotropic liquid crystalline phase. A small quantity of liquid crystal is placed between two glass microslides to let light pass through easily. This is then placed between two polarisers which are adjusted so they cross each other. The crossing ensures that when there is no sample, light does not reach the eyes, giving a black image. This black image is also seen when observing an isotropic liquid because its refractive indices are the same in all directions and thus do not affect plane polarised light, such as in a micellar phase.

A visible image is therefore caused by the effect of the orientational order of liquid crystals on the light, causing anisotropy in the refractive index. The hexagonal and lamellar phases of a lyotropic liquid crystal are birefringent meaning that they contain two different refractive indices at 90^{o} to each other. Therefore under the microscope, a hexagonal phase will give a feathered texture as in Figure 3 while the lamellar phase gives a black and white stripey image in Figure 4. The cubic phases exhibit no birefringence, in the form of a black image with angular bubbles. Micellar solutions are isotropic like any liquid.

Besides optical textures, phase identification is aided by the viscosity of the phase.[32] Some phases look very similar but their viscosities are different. A cubic phase tends to be viscous with irregularly shaped air bubbles trapped in the mixture, and a micellar solution is fluid, although both images appear black under the microscope. By observing phases at the sample edges where water is lost due to heating the sample can help phase identification. Coleman has compiled a table detailing the identification of commonly found structures in lyotropic systems of ethylene oxide surfactants.[33]

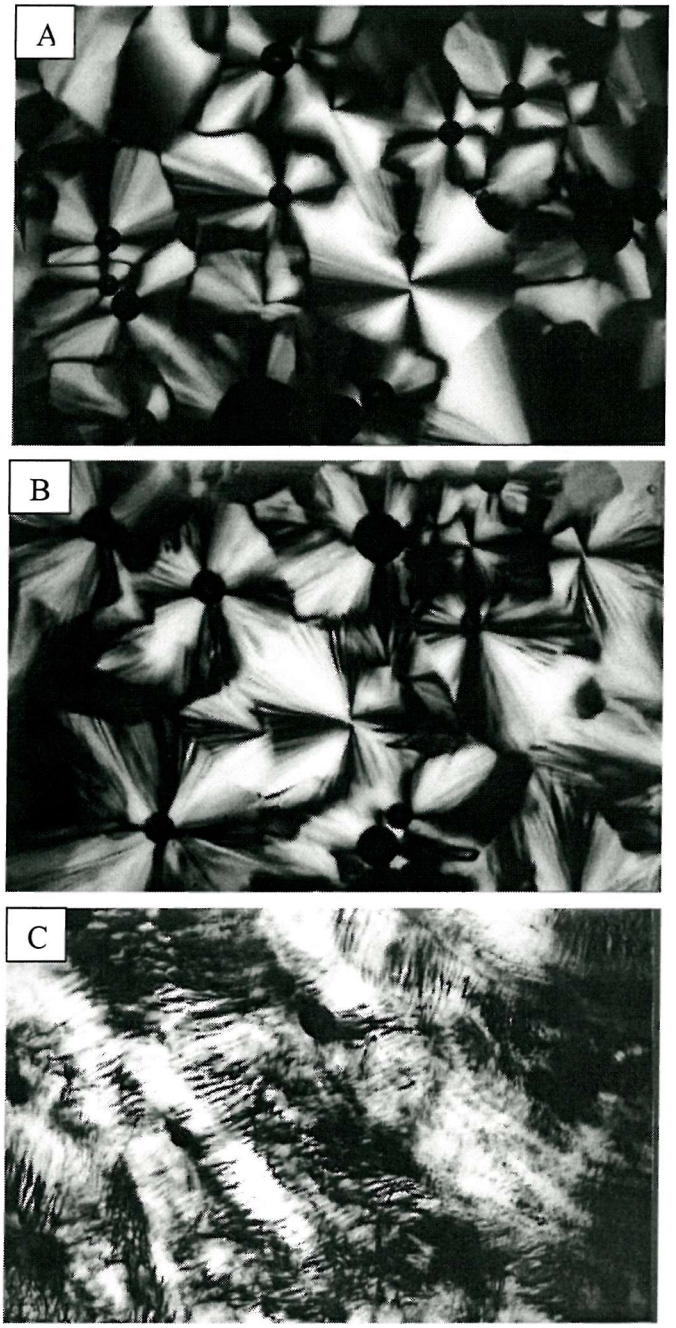

Figure 3 The optical textures of the hexagonal liquid crystal phase of $C_{16}EO_8$ in water A) A sample that has been cooled slowly from an isotropic micellar solution to a hexagonal phase. B) and C) show the hexagonal phase after the domains have been disturbed by rubbing the glass slide and cover slip across the sample.[33]

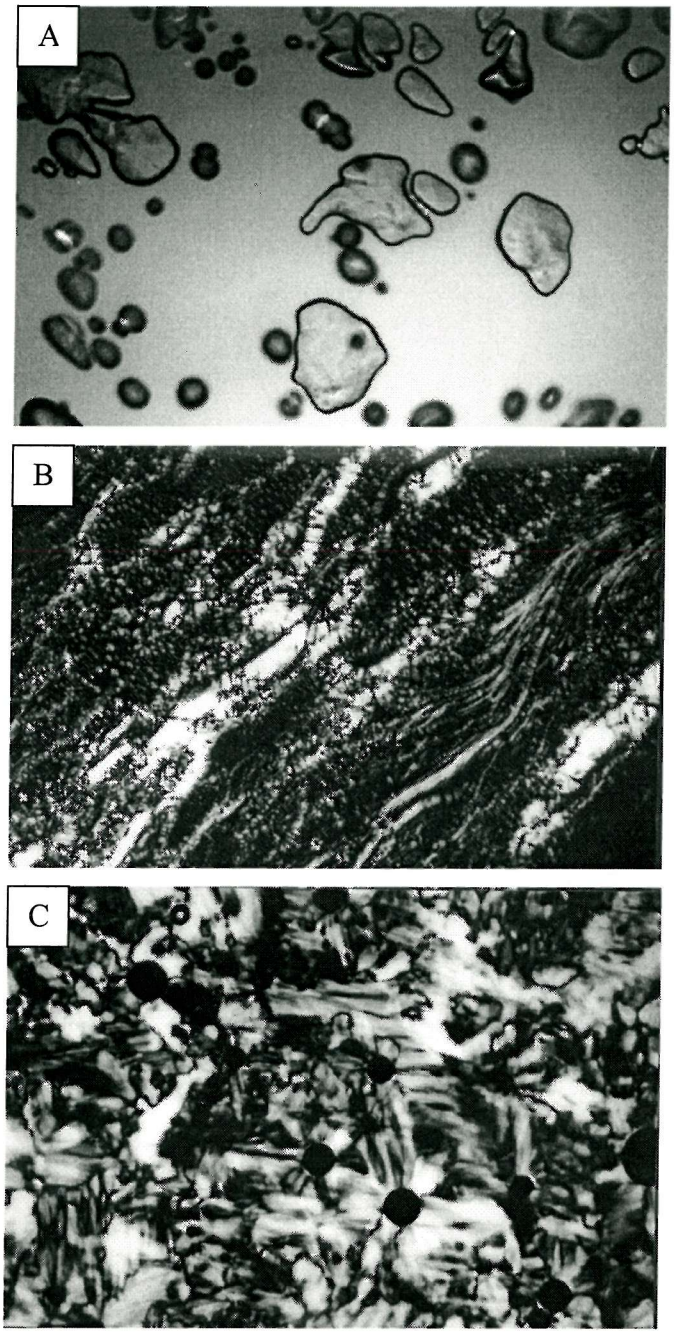

Figure 4 The optical textures of the A) cubic phase (V_1); and B) and C) Lamellar phase (L_α) for $C_{16}EO_8$ + water mixtures.[33]

1.4 Surfactants

The two non-ionic surfactants used in these studies were $C_{16}EO_8$ and Brij® 56. Mixtures were prepared from each surfactant in which the surfactant-to-water ratio was changed, while keeping the concentration of the precursor in water fixed.

1.4.1 $C_{16}EO_8$

Octaethylene glycol monohexadecyl ether [$C_{16}H_{33}(OCH_2CH_2)_8OH$] (supplier – Fluka) is also known as $C_{16}EO_8$. A non-ionic surfactant, these molecules consist of long hydrophobic hydrocarbon chains and large hydrophilic polar headgroups.

From the phase diagram of the binary $C_{16}EO_8$ - water system in Figure 5, a wide stable hexagonal phase exists between about 30 and 70 wt% and between room temperature and 60 ^{0}C. Attard *et al.*[34] discovered that the addition of hexachloroplatinic acid (HCPA) stabilised further the hexagonal phase where it was stable up to temperatures greater than 95 ^{0}C. Hexagonal phases were also formed in the quaternary mixtures containing *n*-heptane.[6]

1.4.2 Brij® 56

In using a non-ionic surfactant, such as $C_{16}EO_8$, it was possible to use a lyotropic liquid crystalline phase of the surfactant as a template to control the nanostructure of electrochemically deposited metal films.[2, 35]

It was also possible to reproduce this work using a cheaper, and more readily available, alternative to $C_{16}EO_8$. The alternative is polyoxyethylene(10) cetyl ether, [$C_{16}H_{33}(OCH_2CH_2)_{10}OH$], commonly known as Brij® 56. It is commercially available from Fluka and Sigma Aldrich amongst others. Currently Brij® 56 is 7 p per gram as opposed to £20 per g for $C_{16}EO_8$. This large price difference reflects the difference in the purity of the two surfactants: Brij® 56 contains a mixture of head group and chain lengths centred on $C_{16}EO_{10}$ (it was not possible to carry out mass spectrometry to determine the exact composition because the relative molecular mass of $C_{16}EO_{10}$ was greater than the

recommended 600 g mol^{-1}). Brij® 56 is also more readily available commercially than $C_{16}EO_8$.

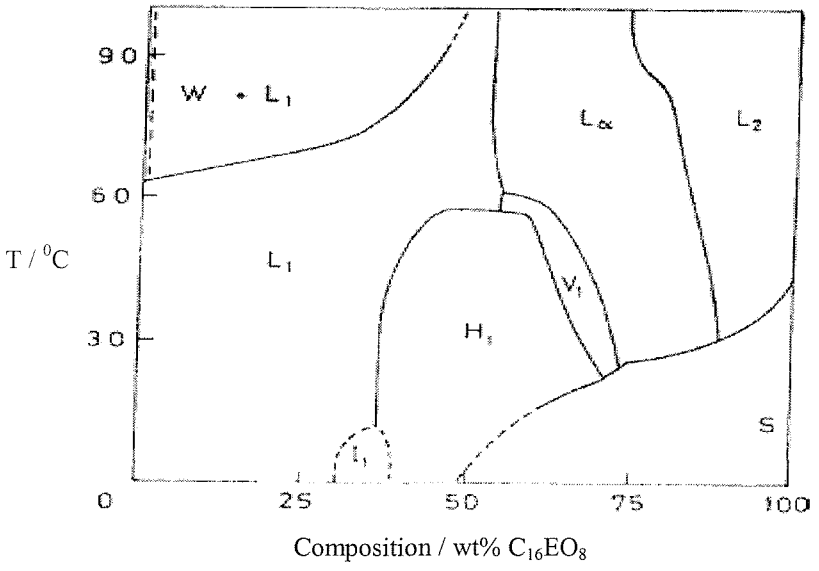

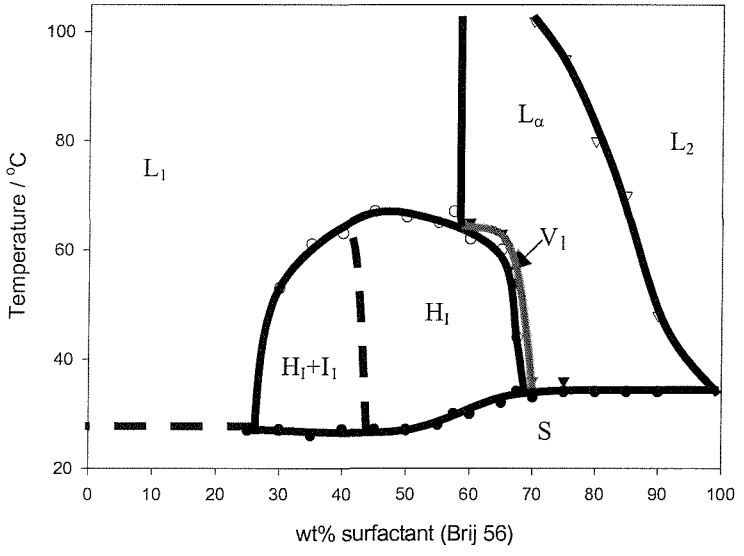

Figure 5 (A) The phase diagram for the binary surfactant-water system of $C_{16}EO_8$[36] and (B) the phase diagram for that of Brij® 56,[33] where L_α, H_1 and V_1 are lamellar, hexagonal and bicontinuous cubic phases respectively, and I_1 is a close-packed spherical micelle cubic phase, L_1 is a micellar phase, S is solid surfactant, W is water and L_2 is a liquid surfactant phase containing dissolved water (only partially miscible).

1.5 Two Methods of Preparation of Mesoporous Materials

1.5.1 Mobil Method – micelles

Recently, one has witnessed the discovery of ordered mesoporous materials (OMMs)[12, 37] and an incredible interest in their development.[38, 39, 40] Despite the considerable research into their synthesis and applications, their structures and mechanisms of formation remain the subject of vigorous debate.

In 1992, Mobil researchers, Kresge *et al*,[3] synthesised a family of silicas with mesopores arranged on a long-ranged periodic lattice, which they named as M41S. This attracted much interest because their synthesis used a micellar solution of ionic surfactant molecules, i.e. quaternary ammonium surfactants, as templating agents for the first time. More strikingly, the pore morphology of the resulting silicas resembled the nanostructure associated with aggregates formed at higher concentrations of surfactant. Monnier *et al*.[41] explained the presence of these structures at low surfactant concentrations in terms of an ionic interaction between the surfactant and silica precursor; the aggregation of the micelles was believed to be brought on by the presence of the negatively charged silicate species. This was later confirmed by Cheng *et al*.[42] in that an ordered mesoporous structure could only form in the presence of micelles.

The Mobil researchers proposed that the materials may be formed via what they called a "liquid-crystal templating" mechanism (LCT).[3, 12] Surfactant aggregates similar to lyotropic liquid crystalline phases were assumed to form within the alkaline colloidal silica synthesis gels, with silicon oxide oligomers polymerised at the surfaces of the aggregates to form the mesoporous silica framework.

To explain the formation, two possible but different routes were initially recommended, as follows:[5]

- The liquid crystalline phase was unaltered before the addition of the silicate species,
- The addition of silicate species created the ordering of the subsequent silicate-encased surfactant micelles

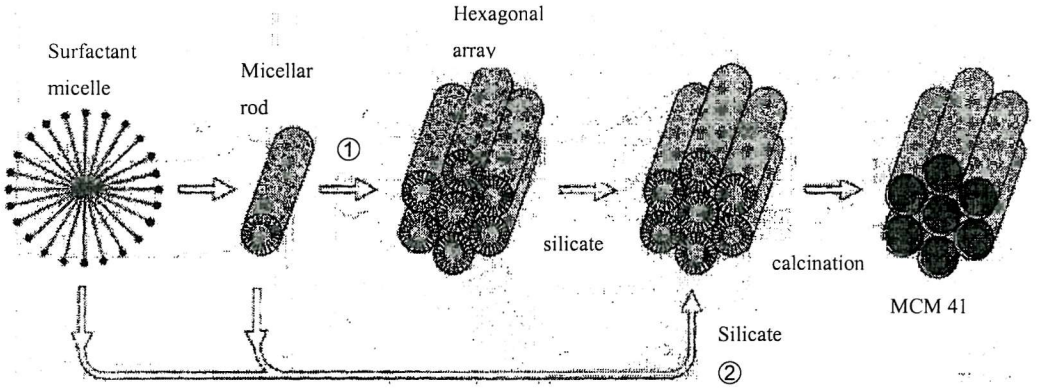

Figure 6 Possible mechanistic routes to form MCM-41: (1) liquid crystal phase initiated and (2) silicate anion initiated (from reference 5).

Figure 6 shows the two routes which produced a structure akin to known liquid crystalline phases. Nevertheless, the second route looks more probable because of the low initial surfactant concentration employed.

Thus, cylindrical micelles were believed to order as hexagonal arrays with polar groups of the surfactants to the outside. The anionic silicate ions entered the solvent (water) region to balance the cationic hydrophilic surfaces of the micelles, forming inorganic silica walls between ordered surfactant micelles, i.e. spaces between the cylinders. Subsequent calcination removes the organic material, leaving behind hollow cylinders of the inorganic material.

The most common materials of the M41S family were MCM-41 (MCM standing for "Mobil composition of matter"). Figure 7 shows the transmission electron microscopy (TEM) image of MCM-41, where the regular hexagonal array of uniform mesopores can be seen.

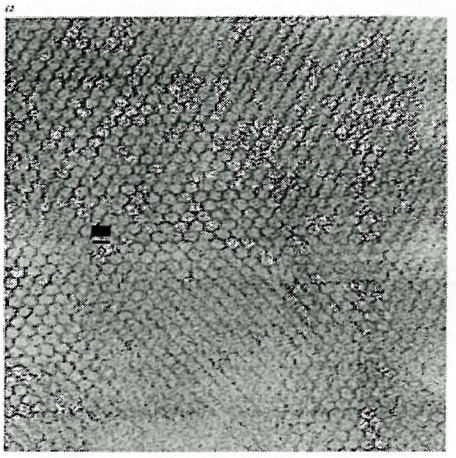

Figure 7 TEM image[3] shows the regular hexagonal array of channels characteristic of MCM-41. (Scale bar approximately 50 Å)

Unlike the micropores found in zeolites, these materials contained regular arrays of uniform channels whose larger dimensions (in the range of 16 Å to 100 Å) seemed dependent on the surfactant type (e.g. the alkyl chain length) and the reaction conditions such as post-synthesis treatments.[43, 44]

Therefore the pore diameter in MCM-41 could be changed by changing the alkyl chain length of the cationic surfactant templates used in the synthesis procedure. Kruk *et al.*[45] characterised a series of highly ordered MCM-41 silicas, which were synthesised using single or mixed alkyltrimethylammonium and alkyltriethylammonium surfactants of alkyl chain lengths from 12 to 22. Pore sizes from 32 to 48 Å with approximately 3 Å increments were observed by the combination of nitrogen adsorption and powder X-ray diffraction techniques. TEM analysis showed the pore wall thickness tending to increase with pore size, and although hexagonal ordering was observed, there was evidence of a decrease in structural ordering upon calcination.

The addition of auxiliary hydrocarbons to the reaction mixture, such as decane, could also swell pore sizes up to 80 Å.[46]

As mentioned previously, the LCT theory proposed that the dominant rate-determining step in the M41S structure formation was the ordering of surfactant molecules into micellar liquid crystals which served as templating agents for the

formation of silica. Firouzi *et. al.*[47] also suggested in 1995 that MCM-41 was usually formed via a multistep mechanism which involved formation of ion pairs between surfactant ions and silicate oligomers. These ion pairs would self-assemble into the hexagonal structure, later stabilised by the condensation of the silicate framework. They proposed that the external surface of particles of uncalcined surfactant-containing MCM-41 would be covered to a significant extent with surfactant molecules electrostatically bonded to the silicate framework and was thus very similar to the internal surface of these materials, see Figure 8.

Low-pressure nitrogen adsorption data collected by Kruk did suggest that the external surface of uncalcined surfactant-containing MCM-41 particles was covered by a relatively dense layer of strongly bonded surfactant molecules. Although this appeared to be a common feature of the MCM-41 samples studied by Kruk, more verification is needed if it is a general property of templated mesoporous materials.

If the LCT theory is valid, this means that the type of materials formed does not need to be restricted to silicas. Changing the surfactant concentration or the addition of co-surfactants or additives like hydrocarbons may cause changes in liquid crystalline phases. Consequently, a change in the structure of the product due to the above may be regarded as evidence in support of the theory.

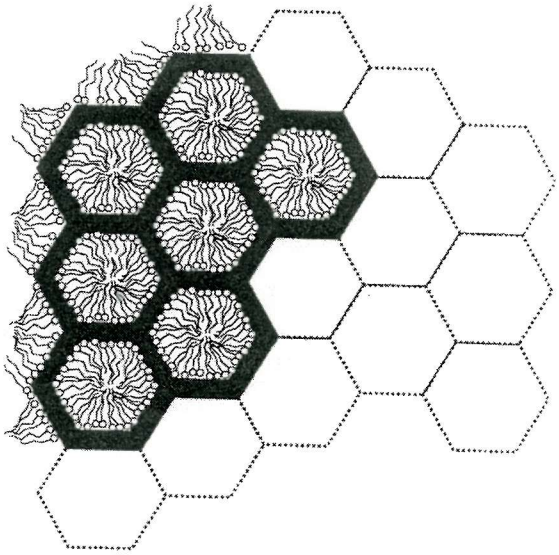

Figure 8 Schematic diagram of a MCM-41 particle.[47]

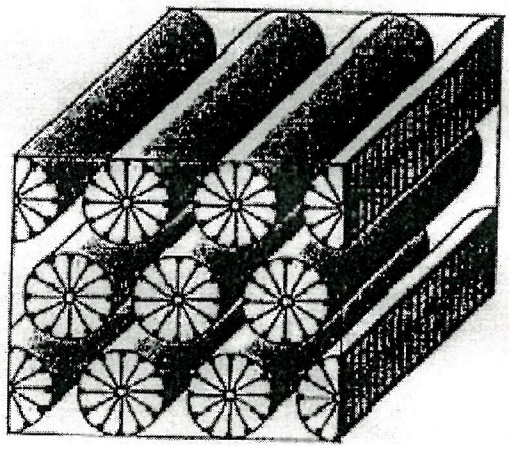

Figure 9 Structure of MCM-41[48]**, consisting of a hexagonal array of unidirectional pores.**

1.5.2 True Liquid Crystal Templating (TLCT) of Mesoporous Materials

In 1995, mesoporous silicas with pore morphologies identical to the M41S materials were formed from aggregates formed by non-ionic polyoxyethylene surfactants. Attard and coworkers[4] in Southampton used higher surfactant concentrations than in the Mobil method, and they employed a non-ionic polyoxyethylene surfactant called octaethylene glycol monododecyl ether, or commonly known as $C_{12}EO_8$. The high surfactant concentrations led to the formation of surfactant aggregates that formed liquid crystalline phases which determined the pore morphology.

They successfully synthesised mesoporous silica from synthesis gels and were able to use the resulting three liquid crystalline phases to template silica with a pore structure typical to the phase in which silica was made, see Figure 11. Products were obtained in the hexagonal, cubic and lamellar phases with the former two stable to calcination.

For example, mesoporous silica was synthesised directly in the hexagonal phase of the surfactant, forming a hexagonal porous structure. The liquid crystalline phase was confirmed by optical microscopy and the hexagonal pore structure by TEM. The liquid-crystalline phase was believed to "direct" the formation of mesoporous silica. Figure 10 shows the TEM evidence of ordered mesostructures of silica formed by the various liquid crystalline phases of the surfactant.

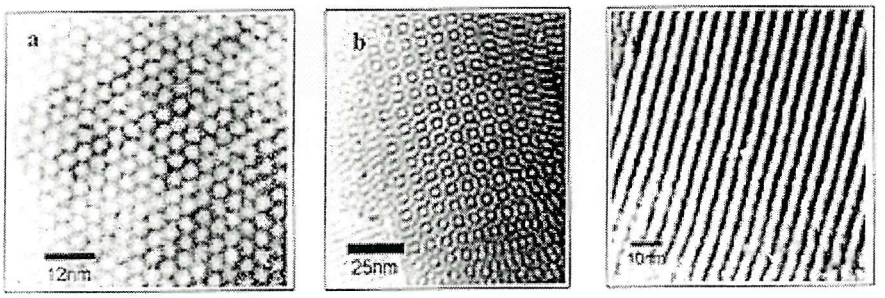

Figure 10 TEM images of mesoporous silica[4, 33] showing the various pore morphologies produced: (a) hexagonal, (b) cubic and (c) lamellar.

With the help of polarising microscopy, obvious likeness was discovered between the birefringent patterns obtained for the surfactant/water mixture, the synthesis gel, the as-synthesised product and the calcined product. This further supported the TLCT theory which proposed that the surfactant would form a liquid crystal phase before the condensation of the silica, maintaining the same phase throughout the synthesis.

The phase behaviour of the original liquid crystal was generally found not to be significantly affected by the presence of inorganic precursor species.

Another non-ionic polyoxyethylene surfactant called octaethylene glycol monohexadecyl ether or commonly known as $C_{16}EO_8$ was employed by Attard *et al.*[2, 4] in the synthesis of a cubic direct-templated structure. The cubic *Ia3d* phase exists in a narrow concentration region as can be seen in Figure 5, making it difficult to obtain this phase. Seddon *et al.*[5] did find that room temperature synthesis of the cubic material frequently led to a product in both cubic and hexagonal phases.

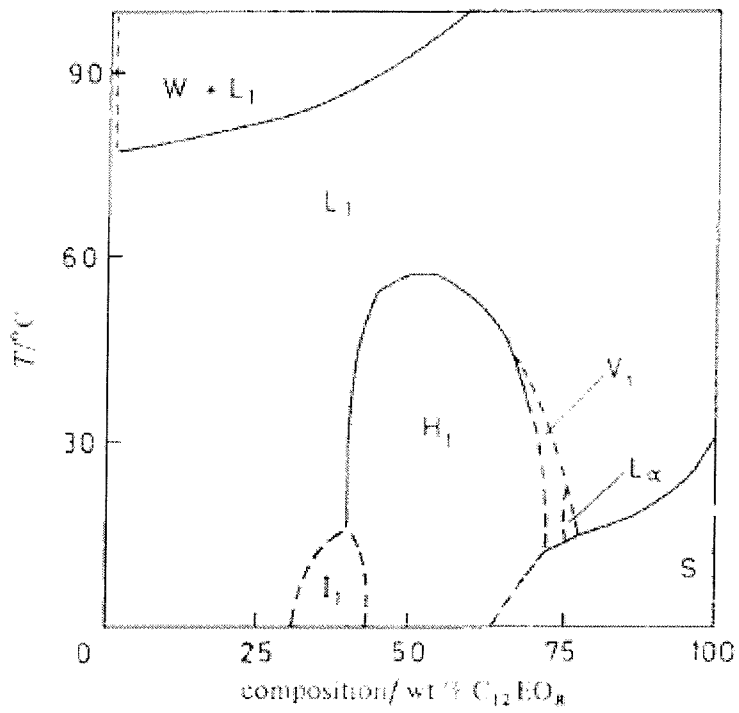

Figure 11 The phase diagram for the binary surfactant-water system of $C_{12}EO_8$,[36] where L_α, H_1 and V_1 are lamellar, hexagonal and bicontinuous cubic phases respectively, and I_1 is a close-packed spherical micelle cubic phase, L_1 is a micellar phase, S is solid surfactant, W is water and L_2 is a liquid surfactant phase containing dissolved water (only partially miscible).

1.5.3 Comparison of the Two Preparation Methods

As mentioned previously, the structures and mechanisms of formation of OMMs are still heavily debated.[5]

The idea of liquid crystalline phases of lytropic liquid crystals influencing the structure of a material was different to the LCT mechanism proposed by Mobil researchers.[3] The Mobil method depended on micelles assembling together at low surfactant concentrations that were above the critical micelle concentration (CMC). Used for the synthesis of M41S materials, these very low surfactant concentrations would not be high enough for any liquid crystalline structures to form in a purely aqueous system.

Thus, silicate ions must help in some way to encourage the liquid crystalline state by serving as counter-ions and stabilisers for the micelle arrays.

Cheng *et al.*[49] managed to synthesise MCM-41 only at surfactant concentrations as low as but not lower than the CMC. This supports further the micellar templating mechanism. If no surfactant was used, an amorphous material would form, and the presence of a surfactant in the synthesis mixture was found to increase the rate of silicate polymerisation by more than 2000 times. This increase in rate further endorses the likelihood of electrostatic interactions between surfactant and inorganic species bringing the silica oligomers physically close together for the polymerisation reaction.

Subsequent work by Kruk *et al.*[45] provided some evidence that MCM-41 materials formed via self-assembly of silicate-surfactant ion pairs. TEM images confirmed hexagonal structure with pores of nanometre dimensions.

Nonetheless, the formation mechanisms are likely to rely heavily on the synthesis routes taken: different silica sources and/or surfactant template concentrations may result in different formation mechanisms.

Conversely, Attard *et al.*[4] employed high surfactant concentrations to form liquid crystalline phases and was able to produce hexagonal structure with pores in nanometre dimensions. The concentrations used were above 30 wt% typically which guaranteed templating in one liquid-crystalline phase.

Furthermore, the latter used non-ionic surfactants unlike the Mobil method which involves charge interaction between the surfactant head group and the material forming. Therefore the Mobil method would be more likely restricted to the type of materials produced, e.g. inorganic oxides like silicas.

So far, liquid crystalline phases were used for their properties, e.g. in shampoos, and not for their structure. This may soon change, as it now appears possible for surfactant aggregates to transfer structure to a material. Choices of surfactants and synthesis conditions can now be controlled to obtain predicted mesophase products.

1.6 Nomenclature

According to IUPAC recommendations,[50] pores are classified as micropores (width below 2 nm), mesopores (width between 2 and 50 nm), and macropores (width greater than 50 nm). In the literature, there seems to be no distinction between mesoporous and nanoporous materials. In fact, Attard *et al.*[1] has used the term *nanostructure(d)* or *mesostructure(d)* to describe such materials. TEM images showed the silica to have a well-ordered structure of nanometre dimensions, see Figure 10.

1.7 Advantages of TLCT

In summary, "liquid-crystal templating" mechanism (LCT) depends on mainly unpredictable heterogeneous precipitation of ordered structures from bulk solution.

On the other hand, the benefits of "true liquid crystal templating" (TLCT) are the high degree of control and predictability over the pore morphology of the material through choice of phase and surfactant (Figure 12). The structure of the product can be known deductively from the binary phase diagram of the surfactant/water system.

The synthesis of a hexagonal direct-templated structure using $C_{12}EO_8$ by Attard *et al.*[4] produced a specific surface area greater than 1000 $m^2\ g^{-1}$ after calcination, with a narrow pore size distribution at 20 Å diameter. These values measured up well with the large surface areas obtained for MCM-41, the hexagonal M41S analogue with the BET surface areas up to 1950 $m^2\ g^{-1}$. The high surface areas of mesoporous materials are attractive in catalytic applications. The regularity of the pore size within the structures is also attractive for size-selective catalysis.

The most interesting would be the versatility of the method, where other materials may be produced, because using a non-ionic polyoxyethylene surfactant such as $C_{12}EO_8$ suggests that charge interactions between surfactant headgroup and a precursor may not be important. Mesoporous materials other than silica could be synthesised. Thus a wide variety of mesoporous materials, from metals to polymers, in the lyotropoic liquid crystal phase may become a reality soon.

So far, the mesoporous materials discussed contained silica. Work on introducing transition metals into mesoporous materials has been reviewed by Seddon *et al.*[5] Their

oxides contained variable oxidation states which may be useful for tailoring catalytic, electronic and magnetic properties of materials.

In 1997, Göltner *et al.*[51] synthesised direct-templated mesoporous materials, i.e. using a lyotropic non-ionic liquid crystalline phase. This led further to studying *in situ* redox reactions where a regularly structured metal colloid such as Pt metal was grown in the aqueous domains of $C_{16}EO_8$ by *in situ* chemical reduction of a metal salt.[1] Solvent extraction removed the surfactant, producing uniform 3 nm cylindrical pores, i.e. mesostructured high surface area Pt metal.

Significantly, this was further developed by Attard *et al.*[2] in 1997 with the help of electrochemistry. Very high specific surface areas in Pt films were confirmed by electrochemical characterisation, and the films were found to contain regular mesostructures and were very flat and of uniform thickness. Furthermore, it was possible to predetermine the nature of the mesostructure through the use of different liquid crystalline phases and to control the dimensions by use of polyoxyethylene surfactant templates of different chain lengths and the addition of *n*-heptane as an auxiliary swelling agent.[1, 6]

The range of mesostructures is therefore restricted to the lyotropic polymorphism of the selected surfactant system, see Figure 12. For instance, materials deposited in the hexagonal phase will contain pores aligned on a hexagonal lattice whereas those in the cubic phase will contain interconnected three-dimensional cylindrical pores.

Possibly the most important advantage of the TLCT method over other routes is that nanostructured monoliths (macroscopic uncracked pieces of material) could be synthesised. The pore size distribution in the materials remain strictly mesoporous, with no microporosity or interparticle macroporosity.

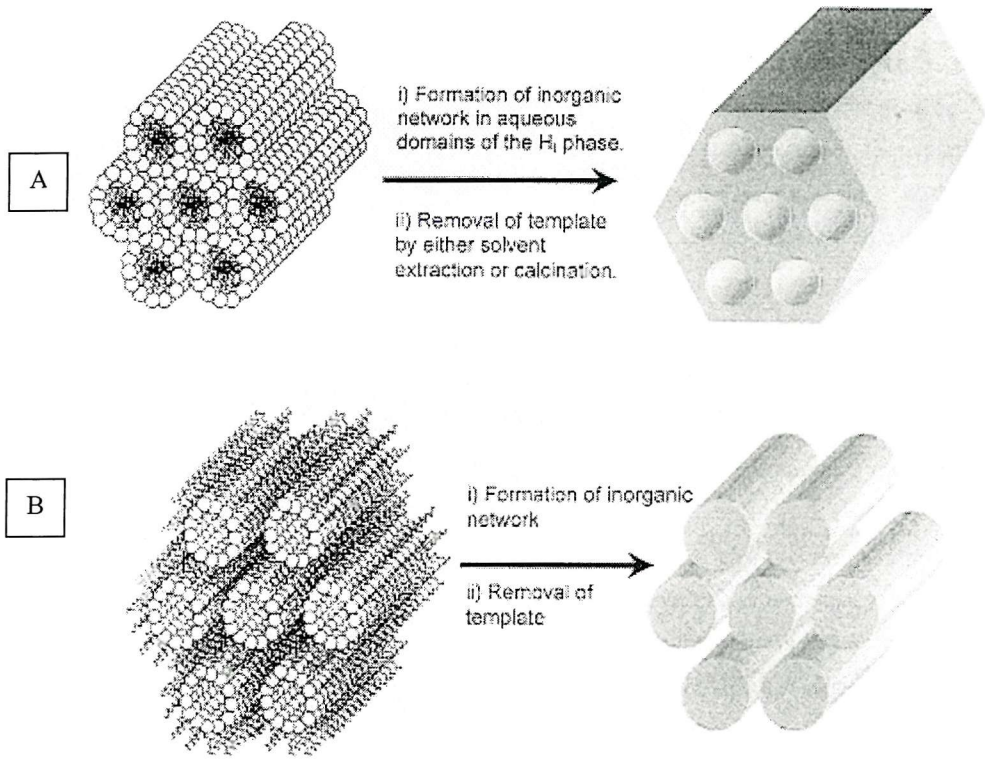

Figure 12 (A) A schematic drawing[33] of the formation of mesoporous materials in the hexagonal phase of a surfactant. Hexagonal arrays of cylindrical micelles form with the polar headgroups of the surfactants (spheres in the drawing) on the outside and with the hydrocarbon chains towards the centre. Removal of the surfactants forms hexagonal arrays of cylindrical pore. (B) A schematic drawing[33] of the formation of mesoporous materials in the inverse hexagonal phase of a surfactant. Inverse hexagonal arrays of cylindrical micelles form with the polar headgroups of the surfactants (spheres in the drawing) on the inside and with the hydrocarbon chains towards the outside. Removal of the surfactants forms inverse hexagonal material (consisting of long cylinders).

1.8 Mesoporous Platinum Templated from $C_{16}EO_8$

1.8.1 Chemical Reduction

Attard and coworkers[1, 33, 6] reduced chemically hexachloroplatinic acid hydrate (HCPA) in the aqueous regions of the hexagonal liquid crystal phase of a non-ionic surfactant called octaethylene glycol monohexadecyl ether ($C_{16}EO_8$). Chemical reduction was achieved by placing a thin layer of the mixture onto a sheet of steel for about 4 h, after which the resulting black mixture was removed and washed successively with acetone, water, 6 M hydrochloric acid, water and acetone.[6] Characterisation of the phase behaviour of these mixtures was carried out by optical polarising microscopy.[34]

This resulted in a Pt film whose nanostructure was representative of the liquid crystalline phase. The specific surface area was found to be approximately 60 m^2g^{-1} which was larger than the commercially available platinum black (35 m^2g^{-1}). This may be advantageous for catalytic applications.

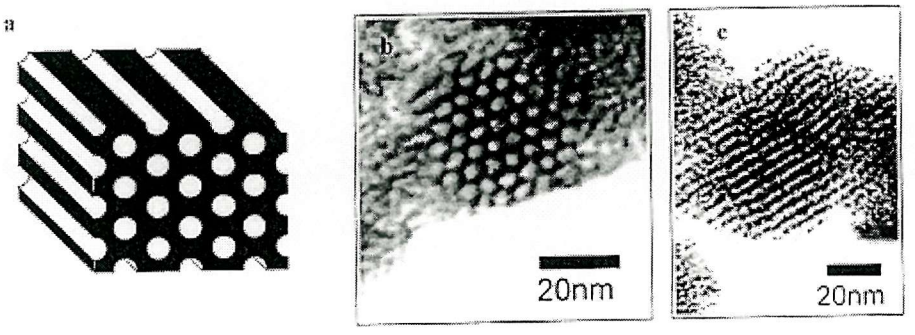

Figure 13 Mesoporous platinum: (A) schematic diagram of the hexagonal pore structure and (B) TEM image of the platinum end on and (c) side on.[33]

1.8.2 Electrochemical Reduction

First reported in 1997 by Attard *et al.*[2], another method for producing nanostructured Pt was electrochemical reduction. The result was a shiny metallic and adherent Pt film with a nanostructure identical to those of Pt powders chemically

synthesized, except that the powders were almost matt black in appearance.[6] Scanning tunnelling microscopy (STM) analysis of the electrodeposited films exposed a remarkably flat surface whose roughness was ± 10 nm over 1 cm^2, accounting for the high reflectance of the films. The thicknesses of the films could be viewed by SEM and varied according to the charge density.

Mesoporous Pt was deposited electrochemically onto gold electrodes from a ternary mixture of H_2PtCl_6, water and $C_{16}EO_8$ surfactant. The surfactant was subsequently removed by soaking the Pt film in water, leaving pores of hexagonal geometry within the Pt film. TEM studies revealed a mesoporous structure consisting of cylindrical holes arranged on a hexagonal lattice; the pore diameter was measured at approximately 25 Å and the wall thickness at 25 Å. The films were estimated to contain, on average, 4.62 x 10^{12} holes cm^{-2}.

Whilst the addition of *n*-heptane to the same plating mixture expanded the pore diameter up to 40 Å, shortening the alkyl chain of the surfactant, i.e. by using $C_{12}EO_8$, reduced the pore diameter to 18 Å approximately. The shorter chained surfactant would form smaller hydrophobic domains than $C_{16}EO_8$. Therefore, the size of the pores was determined by the hydrophobic sections of the hexagonal phase, since Pt was not formed in these domains but in the aqueous domains.

All these observations indicated that the alkyl chain length of the surfactant and the presence of a hydrocarbon additive affected the pore diameter, and that the pore structure was determined by the liquid crystalline phase.

The surface area was thus expected to depend on the pore diameter and the regularity of the nanostructure. Table 1 compares the pore dimensions obtained on Pt films prepared by the two methods of reduction in the presence of $C_{16}EO_8$ and the commercially available platinum black. Electrochemical preparation appears just as capable of producing high surface areas as chemical or industrial preparations. Comparing this data to the Pt electrodeposited in the absence of surfactant but under similar deposition conditions reveals a much lower surface area of 4.5 m^2 g^{-1}.[6] This supports further the highly porous nanostructure of the materials.

Another advantageous outcome is that the surface areas of the Pt films could be electrochemically characterised by cyclic voltammetry. The magnitude of the current

passed from nanostructured Pt was found to be 500 times greater than that obtained for the polished electrode of the same geometric area.[52] This has implications for electrocatalytic applications. In fact, the large electrocatalytic area of nanostructured Pt was confirmed by cyclic voltammetry in the presence of methanol, whose oxidation was observed with the currents passed 100 times greater than at the polished Pt electrode.

Attard *et al.*[53] investigated further the effect of the variables in electrodeposition process on the film properties. As before, electrodeposition was carried out under potentiostatic and thermostatic control, where the potential was stepped from +0.6 V where no chemical change took place to growth potentials ranging from +0.1 to –0.4 V.

Reduction Method	pore diameter by TEM/ Å	Pt wall thickness by TEM/ Å	average pore-to-pore distance by TEM/ Å	Approximate specific surface area / $m^2 g^{-1}$
chemical[6, 33]	30	38	68	60
electrochemical[2, 6]	25	25	50	22
platinum black[6, 53]	no pores	-	no pores	20-35

Table 1 Data comparison of the hexagonal porous structure of platinum films prepared by chemical and electrochemical reduction using $C_{16}EO_8$ surfactant, and platinum black which is commercially available; wall thickness was obtained by subtracting the pore size from the repeat distance.

At 25 ^{0}C, cyclic voltammetric and SEM analyses revealed a considerable increase in surface roughness of the films when the deposition potential was lowered, with the thickest films obtained at –0.1 and –0.2 V and deposition efficiency estimated at 75 %. Changing the deposition potential away from this optimum produced thinner films. Low-angle X-ray diffraction recorded over the range of 0.7 to 3.0 in 2θ degrees exhibited a sharp diffraction peak corresponding to a repeat distance of about 5.3 nm for films deposited at –0.1 V. TEM analysis confirmed a regular nanostructure for films deposited at both –0.1 and –0.2 V.

Temperatures between 25 and 85 ^{0}C were studied for films deposited at –0.1 V. Increasing the deposition temperature noticeably roughened the film morphology in SEM analysis; the repeat distance shifted to 5.6 nm in X-ray diffractograms, and TEM analysis showed rougher inner walls of the pore structure with the nanostructure getting less ordered.

The thickness of the electrodeposited layer of the nanostructured films was found to influence the surface areas.[52] The plot of the electrode roughness factor (real surface area divided by the geometric surface area) versus the deposition charge density (which is proportional to the film thickness) is linear. This suggests uniform accessibility of the internal surface area, i.e. the pore structure, by the electrolyte.

The generic applicability of this method, i.e. electrochemical reduction, could be observed in the preparation of other mesostructured materials. XRD revealed mesoporous metallic tin with a spatially periodic structure with a repeat distance in the range of 5 to 10 nm; the repeat distance was found to depend on the type of non-ionic surfactants used and on the presence of *n*-heptane; and finally the repeat distances of the tin films and the respective plating electrolytes matched well, supporting the TLCT theory.[54]

It must be noted that *nanostructure is obtainable* but not in all cases. For example, the TEM image of mesoporous silver obtained from a hexagonal Brij® 56 phase does not show hexagonal geometry.[52] The reason could be due to Brij® 56 (an average composition of $C_{16}EO_{10}$) being not as pure as $C_{16}EO_8$, but this is contradicted by another example, a typical TEM image of tin electrodeposited in the presence of $C_{16}EO_8$ also not showing nanostructure.[54]

Deposition of a metal, such as Pt, in the hexagonal phase of Brij® 56 has produced a mesoporous structure consisting of cylindrical holes arranged on an hexagonal lattice.[2, 6] When using related surfactants, the diameter of the holes was found to vary according to the alkyl chain length of the surfactant. Therefore, based on the chemical formula of Brij® 56 where there are 36 carbon atoms per surfactant and assuming a carbon-carbon bond length of 1 Å, the radius of a hole is estimated to be 36 Å, i.e. the diameter at 72 Å. This diameter can increase to about 80 Å, if we take into account the headgroup size etc.

The porosity is often less and this is likely to be caused by interactions. In the production of nanostructured Pt, Attard *et al.*[34] suggested that hexachloroplatinate anions interact with the EO headgroups of the surfactant, $C_{16}EO_8$, resulting simultaneously in an increase in the steric cross-section of the headgroups and in an increase in the electrostatic repulsion between headgroups.

However, using lyotropic liquid crystals as templating agents can produce films with highly ordered well-controlled porosity only if the electrodeposition conditions are controlled to eliminate unwanted side reactions. For example, in the case of Pt, films showing a well-defined and ordered nanostructure, i.e. a hexagonal arrangement of pores, were obtained when deposition was carried out at –0.1 V vs. SCE and above;[53] the degree of nanostructure was found to decrease with deposition temperature, where the channels became less straight with a degree of meandering observed. According to Attard *et al.*,[53] side reactions like the evolution of gas at the electrode/electrolyte interface (which is feasible for Pt electrodes held at such potentials) could result in the disruption of nanostructure, as shown by TEM and X-ray diffraction measurements.

Thus, obtaining nanostructure is made possible by changing the deposition conditions. The degree of control afforded by electrochemistry confirmed its simplicity and versatility in producing mesoporous materials which could then be customised for specific applications.

1.9 Mesoporous Palladium

One of the advantages of TLCT is the versatility of the method, where mesoporous materials, other than silica, may be produced, because using a non-ionic polyoxyethylene surfactant such as $C_{16}EO_8$ suggests that charge interactions between surfactant headgroup and a precursor may not be important. Recently, mesoporous metal films containing very high surface areas have been produced electrochemically by using lyotropic liquid crystalline phases as templating agents. Their possible use as gas sensor catalyst material has been one of the driving forces for their studies.

Palladium (Pd) is known to be a suitable catalyst for oxidising methane and has been used in the construction of a gas sensor called the planar pellistor, in the catalyst layer.[8] Micromachined technologies have been developed since 1990s in the field of gas sensors, helping to create a novel catalytic gas sensor, i.e. the planar pellistor. The pellistor is a miniature calorimeter that can measure the energy liberated on oxidation of a combustible gas.[55] They consist of a spiral platinum wire cloaked in porous alumina which contain precious metals, commonly Pd, whose catalytic properties are essential to their sensory performance. Catalytic activity was found to be enhanced by increasing the surface area of catalyst, resulting in lower operating temperatures (about 500 ^{0}C), thus lower power comsumption and longer sensor lifetime.

Mesoporous Pd has already been electrodeposited by Guerin onto Au electrodes in the hexagonal phase of $C_{16}EO_8$ at room temperature for the purpose of constructing a planar pellistor.[35] These Pd films were electrodeposited onto gold electrodes and were prepared under a single set of deposition conditions: 12 % ammonium tetrachloropalladate, $(NH_4)_2PdCl_4$, + 47 % $C_{16}EO_8$ + 2 % heptane + 39 % water; using a single potential, +0.1 V vs. SCE; and at one temperature of 25 ^{0}C. This composition produced a dark brown viscous glue-like mixture, which under the polarised light optical microscope displayed a feathery texture akin to the hexagonal phase. There was some TEM evidence for the existence of a mesoporous structure in the resulting Pd films, which revealed pores of 25 ± 2 Å diameter and walls of the same thickness arranged on a hexagonal lattice. Cyclic voltammetry of these films in sulfuric acid provided an estimation of the specific surface areas, i.e. between 20 and 30 m^2 g^{-1}. Electrochemical

Quartz Crystal Microbalance (EQCM) measurements showed a 97 % faradaic efficiency for the electrodeposition of mesoporous Pd.

After electrodeposition of these Pd films, methane gas was used for gas testing on these pellistors, which responded well to the presence of methane. The response was found to vary linearly and reproducibly with the concentration of methane in air between zero and 2.5 %. However, the reproduciblity did not extend from sensor to sensor, and long time exposure to air at high temperatures, above 500 ^{0}C, reduced their sensitivity, probably due to the formation of bulk palladium oxide. On the other hand, the power consumption and response times were found to be similar to those of commercial pellistors. After testing with methane, the pellistors were subjected to additional cyclic voltammetry in sulfuric acid, showing a reduction in their catalyst electroactive surface.

However, at already stated, these studies were restricted to a single set of deposition conditions: that is using one particular surfactant, at one composition, for one choice of Pd salt composition, and at a single deposition temperature.

Our work in this area set out to recreate and extend the experimental conditions using an alternative cheaper surfactant, Brij® 56. The main purpose of this part of the work was to find the conditions suitable for depositing Pd films on pellistors for comparison with the data obtained by Guerin. A phase diagram of the Brij® 56 system was constructed and showed that the hexagonal phase occurs for a similar composition and range of temperature as for $C_{16}EO_8$. Electrodeposition studies were carried out in both the hexagonal and cubic phases of Brij® 56, examining effects of, for example, varying the deposition potential and temperature. In addition, reproducibility and repeatability studies were analysed, by, for example, looking at different compositions of the Brij® 56 system. SEM and TEM characterisations of the films were also supported by low angle X-ray diffraction.

Therefore, the main objective of this part of the work was to find a much cheaper surfactant for the electrodeposition of mesoporous Pd on planar pellistors, which would respond to methane gas testing.

1.10 PANI and Diffusion

The rest of the thesis looks at the attempts to polymerise aniline in the hexagonal phase of $C_{16}EO_8$ and to characterise the poly(aniline) [PANI] films made. In addition, studies on diffusion of the ferricyanide redox couple in the presence of Brij® 56 may give a clearer picture of carrying out electrochemistry in the lyotropic liquid crystalline phases of a surfactant. Both of these studies are novel because firstly, a conducting polymer was deposited for the first time in a lyotropic liquid crystalline phase, and secondly, diffusion studies of an electrochemical probe were carried out for the first time in a lyotropic liquid crystalline phase.

Most importantly, the combination of this work along with the work of mesoporous Pd expanding the previously limited Pd studies in several important directions, show the different facets to electrodeposition in the lyotropic liquid crystalline phases of a surfactant, and that using a cheap and widely available surfactant, i.e. Brij® 56, can be used to construct a gas sensor.

Chapter Two

2 Experimental Section

Because the thesis contains three different chapters of results and discussion where the different experimental conditions are described in greater detail, this chapter contains information on experimental conditions relevant to all of the chapters.

Electrochemistry was conducted on a purpose-built electrochemical workstation, with a three-electrode system in a Faraday cage. Water used in the experiments and for cleaning glassware was deionised, produced by passing tap water through a Whatman RO 50 water purification system. Glassware was cleaned by soaking in 3 % Decon 90 (Aldrich) solution for 24 h followed by rinsing with deionised water and drying in an oven at 50 ^{0}C. The experimental temperature was controlled to within ± 0.1 ^{0}C of the set temperature over the range 25 to 100 ^{0}C by placing the sample in a Pyrex water-jacketed cell and using a Grant Y6 thermostatted water bath for circulating water round the cell.

2.1 Electrodes

Counter Platinum gauze was used as counter electrode and was cleaned by soaking in Decon 90 and flamed before each experiments.

Reference The reference electrodes used were homemade saturated calomel electrodes (SCE) and stored in saturated potassium chloride solution. All potentials were measured according to SCE, which is a shift of –0.268 V against the hydrogen reference electrode (RHE). Checked against a commercial SCE electrode, a difference of ± 1 mV was tolerated.

Working Three types of gold working electrodes were used depending on the experiments.

2.1.1 Working electrodes

0.2 mm diameter gold disc electrodes and other disc electrodes

For typical electrochemical experiments, they were made from metal wires embedded in epoxy resin. Conducting silver paint ensured electrical contact. They were

cleaned by polishing manually with wet dry paper of various grades from 320 to 1200 and with alumina of various particle diameter from 25 to 0.3 μm, using deionised water for rinsing. They were also cleaned electrochemically in 1 M sulfuric acid by cyclic voltammetry: -0.2 < potential E < +1.8 V vs. SCE at 200 mV/s at room temperature.

In the diffusion experiments, gold microelectrodes were used.

for scanning (SEM) and transmission (TEM) electron microscopy studies

The gold substrate used consisted of a thin evaporated gold layer (about 250 nm thick) on a chromium layer (about 7 nm thick) on glass and were made by Alastair Clark, Department of Chemistry, University of Southampton. They were treated to an ultrasonic bath with isopropanol. The surface area of the gold layer was controlled by using polyimide tape.

for gas sensors

The sensors used for gas testing were known as SRL136a which contained each a gold layer of 1.2 mm^2 surface area. These sensors will be described later. Their fragility only allowed cyclic voltammetry in sulfuric acid for cleaning, see above for details.

2.1.2 Relative Cleanliness of the Gold Substrates

The cleanliness of gold is relative depending on the substrate type, as can be seen in the experimental details described above. For instance, no manual polishing with wet and dry paper or alumina was allowed on gold substrates used for microscopy or sensor work. Another example, no cylic voltammetry in sulfuric acid was performed on gold substrates used for microscopy work.

Thus, only cyclic voltammograms for typical disk and sensor experiments could be used to compare the cleanliness of gold.

The different amplitudes of the currents in Figure 14 show that for a clean gold surface, the cyclic voltammogram for the sensor SRL136a is larger in size due to a larger gold area of 1.2 mm^2, compared to 0.03 mm^2 for a 0.2 mm diameter gold disk electrode. Its shape is also reproducible on the smaller scale, i.e. oxidation peak corresponding to

adsorption of oxygen on gold starting at +1.2 V and the reduction peak being at +0.85 V corresponding to the stripping of the gold oxide.

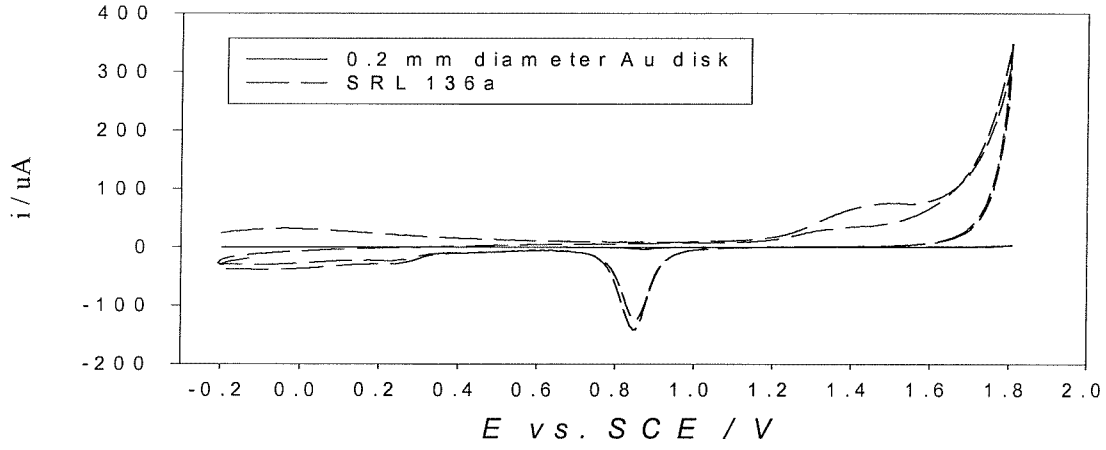

Figure 14 Two cyclic voltammograms of clean gold substrates as labelled above, in 1 M sulfuric acid at room temperature and at 200 mV/s. The scan started at –0.2 V anodically and finished at –0.2 V cathodically.

Both voltammograms do have a double layer capacitance between 0 and +0.6 V, but because this region appears larger in the SRL136a case, this suggests that the gold electrode may not be as clean as the disk electrode which was subjected to additional manual polishing. Because of its fragility, no other technique has been found to be appropriate for cleaning it further.[35] Thus, only clean sensors were used.

The oxidation region can be affected by the degree of polishing with alumina. Sometimes, three merged oxide peaks appear and this is due to the presence of three different types of gold surfaces (e.g. 111, 110, 100). In addition, the more polished the gold surface becomes, the sharper the reduction peak of the oxide becomes due to smoother gold surface.

2.2 Apparatus

2.2.1 Glass Cell

Using the three-electrode setup, experiments on disk electrodes were carried out in a glass cell. Due to the viscosity of the liquid-crystalline mixtures, a simple thermostated glass cell was used, which was also used for aqueous mixtures.

2.2.2 Droplet apparatus

This was used to carry out experiments for SEM, TEM and sensor work. The idea was to control the gold electrode area being used.

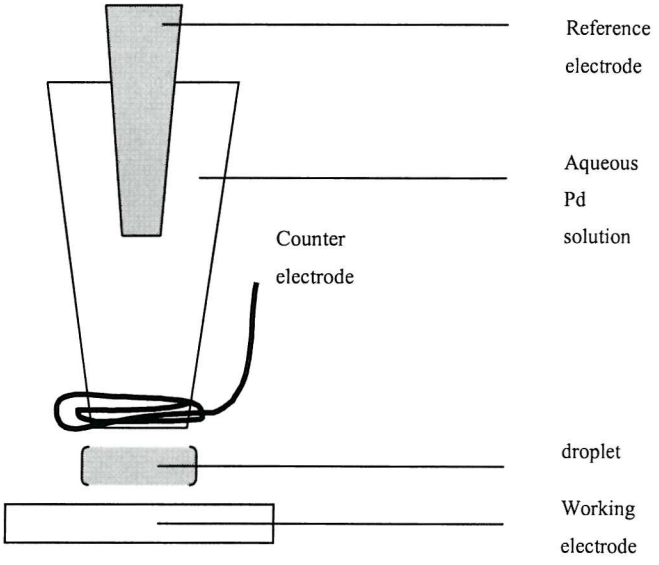

Figure 15 Diagram of the droplet apparatus.

In addition due to the fragility of the SRL136a and its electrical contacts, the droplet method appeared the best for working on this type of sensor. The positioning of the electrodes and the droplet was controlled with the help of *x, y, z* microstage and of an optical microscope. For cleaning the gold electrode area on the sensor and for characterising the electrodeposited Pd film, cyclic voltammetry in 1 M sulfuric acid

droplet was carried out. Otherwise, electrodeposition took place using the droplet of the relevant templating mixture.

2.2.3 Electrochemical apparatus

A scan unit, potentiostat, voltage source and a multimeter were used in this project. The electrochemical responses were recorded by computer and also by a potentiostat [EG&G]. All experiments were performed in a Faraday cage to prevent any noise effect on the experiments.

2.3 Chemicals

2.3.1 PANI and Pd Experiments

As mentioned previously, lyotropic liquid crystals form from surfactants in aqueous media at various compositions and temperatures. It is their phases that could be transferred onto metals or ceramics, increasing their surface areas, hence mesoporous materials.

In summary, the templating solutions consisted of the surfactant, water and a precursor salt.

The deposition of poly(aniline) was carried out in the following systems:

- aqueous solution, of 0.4 M aniline (Sigma Aldrich) and 1 M H_2SO_4 (Sigma Aldrich) solution, at 25 °C; n.b. aniline was purified by filtering it through alumina (BDH);
- hexagonal phase, 50 wt% $C_{16}EO_8$ (Fluka) and 50 wt% (0.4 M aniline and 1 M H_2SO_4 solution), at 25 °C;

The deposition of Pd was carried out in the following systems:

- aqueous solution, 40 mM $(NH_4)_2PdCl_4$ (Johnson Matthey) at 25 °C;
- hexagonal phase, 60 wt% Brij® 56 (Sigma Aldrich), 40 wt% of 1.06 M $(NH_4)_2PdCl_4$ / heptane (BDH) at 25 °C;

- cubic phase, 60 wt% Brij® 56, 40 wt% of 1.06 M $(NH_4)_2PdCl_4$ / heptane at 55 °C.

The equal ratio of the Brij® 56 to the Pd salt solution was also studied. Note, the ratio of 4 mol Brij® 56 to 1 mol heptane was used; heptane was used by Guerin[35] in his work and has been found by Attard *et al.*[2] to increase the pore diameter of a metal film.

2.3.2 Diffusion Experiments

In the diffusion experiments, these were the chemicals used: potassium ferricyanide (99 % purity, Avocado); potassium chloride (Analar, BDH); hexaammineruthenium (III) chloride (99 % purity, Strem Chemicals); Brij® 56 (Sigma Aldrich). All reagents were used as received. Deionised water purified by the Whatman System was used to prepare solutions.

2.4 Constructing a Phase Diagram

The phase behaviour of lyotropic liquid crystalline mixtures was studied using an Olympus BH-2 polarised light microscope connected to a Linkam TMS90 heating stage and temperature control unit. Phases were assigned on the basis of their characteristic optical textures.[33, 36]

Mixtures contained a non-ionic surfactant in which the surfactant-to-water ratio was changed, while the concentration of the precursor in water, was kept fixed, e.g. Pd templating solution at 1.06 M.

It was important to ensure the homogeneity of the surfactant mixtures. Samples for study were prepared by accurately weighing out the required amount of surfactant and aqueous precursor solution into a glass vial. After initial manual mixing for 5 minutes, they were placed in sealed containers which were heated in an oven at low temperature (about 50 ^{0}C) for no more than 15 minutes whereupon they were allowed to return to room temperature for 2 h before use.

To construct a phase diagram, several mixtures of different compositions of surfactant and water, in weight percentage (wt %), were examined. The phase transition boundaries were located to an accuracy of ± 2 ^{0}C by using heating/cooling rates of 0.2 ^{0}C min^{-1}. A phase diagram is therefore a useful summary of the behaviour of lyotropic liquid crystalline systems with the x-axis as the surfactant concentration and the y-axis as the temperature. At any point in the diagram, a phase is stable, and where different phases are stable, curves are used to divide such regions.

2.5 Brief Description of Electron Microscopy

Electron microscopy studies the surface of the metal films deposited. The wavelength of visible light limits light microscopy, and electron imaging of a sample is the best solution for viewing detail on a nanometer scale.

When light falls on an object, the effects can be reflection, scattering, transmission, absorption or light being re-emitted at another wavelength. Electron microscopy makes it possible to cause various effects to take place in the sample, making it a more powerful tool than light microscopy, see Figure 16.

The various effects of the interaction between the primary electron beam and the sample include those used for imaging in scanning electron microscopy (SEM) and transmission electron microscopy (TEM).

When inelastic collisions are produced on the sample surface, outermost electrons are knocked off the specimen atoms and are known as secondary electrons which are used to image surfaces in SEM.

Backscattering is the result of any electron that gets turned back out of the specimen with the amount depending on the atomic number of the elements in the specimen. Collected in the SEM, this imaging can be used to map elemental composition.

Another emission is photons of x-radiation with wavelength and energy characteristic of the elements in the specimen. The spectrum of the radiation is useful for elemental identification, using either wavelength or energy (known as wavelength dispersive or energy dispersive x-ray spectroscopy, WDX and EDX respectively).

In TEM, transmitted electrons are electrons that penetrate a very thin sample and can deflect from the line of the primary beam losing energy through collisions.

In this thesis, the porosity of the structure was studied by TEM while the morphology and the composition were studied using an SEM fitted with an EDX detector.

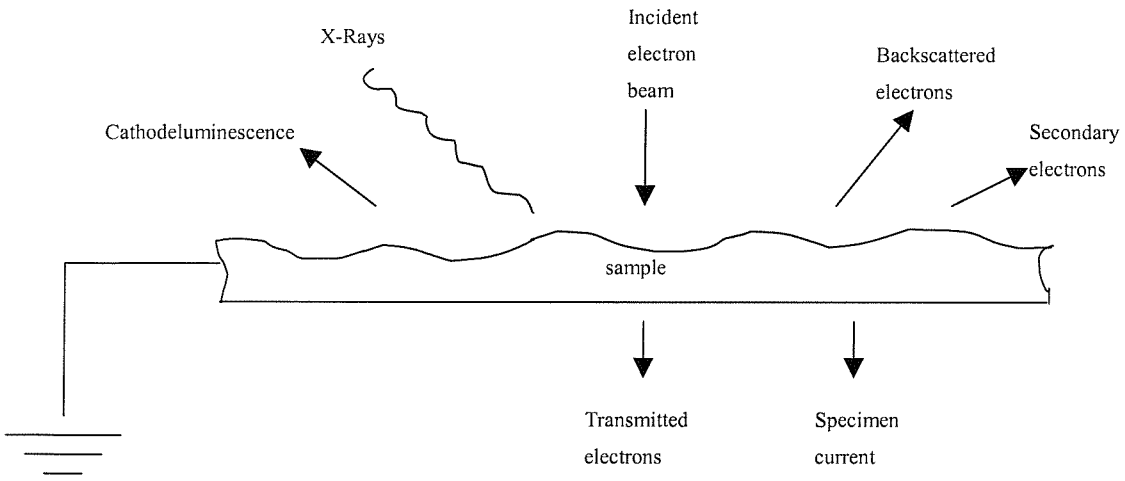

Figure 16 A schematic of the effects of an electron beam striking the sample.[56]

2.5.1 Scanning Electron Microscopy (SEM) and Energy Dispersive X-Ray Spectroscopy (EDX)[57]

Scanning electron microscopy, SEM, is useful for studying the surface morphology of bulk samples whilst EDX looks at elemental composition; both techniques operate on a micron scale. Currently, the resolution of scanning electron microscope is limited to about 25 Å.

A JEOL JSM 6400 Analytical Scanning Electron Microscope was used in this project. A gun shoots a beam of accelerated electrons produced by a filament, with the applied accelerating voltage varied up to 40 keV. Electromagnetic lenses aid focusing and magnification.

Here a fine electron beam scans across the sample surface in a vacuum, interacting with the sub-atomic structure of the sample. The primary imaging method collects secondary electrons released from the surface of the sample; only the electrons closest to the surface have enough energy to escape; hence this technique is surface sensitive. By correlating the sample scan position with the resulting signal, an image forms similar to what would be seen using an optical microscope. A natural looking surface morphology could then be shown by illumination and shadowing.

In EDX, imaging of backscattered electrons can be used to map elemental composition, its yield giving compositional information which is related to the average atomic number of each point on the sample.

2.5.1.1 Sample preparation

Samples made in this thesis were glued to aluminium stubs with conducting cement, with a tiny section of each sample painted with silver conducting paint

2.5.1.2 Surface Analysis

After the samples were inserted into the vacuum chamber of the SEM, magnifications below ×100 000 were studied and recorded on rolls of photographic film. Identification of elements present in the sample was aided by EDX analysis.

2.5.2 Transmission Electron Microscopy (TEM)[57]

In TEM, a JEOL 2000FX instrument was used and a gun shoots a beam of accelerated electrons produced by a filament, with the applied accelerating voltage varied up to 200 keV for sample penetration. Note, with time, this high voltage can induce localised heating of the sample destroying structure porosity. Electromagnetic lenses aid focusing and magnification with image magnified onto a fluorescent screen.

2.5.2.1 Sample preparation

Metal films were scraped onto a 3.05 mm, 400 mesh copper grid that supported a carbon film (supplied by Agar Scientific), which were initially moistened with acetone. The grids were dried under vacuum overnight before placing in a metal sample holder and inserting into the vacuum chamber of the TEM.

2.5.2.2 Imaging

Magnification of ×120 000 was used to observe the nanostructure and the stability of the samples under the electron beam could change with time. Thin edges of sample gave the best viewing for ordered porosity. Images were recorded on photographic plate which were developed into negatives.

The negatives were then imaged with AGFA Duoscan T1200 scanner containing a transparency tray designed for scanning negatives in 12-bit greyscale. The sharpness of images could then be managed with an image software such as Paint Shop Pro. Measurements, from the images, such as pore to pore distance were carried out using Scion Image software.

2.6 Brief Description of Powder X-ray Diffraction

In this technique, the x-ray beam strikes a finely powdered sample containing crystals whose lattice planes cause the beam diffraction, and it has been used in studies of polycrystalline materials.

Powder x-ray patterns recorded can then be interpreted with the Bragg equation (see equation 1). They are a collection of signal peaks that arise due to constructive interference of the x-ray beam by planes oriented at the Bragg angle, 2θ.

$$d = \frac{n\lambda}{2\sin\theta} \qquad \textbf{Equation 1}$$

λ is the incident beam wavelength and *d* the lattice spacing. A Cu $K_{\alpha 1}$ radiation source was used (λ=1.5406 Å). A scintillation counter records the detection of the scattered rays producing signals at wide angles from 10 to 90 ^{0} for crystalline materials.

This technique has proved very useful in examining the phase, quality and repeat distance of the structure when characterising mesoporous silicas.[58] Bragg reflections were observed at low angles where 2θ is lower than 10°, rather than wide angles, identifying the liquid-crystalline phase of the sample, i.e. H_I, V_I and L_α. Note, the sharpness of the peaks recorded in the pattern is dependent on the long range order.

2.6.1 Equipment

Figure 17 shows a conventional diffractometer, Siemens D5000, using copper radiation passed through a single crystal monochromator giving only $K_{\alpha 1}$ radiation. Collimated through an aperture diaphragm, the monochromatic x-ray beam was focused onto the sample, which was mounted flush in a recessed aluminium or plastic holder. A standard scintillation counter detects diffracted x-rays, and when the sample goniometer was rotated at a constant angular velocity, the detector moved at twice this velocity to ensure the diffraction angle, 2θ. Diffraction data were recorded with the help of computer software called the Adjust Software.

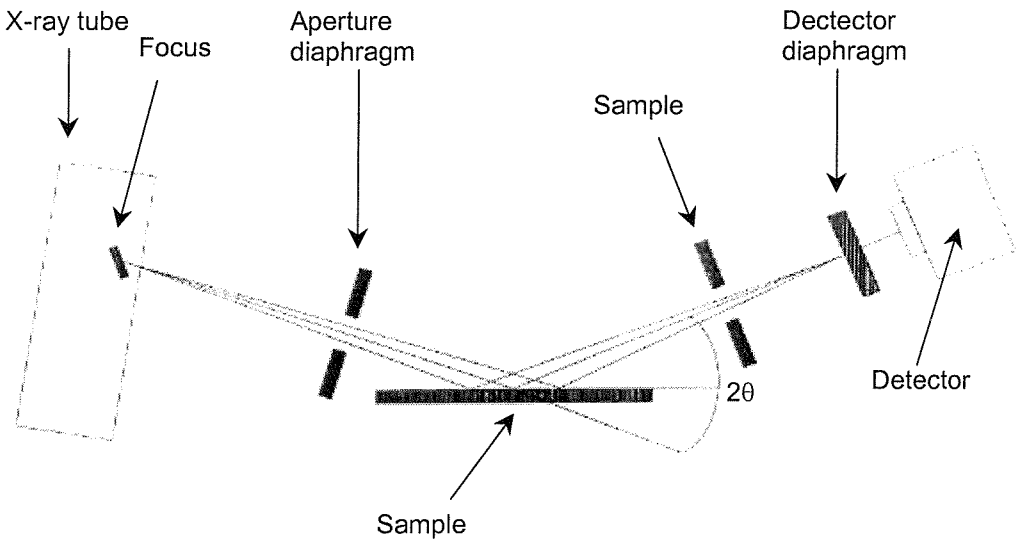

Figure 17 A schematic representation of the Siemens D5000 diffractometer, from reference 13.

2.6.2 Sample preparation and data collection

Metal films were electrdeposited on Au evaporated microslides. For x-ray experiments, a sample was placed onto an aluminium holder of circular indentation which was 30 mm in diameter and 1 mm deep, using blue tack. Gently forcing a glass microslide made sure that the sample was horizontally flat. If the sample was template mixture or in powder form, the surface of the material would be made flush with the sides of the holder. In the case of palladium salt or metal film, a plastic holder would be used to avoid it reacting with the aluminium. Low angle XRD scans were recorded over a 2θ range for 20 minutes.

Chapter Three

3 Electrochemical Study of Diffusion in the Surfactant System

3.1 Introduction

The aim of this chapter was to study the process of diffusion of an electroactive probe, such as ferricyanide, in a lyotropic liquid crystalline phase of a surfactant called Brij® 56. The effects of the formation of the lyotropic liquid crystalline phase by Brij® 56, at the relevant composition and temperature, on the diffusion coefficient of the redox probe could be compared to the aqueous system (i.e. in the absence of surfactant).

This introduction reviews diffusion studies for electrochemical probes in surfactant solutions. Surfactants contain polar or charged head groups and nonpolar hydrocarbon chains and are also known as "surface-active agents". These molecules adsorb at the interface between two phases, e.g. air and water, or electrode and solution; this adsorption (or surface activity) is the direct result of the decrease in interfacial tension, i.e. the minimisation of interfacial free energy.[59]

Micelles are probably the most commonly studied aggregates of surfactants; they form in water when the concentration of a soluble surfactant exceeds the critical micelle concentration (CMC). The physical properties of the solute, like conductivity and surface tension, exhibit sharp discontinuities at the CMC. CMC values for common surfactants range from 10^{-4} to 10^{-2} M.[60] Above the CMC, the micellar structure tends generally towards globular or spherical, where the micellar radius corresponds roughly to the extended hydrocarbon chain length. Increasing the surfactant concentration further causes the globular micelles to turn into larger rodlike micelles.

Not all surfactants form micelles in water; some surfactants disperse in water to form lamellar liquid crystalline phases or vesicles. Lamellar dispersions are layered structures of surfactant bilayers and water. Vesicles are closed bilayer structures and are much bigger than micelles, normally by an order of magnitude. The typical size for a vesicle is in the μm range compared to the thickness of the bilayer in the nm range so that the bilayer appears to be a 2-d system in a 3-d space.[61]

Other liquid surfactant solutions at higher surfactant concentrations form microemulsions. Microemulsions are normally composed of oil, water and surfactant(s), giving thermodynamically stable, optically clear fluids. The oil and water domains are well separated by the organised surfactant monolayers.[61] Microemulsions are normally globular or spherical dispersions with the droplet size usually greater than that of micelles.[61] Microemulsions have practical industrial applications such as secondary oil recovery[62] and in the synthesis of colloids,[63] as well as potential drug delivery systems because of their improved drug solubilization, long shelf life, and ease of preparation and administration.[64]

Diffusion can play an important part in electrochemical measurements, as well as in surfactant solutions.

3.1.1 Diffusion in Micellar Solutions

Electrochemistry has been used since the 1950s to characterise diffusion of micelles.[65, 66, 67, 68] The diffusion coefficients of electroactive probes in micellar solutions have been used to calculate the diffusion coefficients of micelles and can give the average micelle radius through use of the Stokes-Einstein equation.[69, 70] Recently, rotating disk electrode voltammetry was used with ferrocene acting as an electroactive probe to determine the long-time self-diffusion coefficients of Triton X-100 micelles.[71] It is helpful for the probe to have a high equilibrium constant for binding to the micelle and to display reversible electrochemistry.

According to a review by Rusling,[60] the experimentally determined probe diffusion coefficient takes an apparent value, D', due to the equilibrium between the free probe in solution and the probe bound to the micelles.

$$D' = f_a D_o + f_b D_1 \qquad \textbf{Equation 2}$$

where f_a is the fraction of free probe, f_b is the fraction of probe bound to micelles, and D_1 and D_o are the diffusion coefficients of the micelle and free probe in the bulk phase respectively. This equation applies to systems with a single distribution of sizes of

micelles. This equation only holds if the equilibrium between the free and bound probe is faster than the experimental timescale so that the equilibrium is maintained throughout the measurement.[72]

If a system shows slower kinetics, the distribution of the probe between the micelles and the free solute is fixed during measurements, and then the equation, for the measurement of large electrodes, becomes

$$D' = \left(f_a D_o^{1/2} + f_b D_1^{1/2} \right)^2 \qquad \textbf{Equation 3}$$

In his analysis of fast versus slow probe-micelle equilibrium, Rusling found that D_o and D_1 in the two cases were the same within experimental error, and showed that errors were more likely if the slow equilibrium model was used for data for which the other model was more relevant.

If the binding of the electroactive probe to the micelles is strong, it is noticeable that the current and D' are diminished. Ferrocene binds well to cetyltrimethylammonium bromide (CTAB) micelles, with D' being about 0.7 x 10^{-6} cm^2 s^{-1}, whereas its oxidation product, ferrocinium ion, is not bound to the micelles and gives a ten times greater D'.[73] Similar results have been obtained in the case of tetrathiofulvalene (TTF) bound to CTAC micelles and in Brij® 35.[60]

Furthermore, it is important to note that D' for probes decreases with increasing *micelle* concentration,[70, 74] as in the case of ferrocene.[75] The concentrations of probes ranges typically from 0.1 to 5 mM, with surfactant concentrations greater or equal to the cmc.[60] On the hand, D' was found to be independent of *probe* concentration in microelectrode voltammetry experiments.[75]

Electroactive probes in micellar solutions have also been used to determine cmc values of various surfactants. In cyclic voltammetry experiments, adsorption peaks for the methyl viologen cation radical[76] and the peak current of ferrocyanide[77] were used, amongst other electroactive probes.[78]

3.1.2 Diffusion in Microemulsions

Mass transport in microemulsions has been studied using electrochemistry since the 1970s with the early work of Mackay and co-workers, where they found a relationship between the diffusion coefficient obtained by electrochemistry (*D''*) for soluble electroactive ions in microemulsions with the volume fraction of oil (φ_c).[79]

$$D'' = D_p(1+\varphi_c)^{n+1} \qquad \textbf{Equation 4}$$

where D_p is the diffusion coefficient of the hydrophilic probe ion and n is determined from a similar relationship between equivalent conductance and φ_c.[60] This equation was found to hold for microemulsions of nonionic and ionic surfactants with hydrophilic electroactive ions like ferricyanide and ferrocyanide.

D'' for the oil-soluble 1-dodecyl-4-cyanopyridinium ion was not dependent on the water concentration, having a value of 4.4 x 10^{-7} cm^2 s^{-1}, and with the help of the Stokes-Einstein equation,[70] a droplet radius of 45 Å was obtained, which was confirmed by x-ray scattering.[79]

Other workers have also studied mass transport in microemulsions;[80] Georges *et al.*[81] were able to use their diffusion data to demonstrate progressive changes from an oil/water system in the water rich domains of a phase diagram, through a bicontinuous structure, to a water/oil system in the oil-rich regions. As discussed earlier, slow kinetics are not expected to hold for most microemulsions.[60]

Another interesting study by Mackay *et al.*[82] on a range of probes with different solubilities in a microemulsion showed that one of the probes, ferricyanide, gave a D'' of the order of 10^{-6} cm^2 s^{-1} between 19 and 60 % water. The progressive change from a bicontinuous to an oil/water structure was shown by a drop in D'' values for ferrocene of an order of magnitude. This was confirmed by further work by Mackay *et al.*[83] and other workers, using rotating disk voltammetry, microelectrode voltammetry, electrical conductivity and viscosity measurements.[84]

3.1.3 Electrode - Surfactant Interface

When surfactant molecules self-assemble at surfaces, they form structured monolayers known as self-assembled monolayers (SAMs).[85] The interfacial environment of these monolayers is known to differ from the bulk. Probably the most widely studied SAMs are monolayers of alkanethiolates on gold. Besides being the ideal systems for studying physical chemistry in two and three dimensions, such as self-organisation, and interfacial phenomena, SAMs offer flexible opportunities for design, i.e. the ability to tailor both head and tail groups of the constituent molecules. Therefore, SAMs are highly ordered and oriented, and a wide range of groups both in the alkyl chain and at the chain termini can be incorporated, producing a variety of surfaces with specific interactions.

These SAMs may be relevant as models for surfactant films on our electrodes in this thesis, where the electrode surfaces may be coated with a surfactant monolayer. The SAM model, explored here, may give a clearer picture of the electrode-surfactant interface.

For several years, Buttry and coworkers[86] have been studying the effect of ion-pairing on electron transfer processes within SAMs as well as the position of the redox group within the SAMs. Their work has shown that SAMs containing redox groups, like viologen derivatives, can behave as thin ion-exchange materials. For example, electrochemical and quartz crystal microbalance (EQCM) experiments demonstrated that anions and water molecules could exit and enter the monolayer during reduction and oxidation respectively, and there appeared to be some ionic interactions between the anions from the supporting electrolyte and the monolayer of cations. These ionic interactions could affect both the thermodynamics (redox potentials) and the kinetics of electron transfer.

Another technique also suggests that there is ion transport across SAMs. Recently, ex situ reflection-absorption Fourier transform infrared spectroscopy (RA-FTIR) was used by Buttry *et al.* to measure electric field strengths at the interfaces of SAMs and the bulk solution by employing a surface-immobilised and oriented fluorescent dye as a spectroscopic probe.[87] Basically, the local electric field is perturbed by applying different potentials, thereby changing the electronic transition energy of the probe; this is known an example of electrochromism or the Stark effect.[88] Besides

characterising the SAMs, the spectroscopic studies could distinguish in terms of electric field magnitude between the probe species external to the SAMs and those embedded in the SAMs, where the experimental value of electric field magnitude was found to be lower in the former case, probably due to the fact that the probe orientation was relatively unconstrained. However, both their experimental values for the electric field magnitude were lower than those predicted by theoretical models. The reasons for this are believed to be complex and different for the two cases. In the first case, the probe orientation is probably more parallel than perpendicular to the surface due to the influence of the electric field, thus resulting in an underestimation of the electric field. For the second case, ions from the supporting electrolyte penetrate the SAM, causing electrostatic screening. The lower than expected experimental values for the electric field magnitude were also observed by Hanken *et al.* who also employed optical probes.[89]

On the other hand, the formation of pit-like defects in thiolate SAMs have been observed by STM imaging, revealed to be the result of surface diffusion of the adsorbed thiolates molecules.[90] This was later confirmed via cyclic voltammetry by Kakiuchi et al.[91] who were able to estimate the average diffusion coefficient of a binary SAM system at about 10^{-18} cm^2 s^{-1} at 60 ^0C; this value corresponds to 2-d diffusion of thiol SAMs on Au. A similar order of magnitude was observed for single-component SAM system.[92] This very slow surface diffusion of thiols in SAMs is believed to be caused by the presence of a strong lateral interaction between the alkyl chains of close-packed adsorbed thiol films.

The EQCM work by Buttry et al.[86] demonstrated that the self-assembled redox monolayers could be good systems with which to probe the effect of structural design on interfacial redox chemistry. The researchers analysed the redox behaviour of SAMs of viologen derivatives with long alkyl chains and disulfide or thiol groups which attach to the gold electrodes. These materials are easy to synthesise and thus attractive for studying the distance dependence of electron transfer because the position of the redox group is controllable from both the electrode surface and the monolayer/solution interface.

Cyclic voltammetry was also used to analyse ion and solvent transport in these SAMs, confirming that the redox chemistry of the viologen group embedded within the

SAMs could attract or drive out ions.[93] The steric bulk of the SAMs was varied by the incorporation of fluorocarbon chains. Compared with alkyl chains,[94] the fluorocarbon chains were found to be better barriers to ion transport. Other workers have also utilised SAMs as barriers. For example, SAMs on gold electrode can prevent the fouling of electrode surface by oxidation products.[95]

This is interesting for comparison to our diffusion studies of Brij® 56. Although Buttry and coworkers have shown that SAMs could act as barriers to ion and solvent transport, this may not be applicable to our liquid crystalline system. Even though the interfacial environment of these SAMs is known to differ from the bulk for aqueous systems, our surfactant system (i.e. Brij® 56 system) was very viscous because of the heavy proportion of surfactant.

Although there could be a surfactant monolayer of Brij® 56 on the Au electrodes in our lyotropic liquid crystal work, the interfacial phenomena on our Au surfaces are likely to be very different to the SAM-solution interface. This is because unlike the thiol SAMs, the surfactant molecules of Brij® 56 are not covalently bound to the Au surface, resulting in much weaker interactions and adsorption.

3.1.4 Diffusion in Lamellar and Vesicle Dispersions

As mentioned before, not all surfactants form micelles in water; some surfactants disperse in water to form lamellar liquid crystalline phases or vesicles. Lamellar dispersions are layered structures of surfactant bilayers and water. Vesicles are closed bilayer structures and are much bigger than micelles, normally by an order of magnitude. Theoretical treatments of diffusion-assisted reactions in these media have recently been reviewed by Barzykin *et al.*[61] Experimentally, chronocoulometry and microelectrode voltammetry have already been used to study the fluidity and lateral diffusion coefficient of amphiphilic bilayer assemblies.[96]

However, much less research has been carried out on the mass transport of *electrochemical probes* in these media. Diffusion of electroactive probes dissolved in the lamellar phases of 50 wt% cesium pentadecafluorooctanoate (CsPDFO)/D_2O have been detected by cyclic voltammetry by Murray *et al.*[97] Polarised-light optical microscopy of

this system[98] shows that it exists as a simple aqueous amphiphile solution below its CMC, and as disk-shaped micelles above its CMC, i.e. in the form of two phases: the discotic nematic phase (at lower concentrations and higher temperatures) and the lamellar phase (at higher concentrations and lower temperatures). Previous research using ionic conductivity measurements[99] and NMR techniques[100] on this system and other similar aqueous lamellar systems have already shown that transport in the lamellar phase is anisotropic, i.e. more facile perpendicular to the *macroscopic director* (which is oriented parallel to the lamellae). This is confirmed by the cyclic voltammetry studies of Murray *et al.*[97] where the diffusional anisotropy ratios, $D_{perpendicular}$ / $D_{parallel}$, were 2 for ferrocyanide ion and 19.3 for the positively charged (ferrocenylmethyl)trimethylammonium ion ($FcMtMA^+$). For example, this means that diffusion of ferrocyanide perpendicular to the director (i.e. parallel to the lamellae) is twice as fast as that parallel to the director.

Another area where diffusion is important in liquid crystalline media is in the diffusion of the molecules which make up the media, i.e. diffusion of amphiphiles.

There is growing interest in polymer-surfactant systems,[101] where their complex interactions in aqueous solution, such as those between a nonionic polymer (e.g. poly(ethylene) oxide, PEO) and an ionic surfactant (e.g. sodium dodecyl sulfate, SDS), have been studied by physicochemical methods, e.g. surface tension, viscosity, and spectroscopic techniques.[102] These workers[101, 102] and Roscigno *et al.*[103] have measured surfactant diffusion in such systems by Fourier transform pulse-gradient spin-echo (FT-PGSE) NMR technique. The latter showed that the observed intradiffusion coefficients are a population average of the diffusion of the free surfactant and the surfactant bound to the polymer. They found that as expected, even if very little surfactant was bound on the polymer surface, the experimental values were indeed much lower than those observed in the absence of the polymer. In addition, when using Gouy diffusiometer, their interdiffusion experiments showed the surfactant diffusion coefficient to be a function of concentration by looking at the changes of mobility and thermodynamic factors with the increase in solute concentration.

Other amphiphilic diffusion data have been collected, such as (FT-PGSE) NMR data on dendrimers.[104]

In addition, there has been considerable interest in diffusive transport of lipids because it typifies 2-d diffusion and is important in intracellular signaling; these Langmuir films of amphiphilic biomolecules also appear ideal for studying diffusional properties in model membranes under controlled area conditions. One technique used was darkfield microscopy for tracking the diffusion of gold-labelled phospholipids as probe molecules.[105] Another is single molecule fluorescence imaging by Ke *et al.*[106] carried out on phospholipid monolayers at the air-water interface.

Interestingly, labelling amphiphiles with a redox probe has been employed by Murray *et al.*[107], where poly(ethyleneglycol)s were labelled with ferrocene to look at their diffusion coefficients when dissolved in poly(ethyleneglycol)s melts; the diffusion coefficients were found to be independent of probe concentration, being in the range 10^{-7} to 10^{-10} cm^2 s^{-1}.

3.1.5 Mass Transport

In electrochemical experiments where there is continuing chemical change, the continuous conversion of reactant to product will need the supply of reactant to the site of the reaction and the removal of product, as well as electron transfer at the electrode/mixture interface. For example, the reversible conversion of O to R could be described in three steps, with the rate determined by the slowest step.

$O_{bulk} \leftrightarrow O_{electrode}$ **(mass transport)** **Equation 5**

$O_{electrode} \leftrightarrow R_{electrode}$ **(electron transport)** **Equation 6**

$R_{electrode} \leftrightarrow R_{bulk}$ **(mass transport)** **Equation 7**

Looking at mass transport, it is possible to have contributions from three forms of mass transport.[108]

Diffusion is the movement of a species caused by a concentration gradient, where the species moves from a solution region of higher concentration of the species to a more dilute region, until equal concentrations exist.

Convection is the movement of species caused by external mechanical forces, e.g. purging the solution with gas or random vibrations in the laboratory.

Finally migration is the movement of charged species caused by a potential gradient. Migration exists in all electrochemical cells because of the application of a voltage, and it can also be caused by electrostatic forces.

3.1.6 Objectives

As stated at the beginning of this chapter, the aim here was to study the process of diffusion of an electroactive probe, such as ferricyanide, in a lyotropic liquid crystalline phase of a surfactant called Brij® 56. The effects of the formation of the lyotropic liquid crystalline phase by Brij® 56, at the relevant composition and temperature, on the redox chemistry of the redox probe could be compared to the aqueous system (i.e. in the absence of surfactant).

In this section, diffusion was the only mode of mass transport studied. To prevent "natural convection" as much as possible in an unstirred solution, a water bath was used to control the temperature of the solution. Also, the chemical change at the electrode surface may cause a slight variation in the density and temperature to the layer next to the electrode, causing solution movement in the cell.

To avoid migration, a high concentration of a base electrolyte (also known as the inert or supporting electrolyte), i.e. 1 M potassium chloride (KCl), was added to the solution of the electroactive species, ferricyanide ions. This ensured no significant contribution by migration to the transport of ferricyanide ions. Although both the reactant and the product of the electrode reaction were charged species, the large excess of the ions of K^+ and Cl^- would migrate instead, as they do not have any electron transfer chemistry in the potential range of the ferricyanide redox chemistry.

There are several reasons for this study of diffusion of ferricyanide in the presence of Brij® 56. Firstly, ferro/ferricyanide chemistry has been studied for many years, due to its relative stability on standing (approimately a few hours) and due to its fast electron kinetics. For example, the oxidation of potassium ferrocyanide, $K_4Fe(CN)_6$, is often used as a basic electrochemical experiment to calculate the radius of a

microelectrode, from steady-state curves, with the diffusion coefficient reported to be 7.63×10^{-6} cm^2 s^{-1} for 4 mM ferricyanide in 1 M potassium chloride, KCl.[109]

$Fe(CN)_6^{3-} + e^- \leftrightarrow Fe(CN)_6^{4-}$ **Equation 8**

Secondly, since the field of nanostructured / ordered mesoporous materials (OMMs), synthesised via the "true liquid crystalline templating" (TLCT) approach described in the section 1.5.2 in Chapter 1, has recently taken off, studying diffusion processes in a lyotropic liquid crystalline medium, which contains nanostructured channels, would be interesting and is novel. Finally, using an ionic species can help probe the aqueous domains of different regular, liquid crystalline structured phases of a surfactant, such as Brij® 56.

As mentioned before, the Brij® series of surfactants are similar to the C_xEO_y surfactants containing a hydrocarbon tail with an ethylene oxide based head group. Brij® 56, which is $C_{16}EO_{10}$, is very similar to $C_{16}EO_8$, except that the phase boundaries are not as well defined as for $C_{16}EO_8$.

It is important to point out that the lyotropic liquid crystalline phases, including the hexagonal phase, of a surfactant are formed at sufficiently high surfactant concentrations, much higher than the surfactant concentrations used by the Mobil scientists.[3] For example, as seen in Figure 18, Brij® 56, a white waxy solid, forms a hexagonal phase with water between 45 and 68 wt% concentration between 25 and 60 ^0C approximately. As mentioned before in section 1.5.3 in Chapter 1, the Mobil method depended on micelles assembling together at low surfactant concentrations that were above the CMC. Used for the synthesis of M41S materials, these very low surfactant concentrations would not be high enough for any liquid crystalline structures to form in a purely aqueous system. Thus, silicate ions must help in some way to encourage the liquid crystalline state by serving as counter-ions and stabilisers for the micelle arrays.

Therefore, in this thesis, the Brij® 56 mixtures, prepared at these high surfactant concentrations, appeared *viscous*. The formation of the lyotropic liquid crystalline phases of Brij® 56 was confirmed by polarised-light optical microscopy. Besides viscosity, these mixtures contain *ordered channel structures*, which are unlike those of the *solutions* of

microemulsions, micellar and other surfactant dispersion media. Although there is considerable literature on the diffusion of an electrochemical probe in such surfactant media, as described in the introduction of this chapter, diffusion studies of an electrochemical probe in the aqueous domains of different *regular, liquid crystalline structured* phases of a surfactant (formed at sufficiently high surfactant concentrations) have never been carried out until now.

In this thesis, polarised-light optical microscopy showed that the mixture of 50 wt% of solution of 10 mM ferricyanide and 1 M KCl with 50 wt% of Brij® 56 produced a hexagonal phase at room temperature. Cyclic voltammetry and chronoamperometry techniques, including the use of microelectrodes, were employed here to study the redox chemistry of ferricyanide in the surfactant system of Brij® 56, where these results were compared with those obtained in the absence of the surfactant.

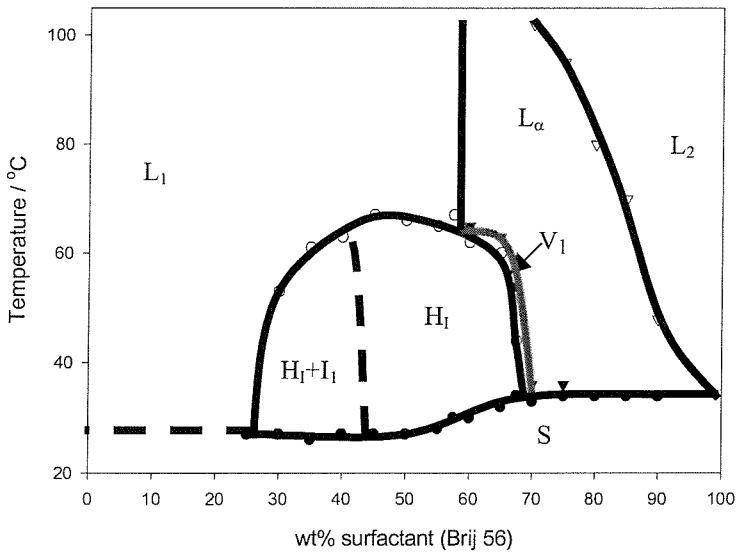

Figure 18 Phase diagram of Brij® 56 / water system: L_1 – micellar solution; L_2 – inverse micellar solution; L_α- lamellar; V_1 – cubic; H_1 – hexagonal; I_1 – cubic spherical micelles; S - solid.[33]

3.2 Experimental

3.2.1 Disk electrodes

Using a 1 mm diameter Au disk working electrode, the cyclic voltammetry (CV) and chronoamperometry techniques were carried out in 10 mM $Fe(CN)_6^{3-}$ / 1 M KCl solutions which were yellow in colour. The first one involved cycling the potential from +0.6 to –0.2 V back to +0.6 V vs. SCE at various scan rates (from 200 down to 10 mV/s). The second involved potential steps, stepping from a potential of +0.6 V down to potentials more negative than 0.2 V vs. SCE, to study the reduction reaction under diffusion control. Similarly, these techniques were repeated when Brij® 56 was introduced into the system.

For the sake of comparison, a platinum working electrode was employed in a similar manner, i.e. to study the system of ferricyanide redox probe in the absence and presence of Brij® 56.

A control experiment was carried out similarly where the ferricyanide redox probe was absent but the Brij® 56 was present. The purpose was to see whether any impurities would show up electrochemically in a Brij® 56 mixture.

All experiments were carried out at 25^0C. All mixtures were freshly prepared. All mixtures containing the Brij® 56 surfactant consisted of 50 wt% Brij® 56 and 50 wt% of the relevant solution; optical microscopy was used to confirm the phase of the mixtures containing Brij® 56 to be hexagonal.

3.2.2 Microelectrodes

Generally only diffusion perpendicular to the electrode surface is considered for macroelectrodes. However when the electrode size decreases such that it is comparable to the diffusion layer, the radial diffusion terms become significant, i.e. edge effects need to be considered. Practically, the order of dimension should be microns in at least one of its dimensions, small enough for the properties to become a function of their size. The geometry can vary from microelectrode arrays to microspheres, but the most commonly used, and the easiest to make, is the microdisc formed by sealing a thin metal wire onto

an insulator and then polishing to expose the cross-section. Microdisc radii range from 0.1 to 100 μm, with 1 to 10 μm the most common.

In the steady state, a hemispherical diffusion field surrounds the microdisc electrode.[108] Thus, when its potential is stepped from a value where no chemical change occurs ($j = 0$) to one where a reaction is diffusion controlled, i.e. non-steady state, the response can be given in the form of

$$j_L = \frac{nFD^{1/2}c}{\pi^{1/2}t^{1/2}} + \frac{4nFDc}{\pi a} \qquad \textbf{Equation 9}$$

where a is the disc radius, n is the number of electrons, F is the Faraday constant, D is the diffusion coefficient ($m^2\ s^{-1}$), c is the concentration of the species (mol m^{-3}) and t is the time (s). It can be seen that the first term is identical to that for a potential step on a planar electrode. The second term is the steady state term. It can also be seen that at short times, the first term dominates and at long times the second term dominates. Thus, there must be an intermediate time period when both terms are of similar magnitude.

The diffusion controlled current density in the steady state is

$$j_L = \frac{4nFDc}{\pi a} \qquad \textbf{Equation 10}$$

with the diffusion controlled current being

$$i_L = 4nFDca \qquad \textbf{Equation 11}$$

To test for diffusion control, plotting the steady state current versus the radii of a series of microdiscs will give a straight line through the origin. If plotting the steady state current density, then $4Dc/\pi a$ is the flux of reactant diffusing to the surface.

Thus it is possible to study high steady state rates of diffusion to the microdisc and this gives valuable insight into fast reactions in the steady state.

Microelectrodes have very useful properties.

Firstly, the overall current going through the reaction cell is very low, frequently in the order of nA. This reduces the problems of *iR* drop, which is useful in experiments where *R* is unusually big. For example, it becomes possible to do experiments in media with very low ionic strength (e.g. water with little or no added electrolyte), in solutions with high concentrations of electroactive species, and in rapid scan cyclic voltammetry.

Secondly, there is considerable reduction in interference from double layer charging currents improving data from experiments with a short timescale such as rapid scan cyclic voltammetry.

In this section, a 25 μm diameter gold microelectrode was used as the working electrode. The diffusion coefficient obtained in the aqueous system, i.e. 10 mM ferricyanide in 1 M KCl, of 7.6×10^{-6} cm^2 s^{-1} was reproducible and agreed very well with the literature value (7.63×10^{-6} cm^2 s^{-1} for 4 mM ferricyanide in 1 M KCl). These results were compared with those of the surfactant system.

3.3 Results and Discussion

3.3.1 $Fe(CN)_6^{3-}$, KCl (Aqueous System)

3.3.1.1 Oxygenated

The diffusion process of ferricyanide in an aqueous system, in this case 1 M KCl solution, which was oxygenated with argon for 10 minutes, was studied at 25 ^{0}C.

Figure 19 is a cyclic voltammogram of the Au disk working electrode of 1 mm diameter cycled in 10 mM $Fe(CN)_6^{3-}$ and 1 M KCl solution at 200 mV/s. The cycling began cathodically at +0.6 V where no reaction occurred, and a peak appeared at about +0.2 V, corresponding to the reduction of ferricyanide. The cycle reversed direction at –0.2 V and returned to +0.6 V, peaking anodically at +0.29 V. Both peaks appeared reproducibly at the correct potential as in the literature.[109, 110] Various scan rates ranging from 200 down to 10 mV/s were studied.

By plotting the peak current against the square root of the various scan rates ranging from 200 to 10 mV/s, a straight line was obtained in accordance with the Randles-Sevčik equation (see equation 9). The diffusion coefficient obtained from the gradient was 5.35 x 10^{-6} cm^2 s^{-1}, although the use of microelectrodes helped to bring *D* even closer to the literature value of 7.6 x 10^{-6} cm^2 s^{-1} as shown later.

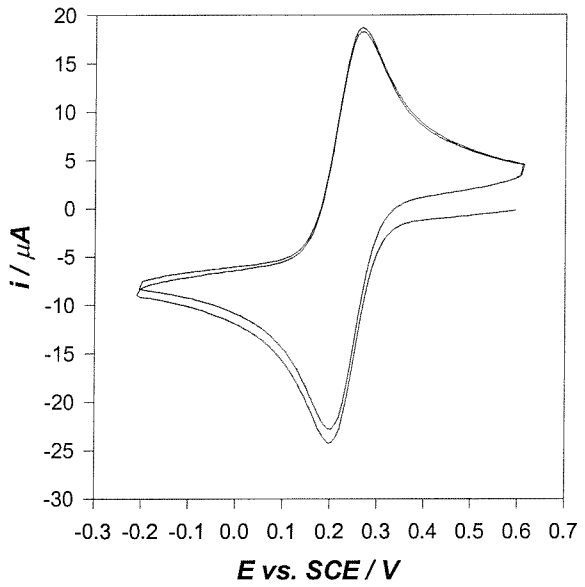

Figure 19 Typical cyclic voltammogram at 200 mV/s of Au disk electrode (1 mm diameter) in 10 mM $Fe(CN)_6^{3-}$ and 1 M KCl solution degassed at 25 ^{0}C.

At 298 K, the Randles-Sevčik equation is

$$i_p = 2.69\times10^5 n^{1.5} AcD^{1/2}\upsilon^{1/2} \qquad \textbf{Equation 12}$$

where i_p is the reduction peak current (A), n is the number of electrons, A is the disk electrode area (m^2), c is the concentration (mol m^{-3}) of the redox ion, D is the diffusion coefficient (m^2 s^{-1}) and ν is the scan rate (mV/s); the peak current used was the peak reduction current recorded on the first scan.

Tests for proving reversibility[108] showed that the peak potentials were independent of scan rate, the ratio of the cathodic and anodic peak currents was about one, and the difference in the cathodic and anodic peak potentials was approximately 0.065 V. This last value is not the expected value of 0.057 V, and this could be the result

of *iR* drop in which case using microelectrodes would be better; also, the ferricyanide redox chemistry is known to exhibit fast electron kinetics.

A more accurate technique was the potential step method, where the potential of the gold disk electrode was stepped from +0.6 to –0.1 V. Potential step experiments are useful for determining exact kinetic parameters, especially when the reaction mechanism is well known and understood, as in the case of ferricyanide reduction. On the other hand, the experimental data tended to look very similar so that for preliminary studies, cyclic voltammetry is a better technique.

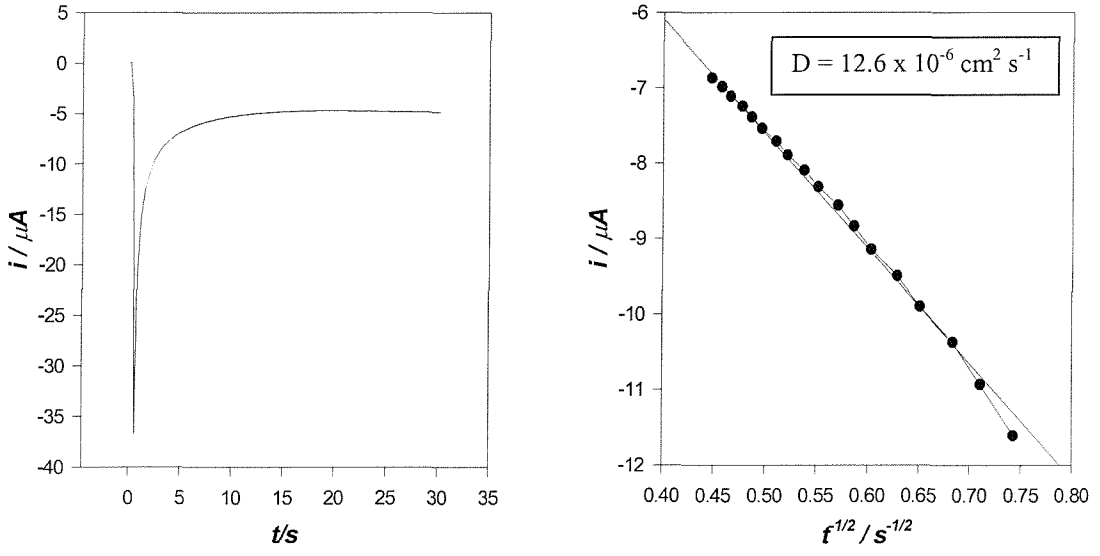

Figure 20 On the right is typical current-time transient of Au disk electrode (1 mm diameter) in 10 mM $Fe(CN)_6^{3-}$ and 1 M KCl solution degassed at 25 ^{0}C; on the left is the Cottrell plot.

In this case, the diffusion coefficient obtained from the linear Cottrell plot was 13 x 10^{-6} cm^2 s^{-1} approximately. The Cottrell equation is

$$j = \frac{nFD^{1/2}c_O}{\pi^{1/2}t^{1/2}}$$ **Equation 13**

where j is the current density recorded, n is the number of electrons, F is the Faraday constant, D is the diffusion coefficient (m^2 s^{-1}), c_O is the concentration (mol m^{-3}) of O, and t is the time (s) recorded.

Cycling 25 μm diameter gold microelectrode in the same degassed solution produced an s-shaped steady-state voltammogram obtained at 5 mV/s, see Figure 21, with the reduction current plateauing at –0.035 μA. The diffusion coefficient was calculated to be 7.25 x 10^{-6} cm^2 s^{-1}, which was even closer to the literature value. This observation coupled with the advantages of using microelectrodes made it attractive to examine in more detail the ferricyanide chemistry in the surfactant system.

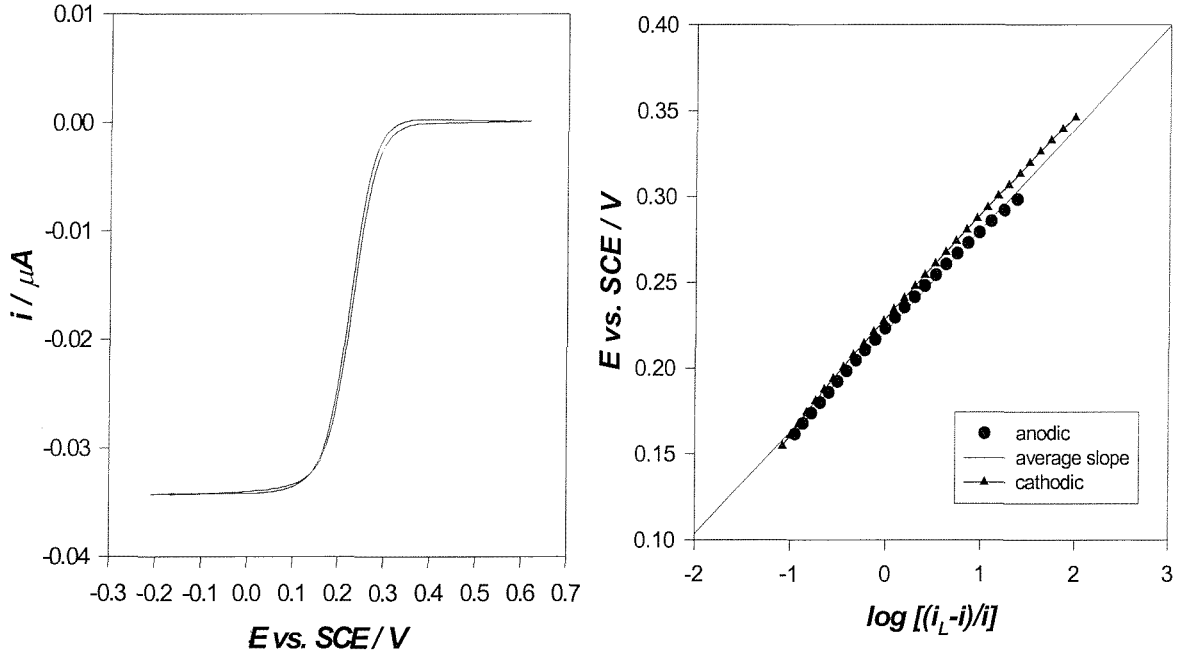

Figure 21 Typical cyclic voltammogram at 5 mV/s of gold disk microelectrode (25 μm diameter) in 10 mM $Fe(CN)_6^{3-}$ and 1 M KCl solution degassed at 25 ^{0}C; and the corresponding Nernst log plots for the cathodic and anodic scan with average slope being 0.059 V and the intercept as 0.23 V.

Applying the Nernst equation where the potential was plotted versus log $[(i_L\text{-}i) / i]$ produced a straight line whose average slope for cathodic and anodic scans was

$(2.3RT)/nF$, i.e. 0.059 V and the intercept was the half-wave potential.[108] In the case of the 25 μm diameter gold disk microelectrode, the average half-wave potential was found to be the same as the mid peak potential for the cyclic voltammetry at the 1 mm diameter gold disk electrode, i.e. 0.235 V, thus supporting reversibility.

3.3.1.2 Not Oxygenated

Because the Brij® 56 surfactant system could not be oxygenated, the data collected in this section are useful for the sake of comparison.

Cycling 25 μm diameter gold microelectrode in the aerated solution of 10 mM $Fe(CN)_6^{3-}$ and 1 M KCl solution at 25 ^{0}C also produced an s-shaped steady-state voltammogram obtained at 5 mV/s, see Figure 22, with the reduction current plateauing at –0.034 μA. The diffusion coefficient was calculated to be 7.05 x 10^{-6} cm^2 s^{-1}, close to the value obtained previously in the degassed solution. Again, the average half-wave potential was 0.235 V and the slope was 0.06 V of Figure 22 (B), thus supporting reversibility.

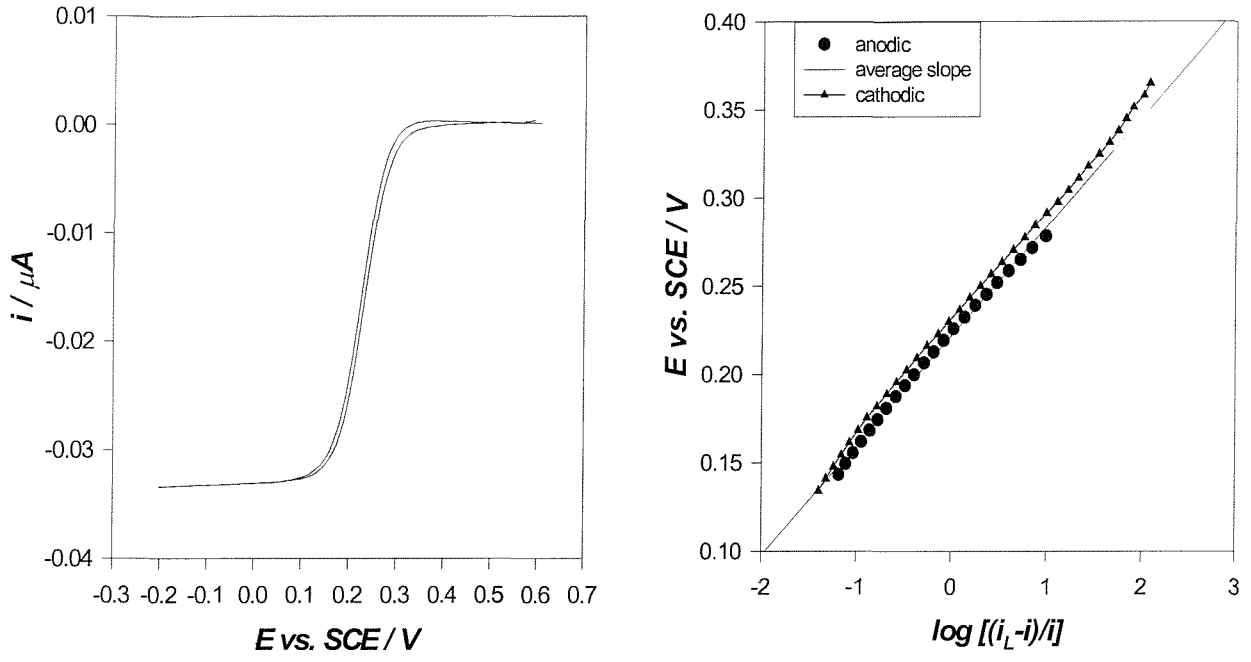

Figure 22 Typical cyclic voltammogram on the left at 5 mV/s of Au disk microelectrode (25 μm diameter) in 10 mM $Fe(CN)_6^{3-}$ and 1 M KCl solution not degassed at 25 ^{0}C; and the corresponding Nernst log plots for the cathodic and anodic scan with average slope being 0.06 V and the intercept as 0.23 V.

3.3.1.3 Conclusions

The aim of this section was to study the process of diffusion of ferricyanide in the absence of a surfactant called Brij® 56. The redox probe in the aqueous system does exhibit fast electron kinetics; the diffusion coefficient measured when using a microelectrode was close to the literature value of 7.63 x10^{-6} cm^2 s^{-1} for 4 mM ferricyanide in 1 M potassium chloride, KCl.[109] The effect of not oxygenating the solution appears not to significantly affect this, which is important as this system is most similar to the surfactant system where degassing was not possible.

3.3.2 Brij® 56, $Fe(CN)_6^{3-}$, KCl (Surfactant System)

3.3.2.1 Large Au Electrode (1 mm diameter)

In this surfactant study, all mixtures containing the Brij® 56 surfactant consisted of 50 wt% Brij® 56 and 50 wt% (10 mM $Fe(CN)_6^{3-}$ and 1 M KCl) solution; optical microscopy confirmed the phase of the mixtures to be hexagonal. Figure 23 is a selection of typical cyclic voltammograms of the Au disk working electrode of 1 mm diameter in this surfactant system at 200 mV/s. The same experimental conditions were applied in each case. The cycling began cathodically at +0.6 V where no reaction occurred, and reversed direction at –0.2 V and return to +0.6 V. Cyclic voltammograms were collected several times at the same scan rate in between polishing, and there is a noticeable degree of distortion with the reduction and oxidation peaks not as distinct as in the aqueous system, although the overall current was observed to be about 10 times less.

Although the decrease in overall currents supports the assumption that the presence of Brij® 56 slowed down the diffusion process of ferricyanide, the distortion and extremely broad reduction peaks made it impossible to calculate the diffusion coefficient using the Randles-Sevćik equation.

On the other hand, the double layer charging current appeared to be approximately 1 μA here which was half the value in the aqueous system at the same scan rate; this could mean that half the surface area of gold was blocked by Brij® 56.

Compared to the aqueous system, there is a noticeable shift in the reduction peak potential in each voltammogram in Figure 23, by about 0.02 V negatively, although the peaks are very broad.

The presence of two reduction peaks seen in all but one cyclic voltammograms, i.e. (A), seems to suggest a distinct water region containing ferricyanide ions because the second peak shows up at +0.22 V.

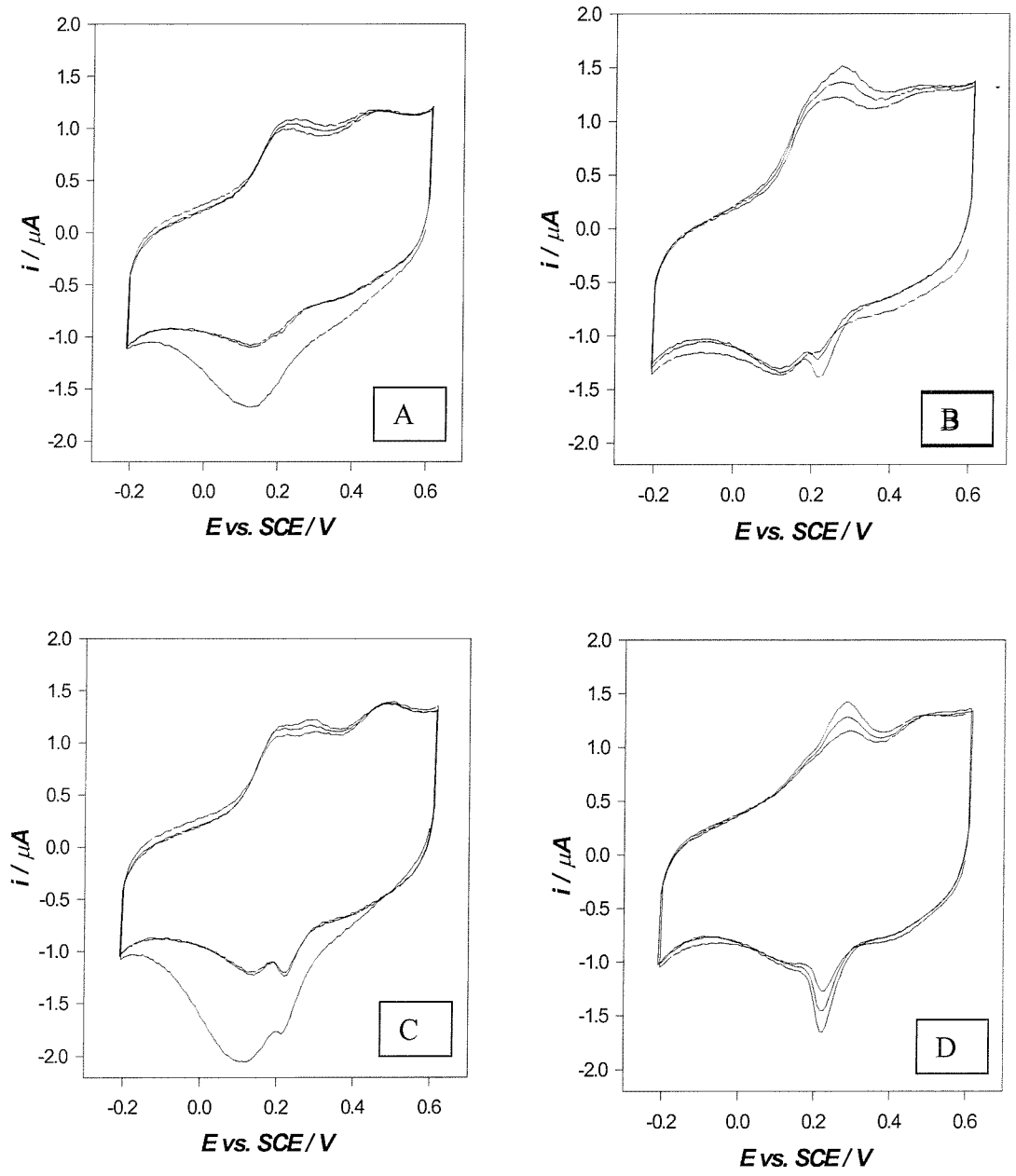

Figure 23 Selection of typical cyclic voltammograms at 200 mV/s of Au disk electrode (1 mm diameter) in 50 wt% Brij® 56 and 50 wt% (10 mM $Fe(CN)_6^{3-}$ and 1 M KCl) mixture at 25 ^{0}C.

When the potential of the electrode was stepped from +0.6 to –0.1 V, the initial current reached 24 μA which was lower than in the aqueous system (37 μA), and diffusion coefficient from the Cottrell plot was 0.05 x 10^{-6} cm^2 s^{-1}, also lower than in the aqueous system, see Figure 20 and Figure 24.

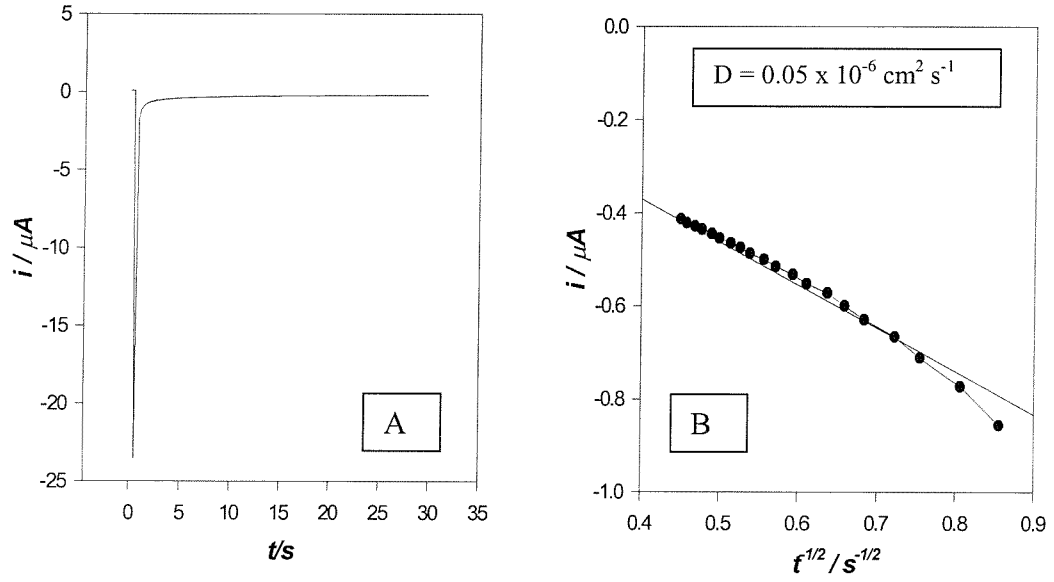

Figure 24 (A) A current-time transient for the potential step of +0.6 to –0.1 V and (B) the corresponding Cottrell plot with the diffusion coefficient D, of Au disk electrode (1 mm diameter) in 50 wt% Brij® 56 and 50 wt% (10 mM $Fe(CN)_6^{3-}$ and 1 M KCl) mixture at 25 ^{0}C.

Using a different metal electrode such as 1 mm diameter Pt appeared not to make much difference, shown in Figure 25.

3.3.2.2 Au Microelectrode (25 mm diameter)

Cyclic voltammetry performed at 5 mV/s on 25 μm diameter gold microelectrode has produced an s-shaped steady-state voltammogram obtained with the reduction current which tended to plateau towards a maximum limiting current of 0.001 μA, i.e. 1 nA, see Figure 26(A). However, because this was not always the case, i.e. the limiting current being lower than 1 nA, several observations could be made.

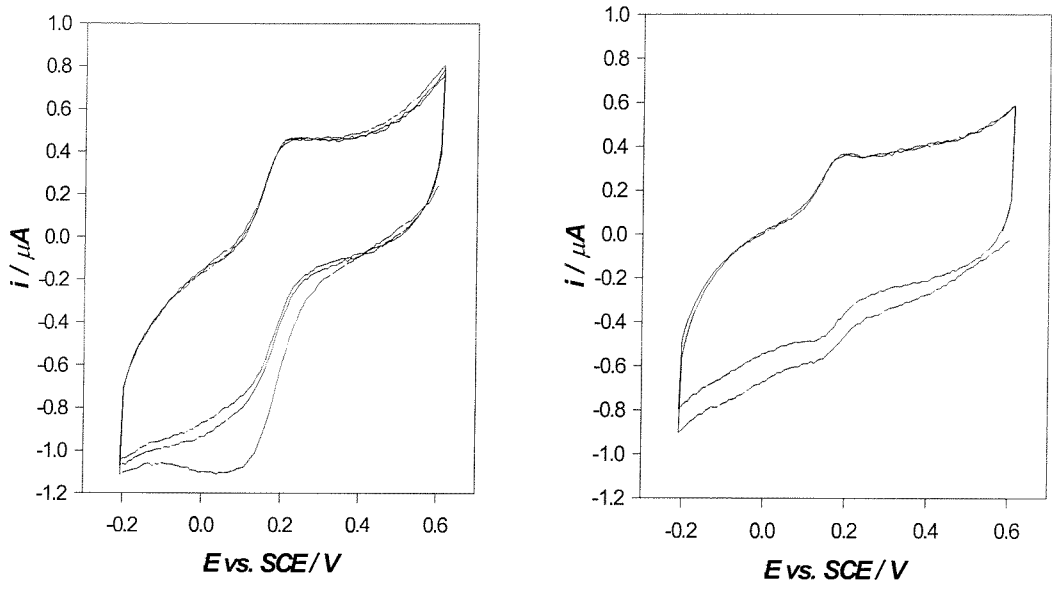

Figure 25 Two cyclic voltammograms of Pt disk electrode (1 mm diameter) at 200 mV/s in 50 wt% Brij® 56 and 50 wt% (10 mM $Fe(CN)_6^{3-}$ and 1 M KCl) mixture at 25 ^{0}C.

The microelectrode was repeatedly polished, and with each polishing, the voltammograms of the microelectrode carried out showed some degree of variation in terms of current magnitude and shape among other things. For example, for the same scan rate of 5 mV/s, the reduction limiting currents could be as low as –0.2 nA as in Figure 26 (B) and (D), and the degree of distortion could increase until the s-shape disappeared.

In addition, the reduction limiting currents were found to increase with the number of cycles in the latter. There appears to be no pattern as to what the minimum limiting current started at but they seem to increase to a common maximum value.

Compared to the aqueous system, the maximum reduction currents obtained here of 1 nA were much lower by a factor of 35 and contained greater hysteresis; in addition, the limiting current plateaux were not as flat.

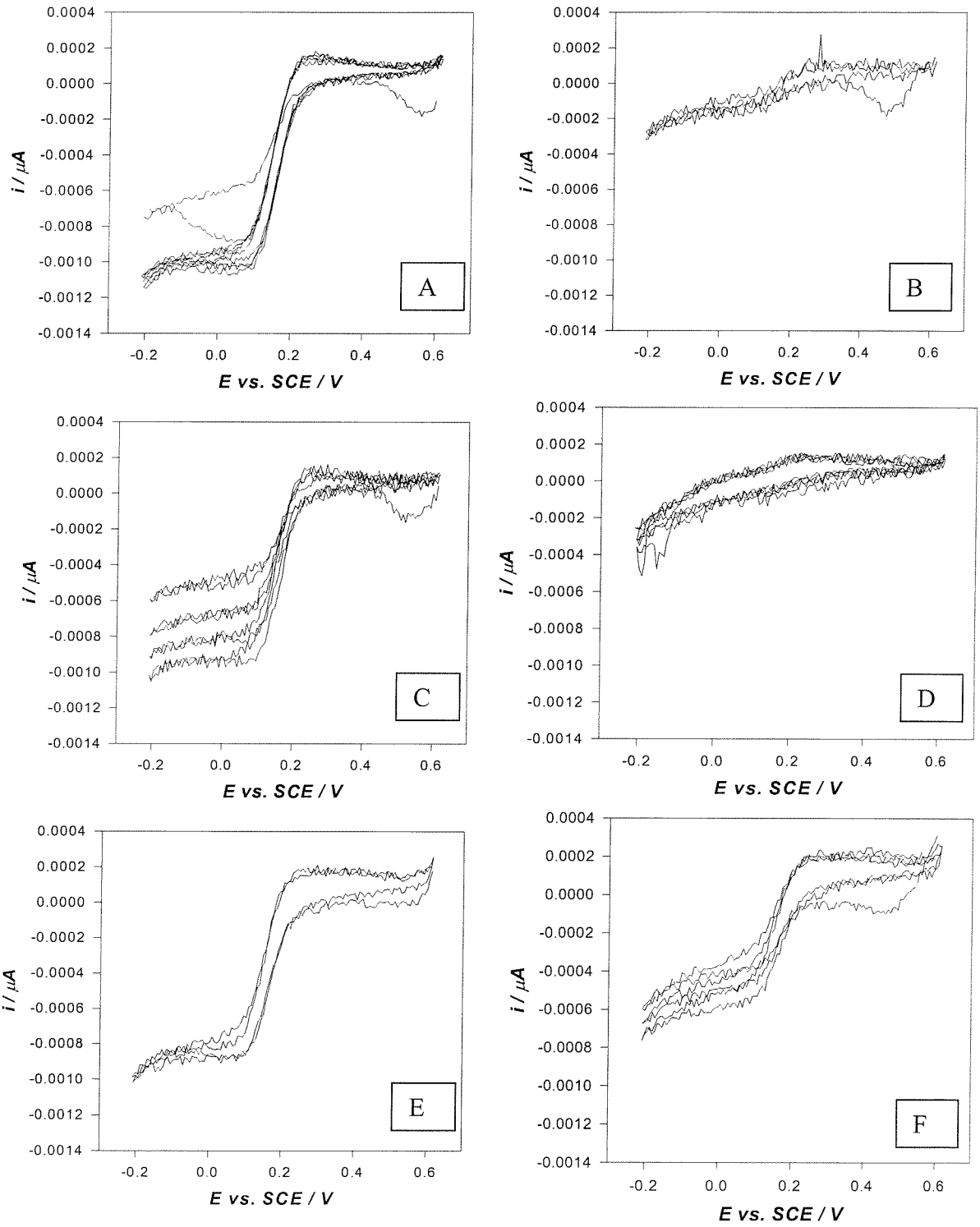

Figure 26 Cyclic voltammograms at 5 mV/s of Au disk microelectrode (25 μm diameter) in 50 wt% Brij® 56 and 50 wt% (10 mM $Fe(CN)_6^{3-}$ and 1 M KCl) mixture at 25 ^{0}C.

Holding the microelectrode in the air over the Brij® 56 mixture showed a negligible amount of noise in Figure 27.

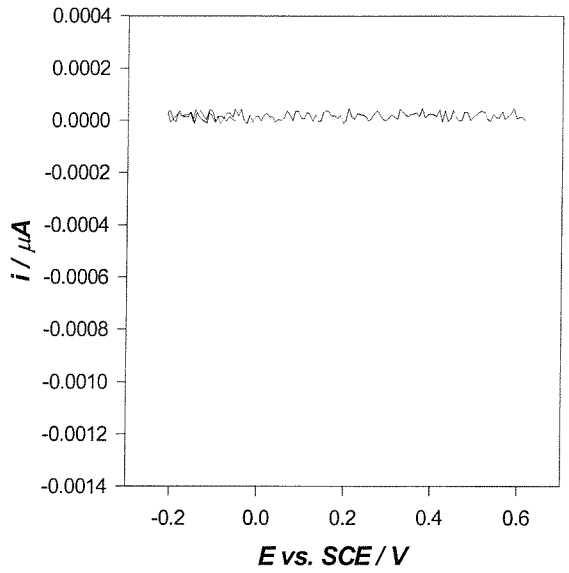

Figure 27 Cyclic voltammogram at 5 mV/s of Au disk microelectrode (25 μm diameter) in air over 50 wt% Brij® 56 and 50 wt% (10 mM $Fe(CN)_6^{3-}$ and 1 M KCl) mixture at 25 ^{0}C.

3.3.2.3 Discussion of Nernst Plots

Proper data analysis was therefore carried out only in cases where the S-shaped wave was clear. Table 2 is a collection of calculations belonging to the corresponding Nernst plots obtained, with a typical example of a Nernst plot shown in Figure 28. For the reduction limiting current at 1 nA, the diffusion coefficient was found to be 0.207 x 10^{-6} cm^2 s^{-1}.

Example	Average half-wave potential / V	Cathodic slope / V	Anodic slope / V	Average slope / V
1	0.15	0.057	0.045	0.051
2	0.15	0.057	0.047	0.052
3	0.15	0.052	0.042	0.047
4	0.16	0.050	0.045	0.048
5	0.15	0.063	0.049	0.056

Table 2 Nernst plots of 50 wt% Brij® 56 and 50 wt% (10 mM $Fe(CN)_6^{3-}$ and 1 M KCl) mixture at 25 ^{0}C.

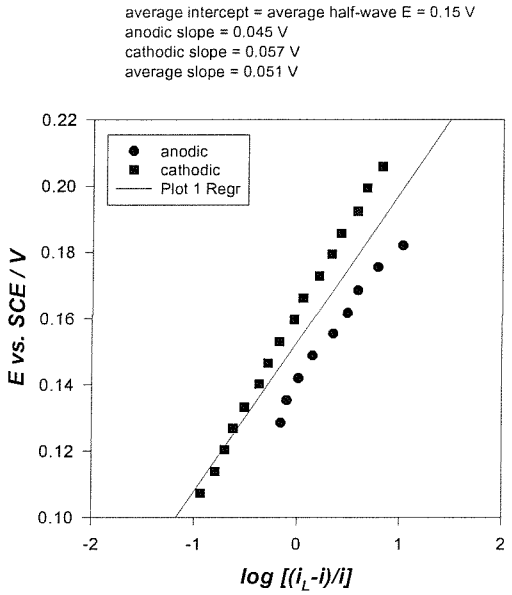

Figure 28 A typical example of a Nernst plot carried out for example marked (1) in Table 1 depicting data for 50 wt% Brij® 56 and 50 wt% (10 mM $Fe(CN)_6^{3-}$ and 1 M KCl) mixture at 25 ^{0}C.

Table 2 shows that the half-wave potential was reproducible in the surfactant system, but it is shifted cathodically (negatively) by approximately 0.06 V compared to the aqueous system. This indicated a more positive Gibbs free energy for the reduction of ferricyanide (Fe^{3+}) to ferrocyanide (Fe^{2+}), relative to the reference electrode; thus ferricyanide chemistry appeared more stable and more reversible in the surfactant system. The Born equation for solvation can shed further light on this; it tells us the electrostatic

free energy change for transfering an ion from a system of a particular dielectric constant to another.[111]

The Born equation expresses that part of the free energy of solvation of ions which arise from interactions outside the first shell, which should apply for the ferricyanide redox couple, $[Fe(CN)_6]^{3-/4-}$.

$$\Delta G_{Born} = \frac{(z_i e_o)^2}{2r_i \varepsilon} - \frac{(z_i e_o)^2}{2r_i} = \frac{(z_i e_o)^2}{2r_i}(1 - \frac{1}{\varepsilon}) \quad \textbf{per ion} \qquad \textbf{Equation 14}$$

where z_i is the charge on the ion, e_o is the charge on the electron, r_i is the radius of ion and ε is the dielectric constant.

If the shift in the half-wave potential for going from the water to Brij® 56 system is –60 mV approximately, then the change in Gibbs free energy is 5.8 kJ mol^{-1}.

In the Brij® 56 system, the change in Gibbs free energy is

$$\delta\Delta G = \Delta G_{Born}\left\{[Fe(CN)_6]^{3-}, water\right\} - \Delta G_{Born}\left\{[Fe(CN)_6]^{3-}, Brij56\right\} - \Delta G_{Born}\left\{[Fe(CN)_6]^{4-}, water\right\} + \Delta G_{Born}\left\{[Fe(CN)_6]^{4-}, Brij56\right\} \qquad \textbf{Equation 15}$$

and assuming r_i is the same in all cases,

$$\delta\Delta G = -\frac{(-3e_o)^2}{2r_i}\left(1 - \frac{1}{\varepsilon_{water}}\right) + \frac{(-3e_o)^2}{2r_i}\left(1 - \frac{1}{\varepsilon_{Brij56}}\right) + \frac{(-4e_o)^2}{2r_i}\left(1 - \frac{1}{\varepsilon_{water}}\right) - \frac{(-4e_o)^2}{2r_i}\left(1 - \frac{1}{\varepsilon_{Brij56}}\right) \qquad \textbf{Equation 16}$$

Thus,

$$\delta\Delta G = \frac{7e_0^2}{2r_i}\left(1 - \frac{1}{\varepsilon_{water}}\right) - \frac{7e_0^2}{2r_i}\left(1 - \frac{1}{\varepsilon_{Brij56}}\right) = \frac{7e_0^2}{2r_i}\left(\frac{1}{\varepsilon_{Brij56}} - \frac{1}{\varepsilon_{water}}\right) \qquad \textbf{Equation 17}$$

For a mole of ions, where N_A is the Avogadro number,

$$\frac{1}{\varepsilon_{Brij56}} = \frac{1}{\varepsilon_{water}} + \frac{2r_i\delta\Delta G\varepsilon}{7e_o^2 N_A} \qquad \textbf{Equation 18}$$

Knowing the radius of ferricyanide ion to be about 6.1 Å,[112] the dielectric constant for the Brij® 56 system, ε_{Brij56}, is calculated to be 76.7, lower than that of water[113], i.e. 78.5.

The Born equation predicts that the smaller the dielectric constant, the greater will be the magnitude of the free-energy change in the negative direction, i.e. greater stability. High dielectric should stabilise the more charged ion. However, this lower value of dielectric constant for the Brij® 56 system may only apply to the local environment of a ferricyanide ion, which is therefore probably different to the overall value for the system.

In addition, the shift in the half-wave potential could be due to the liquid junction potential rather than the redox couple thermodynamics. The first reason can only be explained further if another redox couple was studied, such as hexaammineruthenium ion where the diffusion coefficient is 5.5 x 10^{-6} cm^2 s^{-1} for 1 mM hexaammineruthenium (III) chloride in 0.1 M KCl.[114] In the second case, this potential shift also meant that the ferricyanide ion appeared harder to reduce which was justified by the fact that a more charged ion, from 3- to 4-, was produced and thus less stable.

Besides the potential shift, the average slopes obtained from the average of the cathodic and anodic slopes of the Nernst plots appeared to have shifted by about 0.06 V compared to the aqueous system. The shape of the plots is determined by the balance between the electron transfer kinetics and the mass transport, i.e. their ratio of respective rate constants; thus, the system could either be reversible, irreversible or quasi-reversible. For example, in a reversible system, the electron transfer rate constant is much greater than the mass transport rate constant, and in a quasi-reversible system, the ratio tends towards one. Therefore, in a reversible system, the average slope is steeper than in an irreversible system. In the Brij® 56 system, the slight variation in the slopes present is not due to IR problems as the currents recorded here were very small. In addition, the slopes appeared steeper than in the aqueous system, which further supports the

observation that ferricyanide chemistry appeared more reversible in the surfactant system.

3.3.2.4 Discussion of Reduction Limiting Currents

Regarding the limiting currents, the oxygen solubility needs to be considered for example. In water, the solubility of oxygen is 2.2 mM[167] and in hydrocarbons 10 mM.[115] The solubility of oxygen in water could be likened to the KCl solution and the solubility of oxygen in hydrocarbons to the Brij® 56. This indicated a greater concentration of oxygen in the Brij® 56 walls, i.e. as reservoirs of oxygen. This is important because it could be related to the extra reduction current seen in Figure 26 (A) when recording the limiting currents.

However, in this Brij® 56 system, there was some variability observed in the limiting currents recorded by Au microelectrodes. The answer could not lie in poor mixing and thus concentration fluctuations of ferricyanide, because the same maximum reduction limiting currents have been recorded several times. There are several possible explanations.

One explanation could be the presence of a thin layer of aqueous solution between the microelectrode and the surfactant, like a thin layer cell. This may explain the extra reduction peak observed in cyclic voltammograms of the larger electrodes in Figure 23.

Polarised-light optical microscopy may not explain the variability in the reduction limiting currents observed in the Brij® 56 system. This technique, described in greater detail in section 1.3.2 in Chapter 1, is used for assigning phases of a surfactant mixture based on their characteristic optical textures.[36] However, it cannot give accurate estimates of coexistence domains, except in the case when one of the phases is isotropic, eg. the cubic phases. In the cases of mixtures which do exhibit isotropic phases (which are characterised by high viscosity), such systems may not have reached true thermodynamic equilibrium over the optical experimental timescales. To test this, Attard *et al.*[34] checked the phase behaviour over the timescales typically employed in the synthesis of nanostructured platinum by electrodeposition (about 3 h) and by chemical reduction (about 7 h); no phase change was observed, and their conclusion was that the equilibrium behaviour was effectively represented by phase diagrams determined by

polarised-light optical microscopy. This suggests that the experimental timescales employed here in this thesis, much less than 3 h, were likely to have little or no effect on our results.

It is more likely that the reproducibility of the data obtained by cyclic voltammetry depends on the time for the surfactant system to settle down, i.e. into the equilibrium state. Although all our mixtures were freshly prepared at the start of the experiments, a stabilising time of 2 h was allowed before the experiments were conducted, in order for the surfactant mixtures to settle down. Attard *et al.*[34] also allowed all their surfactant mixtures to equilibrate for at least 2 h before use; evidence for equilibration was obtained from polarised light microscopy, which showed that thermally induced phase transitions observed were within ± 2.5 ^{0}C of the values measured one week after preparation and storage at 20 ^{0}C.

Another aspect of the equilibrium state of the surfactant system regards the situation where the insertion of an electrode into the surfactant mixture could perturb the local environment, after letting the surfactant mixture stabilise for 2 h. Thus, it is possible that data reproducibility also depends on the time for the local environment, i.e. the surfactant mixture in the vicinity of the electrode, to settle down. In our work, the increase observed in the reduction limiting currents of the Au microelectrode with the number of potential scans during cyclic voltammetry seemed to suggest this; the average time taken for the limiting current to reach a maximum of 1 nA appeared to be about 20 min. As mentioned previously, there appeared to be no pattern as to what the minimum limiting current started at but they seemed to increase to a common maximum value.

The discussion so far concerns the use of Au microelectrodes (25 μm diameter) at 5 mV s^{-1}. As stated previously in section 3.2.2, microelectrodes have very useful properties. Firstly, the overall current going through the reaction cell is very low, frequently in the order of nA. This reduces the problems of *iR* drop, which is useful in experiments where *R* is unusually big. For example, it becomes possible to do experiments in media with very low ionic strength (e.g. water with little or no added electrolyte), in solutions with high concentrations of electroactive species, and in rapid scan cyclic voltammetry. Secondly, there is considerable reduction in interference from double layer charging currents improving data from experiments with a short timescale

such as rapid scan cyclic voltammetry. Therefore, employing microelectrodes is more suitable than employing large electrodes for studying a surfactant system, such as the Brij® 56 system.

Although employing low scan rates during cyclic voltammetry on large electrodes will slow down the experimental timescale to allow the surfactant system to settle down, the combination of the useful microelectrode properties and the low scan rate of 5 mV s^{-1} of Au microelectrodes (25 μm diameter) in the Brij® 56 system should be sufficient for studying diffusion of an electrochemical probe in a surfactant system.

In addition, the continuous potential cycling of the electrode potential during cyclic voltammetry may have an effect on the reproducibility of the data, by perhaps causing a change in the liquid crystalline arrangement in the vicinity of the electrode. If this is the case, the cyclic voltammograms obtained would change shape with time, for example in the form of additional peaks, which were not observed in the Brij® 56 system. In addition, microelectrode responses in the Brij® 56 system showed that the double layer capacitance was hardly changed by the presence of an ordered lyotropic liquid crystalline surfactant; in other words, the double layer capacitance did not appear to be affected by the increase in surface areas caused by the surfactant structure. All this makes it unlikely for the continuous potential cycling of the electrode potential to affect the data reproducibility.

Having said that, Attard and coworkers have successfully used both cyclic voltammetry and potential step techniques to electrodeposit nanostructured Pt, where the latter technique allowed the change in Pt surface area by varying the growth charge.[52, 53]

Another answer could be the physical environment, where there could be no good contact between the microelectrode and Brij® 56 / ferricyanide mixture due to the presence of a trapped air bubble (or bubbles as in the case of large electrode). This leads to the questions as to how close the bubble would be to the electrode to get the decrease in the limiting current. This can be likened to scanning electrochemical microscopy (SECM) studies of hindered diffusion where the microelectrode tip is brought close to an insulating substrate.[116] The steady-state current flowing through the tip becomes smaller than the bulk steady-state value because the substrate partially blocks the diffusion of a redox species to the tip. Simulations have shown that the typical distance for a 20 %

reduction in current for instance is between 5.5 and 6 times the radius of the microelectrode tip, when the ratio of the radius of the insulating ring round the tip to the tip radius, R_g, is between 100 and 1000 times.[117]

Another question would be whether the bubble would eventually move away from the microelectrode caused by the organisation of the liquid crystalline phase of Brij® 56 into equilibrium. The increase in the reduction limiting currents with the number of scans in Figure 26 seems to support this. Again, this suggests that a timescale exists for the microelectrode or the liquid crystal to adapt to the situation; in Figure 26, the average time taken for the limiting current to reach the maximum of 1 nA appeared to be about 20 minutes.

It would therefore be interesting to investigate the timescale of the motion of water molecules in a lyotropic liquid crystalline system by NMR. The NMR properties of water in the vicinity of molecules in solution differ from those of water in the pure state. Water molecules interact with the solute via hydrogen bonds and/or electrostatic forces related to their high dipolar momentum. At room temperature, the correlation times of rotational and translational movements of the order of 10^{-11} to 10^{-12} s in pure water may increase to 10^{-8} or even 10^{-6} s in the hydration layer of macromolecules.[118, 119]

Deuterium (^2H) NMR spectroscopy is known to be a method sensitive to ordering phenomena and phase changes in liquid crystals.[120] In a lyotropic liquid crystal, molecular motion stays relatively fast on ^2H NMR timescale, i.e. 10^{-5} to 10^{-4} s, appearing slower than in the case of water molecules, and it is believed to stay generally confined within the anisotropic geometry of the individual aggregates. This is evident in a time-averaged value for the quadrupolar interaction that is non-zero; thus the quadrupolar splitting in the spectrum can give information on the shape of the aggregates and the average local order parameter of the C-^2H bonds. For example, a lamellar phase is calculated to give a quadrupolar splitting twice as large as a hexagonal phase.

This method has already been used by Attard *et al.* to monitor *in situ* the formation of mesoporous silica in a liquid crystalline phase, i.e. hexagonal, H_1-silica;[121] one of their objectives was to prove that the inorganic nanostructure ordering was the result of the liquid crystal templating. Their spectra reflected the phase behaviour of the reaction mixture as it changed with time; the time taken for the liquid crystalline phase to

form was found to be 10 min, and optical microscopy showed textures typical of a hexagonal phase.

Thus, in Figure 26, the average time of 20 min taken for the limiting current to reach the maximum of 1 nA seems reasonable.

On the other hand, it is well known that the liquid crystalline domains in the hexagonal phase can be aligned in a magnetic field.[122] The orientation order of water molecules and the magnetic alignment of surfactant molecules can be studied using the same NMR technique. Recently, Rapp *et al.*[123] discovered that the magnetic alignment of lyotropic liquid crystals formed by hexadecyltrimethylammonium bromide (CTAB, where C stands for cetyl) at CTAB/D_2O concentrations between 1.01 and 1.29 mol/kg could take a few hours depending on the strength of the magnetic field.

Moreover, Owen *et al.*[124] found from the electrochemical impedance method applied to nanostructured platinum that the tortuosity factors for the double layer and hydrogen adsorption regions were greater than calculated for the ideal structure. They suggested that a large proportion of the water molecules within the pores have a reduced mobility due to their close proximity to the platinum surface.

Therefore, it appears reasonable to conclude that the diffusion coefficient of ferricyanide in the surfactant system should be calculated from the maximum reduction limiting currents obtained in the Brij® 56 mixture.

The next question would be why the limiting currents and thus the diffusion coefficient value were lower by a factor of 35 in the surfactant system, which suggests a lower mass transport rate. The answer could lie in the cross-sectional area available for reaction.

The average value of double layer capacitance (or charging current) in the Brij® 56 system seem to be 0.1 nA and in the aqueous system, 0.16 nA. This could mean that a lower cross-sectional area was available for reaction in the former. Based on the geometry of the hexagonal phase of Brij® 56, where the liquid crystalline rods align hexagonally on the microelectrode surface, calculations could be made as follows:

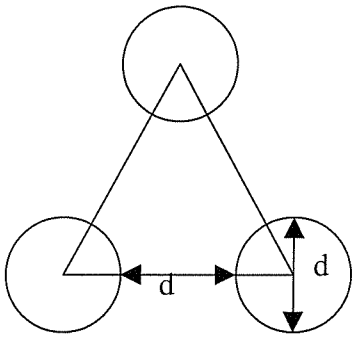

Figure 29 Diagram of circles (representing the pores of the surfactant rods) and triangle (representing the hexagonal geometry) for calculating the area occupied by the water molecules in the pores.

$$area_{triangle} = 0.5(base \times height) = 0.5\left(2d(3d)^{1/2}\right) = 3^{1/2}d^2 \qquad \textbf{Equation 19}$$

$$area_{circle} = \pi(0.5d)^2 = 0.25\pi d^2 \qquad \textbf{Equation 20}$$

$$area_{circularoverlap} = 0.5 \times 0.25\pi d^2 = 0.125\pi d^2 \qquad \textbf{Equation 21}$$

$$area_{triangle} - area_{circularoverlap} = 1.34d^2 \qquad \textbf{Equation 22}$$

$$\frac{area_{triangle} - area_{circularoverlap}}{area_{triangle}} = 77.3\% \qquad \textbf{Equation 23}$$

Thus, the area occupied by the water molecules within the pores = 77.3 %.

From the calculations, it could be seen that the geometry does not account for the factor of 35 decrease because the area occupied by the water molecules within the pores was calculated to be about 77.3 %. Therefore, the diffusion in the aqueous domains of the surfactant system must be different from the diffusion in the bulk, i.e. the aqueous system.

This difference could be due to the effect of viscosity. The Stokes-Einstein equation[125] relates the diffusion coefficient to viscosity.

$$D = \frac{kT}{6\pi\eta r}$$ **Equation 24**

where k is Boltzmann's constant (J K^{-1}), η is viscosity (cP or 10^{-3} kg m^{-1} s^{-1}), r is the effective hydrodynamic radius of the spherical particle and T is temperature (K). At 25 ^{0}C, the viscosity of water is known to be 0.88 cP; the viscosity of 1 M KCl solution is 1.13 cP; and the viscosity of 17 mM potassium ferricyanide solution is 1.14 cP.[126]

In a review by Rusling on using microelectrodes to study diffusion in micelles for example, diffusion coefficients measured for electroactive probes in micellar solutions from the limiting steady-state current can give diffusion coefficients of the micelles themselves; assuming only spherical micelles, the average micelle radius is given by the Stokes-Einstein equation.[60] However, the diffusion coefficient is believed to be an apparent value, D', due to equilibrium of the free probe in solution with probe bound to micelles, see equation 2 in section 3.1.1 in this chapter.

In addition, critical micelle concentrations (CMCs) of various surfactants have been obtained by monitoring for example the peak current of ferrocyanide in cyclic voltammetry.[127] The CMC value for Brij® 30 for example is known to be about 16.7 mg L^{-1} or 0.004 mM, and for Brij® 56, the CMC value is about 13.6 mg L^{-1} or 0.002 mM .[128]

Huibers *et al.*[129] used software developed at the University of Florida called Codessa to predict the CMC in mM values of 77 nonionic surfactants by studying the size of the hydrophobic group, the size of the hydrophilic group and the structural complexity of the hydrophobic group, and found their predictions match well the literature CMC values. For instance, for $C_{16}EO_7$, the predicted $\log_{10}$ CMC value was 5.825 and the observed was 5.770, and for for $C_{16}EO_9$, the predicted $\log_{10}$ CMC value was 5.768 and the observed was 5.678.[129, 130]

Although the CMC values are known for the Brij series of surfactant, the viscosity of Brij® 56 micelles with water before liquid crystalline structures are formed has not yet been found in the literature. On the other hand, there is a semi-empirical mathematical relationship for the viscosity of dilute polymer solutions; according to Atkins,[125] at low concentrations, the viscosity of the solution, η, is related to the viscosity of the pure solvent, η^*, by

$$\eta = \eta^{*}(1 + [\eta]c + ...)$$ **Equation 25**

where in our case, the solution corresponds to the Brij® 56 system and the pure solvent to water, and *c*, concentration in M, to the CMC value of Brij® 56. Thus, with *c* as 0.002 M and η^{*} for water as 0.88 cP, η is calculated to be 1 cP, confirming a higher degree of viscosity in the surfactant system. From the Stokes-Einstein equation, the diffusion coefficient of Brij® 56 micelles is found to be 3.6 x 10^{-9} cm^2 s^{-1}.

There is, however, evidence that strong binding of an electroactive solute to micelles in micellar solutions results in a diminished current and diffusion coefficient value when compared to homogeneous solutions. For instance, ferrocene in mM concentrations in 0.11 M CTAB / 0.1 M NaCl is almost totally bound giving a diffusion coefficient value of about 0.8 x 10^{-6} cm^2 s^{-1},[73] whereas ferrocinium ion, its oxidation product, is not bound to the CTAB micelles and gives a value of 6 x 10^{-6} cm^2 s^{-1}.

This approximate 10-fold decrease in the diffusion coefficient value is also noticeable in our results for ferricyanide reduction: 0.2 x 10^{-6} cm^2 s^{-1} in the Brij® 56 system and 7.6 x 10^{-6} cm^2 s^{-1} in the aqueous system. However one must be careful because the CTAB solution discussed above is different to the Brij® 56 system studied in this thesis, which was viscous and displayed *regular, liquid crystalline structured* phases under the polarised-light optical microscope. Therefore, as stated previously, the diffusion processes of a redox probe in the micellar and other surfactant solutions, which resemble more like bulk aqueous solutions, must be different to the diffusion processes of a redox probe in the aqueous domains of surfactant systems.

Finally, if the SAM model described in section 3.1.3 is applied to our diffusion studies of ferricyanide redox chemistry, this supports the theory that the electrode surface of the Au microelectrode may be covered with a monolayer of Brij® 56. In our diffusion studies, the reduction limiting currents were observed to increase with continuous potential cycling of the Au microelectrode, i.e. with time. If applying the SAM model, this means that this surfactant monolayer would become thinner with time.

3.3.3 Summary

Although there is considerable literature on the diffusion of an electrochemical probe in such surfactant media, as described in the introduction of this chapter, diffusion studies of an electrochemical probe in the aqueous domains of different *regular, liquid crystalline structured* phases of a surfactant (formed at sufficiently high surfactant concentrations) have never been carried out until now.

The aim of this section was to study the diffusion processes of ferricyanide in the regular, lyotropic liquid crystalline structures of Brij® 56. The effect by the lyotropic liquid-crystalline phase formed by Brij® 56 on the diffusion coefficient of the redox probe could be compared to the aqueous system.

The diffusion coefficient of ferricyanide in the surfactant system should be calculated from the maximum reduction limiting currents obtained. A noticeable 10-fold decrease in diffusion coefficient for ferricyanide reduction was observed. Ferricyanide chemistry appeared more reversible in the surfactant system, and a timescale appeared to exist for the organisation of the liquid crystalline phase of Brij® 56 into equilibrium. Finally, the diffusion in the aqueous domains of the surfactant system seemed different from the diffusion in the bulk, i.e. the aqueous system.

Chapter Four

4 Electronic Conducting Polymers

4.1 A Brief Introduction

Electronic conducting polymers are organic polymers which conduct because they possess a π-electron conjugation on the polymer backbone. Thus, the delocalisation and transport of these charge carriers opened up a new world of research. A brief review of conducting polymers and their development is given by Inzelt *et. al.*[131] Their potential applications range from corrosion protection to batteries.[132]

Most conducting polymers have conductivities in the range of 10^{-6} to 10^{2} S/cm. The simplest conducting polymer is poly(acetylene) and has the highest known conductivity, of 10^{5} S/cm. Unfortunately, this polymer is susceptible to attack by oxygen. Aromatic conducting polymers are more stable but have lower conductivities. For example, poly(aniline) tends to have conductivity in the range of 1 to 100 S/cm.

Another attractive property of conducting polymers is their ability to switch reversibly between insulating and conducting states. Figure 30 gives three examples of aromatic conducting polymers.

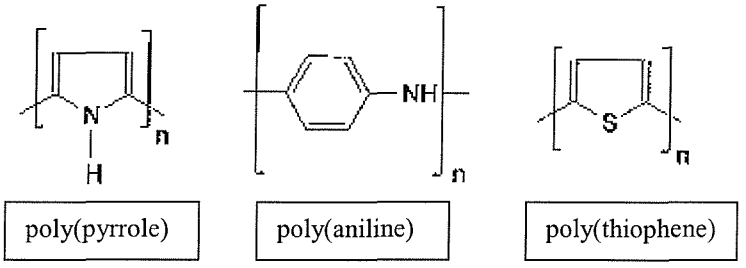

Figure 30 Examples of aromatic conducting polymers.[56]

This conductivity of conducting polymers arises from chemical or electrochemical oxidation, or in some cases reduction, of the polymer backbone by a number of anionic or cationic species known as dopants. This doped state exists to introduce charge centres where the polymeric backbone attracts anions or cations from the solution to balance the charge.

Although they are complex systems, several features were found necessary for charge conduction in conducting polymers.[56] Firstly, a π-electron system must exist. Secondly, doping in the form of oxidation and reduction of the polymer chain must take place; charge carriers are introduced into the conductance or valence band of the polymer. For example, the oxidation of the polymer backbone causes positively charged species known as holes whose charge is balanced by the incorporation of counterions from the solution.

In the simplest case, materials may be broadly classified into three classes according to their conductivities at room temperature: insulators, semiconductors and conductors. The individual molecular electronic states overlap to produce electronic bands. Valence electrons overlap to produce a valence band, and the electronic levels above these overlap to produce a conduction band. The gap existing between these bands is known as a bandgap, generally denoted as E_g, measured in eV. A 10 eV bandgap results in an insulator at room temperature because it is difficult to excite electrons into the conduction band. At 1 eV, excitation is possible thermally, vibrationally or by photons, resulting in a semiconductor.

"Doped" conducting polymers are semiconductors because of their π-conjugation; the extended-overlap π-orbitals become the valence band and the π* orbitals become the conduction band. Generally the bandgap is greater than 1 eV in most conducting polymers.[132] If the gap disappears leading to an overlap of both bands, metallic conduction exists.

The only example of conducting polymers used in this project is poly(aniline) (abbreviation: PANI). A historical review of PANI electrochemistry is given by Geniès *et al.*[133] Polymerisation takes place through radical intermediates coupling head to head and head to tail of the monomer units. The number of publications on the subject of PANI is increasing all the time; besides the diversity of their potential applications, aniline is a cheap product and PANI is a very stable material.

On the other hand, the fundamental questions on their behaviour, structure and other observed phenomena are still quite complex and being investigated.[131] For example, when PANI is prepared by electrochemical oxidation on different electrode materials, Bard *et al.*[134] and Geniès *et al.*[135] noticed that the first "layers" of PANI

deposited on an electrode were denser compared to subsequent "layers"; the probability of oxidising the monomer directly at the electrode was reasoned to be greater than after the formation of these initial "layers".

PANI can also be synthesised chemically with the help of a suitable chemical oxidant. However, electrochemical synthesis is more advantageous because the resulting product is "clean" and does not require any extraction method from the initial monomer/oxidant/solvent mixture.

Electrochemical polymerisation conditions, such as the electrodeposition technique and the solvent, can influence considerably the mechanical and electrical properties of the films.[136] For instance, aniline electropolymerises easily under aqueous acidic conditions because the presence of protons encourages conduction.

As in Figure 31, there are several forms of PANI: leucoemeraldine, emeraldine and pernigraniline, which are different oxidation states; a partially protonated leucoemeraldine, and two protonated emeraldine forms. Regarding the oxidation states, the emeraldine is the conducting state, and the other two forms are insulating. Figure 32 is the scheme of redox transformations and protonation equilibria of PANI.

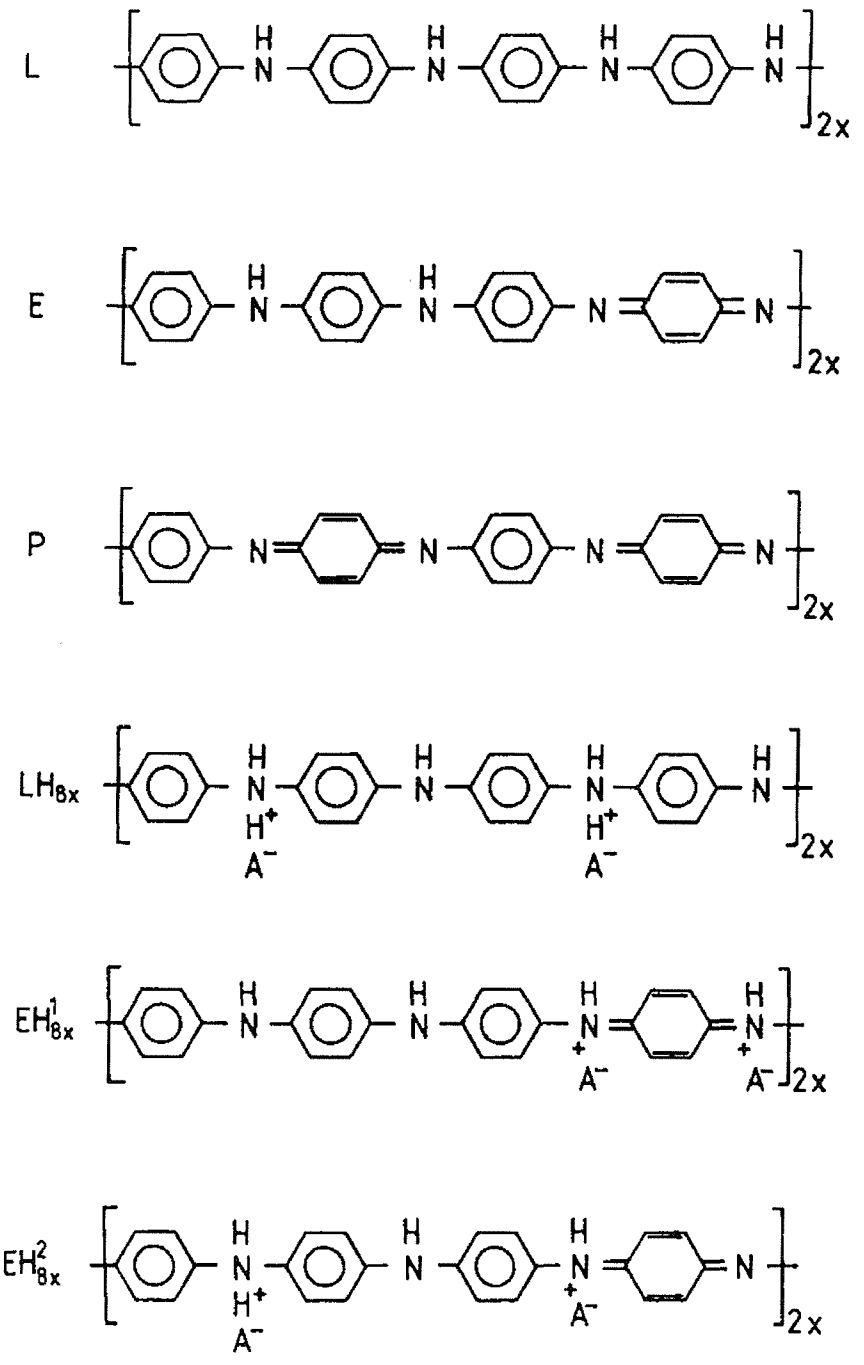

Figure 31 There are several forms of PANI: leucoemeraldine (L), emeraldine (E) and pernigraniline (P), which are oxidation states; a partially protonated leucoemeraldine (LH_{8x}), and two protonated emeraldine forms, (EH_{8x}^{1}) and (EH_{8x}^{2}).[137]

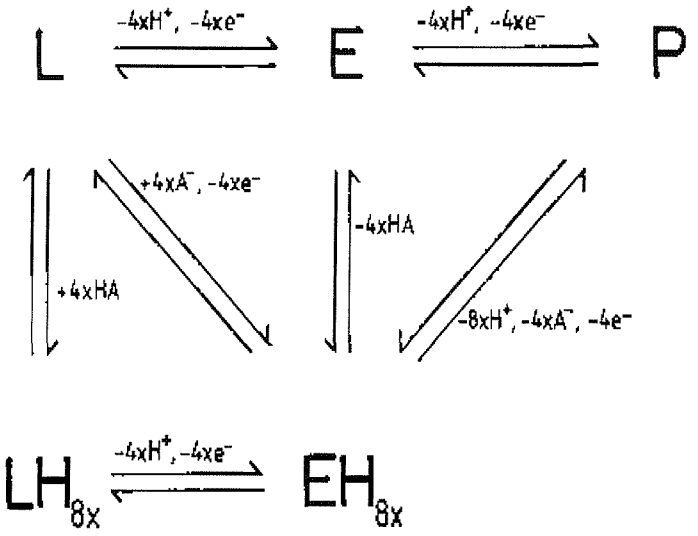

Figure 32 Scheme of redox transformations and protonation equilibria of PANI, where abbreviations such as L come from Figure 31.[137]

In cyclic voltammetry of PANI, two sets of distinct peaks are obtained, and the electrochemistry of PANI can be dependent on the incorporated anion.[138] The first set is representative of the transition from leucoemeraldine to emeraldine, and the second set corresponds to a further oxidation to pernigraniline. This complete oxidation of PANI unfortunately precedes the breakdown of PANI due to acid hydrolysis of diimine sites within the polymer and the decomposition products lead to a third peak in between the two peaks.[139] That is why the upper limit of +0.5 V was used in cyclic voltammetry of PANI films in sulfuric acid in this project.

Figure 33 shows a typical cyclic voltammogram of a PANI film in aqueous acidic conditions, with the colour changes depicted as associated with the different redox states as PANI is an electrochromic material.[133]

The original aim was to study the electropolymerisation of a conducting polymer in a lyotropic liquid crystalline surfactant system such as $C_{16}EO_8$. Aniline was chosen because aniline electropolymerises easily under aqueous acidic conditions because the presence of protons encourages conduction, and it is this presence of protons that ensures it stays in the aqueous domains of the surfactant system and does not partition into

surfactant micelles, see Figure 34. Furthermore, PANI has been observed by De Surville *et al.*[140] to have a strong affinity for water; NMR spectroscopy has shown a permanent exchange between the fixed protons of the nitrogens in the polymer and the water of hydration of the polymer.[141]

The following sections will discuss how a conducting polymer like polyaniline may be formed electrochemically in the hexagonal phase of a non-ionic surfactant like $C_{16}EO_8$, and describe the attempts to characterise the structural properties of conducting polymers grown from liquid crystalline phases.

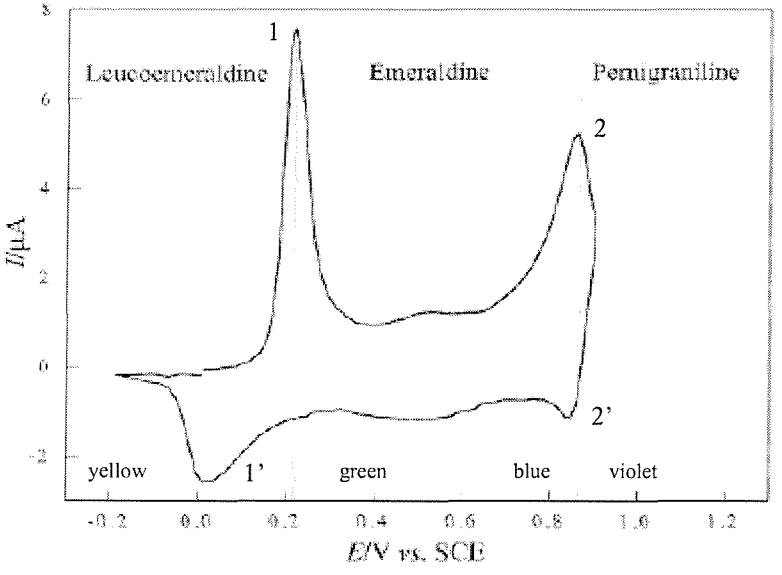

Figure 33 Typical cyclic voltammogram of PANI film in acidic aqueous conditions, recorded at 20 mV/s in 2 M H_2SO_4. The PANI film was grown on a 0.5 mm diameter Pt electrode at +0.9 V from a solution of 0.4 M aniline in 2 M H_2SO_4. The colour changes associated with the different redox states are shown and the two principal redox couples are labelled 1, 1' and 2, 2' respectively. Potential is quoted versus SCE.[56, 142]

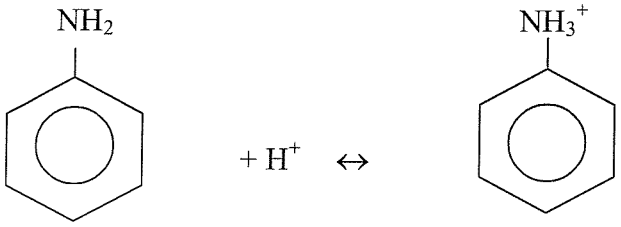

Figure 34 Schematic diagram of the equilibrium between the aniline monomer and its protonated form in sulfuric acid.

4.2 Electropolymerisation of Aniline and Characterisation (Aqueous System)

PANI films were grown on gold electrodes by potential step and were compared with those electrodeposited in the liquid crystalline hexagonal phase of $C_{16}EO_8$.

The growth solution consisted of 0.4 M aniline and 1 M sulfuric acid solution at 25 ^{0}C. The potential was stepped from 0 V up to potentials ranging from +0.70 to 0.90 V.

The aim was to pass 500 μC of charge over the gold surface (0.2 mm diameter) to produce a charge density of 1.6 C cm^{-2}, achieving very short time scales of PANI electrodeposition (of the order of 1 min).

Table 3 shows that generally, the slowest deposition of PANI films took place when the potential was stepped from 0 to +0.7 V taking about 1 500 s, with the fastest electrodeposition being +0.9 V.

The different shapes of growth current-time transients can be clearly seen in Figure 38; electrodeposition at +0.8 V appeared similar to the one at +0.9 V, especially in terms of time taken to pass the same charge.

After deposition, the PANI films were soaked in deionised water for two days like those produced in the surfactant ($C_{16}EO_8$) system (see below) in order to compare like with like. In the latter system, soaking in water was necessary to remove excess surfactant.

Potential stepped from 0 to this potential / V	time/s	max deposition current /μA
0.7	1553	0.73
0.8	52	43
0.8	52	44
0.9	43	36
0.9	42	44
0.9	43	30

Table 3 Table showing information relating to the PANI films grown on Au (0.2mm diameter), from 0.4 M aniline / 1 M H_2SO_4 solution at 25 ^{0}C; the deposition or growth charge passed was approximately 500 μC.

The mechanism and kinetics of the electropolymerisation of aniline are very complex and not completely known. In Figure 38, the deposition currents recorded by potential step are not as high as expected. The order of magnitude appears similar to that of the currents recorded by potential step in 10 mM ferricyanide aqueous system. This is strange because the growth mixture here contains 0.4 M or 400 mM aniline, which should produce a current that is 40 times greater, and it is not the case. This suggests that the electrodeposition of PANI is not controlled by mass transport but by kinetics, either electron transfer or some other polymerisation reactions or both types.

Geniès *et al.*[133] reviewed PANI over ten years ago and found the fundamental questions concerning the polymerisation mechanism and observed phenomena of PANI for example not completely understood. A very recent review carried out by Inzelt *et al.*[131] records the incredible progress made so far, but acknowledges the need for more research.

Recently, Chandrasekhar[132] describes the mechanisms of the polymerisations in a simple manner for poly(aniline) and poly(pyrrole). In both the chemical and the electrochemical cases, the generation of the radical cation is the initial step, see Figure 35. The next step is where according to some studies,[143] the chemical and electrochemical polymerisations differ.

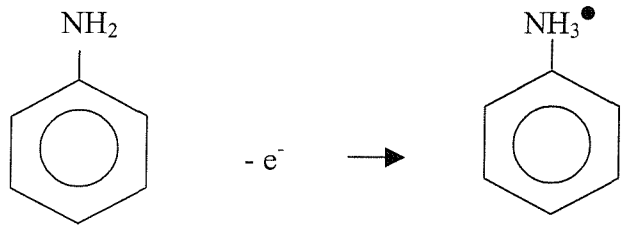

Figure 35 For both chemical and the electrochemical polymerisations, the generation of the radical cation is the initial step.

In the chemical case, the radical cation attacks another monomer molecule, of which there are plenty in the reaction sphere, producing a dimer radical cation. This continues till termination producing the polymer chain, see Figure 36.

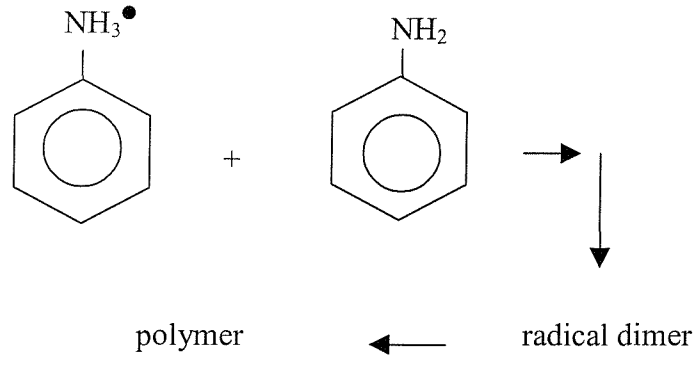

Figure 36 Scheme showing the polymer propagation steps for chemical polymerisation.

According to Chandrasekhar[132], most electrochemical polymerisations of conducting polymers appear to follow a generic reaction pathway. After the initiation step, it is believed that there is a greater concentration of radical cations than neutral monomers near the electrode, and radical-radical coupling results in radical dication. This loses two protons to generate a neutral dimer which is then oxidised to a radical cation, i.e. an "oligomeric" radical. The combination of this or similar radicals with monomer radicals etc. builds up the polymer, and termination occurs through depletion of reactive radical species in the vicinity of the electrode. Therefore, *radical-radical*

coupling (not radical-monomer coupling) and the loss of two protons from the radical-radical intermediate species are widely accepted as the main features of the propagation mechanism for most electrochemical polymerisations generally, see Figure 37.

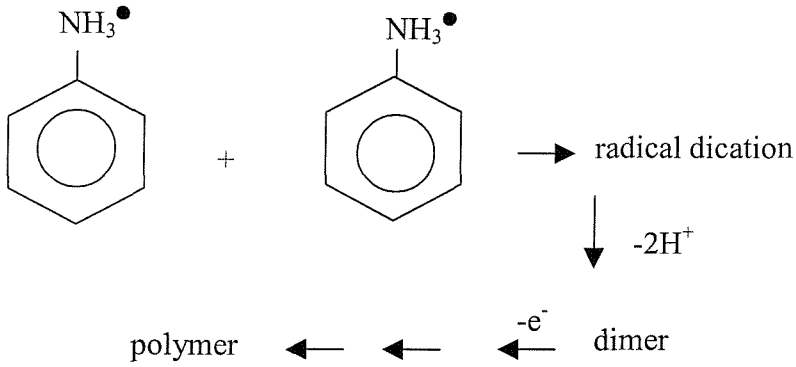

Figure 37 Scheme showing the polymer propagation steps for electrochemical polymerisation.

One of the first characteristics to note for electrochemical polymerisation is that once the initiating electrochemical potential is applied, the population of radical cations tends to exceed that of neutral monomer in the vicinity of the electrode. This means that a generated radical cation will more likely be surrounded by other radical cations than by neutral monomers or oligomers or other species. This is seen in the rapid electron kinetics for electro-oxidation of the monomer, in this case aniline, when compared to the slower diffusion of monomer from the bulk of reaction medium to the electrode, thereby resulting in a rapid depletion of monomer concentration at the electrode.

The model described above is not consistent with the currents observed in Figure 38 and commented on earlier, because the model would advocate the reaction to be diffusion controlled.

Therefore, the relatively high concentration of aniline in solution (0.4 M) and the magnitude of the deposition currents in Figure 38 compared to that of the currents seen in in 10 mM ferricyanide aqueous system suggests that the PANI electrodeposition is not controlled by mass transport but by kinetics, either electron transfer or some other

polymerisation reactions or both types. This disagrees with the model described from the literature above.

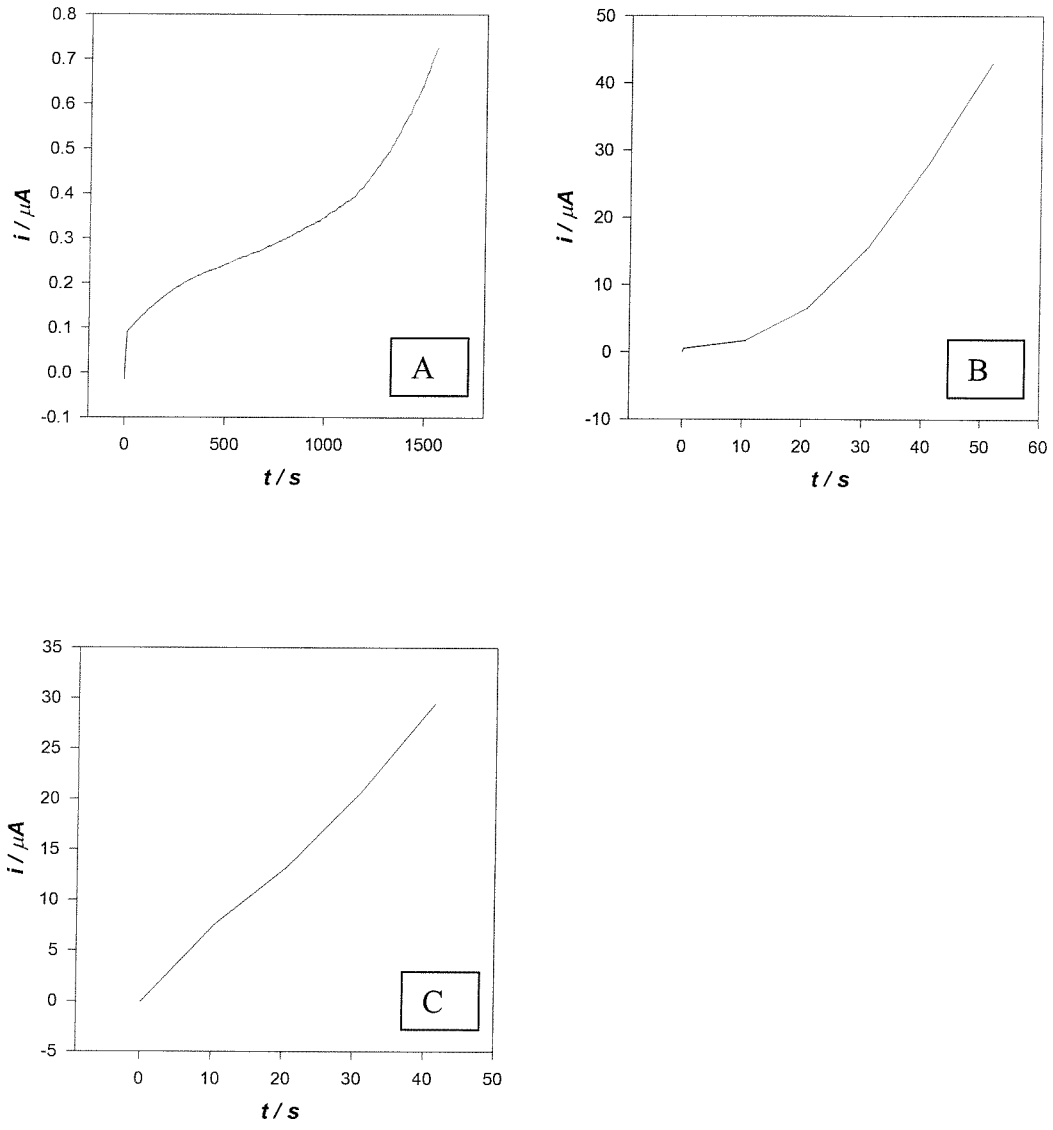

Figure 38 Current-time transients showing the electrodeposition of PANI films grown on Au (0.2mm diameter), from 0.4 M aniline / 1 M H_2SO_4 solution at 25 ^{0}C, with potential stepped from 0 V to : (A) +0.7, +0.8 and +0.9 V vs. SCE, passing 500 μC.

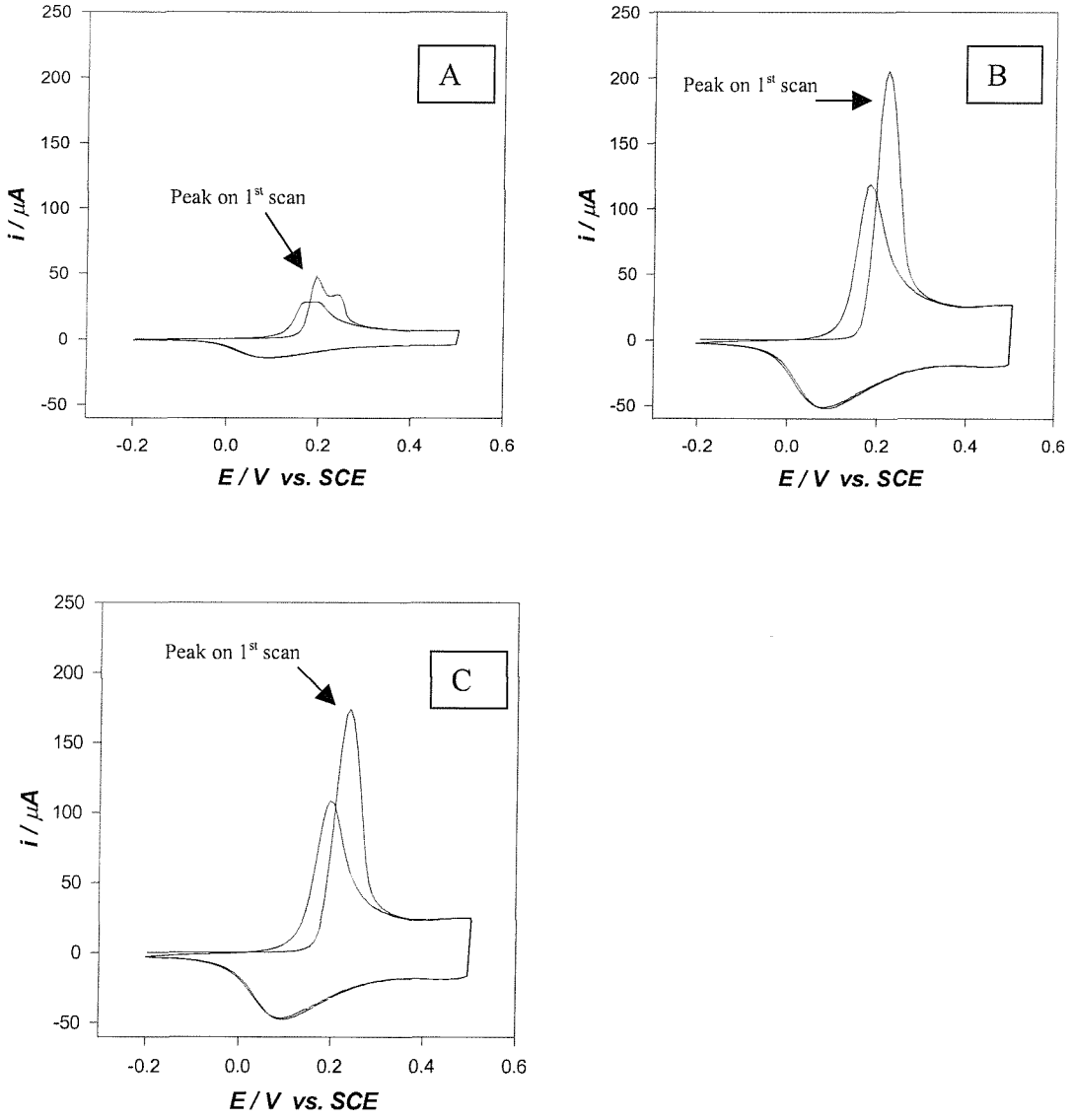

Figure 39 Cyclic voltammograms in 1 M sulfuric acid at 200 mV/s of PANI films grown on Au (0.2mm diameter), from 0.4 M aniline / 1 M H_2SO_4 solution at 25 ^{0}C, with potential stepped from 0 V to : (A) +0.7, +0.8 and +0.9 V vs. SCE, passing 500 μC.

According to Bard,[144] the behaviour of the electrode-solution interface is analogous to that of a capacitor, when the potential across it is changed. The capacitance can be defined as the charge accumulated on the plates of the capacitor divided by the

potential across it. During this charging process, a current called the charging current will flow, with the charge consisting of an excess of electrons on one plate and a deficiency of electrons on the other. Therefore at the electrode-solution interface at a given potential, a charge will exist on the metal electrode, represented by an excess or deficiency of electrons, and a charge will exist in the solution, represented by an excess of cations or anions in the vicinity of the metal electrode surface. The applied potential across it will determine whether the charge on the metal is negative or positive with respect to the solution. The whole array of charged species existing at the interface is called the electrical double layer.

Electronic conducting polymers can be oxidised and reduced, with the ability to store charge and discharge it. The charge/discharge process can be observed by cyclic voltammetry over a suitable potential range.

In our work, PANI films were firstly electrodeposited on gold electrodes by potential step technique, from a growth solution of 0.4 M aniline and 1 M sulfuric acid at 25 ^{0}C. The potential was stepped from 0 V up to potentials ranging from +0.7 and +0.9 V, at one charge density of 1.6 C cm^{-2}. After deposition, the PANI films were soaked in deionised water for two days. These films were then characterised by cyclic voltammetry in 1 M sulfuric acid at 25 ^{0}C in the potential range between –0.2 and +0.5 V at various scan rates ranging from 10 to 200 mV/s. The initial voltage was held at –0.2 V for 2 min to ensure complete reduction of the films. Then the potential was scanned anodically, reversing direction at +0.5 V and ending at –0.2 V. This acid characterisation allowed estimations of the capacitance and thus surface area of each film made, to be discussed in greater detail below.

For each film, the first cyclic voltammogram was obtained at 200 mV/s for five cycles, to stabilise the film for subsequent cycling. Then two cycles at 200, 100, 50 , 20 and 10 mV/s were recorded in that order, with each time the film potential being held at -0.2 V for 2 minutes.

The anodic current at +0.5 V on the first cycle was then plotted versus the scan rate for calculating capacitance of the films grown. At this potential, the conducting emeraldine state would be formed, and this accounts for the large capacitive current observed at the positive limit of the cyclic voltammograms. SEM analyses have shown

the PANI films to be highly porous and thus to have high surface areas.[56] This capacitive current thus corresponds to the charging of the double layer of the now conducting film on the electrode surface. This has been the subject of some debate in the literature;[145] however, since we are interested in comparing films grown by different methods, the comparison is still valid even if the origin of the "capacitive" current is open to some debate.

As mentioned previously, the upper limit of +0.5 V was chosen because cycling the potential beyond this would change the films irreversibly as seen in Figure 33. Both Diaz *et al.*[146] and Kobayashi *et al.*[147] reported the colour changes depending on the potential applied following the redox reactions which occurred between –0.2 and 1.0 V vs. SCE. The electrochromic material was found to be unstable during cycling; however, if the upper limit was limited to +0.6 V, its behaviour was stable up to 10^6 successive cycles.

For each potential step, Figure 39 shows typical cyclic voltammograms at 200 mV/s of PANI films characterised in 1 M sulfuric acid. A greater and sharper oxidation peak would appear noticeably on the first scan than on the next scan, and this was noticeable for all scan rates recorded, ranging from 10 to 200 mV/s. The reason could be that when the potential was initially held at –0.2 V in order to reduce the films completely, subsequent scans did not allow complete reduction thereby decreasing the area of the oxidation peak.

This slower electron transfer kinetics for the first cycle in each case was confirmed by Peter *et al.*[148] who studied the rate of switching in PANI films in 1 M sulfuric acid using a 10 μm diameter microelectrode at 100 V/s. They found their first voltammogram to differ from subsequent ones, believing the cause to be to imperfect rereduction. This was also observed in the cyclic voltammetric responses of microelectrodes of 5- 20 μm diameter obtained at very fast scan rates such as thousands of V s^{-1} by Andrieux *et al.*[149]

In Figure 39, the anodic shift in the peak potential of the oxidation wave on the first cycle is likely to be caused by the need for nucleating and growing emeraldine centres, according to Inzelt.[137] Peter *et al.*[148] assumes a very fast proton migration at

short times followed by equilibration of the oxidised phase by the diffusion-controlled movement of the acid.

In addition, the maximum oxidation current recorded in the characterisation cyclic voltammograms for the deposition potential of +0.7 V was smaller than the other two deposition potentials, but the oxidation peak potential did not shift. However, there appeared to be no marked difference in the oxidation current between films grown at +0.8 and +0.9 V.

Looking at the oxidation charge in the first cycle of acid characterisation for all the films in Figure 39, the charge for the film grown at +0.7 V relative to the others was much smaller, although the same growth charge was passed. Again this supports the complex kinetics of PANI growth.

The capacitance of the films can be calculated from the slope of the plot of the anodic current at +0.5 V on the first cycle versus the scan rate. The plot was based on the following equations, where Q, C, i, t and V represent charge, capacitance, current, time and voltage respectively:

$$Q = CV \qquad \textbf{Equation 26}$$

$$\frac{dQ}{dt} = C\left(\frac{dV}{dt}\right) \qquad \textbf{Equation 27}$$

$$i = C\left(\frac{dV}{dt}\right) \qquad \textbf{Equation 28}$$

The capacitance could be then be normalised with respect to the geometric area of the gold electrode or with respect to the growth charge passed to deposit the film, i.e. F cm^{-2} or F C^{-1} respectively. For the latter, this normalisation removes the effect of the differences in the film thickness.

There are limitations in these measurements of capacitance. A completely efficient polymerisation of aniline was assumed. However, if we simply compare values for different films, then we need only assume the same faradaic efficiency for the electrodeposition.

Firstly, the mechanical strength of the PANI films has been shown by Elliott[56] to depend on the growth potential in the potential step depositions, where at low growth potentials like +0.7 V, the black films formed did not adhere well to the electrode surface; transfering the electrode from the growth solution to the sulfuric acid for characterisation and thus rinsing the electrode in the process with water can lead to some of the film being washed away; electrodeposition at potentials higher than +0.85 V on the other hand, can result in the formation of undesirable side products.[150] Also, no loss of material during cycling was assumed.

Secondly, unlike other electronic conducting polymers, PANI may be switched from an insulating to a conducting state by the movement of protons only.[151] Although the pH of the electrolyte and the nature of the incorporated anion are important factors,[152] our work concerns only the studies of PANI in one electrolyte, i.e. sulfuric acid. What could be more important is that solvent molecules are known to be directly involved in the process causing the polymer films to swell and shrink during the redox process, thus affecting the capacitive current at the positive potential limit.

Thirdly, Peter *et al.*[153] have obtained lower capacitance values by a.c. impedance compared to those obtained by cyclic voltammetry, and suggested that depending on the time scale of the redox process, the contributing processes to the current in the plateau region may vary. For example, as the film was oxidised, anions were assumed to enter the film to balance the positive charge created by the loss of electrons.

In addition, for poly(aniline) hexane sulfonate films, Elliott found that increasing the scan rate moved the relationship between the first anodic peak height and scan rate from a linear dependence to a square root dependence, indicative of a surface confined process transforming to a diffusion controlled process, with the effect getting more pronounced with increasing film thickness.[56] This is important because the relationship between the current passed at +0.5 V and the scan rate was found to vary according to film thickness; increasing the film thickness resulted in a greater deviation from linearity.

Therefore, while comparison of values from one film to the next appears acceptable and conclusions could be drawn, the absolute values should be treated with some care because of all these complicating factors. However, what we are really interested in is comparing one film with another.

Potential stepped from 0 to this potential / V	Maximum oxidation current in acid at 200 mV /s /μA	Capacitance per Au area / μF cm^{-2}	Capacitance per growth charge / F C^{-1}
0.7	50	103 000	0.06
0.8	200	423 000	0.27
0.8	200	419 000	0.26
0.9	250	378 000	0.24
0.9	260	462 000	0.29
0.9	170	398 000	0.25

Table 4 Table showing sulfuric acid characterisation information relating to the PANI films grown on Au (0.2mm diameter), from 0.4 M aniline / 1 M H_2SO_4 solution at 25 ^{0}C; the deposition or growth charge passed was approximately 500 μC.

Table 4 shows that the capacitance calculated per growth charge again was smaller for the deposition potential of +0.7 V, by a factor of 5 when compared to the other two deposition potentials; there was also no marked difference when comparing films grown at +0.8 and +0.9 V.

Both the comparison of the oxidation charge and the capacitance of the films characterised in acid suggest that films grown at +0.8 and +0.9 V were more stable and contained larger surface areas, up to five times the surface area of the film grown at +0.7 V.

Tanguy *et al.*[154] studied the electrochemical response of chemically synthesised PANI with the help of complex impedance measurement methods. During electrochemical oxidation (doping), anions in the solution would penetrate the polymer to compensate the positive charges in the chain, and two types of doping sites were believed to exist in the chain which explains the significance of the capacitive charge of conducting polymers, as supported by mass spectrometric data on emeraldine chloride.[155]

4.3 Electropolymerisation of Aniline in $C_{16}EO_8$ and Characterisation (Surfactant System)

Similar potential steps were carried out for growing PANI in the presence of $C_{16}EO_8$ for the same charge density of 1.6 C cm^{-2}. A phase diagram for this ternary system was not obtained at the time due to shortage of $C_{16}EO_8$. Based on the phase diagram of the binary system of $C_{16}EO_8$ and water in , a hexagonal phase was expected at 50 wt% of $C_{16}EO_8$. Thus, the growth mixture consisted of 50 wt% $C_{16}EO_8$ and 50 wt% (0.4 M aniline and 1 M sulfuric acid solution) at 25 ^{0}C. Polarised light optical microscopy confirmed a hexagonal liquid crystalline phase.

It was not possible to grow PANI films in the presence of $C_{16}EO_8$ by stepping the potential from 0 to +0.7 V as the maximum deposition current was too low to be recorded on our equipment, i.e. of the order of nanoamperes.

Compared to the aqueous system, there was a marked difference in the times and deposition currents recorded here; generally, the electrodeposition took ten times longer and the currents were smaller by a factor of ten in the surfactant system. This meant that electrodeposition in the surfactant system was slower and more difficult.

Looking at the concentration of aniline (0.4 M) in the surfactant system, this reaction could not have been diffusion limited, i.e. not controlled by mass transport. Thus, the decrease in deposition currents must be because the electrode area in contact with the water regions was less and because the rate of reaction was less. The area occupied by the water molecules within the pores of the surfactant have been calculated to be 77.3 %, and the electrochemical polymerisation of aniline is believed to occur in the aqueous domains of $C_{16}EO_8$.

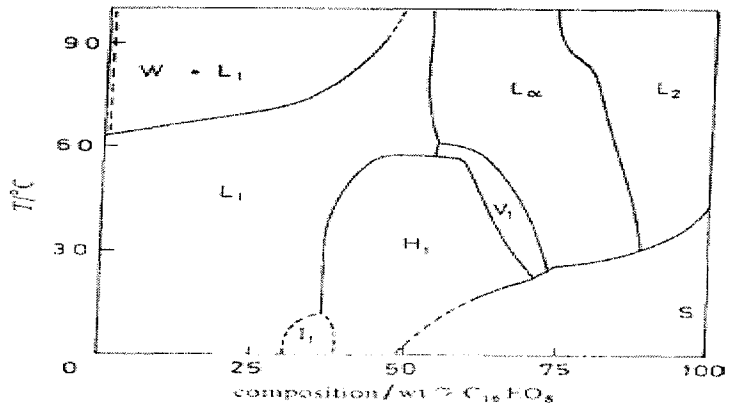

Figure 40 The phase diagram for the binary surfactant-water system of $C_{16}EO_8$ where L_α, H_1 and V_1 are lamellar, hexagonal and bicontinuous cubic phases respectively, and I_1 is a close-packed spherical micelle cubic phase, L_1 is a micellar phase, S is solid surfactant, W is water and L_2 is a liquid surfactant phase containing dissolved water (only partially miscible).[36]

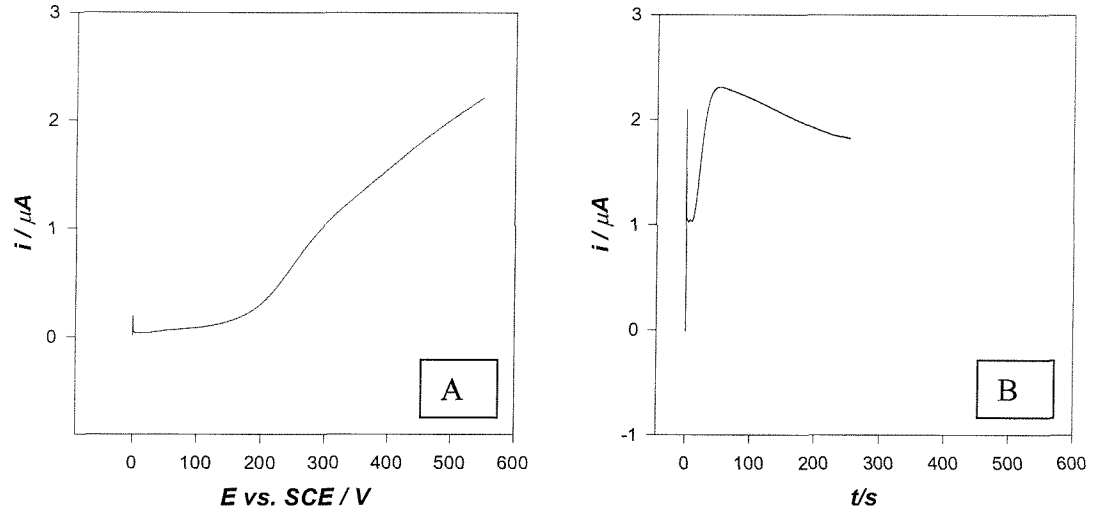

Figure 41 Current-time transients showing the electrodeposition of PANI films grown on Au (0.2mm diameter), from 50 wt% $C_{16}EO_8$ and 50 wt% (0.4 M aniline / 1 M H_2SO_4) at 25 ^{0}C, with potential stepped from 0 V to : (A) +0.8 and (B) +0.9 V vs. SCE, for approximately the same deposition charge passed, i.e. 500 μC.

Potential stepped from 0 to this potential / V	time/s	max deposition current /μA
0.8	550	2.3
0.8	555	2.5
0.9	200	3.0
0.9	250	2.4

Table 5 Table showing information relating to the PANI films grown on Au (0.2mm diameter), from 50 wt% $C_{16}EO_8$ and 50 wt% (0.4 M aniline / 1 M H_2SO_4) at 25 ^{0}C; the deposition or growth charge passed was approximately 500 μC.

If it obeys the Tafel type relationship, the standard potential for the reaction must shift by about 120 mV to slow it down by a factor of ten. As the process is an oxidation of aniline or a protonated form of aniline, it becomes more charged in the first electron transfer step, which is therefore broadly consistent with an effect on the standard potential of the type seen for the ferricyanide couple.

Figure 41 shows PANI films grown by the two potential steps of +0.8 and +0.9 V for the same deposition charge of 500 μC. The currents recorded were positive and corresponded to oxidation reactions. The shapes of the transients appeared different and the deposition at +0.9 V produced a film of similar thickness in half the time taken for the potential step of +0.8 V. This assumed that the faradaic efficiency of the process was 100 %, i.e. that all the charge passed in both cases was consumed in the process to polymerise the aniline. In reality, not all the monomer units may polymerise during the potential steps; as mentioned previously, Bard *et al.*[134] and Genies *et al.*[135] did observe that the first "layers" of PANI deposited on an electrode were denser compared to subsequent "layers"; it was reasoned that the probability of oxidising the monomer directly at the electrode was greater than after the formation of these initial "layers". In addition, Doriomedoff[156] found PANI to be slightly soluble in very acidic solutions. Furthermore, the lyotropic phase can affect the diffusion of the intermediate products away from the electrode; for example, if the diffusion was slowed down, there would be more of the intermediate products near the electrode and this could change the polymerisation.

After deposition, the PANI films were soaked in deionised water for two days to remove excess surfactant. As in the aqueous system, the films were then characterised by cyclic voltammetry in 1 M sulfuric acid in the potential range between -0.2 and +0.5 V at various scan rates. The initial voltage was held at -0.2 V for 2 min to ensure complete reduction of the films. Then the potential was scanned anodically, reversing direction at +0.5 V and ending at -0.2 V.

Potential stepped from 0 to this potential / V	Maximum oxidation current in acid at 200 mV /s /μA	Capacitance per Au area / μF cm^{-2}	Capacitance per growth charge / F C^{-1}
0.8	100	199 000	0.13
0.8	70	211 000	0.13
0.9	230	217 000	0.14
0.9	220	215 000	0.14

Table 6 Table showing sulfuric acid characterisation information relating to the PANI films grown on An (0.2mm diameter), from 50 wt% $C_{16}EO_8$ and 50 wt% (0.4 M aniline / 1 M H_2SO_4) at 25 ^{0}C; the deposition or growth charge passed was approximately 500 μC.

For both potential steps, Figure 42 shows typical cyclic voltammograms at 200 mV/s of PANI films characterised in 1 M sulfuric acid. Like in the aqueous system, a noticeably greater and sharper oxidation peak appeared on the first scan than on the next scan, and this was noticeable for all scan rates recorded, ranging from 10 to 200 mV/s. As mentioned previously, the reason could be that when the potential was initially held at –0.2 V in order to reduce the films completely, subsequent scans did not allow complete reduction thereby decreasing the area of the oxidation peak.

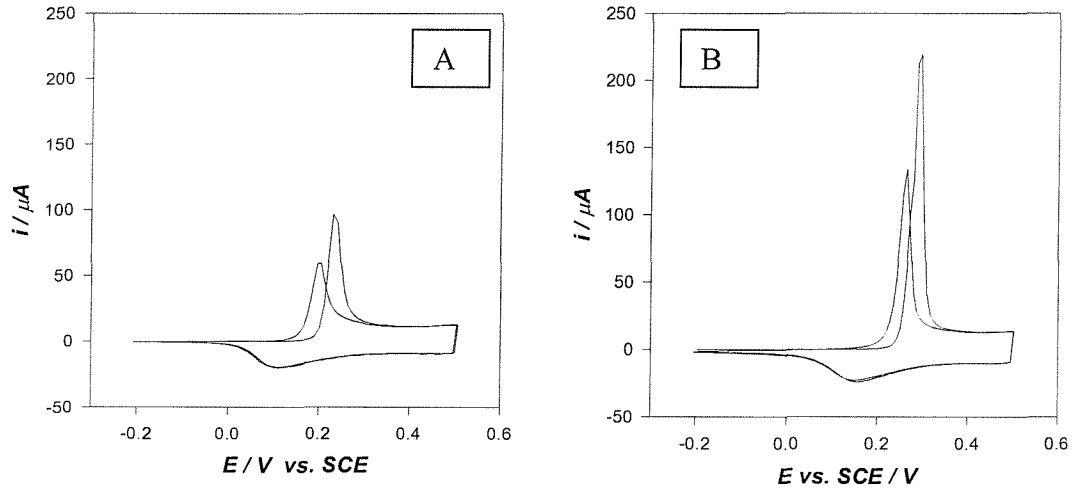

Figure 42 Cyclic voltammograms in 1 M sulfuric acid at 200 mV/s of PANI films grown on Au (0.2mm diameter), from 50 wt% $C_{16}EO_8$ and 50 wt% (0.4 M aniline / 1 M H_2SO_4) at 25 ^{0}C, with potential stepped from 0 V to +0.8 on the left and +0.9 V vs. SCE on the right, for approximately the same deposition charge passed, i.e. 500 μC.

For the film grown at +0.9 V, the oxidation current recorded in the acid characterisation cyclic voltammograms was greater than that recorded for the film grown at +0.8 V. This suggested a greater surface area for the former film as confirmed by the capacitance values, see Table 6. Compared to the aqueous system, the difference here appears to be a greater degree of sharpness in the oxidation peaks.

However, the redox peaks were not in exactly the same position; for instance, the reduction peak for the film grown at +0.9 V was +0.08 V in the aqueous system and +0.15 V in the surfactant system.

On the other hand, the capacitance per growth charge of the films in the surfactant system was generally half the corresponding value in the aqueous system for both potential steps, see Figure 43, Table 4 and Table 6. This was surprising because the expectation was for a greater capacitance value and therefore surface area in PANI films in the surfactant system if the hexagonal geometry afforded by the surfactant, $C_{16}EO_8$, was transferred onto PANI.

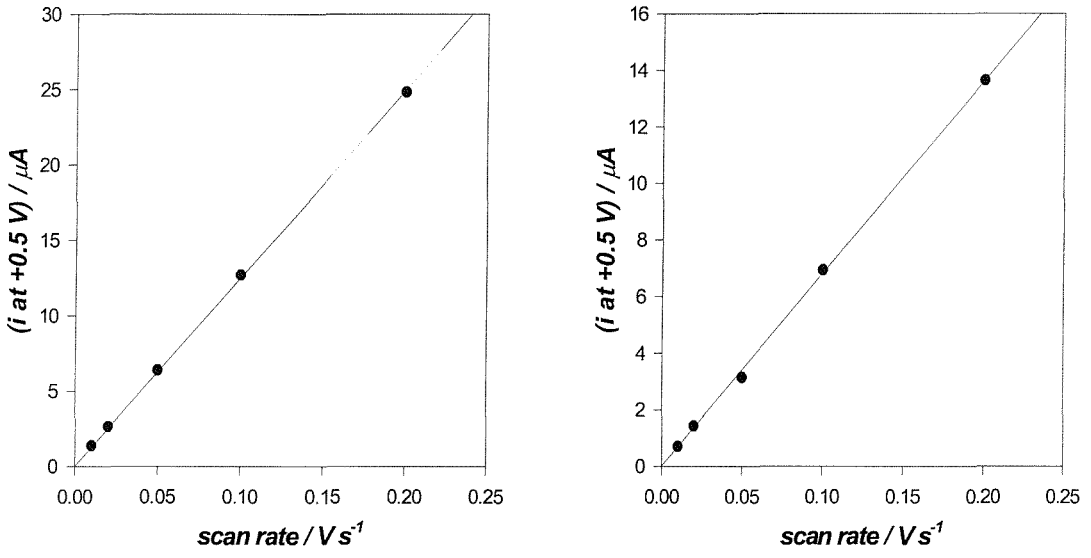

Figure 43 Typical capacitance plots of (A) the aqueous system and (B) the surfactant system for PANI film grown at +0.9 V; current at +0.5 V was plotted versus the scan rate, obtained from the acid characterisation cyclic voltammograms.

When calculated per unit area, the values of capacitance per electrode area are typically in the range of 10 - 40 μF/cm^2.[157] PANI films deposited in both the aqueous and surfactant systems contained large values of capacitance, and this was not surprising, since SEM microscopy has shown that PANI tends to be fibrous anyway.[56] However, the answer as to why the capacitance values were unexpectedly lower in the surfactant system is still unclear. So far, there is no evidence that supports the idea that the electrodeposition in the hexagonal phase of $C_{16}EO_8$ introduces the hexagonal geometry and thus a denser film.

4.4 Other Characterisation Techniques

4.4.1 Scanning Electron Microscopy

Figure 44 is a SEM image of poly(aniline) deposited on a gold evaporated microslide at a potential of +0.9 V vs. SCE in the aqueous system for the same charge density of 1.6 C cm^{-2}. The film was soaked in water for two days. It can also be seen that soaking the PANI films in water did not affect their morphology significantly, i.e. both types were fibrous.

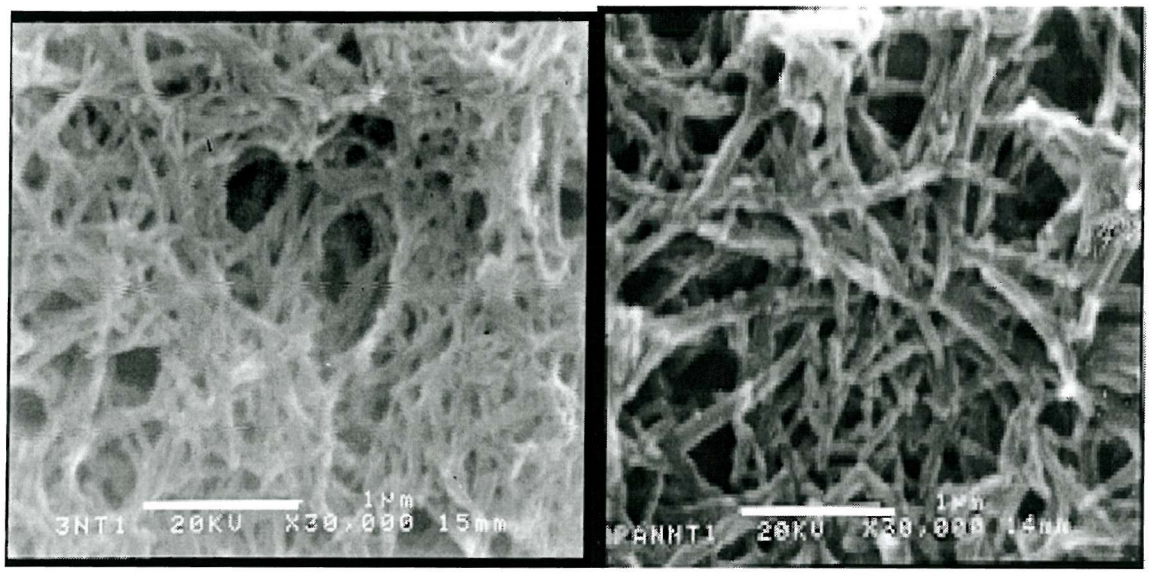

Figure 44 On the left is an SEM image (magnification x 30 000) of PANI at 25 ^{0}C, from a mixture of 0.4 M aniline and 1 M sulfuric acid, electrodeposited by potential step from 0 to +0.9 V vs. SCE on a charge density of 1.6 C cm^{-2}; the film was soaked in water for 2 days. On the right is another SEM image of PANI grown under the same conditions but was not soaked in water [bar scale corresponds to 1 μm].

Figure 45 shows an SEM image of $C_{16}EO_8$ - templated poly(aniline) also deposited at a potential of +0.9 V for the same charge density, and the film was soaked in water for two days to remove excess surfactant, i.e. $C_{16}EO_8$. It shows a different physical appearance in the $C_{16}EO_8$-templated PANI film contained compared to a non-templated film. The morphology of the templated films was not fibrous at all and instead appeared globular.

Although the $C_{16}EO_8$ – templated poly(aniline) films were soaked for two days in deionised water to remove excess surfactant, there could still be some surfactant trapped inside in the PANI films. If this is the case, this will change the structure of the material. PANI is known to be a brittle material, and having the surfactant, $C_{16}EO_8$, incorporated into PANI could make the film more flexible where the surfactant may act as a plasticiser.

A plasticiser is a substance which upon addition to a material, usually a plastic, allows the material to become more flexible, reslient and easier to handle and process. Early examples of plasticisers include water which softens clay and oils for waterproofing ancient boats, and modern examples are manmade organic chemicals, mainly esters, e.g. phthalates.[158] Pron *et al.*[158] have recently developed poly(aniline) doping agents called diesters of 5-sulfo-*i*-phthalic acid (SIPA) which were introduced to the polymer matrix to improve the mechanical properties, especially flexibility. Diesters of phosphoric acid have also been used to plasticise PANI, where the long and branched substituents facilitate plasticisation.[159] Furthermore, conductive flexible blends of protonated PANI with poly(vinylchloride) (PVC) have been synthesised and studied for their conductivity and related properties.[160]

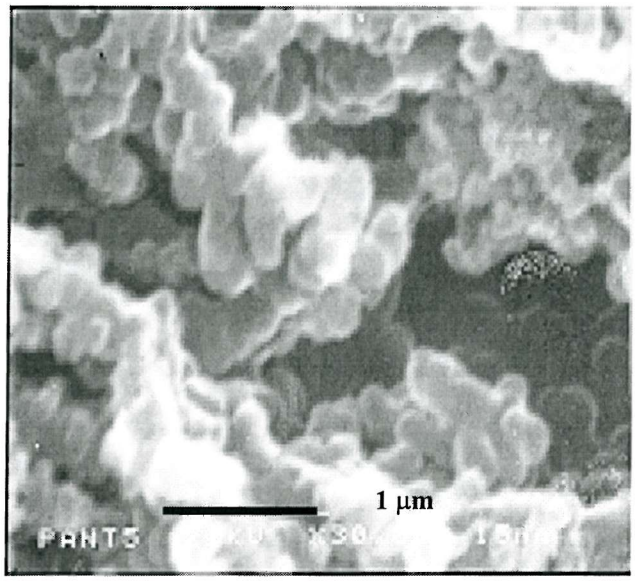

Figure 45 SEM image (magnification x 30 000) of PANI deposited at +0.9 V vs. SCE for charge density of 1.6 C cm^{-2} from 50 wt% $C_{16}EO_8$ and 50 wt% (0.4 M aniline / 1 M H_2SO_4) at 25 ^{0}C. The film was soaked in water for 2 days.

Untreated, as-synthesised conducting polymers are known to fall generally into three categories in terms of morphology: fibrillar, which is most common; globular; and filmlike which is quite rare and is actually extremely fine-structured globular.[132]

As opposed to the idealised head-tail-coupled, single-chain structures, a good degree of random coupling (head-head, side-chain, other) and crosslinking is believed to exist in conducting polymers.[132] Such crosslinking may disturb the extended electronic delocalisation, limiting properties such as conductivity for example or resulting in highly intermingled and branched fibres. Polymerisation conditions are thus an important factor of these structural variations. For instance, in the electropolymerisation of aniline, a change of dopant concentration from 0.5 to 2 M can transform from a globular to fibrillar morphology.[161] The conditions used in the aqueous system here produced a fibrillar morphology seen in the SEM images in Figure 44.

MacDiarmid *et al.* [162] used Atomic Force Microscopy to show that the "filmlike" conducting form of PANI obtained by *in situ* chemical polymerisation exhibited a surface roughness of about 3 nm and consisted of aggregations of globules of about 50 nm diameter. The average diameter of the globules seen in the PANI electrodeposited in the presence of $C_{16}EO_8$ appears to be about 200 nm diameter.

Chandrasekhar has suggested that if fibrillar, fibrils may be of widely varying length and width, and may be highly disconnected, and if globular, large void spaces may be routinely present.[132] This supports the electrochemical data shown in previous sections that PANI electrodeposited in both the aqueous system and in the surfactant system, i.e. in the hexagonal phase of $C_{16}EO_8$, both contained high surface areas.

4.4.2 Transmission Electron Microscopy (TEM) and Low-Angle X-ray Diffraction (Low angle X-RAY)

Although the electrochemical and SEM studies showed differences in the behaviour and morphology respectively between the aqueous and surfactant systems of PANI, they did not show conclusively that hexagonal nanostructure was transferred from $C_{16}EO_8$ to PANI films. A better technique would be TEM imaging, but it was discovered that the TEM electron beam tended to destroy the samples.

The bulk of previous x-ray diffraction studies on conducting polymers suggested a high degree of disorder,[163] where this depended on the deposition conditions such as the choice of counterion. For example, when studying poly(pyrrole) doped with a wide range of sulfonate anions, Warren *et al.*[163] found that large aromatic sulfonic acid groups produced the highest degree of order.

In this project, low angle x-ray work carried out on $C_{16}EO_8$-templated PANI films did not reveal any peaks, see Figure 46. The absence of peaks suggests that no hexagonal nanostructure was present. On the other hand, Elliott[56] also did not find peaks in low angle x-ray work on PANI films such as PANI butane sulfonate, when studying the effect of the length of alkyl chain of the counterion, alkyl sulfonate; the absence of peaks was believed to be that the counterion did not affect the short range order of the PANI films.

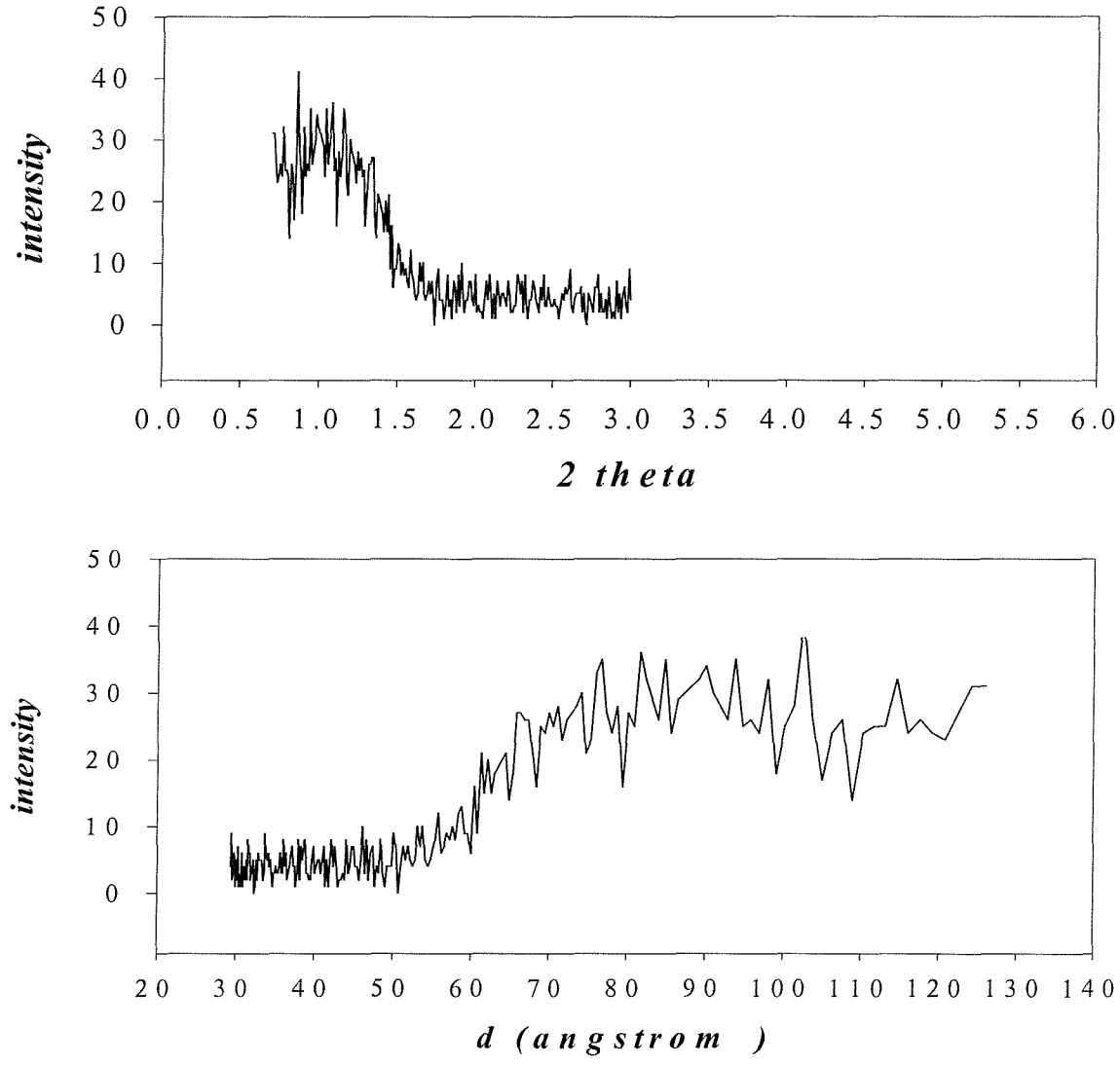

Figure 46 Low-Angle X-ray diffraction work (exposure time ~ 10 min) obtained for $C_{16}EO8$-templated PANI film deposited at +0.9 V vs. SCE for charge density of 1.6 C cm^{-2} from 50 wt% $C_{16}EO_8$ and 50 wt% (0.4 M aniline / 1 M H_2SO_4) at 25 ^{0}C.

4.5 Conclusions

Electrodeposition of metal films in the presence of lyotropic liquid crystals has shown that nanostructural geometry could be transferred from the liquid crystalline system onto the metal films, thereby enhancing the surface area.

This work is now extended to the field of conducting polymers, and the electropolymerisation studies of PANI films in the presence of $C_{16}EO_8$ revealed several things.

Firstly, PANI could be electrodeposited in a lyotropic liquid crystalline system. The deposition mixture exhibited hexagonal phase under polarised light optical microscopy. The electrodeposition current-time transients, when applying the potential step method, were reproducible for the same deposition charge passed. However, the values of capacitance per deposition charge were found to be lower in the surfactant system than in the aqueous system, and the reason for this is unclear.

Secondly, although SEM work did show different morphology for a $C_{16}EO_8$-templated PANI film compared to an untemplated PANI film, it could not prove nanostructure. Thus TEM studies were carried out and unfortunately PANI films were found to be unstable in TEM imaging; low-angle x-ray diffraction studies did not reveal any peaks.

Although aniline could electropolymerise in a lyotropic liquid crystalline system, no evidence for nanostructure could be obtained.

Chapter Five

5 Mesoporous Pd

5.1 Introduction

In work carried out in colloboration with the Department of Engineering of the University of Warwick and City Technology Ltd., mesoporous Pd prepared electrochemically from the hexagonal phase of $C_{16}EO_8$ at room temperature has been shown by Guerin to improve the performance of pellistors.[35] The plating salt used was ammonium tetrachloropalladate, $(NH_4)_2PdCl_4$, and had been mixed with $C_{16}EO_8$, water and heptane at the relevant composition to produce a dark brown viscous glue-like mixture in the hexagonal phase. However, the studies were restricted to a single set of deposition conditions: that is using one particular surfactant, at one composition, for one choice of Pd salt composition, and at a single deposition temperature. These studies have been expanded in this thesis to examine the effects of variations in deposition conditions, such as changing the surfactant type and composition, the potential and liquid crystalline phase. Eventually, the obtained conclusions from these results obtained could be applied to the manufacture of better pellistors, i.e. in terms of sensor performance.

Described in greater detail in section 5.11 in this chapter, a pellistor consists essentially of a coiled platinum wire (10 to 38 μm diameter approximately) embedded in a porous refractory bead loaded with a precious metal catalyst. The substrate used in this work was designed in the Sensor Research Laboratory, Department of Engineering at the University of Warwick and was made in Neuchatel (Switzerland). The substrate used for making a planar pellistor must meet criteria like robustness at high temperatures.

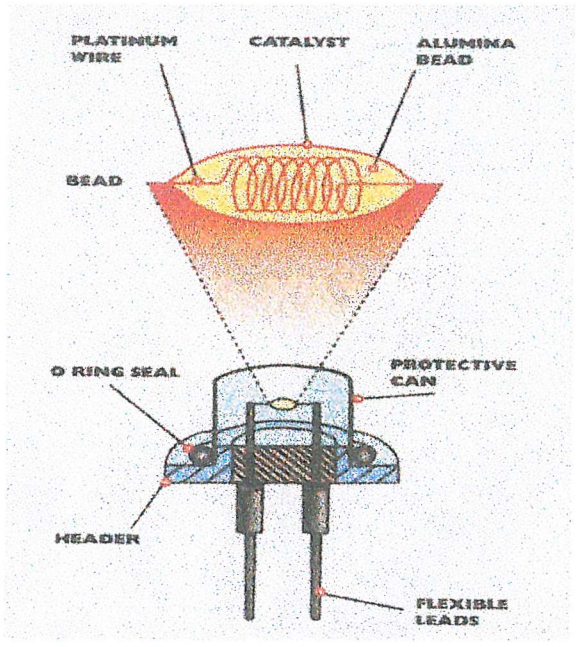

Figure 47 Diagram of pellistor mounted on a T05 header, where the catalyst is the Pd film.[164]

Another significant factor is the precious metal catalyst layer used to detect the gas, see Figure 47. Pd particles supported on γ-alumina (which is a porous type of alumina) are used in commercial pellistors. The surface area of the catalyst layer can affect the sensitivity, lifetime and poison resistance of the gas sensor; and usually the surface area of a gas sensor has to be as high as possible. In 1997 Attard *et al.* were able to obtain nanostructured Pt films from lyotropic liquid crystalline phases.[2] Since Pd is in the same group in the periodic table, the aim was to develop nanostructured palladium films.

This section discusses the work carried out to recreate and extend the experimental conditions when using a cheaper alternative surfactant, i.e. Brij® 56. In this work, mixtures were prepared in which the surfactant-to-water ratio was changed, while the concentration of the precursor in water, e.g. Pd, was kept fixed , e.g. at 1.06 M. Once mesoporous Pd was prepared either by cyclic voltammetry or potential step method, the

film was characterised in sulfuric acid by cyclic voltammetry and by electron microscopy and powder x-ray diffraction.

A fundamental electrochemical study of mesoporous Pd was not the purpose of this work; the purpose was to find the conditions suitable to deposit Pd on pellistors for comparison with the data obtained by Guerin.[35]

Comparisons between the two surfactants are made and possible explanations are discussed, and the effect of changing surfactant on the results of gas sensing will be discussed later in the thesis.

5.2 The Aqueous System

Metal deposition from aqueous solutions is still an integral part of industrial processes. The manufacture of metal coatings for either protection or decorative purposes demands a detailed knowledge of all the deposition parameters such as electrolyte composition.

Our study of Pd electrodeposition from the aqueous system provided the background to the electrodeposition of nanostructured Pd films on Au electrodes, i.e. deposition from the surfactant system.

The electrodeposition of Pd from palladous chloride salts has already been widely studied for the past three decades.[165]

5.2.1 Mechanism of Reduction of Pd

In our work, 40 mM $(NH_4)_2PdCl_4$ solution was prepared in the absence of electrolyte and surfactant, giving a dark brown liquid.

Although anions can play an important role in metal deposition,[166] Guerin found that the addition of 0.1 M hydrochloric acid (HCl) to the 40 mM $(NH_4)_2PdCl_4$ solution did not change the reduction potential or the magnitude of the reduction current.[35] The solution without supporting electrolyte is more similar to the surfactant system (also not containing supporting electrolyte), thereby preventing any possible effect on the liquid crystalline phases and pore geometry.

At pH 2, ultraviolet-visible spectroscopy and cyclic voltammetry showed that the main species present in an electroplating bath of 10 mM *trans* – diamminedichloropalladium (II), $[Pd(NH_3)_2Cl_2]$, in 1 M aqueous ammonium chloride, NH_4Cl, was the complex, tetrachloropalladate, $[PdCl_4]^{2-}$.[167]

In our solution, 40 mM $(NH_4)_2PdCl_4$, Pd exists as a chloride complex, $[PdCl_4]^{2-}$. At 25 ^{0}C, Latimer[168] calculated the log K, the equilibrium constant, as 12.3 for the complex formation seen in equation 29.

$$Pd^{2+} + 4Cl^- \rightleftarrows [PdCl_4]_2^- \qquad \textbf{Equation 29}$$

On the other hand, this equilibrium has been broken down into a multi-sequence by Droll *et al.*[169], and they reported the log *K*, the equilibrium constant, for the overall reaction between Pd^{2+} and Cl^- in the formation of $[PdCl_4]^{2-}$ to be 15.8, which is of the same order of magnitude as seen above. Based on Le Chatelier's Principle, the overall equilibrium lies strongly to the right, i.e. with $[PdCl_4]^{2-}$ being the dominant species in solution. The log *K* for each sequence is listed below, taken from reference 169.

$$Pd^{2+} + Cl^- \rightleftharpoons [PdCl]^+ \qquad \log K \text{ at } 21\ ^0C \sim 6.2 \qquad \textbf{Equation 30}$$

$$[PdCl]^+ + Cl^- \rightleftharpoons PdCl_2 \qquad \log K \text{ at } 21\ ^0C \sim 4.7 \qquad \textbf{Equation 31}$$

$$PdCl_2 + Cl^- \rightleftharpoons [PdCl_3]^- \qquad \log K \text{ at } 21\ ^0C \sim 2.5 \qquad \textbf{Equation 32}$$

$$[PdCl_3]^- + Cl^- \rightleftharpoons [PdCl_4]^{2-} \qquad \log K \text{ at } 21\ ^0C \sim 2.6 \qquad \textbf{Equation 33}$$

The electrochemical reaction for the reduction of Pd^{2+}, i.e. the deposition of Pd, is

$$Pd^{2+}(aq) + 2e^- \rightleftharpoons Pd(s) \qquad \textbf{Equation 34}$$

where Templeton *et al.* [170] measured the standard reduction potential, E^0, as –0.987 V vs. SHE. To date, the mechanism of the reduction of Pd is not clearly known in the literature.

5.2.2 Complications of Pd Electrochemistry

The complications of Pd electrochemistry are briefly explained here.

Firstly, it is well known that Pd can absorb between 600 and 900 volumes of gas per metal volume depending on its physical condition.[171] This corresponds to an atomic ratio of 0.69 atoms of hydrogen for each atom of Pd when a Pd electrode is in equilibrium with 1 atm of H_2 gas.[172] When this atomic ratio exceeds 0.05, the structure of the Pd metal expands considerably.

H_2 is also known to adsorb on Pd, i.e. H_2 is considered to reside as $H^{\bullet}_{ads}$ at the surface, and literature on the dissociative adsorption of H_2 on unmodified Pd and Pd overlayers on early transition metals have suggested that electron transfer from the surface into the σ^* antibonding orbital of the hydrogen molecule plays a dominant part in the breaking of the H-H bond, lowering the activation energy associated with the process. Transition metals like Pd are good electron donors, and dissociation of H_2 on these surfaces takes place readily at room temperature.[173]

Furthermore, Marković *et al.*[174] reported the activation energy for the hydrogen evolution / oxidation reaction on Pd films grown on Pt(111) in 0.05 M H_2SO_4 to be about 9 kJ mol^{-1}, half the value for the hydrogen reaction on Pt(111).

Figure 48 is a selection of typical voltammograms of Pd in different concentrations of H_2SO_4 showing the absorption of hydrogen in the metal. The region of hydrogen oxidation and reduction appears between 0.15 and 0.30 V vs. RHE (i.e. -0.09 and 0.06 V vs. SCE) for all cases including Pd black in 1 M H_2SO_4 at 25 ^{0}C.[175] According to Rand *et. al.*[176], whilst gold would absorb hydrogen to an insignificant extent above potentials of hydrogen evolution, palladium on the other hand could absorb large amounts of hydrogen which were difficult to remove and could lead to surface roughening. For example, studies of the hydrogen region suggest that adsorption is not completed until about 0 V vs. RHE or –0.24 V vs. SCE, which highlights the additional problem of correcting for H_2 evolution currents.[172] Thus, scanning the potential below 0.3 V vs. RHE or 0.06 V vs. SCE is not recommended.

Secondly, surface roughening can also be caused by oxygen adsorption at high potentials. Voltammograms have been shown by Sashikata *et al.* to depend significantly on the crystal orientation of Pd in the oxide film formation region.[177] The electrochemistry of Pd is known to be complex at very positive potentials: oxide film formation, competitive adsorption[178] of HSO_4^- / SO_4^{2-} and anodic dissolution[176] of Pd are involved. In our work, identifying Pd coverage of Au is thus by observing the reduction peak for palladium oxide at +0.5 V vs. SCE or +0.74 vs. RHE, see Figure 49.

The study of oxygen adsorption from water on Pd by Rand demonstrated increasing irreversibility when the anodic upper limit of scan reversal was increased.[172] The quantity of oxygen adsorbed increased linearly with potential approximately.

Studying oxygen adsorption at constant potential in 1 M H_2SO_4 at 25 ^{0}C, Rand found the coverage to increase linearly with potential till reaching a plateau at 1.4 V vs. RHE or 1.16 V vs. SCE; however beyond 2.0 V vs. RHE or (1.76 vs. SCE), it increased sharply and did not reach a limiting value.[179] The reduction of the oxide layer formed at these high potentials was expressed as a series of broad peaks in cyclic voltammetry instead of the single well-defined peak of the type shown in Figure 49. This led to substantial roughening of the electrode surface, caused by the formation of a distinct phase oxide. This phase oxide is different to the initial oxide layer which is believed to be a chemisorbed layer, where randomly adsorbed atoms reside above undisturbed surface metal atoms.[180]

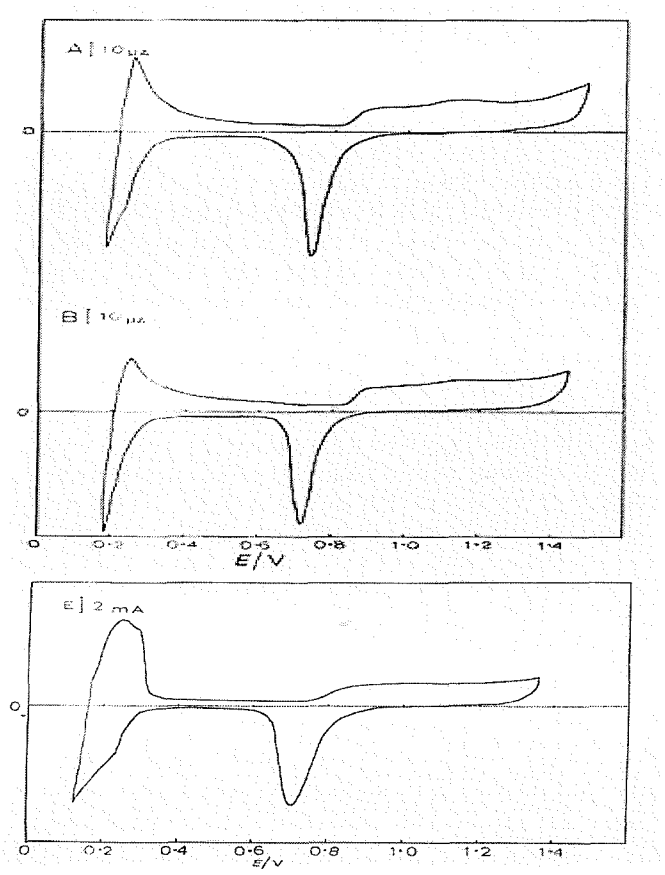

Figure 48 Cyclic voltammograms of Pd in different H_2SO_4 concentrations: (A) 1 M and (B) 2 M; (C) Pd Black in 1 M H_2SO_4 at 25 ^{0}C. Potentials are quoted vs. RHE and the scan rate used was 140 mV/s.[175]

To prevent such complications in our work, the potential limits were carefully chosen in the cyclic voltammetry experiments in sulfuric acid; the potential of the Pd

films was cycled only between 0.2 V and 1.2 V vs. SCE. These limits would allow the potential cycling of Pd with no risk of structural change caused by continuous hydrogen absorption, adsorption and desorption or evolution. They also ensure that no appreciable amount of O_2 was evolved before scan reversal and complete reduction of adsorbed or chemisorbed oxide had taken place before reaching the cathodic limit.

Assessing accurate real surface area determination of Pd can be difficult; our work followed the same area calculation method used by Guerin based on the work of Rand and Woods.[35, 179] The charge of the oxide stripping peak seen at 0.74 V vs. RHE or 0.5 V vs. SCE in Figure 49 can be used to calculate the area of the Pd film. Guerin found that cycling the potential of the Pd film in 1 M sulfuric acid continuously at 200 mV s^{-1} actually resulted in an increase in the reduction peak area until a maximum was eventually reached.[35] Integration of the area of the largest reduction peak obtained gives the charge; dividing this charge by the conversion factor (discussed below) gives the surface area (cm^2); Faraday's Law gives the mass deposited based on the deposition charge passed; and dividing the surface area by the mass gives the specific surface area (m^2 g^{-1}) of the Pd film (real or accessible).

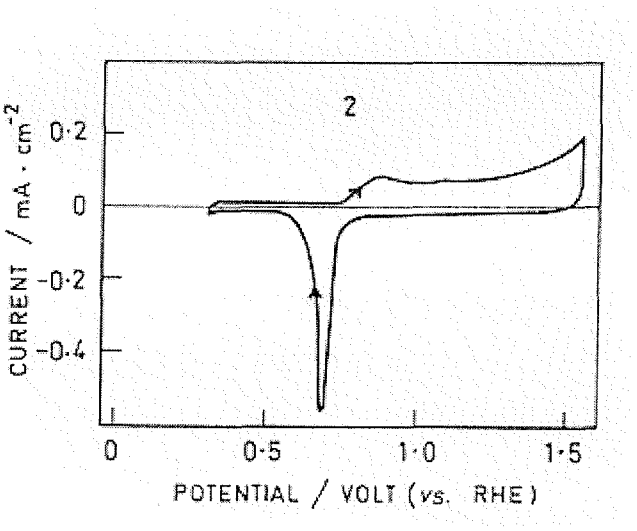

Figure 49 Cyclic voltammogram at 40 mV/s for the 20th scan of a Pd electrode in 1 M H_2SO_4 at 25 ^{0}C. [from literature 181]

Rand and Woods proposed 1 cm^2 of a (100) plane to be accepted as the conventional standard of surface area for noble metals; in our case, 1 real cm^2 is equivalent to a change of 424 $\mu C\ cm^{-2}$ for the two-electron process of oxide adsorption.[179] This conversion factor value was used for all future estimates of Pd surface areas. However, this method assumes a (100) plane and Pd is known to contain other planes, which may not have the same charge per unit area.

Besides the conversion factor, another assumption made was that of a 100 % faradaic efficiency for the electrodeposition of Pd. Electrochemical and quartz crystal microbalance (EQCM) work by Guerin revealed the Faradaic efficiency to be 95 % for Pd films electrodeposited in the hexagonal phase of $C_{16}EO_8$. Using this assumption therefore seems reasonable since the surfactant is similar to Brij® 56 in terms of chemical composition, and since electrodeposition of Pd has also been carried out in the hexagonal phase here in our work.

5.2.3 Electrodeposition of Pd by Cyclic Voltammetry

Cyclic voltammetry is useful for initial studies of the system, having the advantage of providing quick, qualitative data for interpretation. In Figure 50A, the electrochemical deposition of Pd is shown by the reduction wave with the cathodic current increasing rapidly until reaching the lower limit of 0.1 V; this resulted in a black film on the surface of the Au working electrode after a full scan. Although there appears to be no obvious nucleation loop typical for an electrode reaction involving nucleation and growth of a metal layer on a foreign substrate,[108] this does not mean that nucleation and growth of Pd were not taking place. The reduction current on the reverse scan is larger, like a nucleation current on the reverse scan.

Although the reduction wave is thought to be mainly due to Pd deposition, contributions to the cathodic current could also come from other competing reactions such as the formation of palladium hydride (i.e. absorption of hydrogen in the lattice of the growing Pd) or hydrogen gas evolution.

There could also be a contribution to the cathodic current from O_2 reduction because the solution was not deoxygenated. Depending on the electrode type or surface, the reduction of O_2 takes place by two steps:[167]

$$O_2 \xrightarrow{+2e^- + 2H_2O - 2OH^-} H_2O_2 \xrightarrow{+2e^-} 2OH^- \qquad \textbf{Equation 35}$$

However, the solubility of O_2 is known to be only 2.2 mM at room temperature,[167] and no other significant reduction wave shows up in Figure 50A. The reason for the solution not being deoxygenated was to compare like data with the surfactant templating mixtures because it was not possible to deoxygenate when electrodeposition studies of Pd was later carried out in the presence of Brij® 56.

Furthermore, the diffusion coefficient for the Pd (II) species in 10 mM *trans*-$[Pd(NH_3)_2Cl_2]$ in 1 M NH_4Cl has been measured at about 10.2 x 10^{-6} cm^2 s^{-1} by Pletcher *et al.*[167] In the same system, the diffusion coefficient for O_2 was estimated to be 5.4 x 10^{-6} cm^2 s^{-1}. This suggests that if the mass transport plays a dominant role, Pd (II) species will diffuse faster than O_2, making the latter reduction a less significant competing reaction. EQCM measurements by Guerin[35] show the Faradaic efficiency to be 95 % for Pd films electrodeposited in the hexagonal phase of $C_{16}EO_8$.

5.2.3.1 Acid Characterisation of Pd

After soaking in water overnight, to ensure consistency with the later studies on films deposited from surfactant solutions, the Pd film was subjected to fast potential cycling in 1 M H_2SO_4, see Figure 50B.

This was useful for identifying the deposited material on the Au; the voltammogram is typical for a Pd film being oxidised and reduced, and is significantly different from the corresponding voltammogram for a bare Au electrode. As in the literature (Figure 49), a reduction peak is observed around 0.5 V characteristic of oxide stripping on Pd and significantly removed from the potential expected for oxide stripping on Au under the same conditions (0.8 V vs. SCE). Therefore we can conclude from the

voltammogram that complete coverage of the Au by Pd has occurred. It also confirms that there are no significant quantities of impurities in the Pd film.

As mentioned previously, cycling the potential of the Pd film in 1 M H_2SO_4 continuously actually resulted in an increase in the size of the reduction peak at 0.5 V. Based on the area calculation method described above, the area of the maximum reduction peak can give the specific surface area (m^2 g^{-1}) of the Pd film (real or accessible) after several steps of calculations. Note, two assumptions have been made; the 100 % Faradaic efficiency of the deposition process and the conversion factor, 424 μC cm^{-2}.

For example, the surface area of Pd film grown when the lower limit was 0.1 V in Figure 50A, was found to be approximately 0.07 m^2 g^{-1}. The roughness factor can be calculated by dividing the film surface area by the electrode geometric area; it is not the specific roughness factor which is surface area divided by the specific surface area. Based on the geometric area of the Au electrode (0.000314 cm^2), the roughness factor of the film was calculated to be 6.76, which means that the film area was 6.76 times larger than the geometric area.

Oxide adsorption is seen to start at about 0.6 V on the anodic scan, and on scan reversal, the reduction peak at 0.5 V corresponds to the stripping of the oxide. Therefore, charges, Q_o^a and Q_o^c, associated with the adsorption of oxygen and reduction of the oxide can be calculated.[176] A charge imbalance can result if the anodic charge also contains a contribution from anodic processes other than the adsorption of oxygen or incomplete reduction of the adsorbed oxide layer. Contribution can come from the dissolution of Pd or oxygen evolution at the sweep limit. It could also come from the oxidation of adsorbed organic impurities, but this is not likely since experiments had been carried out with care and no other significant reduction peak had ever been observed in a acid characterisation voltammogram.

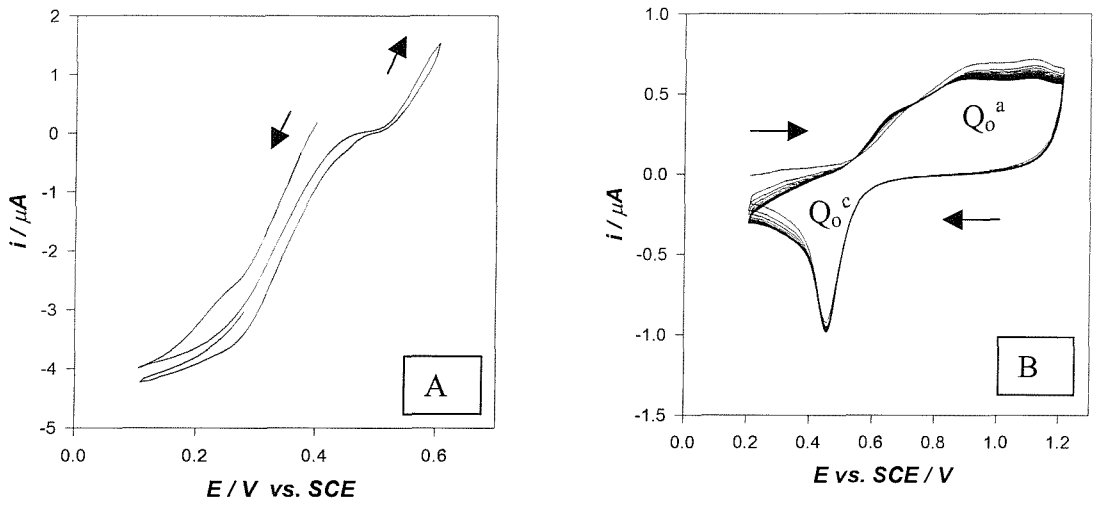

Figure 50 The cyclic voltammogram on the left (A) shows typically the electrochemical deposition of Pd film from an aqueous solution of 40 mM $(NH_4)_2PdCl_4$ at 25 ^{0}C at 10 mV/s. The voltammogram on the right (B) shows the characterisation of the Pd film cycled in 1 M H_2SO_4 at 25 ^{0}C at 200 mV/s. The arrows show the direction of the scan.

Charge imbalance was also observed by Rand *et al.*[176] when cycling Pd, Pt, Rh and Au in 1 M H_2SO_4 at 25 ^{0}C. Experiments were carried out to determine whether this was caused by metal dissolution. In the case of Pd, continuous cycling was performed between 0.17 and 1.22 V. After 734 cycles, atomic absorption spectroanalysis of the cell solution indicated that the charge corresponding to the amount of metal dissolved per cycle was found to match the measured anodic charge difference between Q_o^a and Q_o^c. The charge due to Pd dissolution during continuous cycling to 1.3 V contributed to 17% of the total anodic charge passed in the oxygen adsorption region. In addition, out of those metals studied, the highest dissolution rate at 25 ^{0}C was actually found for Pd.

In our case, Q_o^a appeared to be double that of Q_o^c as seen in Figure 50B. This value was calculated from the baseline of the steady-state current on the forward scan. The reason for the difference can be due to the nature and pretreatment of the electrode and on the experimental conditions; Rand *et al.*[176] cleaned their electrodes by immersing them in cold chromic acid and then thorough washing in distilled water; different surface

structures are known to change the rate of metal dissolution.[182] In addition, any stirring of solution will remove dissolved metal from the proximity of the cathode surface, and in our case, there was no stirring involved so the effect should be less.

The mechanism for dissolution of Pd is believed to involve anodic reactions,[176, 183, 184] either by direct dissolution of the metal

$$Pd \rightarrow Pd^{2+} + 2e^- \qquad \text{Equation 36}$$

or via an intermediate surface oxygen species.

$$Pd + H_2O \rightarrow PdO + 2H^+ + 2e^- \qquad \text{Equation 37}$$

$$PdO + 2H^+ \rightarrow Pd^{2+} + H_2O \qquad \text{Equation 38}$$

In addition, Pd was found to dissolve only when the anodic potential of scan reversal was greater than 0.98 V vs. RHE (or 0.74 vs. SCE) in 1 M H_2SO_4 at 25 ^{0}C.[176] If the dissolution of Pd proceeds by direct dissolution in equation 32, then this potential should approximate to the standard potential of the Pd/Pd^{2+} couple, i.e. 0.987 V vs. SHE.[170]

5.2.3.2 The Effect of Deposition Potential (i.e. Lower Limit) in Cyclic Voltammetry

In cyclic voltammetric deposition of Pd, the lower limit so far was 0.1 V. The effect of changing the lower limit was investigated in Table 7 where the data were obtained by cycling the working electrode, deposited with Pd films, in 1 M H_2SO_4 at 25 ^{0}C at 200 mV/s.

As the deposition potential decreased from 0.1 to –0.2 V, a steady increase in Pd specific surface area was observed, from 0.05 to 0.44 $m^2\ g^{-1}$, and in the roughness factor, i.e. from 12 to 51.

Figure 51 shows a selection of typical deposition voltammograms of Pd films grown by cyclic voltammetry at one scan rate, i.e. 10 mV/s, and although the lower limits were different, the voltammograms have a similar reduction wave and similar currents

(about 4 μA) to Figure 50A. In all of them, the cathodic current increased rapidly until reaching the lower limit with an onset of a plateau where there is no change in the rate of electrodeposition.

The S-shape voltammograms, the presence of a plateau in them and the size of the working electrode (0.2 mm diameter gold) seem to suggest microelectrode behaviour and that the reduction is mass transport limited.

However, in Figure 51C near the lower limit of –0.2V, there is a noticeable nucleation loop. The extra peak at the lower limit is likely to be the onset of hydrogen evolution.

The oxidation current seen at 0.6 V on the reverse scan in the deposition voltammograms is quite substantial, reaching about 3.5 μA in Figure 51C. This cannot be due to oxidation of the absorbed hydrogen since this occurs at a much lower potential, i.e. 0.23 V vs. RHE (or –0.01 V vs. SCE)[185], and it is more likely to be Pd dissolution without passivation of the surface since the current did not reach a plateau. Kolb *et al.*[166] studied the influence of the coverage of Pd on Au(111) and observed the anodic current peak at about 0.66 V, getting more pronounced with coverage of Pd; the anodic peak was attributed to the oxidative dissolution of the Pd deposit.

Deposition by cyclic voltammetry seems to confirm that the more cathodic the lower limit, the greater the surface area of Pd was obtained. The high area value at deposition potential of –0.2 V is likely to be associated with the codeposition of hydrogen, whereas the other values are all about the same. This fits with the voltammograms in Figure 51. In addition, Figure 51 (C) shows that the reduction current increases with cycling as the area of the electrode increases with Pd deposition.

However, it is important not to analyse in great detail the data obtained in Table 7 because the main objective is to compare the data with the surfactant system. For instance, the order of magnitude in specific surface areas is much lower here than in the surfactant system. This supports the studies carried out by Guerin[35] in that electrodeposition in the lyotropic liquid crystalline phases improves the specific surface area of Pd films.

Deposition potential / V vs. SCE	Deposition charge / C	Reduction peak charge/ μC	Number of Scans in acid	Pd area / cm^2	Roughness Factor	Pd specific surface area/ m^2 g^{-1}
0.10	0.0122	1.54	1	0.0036	12	0.05
0.05	0.0097	1.85	4	0.0044	14	0.08
0.00	0.0105	2.17	2	0.0051	16	0.09
-0.05	0.0101	2.60	3	0.0061	20	0.11
-0.10	0.0095	3.29	2	0.0078	25	0.15
-0.20	0.0066	6.79	2	0.0160	51	0.44

Table 7 Table of data of Pd vs. the deposition potential lower limit, obtained by the characterisation of the Pd film cycled in 1 M H_2SO_4 at 25 ^{0}C at 200 mV/s. The films had been grown by *cyclic voltammetry* on 0.2 mm diameter gold electrodes from 40 mM $(NH_4)_2PdCl_4$ solution at 25 ^{0}C; at 10 mV/s, a full scan started cathodically at +0.4 V and finished anodically at +0.3 V, with the upper limit at +0.6 V.

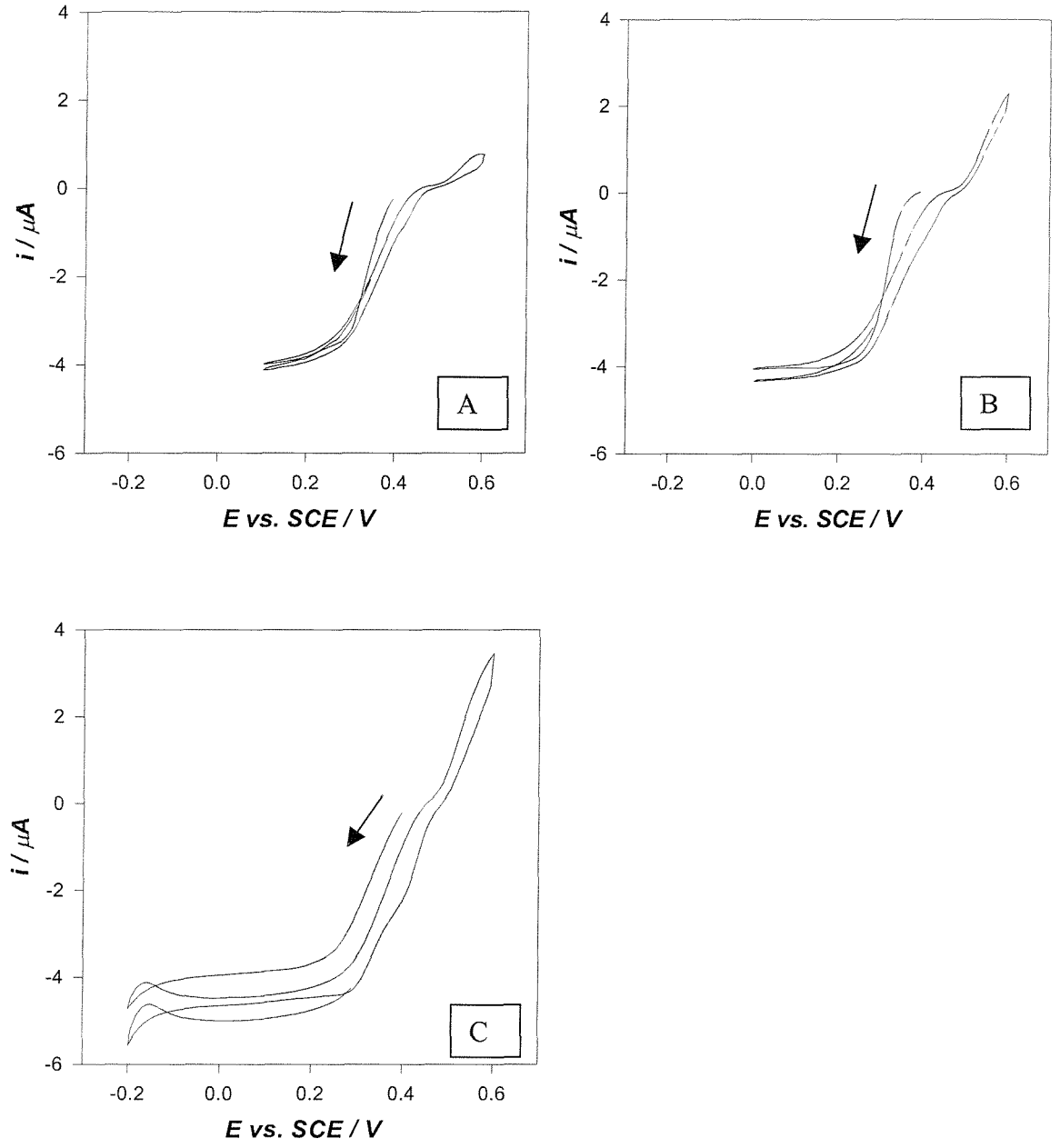

Figure 51 A selection of typical cyclic voltammograms of Pd films grown by cyclic voltammetry on 0.2 mm diameter Au electrodes from 40 mM $(NH_4)_2PdCl_4$ solution at 25 ^{0}C. The deposition started cathodically at +0.4 V and ended anodically at +0.3 V. The upper limit was +0.6 V with the lower limit changed to +0.1 V in (A), 0 V in (B) and –0.2 V in (C). A full scan was obtained in each case at 10 mV/s.

5.2.3.3 The Effect of Scan Rate

As scan rate increased for the cyclic voltammetric deposition from 1 to 20 mV/s, the surface area was found to increase from 0.01 to 0.24 m^2 g^{-1} when maintaining the lower potential limit at +0.1 V, see Table 8.

Although there is scatter in the data, again the important point is to compare the order of magnitude of the values with that of the mesoporous Pd films, where the latter is much bigger.

Deposition Scan rate/ (mV s^{-1})	Deposition Charge / C	Reduction peak charge / μC	Number of Scans in acid	Pd area/ cm^2	Roughness factor	Pd specific surface area/ m^2 g^{-1}
20	0.01	5.61	3	0.0132	42	0.24
10	0.01	1.54	1	0.0036	12	0.07
5	0.02	1.81	2	0.0043	14	0.04
2	0.05	1.82	2	0.0043	14	0.02
1	0.11	1.99	2	0.0047	15	0.01

Table 8 Table of acid characterisation data of Pd obtained vs. the deposition scan rate. The films were grown by *cyclic voltammetry* on 0.2 mm diameter gold electrodes from 40 mM $(NH_4)_2PdCl_4$ solution at 25 ^{0}C. A full scan started cathodically at +0.4 V and finished anodically at +0.3 V, with the upper limit at +0.6 V and the lower limit at +0.1 V.

5.2.4 Electrodeposition of Pd by Potential Step

As mentioned before, to date, the detailed mechanism for the reduction of $[PdCl_4]^{2-}$ has not been described in the literature. What is known is that two electrons are involved in the reduction (see equation 29); at pH 2, ultraviolet-visible spectroscopy and cyclic voltammetry showed that the main species present in an electroplating bath of 10 mM trans – diamminedichloropalladium (II), $[Pd(NH_3)_2Cl_2]$, in 1 M aqueous ammonium chloride, NH_4Cl, was the complex, tetrachloropalladate, $[PdCl_4]^{2-}$.[167] According to Droll *et al.*,[169] the complex exists as the dominant species in the aqueous palladate solutions.

The overall process of metal deposition is believed to be

$$MX_n + nX^-_m \rightleftharpoons MX_m + mX^-_n \xrightarrow{e^-} M + nX^-_m + mX^-_n \qquad \text{Equation 39}$$

where a complex [M is the metal, X is the anion] is discharged producing metallic particles on an inert electrode.[186] Assuming an idealised cathode surface, smooth on an atomic level and defect-free, the stages of the formation and growth of metal deposition are described by Pletcher as follows:[108]

(i) transport of solvated metal ions through the solution to the electrode surface;
(ii) electron transfer;
(iii) partial or complete loss of solvation sheath forming an adatom;
(iv) surface diffusion of adatoms;
(v) clustering of the adatoms to form a nucleus of sufficient size for it to be stable;
(vi) growth of the nucleus by incorporation of adatoms at favourable sites in the lattice structure of the metal;
(vii) nuclei formation;
(viii) growth of each isolated centre;
(ix) overlap of the expanding centres;
(x) formation of a continuous layer over the whole cathode surface;
(xi) and thickening of this complete layer.

Therefore, it can be seen that the formation of nuclei resulting in the deposition of a thick layer of the metal consists of several steps, each of which can be the rate-determining step. Thus, a wide range of responses to electrodeposition techniques is likely to be observed in practice.

There are two types of nucleation: instantaneous and progressive. The first describes the situation in which all nuclei form at the same time immediately after the potential step; in this case, all the nuclei are expected to be of the same size. In contrast, progressive nucleation describes the situation in which the nuclei form at different times, and as a result, a broad range of sizes occurs. Note, the discussion above assumes an ideal surface, and the real surfaces tend to have many defects as well as sites which are more advantageous than others for nucleation.

The latter stages of layer formation, where individual nuclei grow and start to overlap, will see the nuclei centres growing at a slower rate, and the current will increase less rapidly than before. According to Pletcher,[108] interpreting such responses tends to be very complex.

The best technique for studying the early processes of metal deposition is potential step, i.e. stepping the potential of a clean working electrode where no reduction takes place to a potential where nucleation occurs. Figure 52 shows the electrodeposition of Pd from 40 mM $(NH_4)_2PdCl_4$ at 25 ^{0}C where the potential was stepped from 0.4 to 0.12 V. The reduction current initially reaches –6.3 μA and after 12s, reaches a plateau of almost –4.5 μA. It can be seen later that both an initial reduction current and a plateau do show up in the transients in both the aqueous and surfactant systems, which can be explained as follows.

Before the potential was changed, no nuclei were present on the electrode surface, thus giving a zero reduction current. When the potential was stepped to the more cathodic potential, the current initially increased (more negative values on the current scale because it is a reduction process) since (a) nuclei were formed and (b) the surface area of each nucleus got larger with time.

According to Pletcher,[108] for a planar electrode, the detailed shape of the rising transient depends on the kinetics of nucleation, whether the growth is 2- or 3- d, and the rate determining step during growth. The slope of the transient will decrease at the start

of the overlap of the centres. Once a complete layer forms, the current will either plateau (if thickening is controlled by electron transfer), or pass through a peak and decrease (if thickening is diffusion controlled) for a macroelectrode.

In both the aqueous and surfactant systems for deposition at 0.1 V vs. SCE, it is difficult to say whether the nucleation is progressive or instantaneous, see figures 53 and 63, because the effects of double layer charging and the initial stages of deposition are not well resolved.

The current plateau in Figure 52(A) shows that in the aqueous system, the formation of Pd layer on the Au cathode appears to be controlled by mass transport, but this can be confirmed only by cyclic voltammetry. However, one must be careful because only the first 20 % of the rising transient is completely free of overlap effects, and this time range is often distorted by charging and other background currents.[108]

The plateau current seems to increase slightly, to -5 μA, with time which suggests that the current increases with time because the electrode area is getting larger due to plating. This is consistently seen in the current-time transients for various potential steps in Figure 53, with (A) being the most pronounced. This means that in the aqueous system, the formation of Pd layer on the Au cathode is not controlled by electron transfer.

Figure 52(B) is a theoretical Cottrell plot based on the diffusion coefficient of 10.2 x 10^{-6} cm^2 s^{-1} of Pd(II) obtained from reference 91. The Cottrell current actually turns out to be much smaller than the actual plateau current of 4 μA, which is at first, unexpected. However, when taking into account the size of the working electrode, 0.2 mm diameter, it is more likely that microelectrode behaviour was observed; the theoretical microelectrode current calculated from equation 8 in section 3.2.2 is 3.2 μA, for a microelectrode (0.1 mm radius), the diffusion coefficient at 10.2 x 10^{-6} cm^2 s^{-1} and the concentration of Pd (II) at 40 mM. The difference between the actual deposition current of 4 μA and the theoretical microelectrode current of 3.2 μA is most likely due to the effect of migration, since no added electrolyte was present. Daniele *et al.*[187] applied steady-state voltammetry to the study of hydroxide ion (OH^-) oxidation in aqueous solutions and found that as the OH^- ion was negatively charged species, the absence of and low concentrations of supporting electrolyte actually produced currents enhanced by migration. In sodium hydroxide solutions, the limiting current obtained was a factor of

1.8 greater in the absence of, than in the presence of excess supporting electrolyte. The experimental values were close to the theoretical predictions.[188]

The reason for the absence of excess electrolyte was because the solution without supporting electrolyte is more similar to the surfactant system, thereby preventing any possible effect on the liquid crystalline phases and pore geometry.

The advantage of deposition by potential step is that the deposition charge passed can be controlled. Table 9 shows information on the Pd films deposited at various potentials from aqueous solution where all potentials were stepped from +0.4 V vs. SCE. The potentials chosen correspond to the plateau current seen in Figure 51(C). One charge density of 2.55 C cm^{-2} was used, and a 100 % Faradaic efficiency was assumed for the electrochemical deposition process.

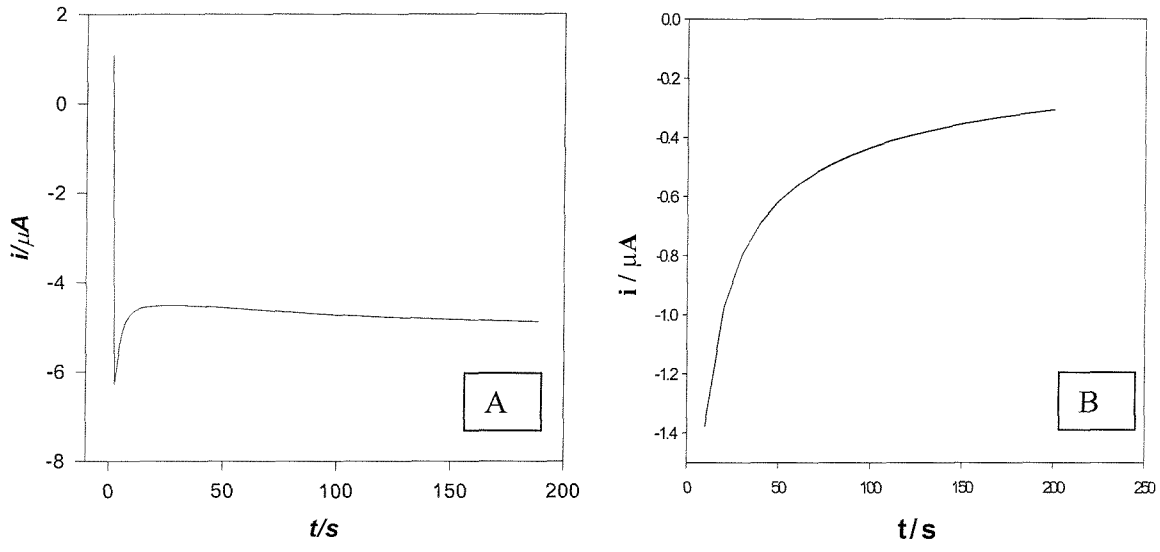

Figure 52 (A) The current-time transient shows typically the electrochemical deposition of Pd film from an aqueous solution of 40 mM $(NH_4)_2PdCl_4$ at 25 ^{0}C. Using the same charge density of 2.55 C cm^{-2}, the potential was stepped from 0.4 to 0.12 V vs. SCE. The films were grown on 0.2 mm diameter gold electrodes. (B) The theoretical Cottrell equation based on diffusion coefficient of 10.2 x 10^{-6} cm^2 s^{-1} obtained from reference 91.

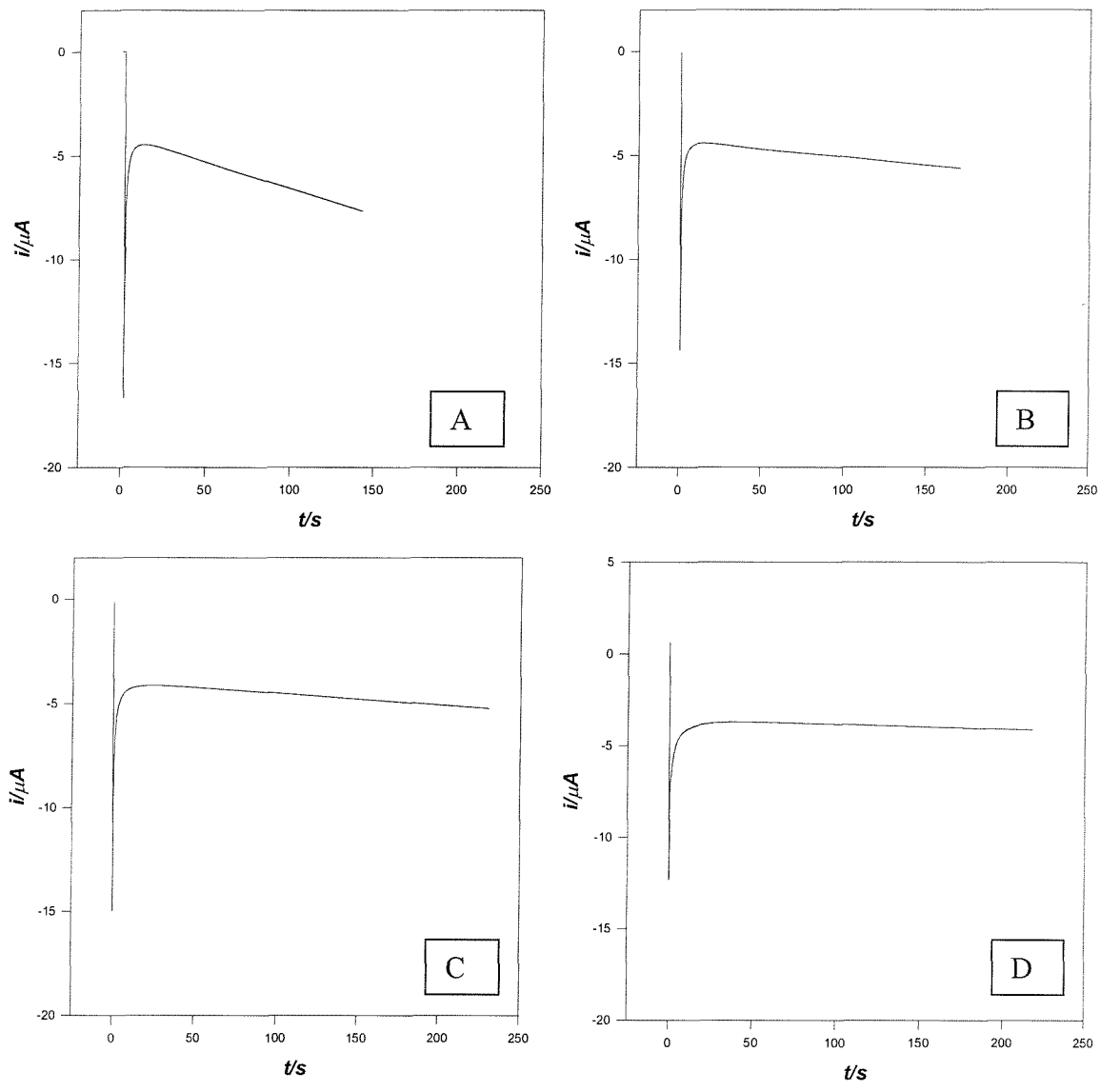

Figure 53 A selection of typical current-time transients showing the electrochemical deposition of Pd film from an aqueous solution of 40 mM $(NH_4)_2PdCl_4$ at 25 ^{0}C. Using the same charge density of 2.55 C cm^{-2}, the potential was stepped from 0.4 V vs. SCE to (A) –0.2 V, (B) –0.1 V, (C) –0.05 V and (D) 0.1 V. The films were grown on 0.2 mm diameter gold electrodes.

Although Figure 54 and Table 9 show scatter in the data, the more cathodic the deposition potential, the greater the specific surface area appears to be, from 0.5 m^2 g^{-1} at 0.26 V and 10.8 m^2 g^{-1} at –0.20 V. The big increase seen at –0.1 and –0.2 V seems to be when H is codeposited. In addition, the deposition time and thus the rate of electrodeposition seem to increase.

What is more important to note is to compare the order of magnitude for example in surface area in the aqueous system with the surfactant system, where the latter shows much larger surface area, as discussed in later sections.

Deposition potential vs. SCE / V	Deposition time/ s	Reduction peak charge / μC	Number of scans in acid	Pd area / cm^2	Roughness factor	Pd surface area / $m^2 g^{-1}$
0.26	247	-0.99	36	0.0023	7	0.53
0.24	262	-2.20	18	0.0052	16	1.17
0.22	231	-2.80	18	0.0066	21	1.50
0.20	217	-2.64	9	0.0062	20	1.41
0.16	235	-1.85	17	0.0044	14	0.99
0.14	169	-2.60	3	0.0061	20	1.39
0.12	189	-2.30	17	0.0054	17	1.23
0.10	218	-5.89	6	0.0139	44	3.15
0.05	207	-5.77	9	0.0136	43	3.08
0.00	232	-8.76	3	0.0207	66	4.68
-0.05	231	-13.09	2	0.0309	98	7.00
-0.10	170	-17.80	3	0.0420	134	9.52
-0.20	143	-20.12	1	0.0475	151	10.76

Table 9 Data for Pd films electrochemically deposited from an aqueous solution of 40 mM $(NH_4)_2PdCl_4$ at 25 ^{0}C. Using the same charge density of 2.55 C cm^{-2}, the surface area of the Pd films could be compared vs. the deposition potential, and all potentials were stepped from +0.4 V vs. SCE.. The films were grown on 0.2 mm diameter gold electrodes, geometric area 0.000314 cm^{-2}.

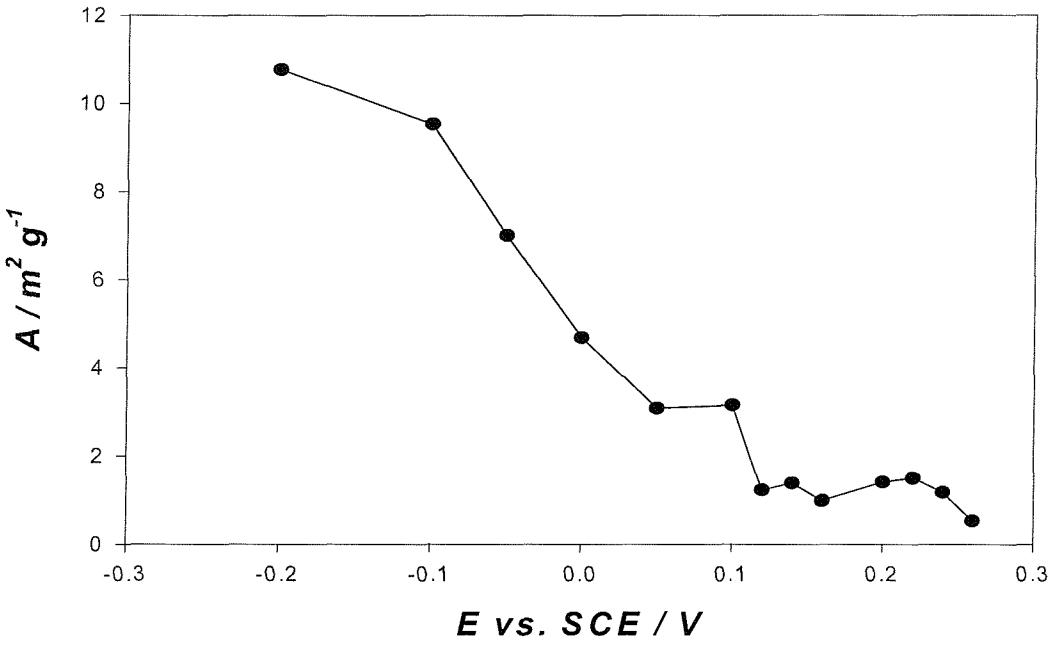

Figure 54 Using the same charge density of 2.55 C cm^{-2}, the deposition time of the Pd films (A) and the surface area (B) can be compared as a function of the deposition potential. All potentials were stepped from +0.4 V vs. SCE. The films were grown on 0.2 mm diameter gold electrodes from 40 mM $(NH_4)_2PdCl_4$ at 25 ^0C.

5.2.5 Summary and Conclusions

The study of the electrochemical deposition of Pd from the aqueous system, provided the background to the electrochemical deposition of nanostructured Pd films on Au electrodes.

The electrochemical deposition of Pd was carried out by cyclic voltammetry and potential step methods. After soaking in water overnight, to ensure consistency with the later studies on films deposited from surfactant solutions, the Pd film was subjected to fast potential cycling in 1 M sulfuric acid. This confirmed the identity of the Pd films grown on the Au electrodes and their specific surface areas.

Cyclic voltammetric depositions showed that the more cathodic the deposition potential, i.e. the lower limit, the greater the surface area of Pd was obtained when one

scan rate was studied. When the deposition potential was kept the same, increasing the scan rate was found to increase the surface area.

Based on one charge density of 2.55 C cm^{-2}, and assuming a 100 % Faradaic efficiency for the electrochemical deposition process, the potential step method showed that as the deposition potential became more cathodic, i.e. negative, the rate of electrodeposition increased resulting in a higher surface area of Pd. The greatest surface area was found to be 10.8 m^2 g^{-1} at the most cathodic deposition potential, i.e. –0.2 V, and the deposition took the shortest time, i.e. about 140 s.

Although scatter can be seen in the data, the main purpose of studying the aqueous system was to compare the order of magnitude of the specific surface areas with the surfactant system. It can later be seen that the surfactant (Brij® 56) system does give greater specific surface areas than the aqueous system.

5.3 Phase Diagram of Pd in Brij® 56

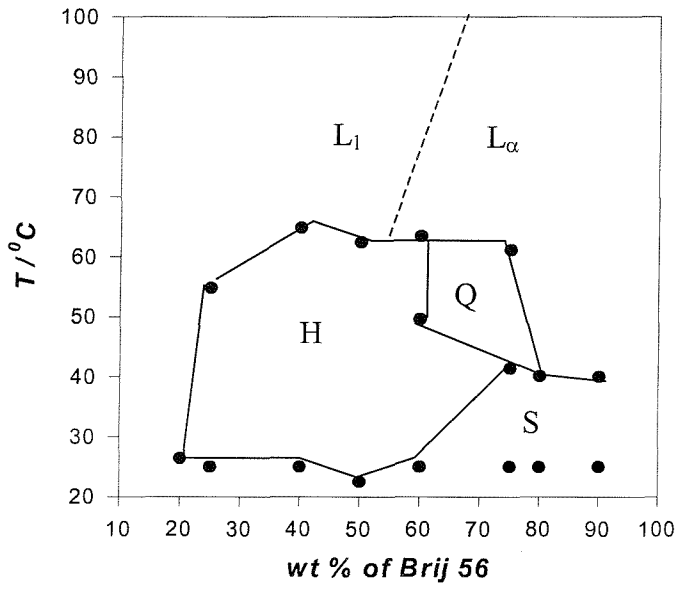

Figure 55 Phase Diagram of a ternary system of Brij® 56 and 1.06 M $(NH_4)_2PdCl_4$ solution, whose phase domains are similar to those of $C_{16}EO_8$ in water. The abbreviations for the domains are as follows: S = solid, H = hexagonal, Q = cubic, L_1 = micellar and L_α = lamellar. [n.b. the points obtained near 20 ^{0}C correspond to the starting point of each measurement]

Figure 5 in Chapter 1 shows two phase diagrams of a binary system of water and surfactant: $C_{16}EO_8$[36] and Brij® 56[33]. In the former surfactant system, a wide stable hexagonal phase exists between about 30 and 70 wt% and between room temperature and 60 ^{0}C. In the latter, it exists between about 45 and 70 wt% and between room temperature and 70 ^{0}C. This means that the surfactants display similar phase behaviour.

The addition of the Pd salt to the $C_{16}EO_8$ system gives a wide hexagonal phase over similar concentration and temperature ranges, see Figure 56. This can also be said of the Brij® 56 system in Figure 55. Similarly, a cubic phase exists between 60 and 80 wt% $C_{16}EO_8$ in water and from 30 to 60 ^{0}C, which is also observed approximately in Brij® 56.

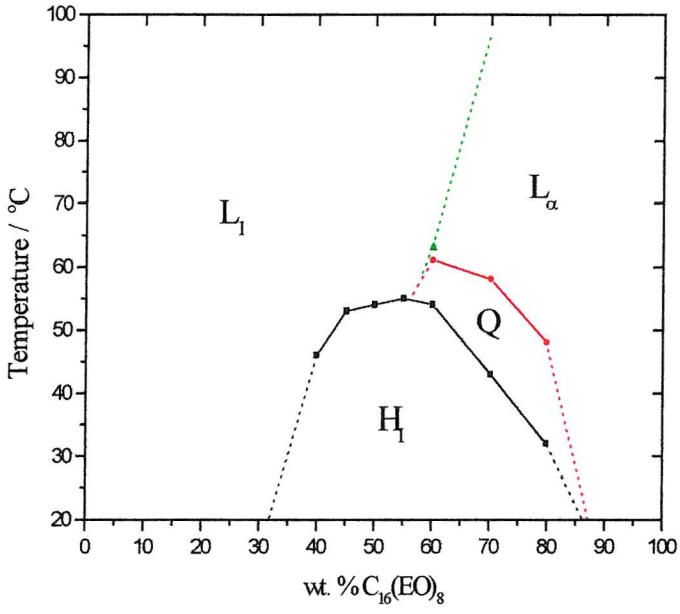

Figure 56 Phase diagram of $C_{16}EO_8$ and $(NH_4)_2PdCl_4$ solution.[35] The weight ratio salt/water was kept constant at 0.4. The abbreviations for the domains are as follows: S = solid, H = hexagonal, Q = cubic, L_1 = micellar and L = lamellar.

Therefore, the addition of the Pd salt to both the surfactant systems does not change fundamentally the phase behaviour, and in fact, Brij® 56 can be used as an alternative to $C_{16}EO_8$.

5.4 Brij® 56 – Electrodeposition of Pd from the hexagonal phase

Like the aqueous system, the same set of electrodeposition conditions were applied to the surfactant system consisting of 60 wt% Brij® 56 and 40 wt % of the aqueous solution of $(NH_4)_2PdCl_4$. The deposition data and the film characterisation data can be compared with data for the aqueous system presented above. This section discusses the data relating to electrochemical deposition from the hexagonal phase of Brij® 56 at 25 ^{0}C. The phase was checked under the polarising light optical microscope.

5.4.1.1 Deposition by Cyclic Voltammetry

With the potential range between 0.1 and 0.6 V, the surfactant and aqueous system at 25 ^{0}C show similar deposition voltammograms, see Figure 57(A) and (C). At 10 mV/s, the potential was cycled from 0.4 V on the cathodic scan and was stopped at 0.3 V on the anodic scan after a full scan between 0.1 and 0.6 V. Common features include a steep reduction wave in the same potential region, i.e. between 0.1 and 0.4 V, indicating Pd deposition, and a broad oxidation wave between 0.4 and 0.6 V.

However, there appears to be a significant cathodic shift in potential. In fact, extending the lower limit to as low as –1 V does not even produce a plateau on the initial cathodic scan in Figure 57(D), and the increasing cathodic current is likely to be due to hydrogen evolution. The extra oxidation peak near 0 V is therefore hydrogen oxidation.[185] The absence of a plateau in cathodic current does not enable the half-wave potential to be calculated, but the shift is cathodic. This is reminiscent of the –60 mV shift found in the ferricyanide system upon addition of Brij® 56.

Therefore, at 0.1 V, there is a noticeable difference in the magnitude of the reduction current: 4 μA for the aqueous system and 1.5 μA for the surfactant system. Other reasons could be the differences in the viscosity in both systems and in the accessible surface area of the Au electrode.

Figure 57 (B) is the cyclic voltammogram showing the acid characterisation of the Pd film. Based on the reduction peak area near 0.5 V, the specific surface area of Pd was found to be actually greater in the surfactant system at 1.01 $m^2\ g^{-1}$, a factor of 14 greater

than in the aqueous system. This suggests that cyclic voltammetric electrodeposition from the hexagonal phase of Brij® 56 does increase the surface area of Pd.

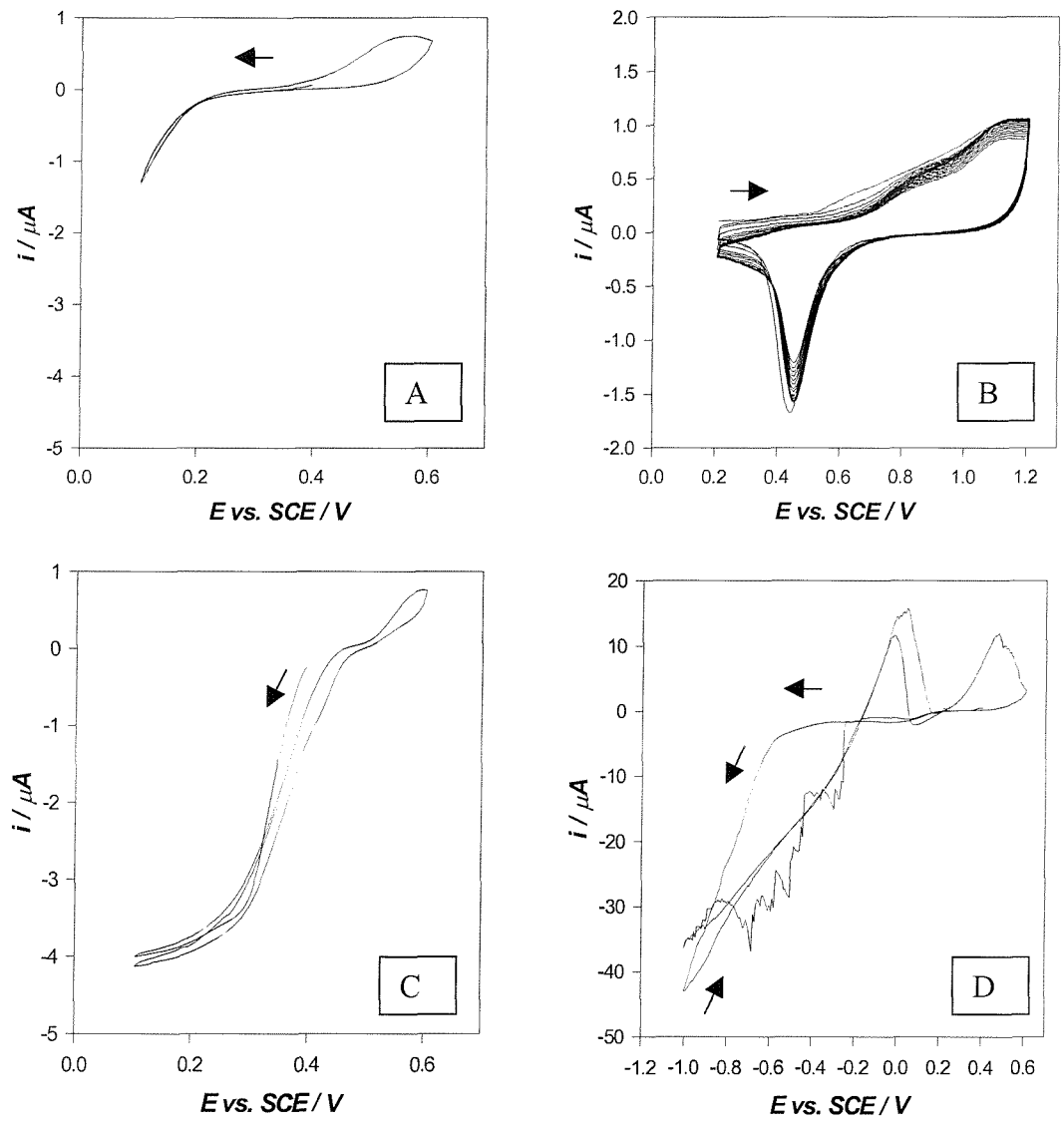

Figure 57 Cyclic voltammetry: (A) Electrodeposition of Pd film from a templating mixture of 60 wt% Brij® 56 and 40 wt% of $(NH_4)_2PdCl_4$ (aq) at 25 ^{0}C at 10 mV/s. (B) Characterisation of the previous Pd film cycled in 1 M H_2SO_4 (aq) at 25 ^{0}C at 200 mV/s. (C) Electrodeposition of Pd film from 40 mM $(NH_4)_2PdCl_4$ (aq) at 25 ^{0}C at 10 mV/s. (D) Same as (A) but extending the lower limit. The films were grown on 0.2 mm diameter Au electrodes. The arrows show the direction of the scan.

5.4.1.2 Deposition by Potential Step

In addition, this increase in surface area is confirmed by electrodeposition by potential step. Table 10 shows information on the Pd films deposited at various potentials from 60 wt% Brij® 56 and 40 wt% $(NH_4)_2PdCl_4$ (aq) at 25^0C, i.e. in the hexagonal phase. All potentials were stepped from +0.4 V vs. SCE, using the same charge density of 2.55 C cm^{-2}. The reason for choosing deposition potentials as low as 0.12 V, and not going more negative, was to compare like data with the $C_{16}EO_8$ system studied by Guerin.[35]

Deposition potential vs. SCE / V	Deposition time / s	Reduction peak charge / μC	Number of scans in acid	Pd area / cm^2	Roughness factor	Pd surface area / $m^2\ g^{-1}$
Cyclic voltammetry	150	-1.3	1	0.003	10	1.0
0.28	>6000	-2.2	32	0.005	17	1.2
0.24	5719	-15.8	73	0.037	119	8.4
0.22	3188	-19.8	63	0.047	149	10.6
0.20	3580	-34.7	56	0.082	260	18.5
0.18	4091	-36.4	57	0.086	274	19.5
0.14	2755	-42.0	54	0.099	316	22.5
0.12	1587	-53.3	49	0.126	400	28.5

Table 10 Data for Pd films electrochemically deposited from a templating mixture of 60 wt% Brij 56 and 40 wt% $(NH_4)_2PdCl_4$ (aq) at 25^0C. Using the same charge density of 2.55 C cm^{-2}, the data could be compared against deposition potential, and all potentials were stepped from +0.4 V vs. SCE. Note, the data for deposition at 0.28 V are based on a lower charge density. The films were grown on 0.2 mm diameter gold electrodes.

As Table 10 and Figure 58 show, with increasing cathodic deposition potential, the deposition time in the surfactant system tends to decrease, suggesting increasing rate of deposition; and the specific surface area of Pd tends to increase with the greatest surface area here obtained at about 28.5 $m^2\ g^{-1}$ at 0.12 V. However, the trends are not smoothly defined; this could be due to the "bubble" problem described in section 3.3.2, where bad contact between the working electrode and the mixture could be caused by the presence of trapped air bubbles.

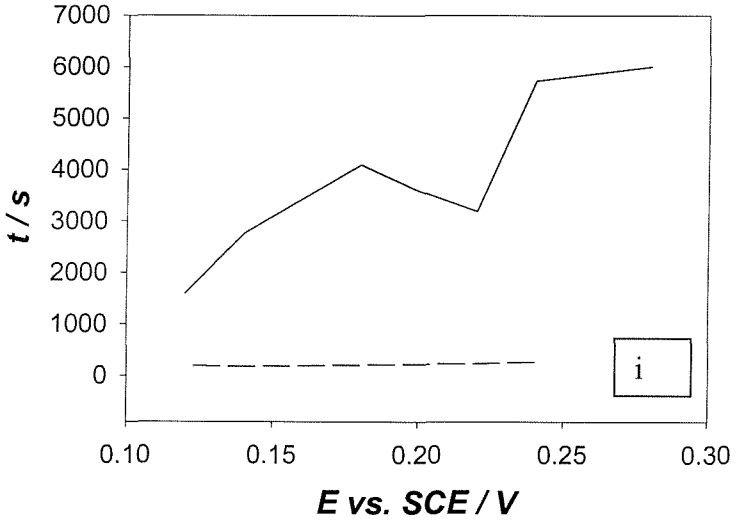

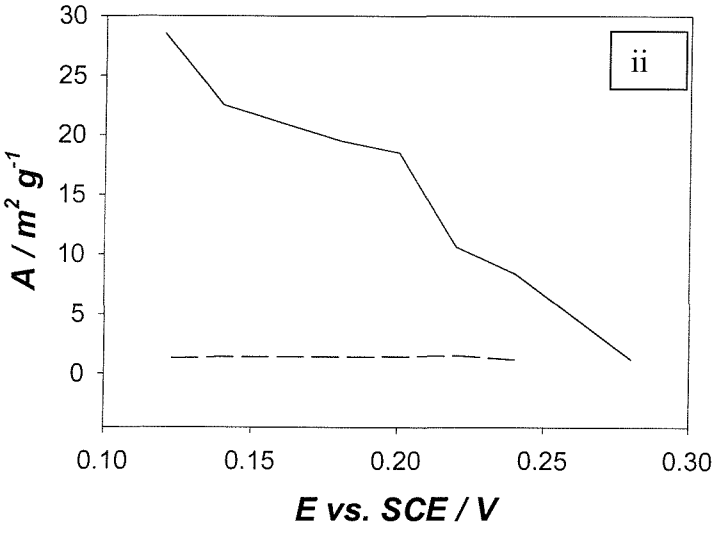

Figure 58 Data based on the electrodeposition of Pd in the aqueous system (– – – –) and in the surfactant system (———). All potentials on x-axis were deposition potentials stepped from +0.4 V vs. SCE. Plot (i) looks at the variation of deposition times (t) and plot (ii) at the variation of specific surface areas (A). Using the same charge density of 2.55 C cm^{-2}, the films were grown on 0.2 mm diameter gold electrodes at 25^0C.

Finally, Figure 58 clearly shows that electrodeposition is much slower in the surfactant system by up to 25 times, and specific surface areas are greater by up to 15 times.

5.5 Brij® 56 – Electrodeposition of Pd in the cubic phase

Like the aqueous and hexagonal systems at 25 ^{0}C, the same set of electrodeposition conditions were applied to the surfactant system in the cubic phase, consisting of 60 wt% Brij® 56 and 40 wt % of the aqueous solution of $(NH_4)_2PdCl_4$. This section discusses the data relating to electrochemical deposition of Pd from the cubic phase of Brij® 56 at 55 ^{0}C.

5.5.1.1 Deposition by Cyclic Voltammetry

Figure 59 shows the comparison of cyclic voltammetric deposition of Pd in the three systems: cubic, hexagonal and aqueous.

All three systems show somewhat similar deposition voltammograms. The potential was cycled at 10 mV/s from 0.4 V cathodically and was stopped at 0.3 V on the anodic scan after a full scan between 0.1 and 0.6 V. Common features include a steep reduction wave in the same potential region, i.e. between 0.1 and 0.4 V, indicating Pd deposition, and a broad oxidation wave between 0.4 and 0.6 V.

However, the reduction plateau current only appears in the aqueous system, Figure 59(C). There appears to be a significant cathodic shift in potential going from aqueous to surfactant systems, and the absence of a plateau in cathodic current does not enable the half-wave potential to be calculated. Even going from hexagonal to cubic systems appears to result in a potential shift. What seems clear is that the presence of Brij® 56 is an important factor, but what is not clear is whether the potential shift, when going from hexagonal to cubic, is caused by the temperature or by the change of phase. More experiments are needed to clarify this last point, where several deposition cyclic voltammograms are taken along the temperature curve.

The need for more experiments is seen more clearly in the overall magnitude of the deposition current, where at the lower limit of 0.1 V, the reduction current is 9 μA in the cubic system, 1.5 μA in the hexagonal system and 4 μA in the aqueous system. The addition of the surfactant causes a decrease in current, but increasing the temperature to where the phase changed causes an increase in current. The most likely reason for the

decrease in cathodic current is the increase in viscosity, whereas the greatest current seen in the cubic system is either caused by the effect of temperature or phase change.

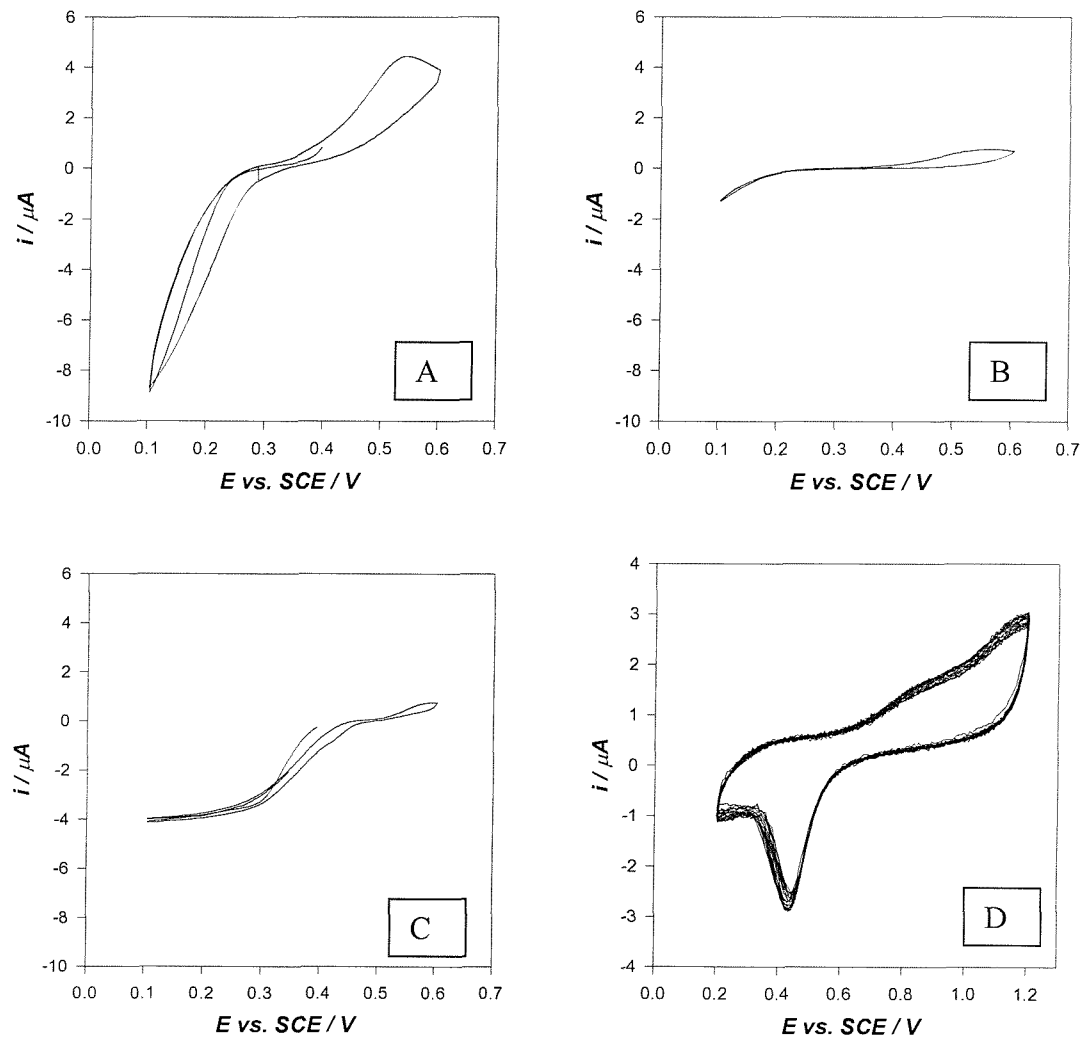

Figure 59 Electrodeposition of Pd film on 0.2 mm diameter Au electrodes by cyclic voltammetry from: a templating mixture of 60 wt% Brij® 56 and 40 wt% of $(NH_4)_2PdCl_4$ (aq) at (A) 55 ^{0}C – i.e. cubic system and (B) 25 ^{0}C – i.e. hexagonal system; (C) 40 mM $(NH_4)_2PdCl_4$ (aq) at 25 ^{0}C – i.e. aqueous system. The deposition started cathodically at +0.4 V and ended anodically at +0.3 V. The upper limit was +0.6 V with the lower limit at +0.1 V. A full scan was obtained in each case at 10 mV/s. (D) Typical cyclic voltammogram of Pd film cycled in 1 M H_2SO_4 at 25 ^{0}C at 200 mV/s, starting and ending at 0.2 V; this voltammogram is the acid characterisation one corresponding to (A).

Figure 59(D) shows the typical acid characterisation of Pd film deposited in the cubic system after the soaking in deionised water. As in the aqueous and the hexagonal systems, the reduction peak was found to increase in area and reached a maximum as the film was cycled several times. Based on the reduction peak area at 0.45 V, the specific surface area of Pd could be calculated and was found to be actually greatest in the hexagonal system at 1.01 $m^2 g^{-1}$, a factor of 14 greater than in the aqueous system and a factor of 3 greater than in the cubic system, as seen in Table 11.

System	Reduction peak charge / μC	Number of Scans in acid	Pd area/ cm^2	Roughness factor	Pd specific surface area/ $m^2 g^{-1}$
aqueous	-1.54	1	0.0036	12	0.07
hexagonal	-1.26	1	0.0030	9	1.01
cubic	-2.36	14	0.0056	18	0.36

Table 11 Table of acid characterisation of Pd films deposited by cyclic voltammetry on 0.2 mm diameter Au electrodes in three systems. The films were cycled in 1 M H_2SO_4 at 25 ^{0}C at 200 mV/s, starting and ending at 0.2 V.

The smaller surface area found in the aqueous system is not surprising because electrodeposition in a liquid crystalline phase has been shown to increase the surface area of a metal.[2] On the other hand, it is surprising to observe the largest surface area in the hexagonal system because the cubic system contains a 3-d network.

These results were obtained for films deposited by cyclic voltammetry and are further confirmed by potential step depositions.

5.5.1.2 Deposition by Potential Step

Table 12 shows information on the Pd films deposited at various potentials from 60 wt% Brij® 56 and 40 wt% $(NH_4)_2PdCl_4$ at 55 ^{0}C, i.e in the cubic phase. All potentials were stepped from +0.4 V vs. SCE, using the same charge density of 2.55 C cm^{-2} as before, and we have assumed a 100 % Faradaic efficiency for the electrochemical deposition process.

Deposition potential vs. SCE / V	Time of deposition / s	Reduction peak charge / μC	Number of scans in acid	Pd area / cm^2	Roughness factor	Pd surface area / $m^2 g^{-1}$
0.24	1039	-1.23	174	0.0029	9	0.66
0.22	603	-3.72	91	0.0088	28	1.99
0.20	364	-3.42	184	0.0081	26	1.83
0.18	226	-2.74	106	0.0065	21	1.47
0.16	220	-6.76	169	0.0160	51	3.61
0.14	143	-12.91	125	0.0300	97	6.90
0.12	120	-5.17	87	0.0120	39	2.76

Table 12 Electrodeposition of Pd film from a templating mixture of 60 wt% Brij® 56 and 40 wt% of $(NH_4)_2PdCl_4$ (aq) at 55 ^{0}C – i.e. cubic system. Using the same charge density of 2.55 C cm^{-2}, the data could be compared against deposition potential, and all potentials were stepped from +0.4 V vs. SCE. The films were grown on 0.2 mm diameter gold electrodes.

Figure 60 compares the deposition time and the specific surface area as functions of the deposition potential between three systems: aqueous, hexagonal and cubic. As the deposition potential becomes more cathodic, the deposition time in all the systems tends to decrease, suggesting increasing rate of deposition; electrodeposition appears to be the slowest in the hexagonal system. On the other hand, the specific surface area of Pd appears to increase in all the systems, but the values were clearly the greatest in the hexagonal system.

In addition, both the surfactant systems give greater surface areas and longer deposition times than the aqueous system. This confirms that electrodeposition in a liquid crystalline phase has been shown to increase the surface area of a metal.[2] The greatest surface area here was obtained at about 28.5 $m^2 g^{-1}$ at a deposition potential of 0.12 V in the hexagonal system, see Table 13.

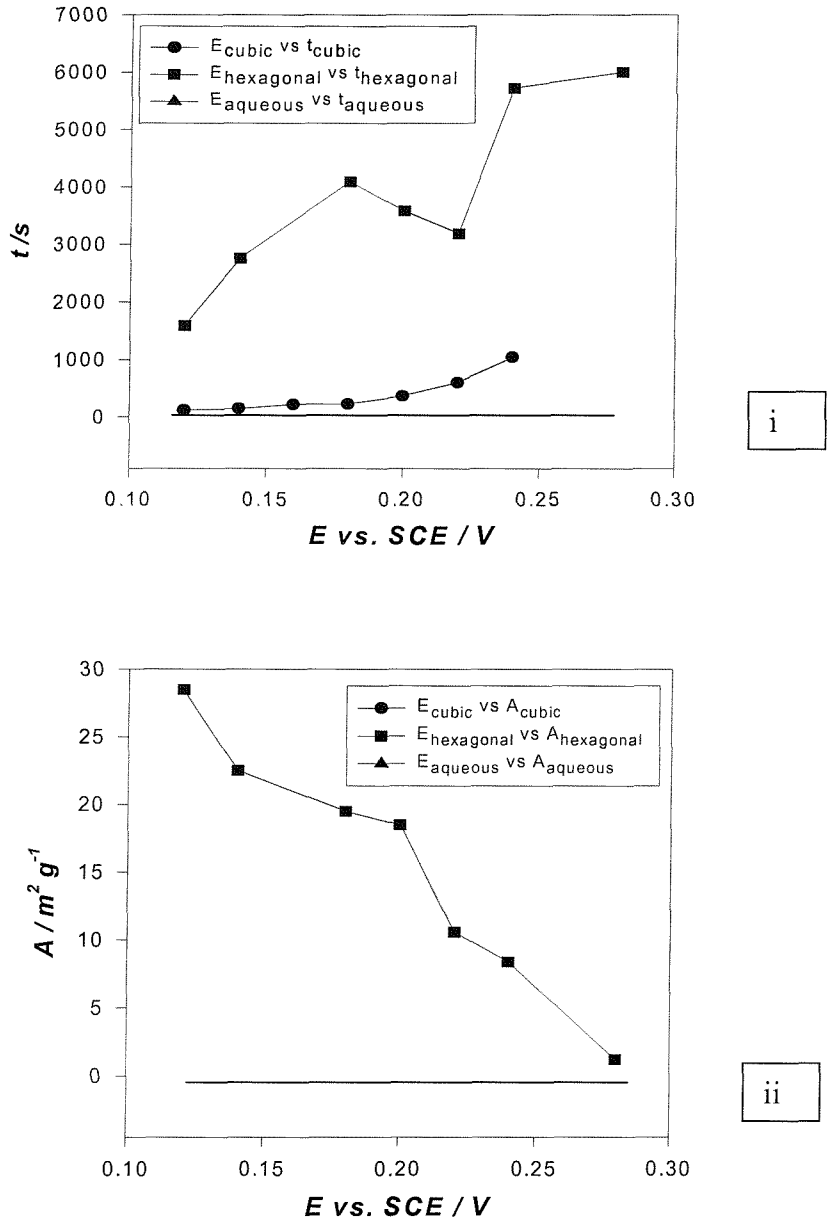

Figure 60 Data based on the electrodeposition of Pd in three systems: aqueous (▲), hexagonal (■) and cubic (●); if a line is shown at zero, the values are too small. All potentials on x-axis were deposition potentials stepped from +0.4 V vs. SCE. Plot (i) looks at the variation of deposition times (t) and plot (ii) at the variation of specific surface areas (A). Using the same charge density of 2.55 C cm^{-2}, the films were grown on 0.2 mm diameter gold electrodes at 25 ^{0}C. [data may be invisible above due to the y-axis scale, but data can be found in the tables]

System	Time of deposition / s	Reduction peak charge / μC	Number of Scans in acid	Pd area/ cm^2	Roughness factor	Pd specific surface area/ $m^2 g^{-1}$
aqueous	189	-2.30	17	0.0054	17	1.23
hexagonal	1587	-53.26	49	0.1260	400	28.48
cubic	120	-5.17	87	0.0120	39	2.76

Table 13 Table of acid characterisation of Pd films deposited by potential step in three systems. Using the same charge density of 2.55 C cm^{-2}, all potentials were stepped from 0.4 to 0.12 V vs. SCE. The films were grown on 0.2 mm diameter gold electrodes.

5.6 Summary

Instead of analysing the numbers in detail, several interesting observations can be made.

The addition of a surfactant, i.e. Brij® 56, gives greater specific surface areas of Pd and longer deposition times than the aqueous system, confirming that electrodeposition in a liquid crystalline phase increases the surface area of a metal.[2] In addition, there is a significant cathodic shift in potential, with the plateau current only observed in the aqueous system; thus it was not possible to compare the half-wave potentials.

The cubic system actually gave lower specific surface areas of Pd than the hexagonal system. When the films were grown by potential step, the areas were found to be about 10 times smaller, and the deposition times were shorter. This is surprising because the cubic system is believed to contain a 3-d network, and the cubic pore geometry had been predicted to give the largest surface area of Pd.

It is not clear whether the effects described are the result of temperature or phase change, but it is clear that they are the result of the presence of a surfactant.

In this work, Pd films were electrodeposited in the presence of Brij® 56, using the same charge density as Guerin, i.e. 2.55 C cm^{-2}.[35] Thus the effects of deposition conditions could be compared, for example in terms of potential step transients.

Figure 53(D) gives the current-time transient when the potential of the gold working electrode was stepped from 0.4 to 0.1 V vs. SCE to deposit Pd on a 0.2 mm diameter gold electrode in the aqueous system, i.e. in the absence of surfactant. The reduction current initially reaches about –12.5 μA and after about 20 s, reaches a plateau of almost –4.5 μA. The time taken to complete the potential step was almost 200 s. The shape of the transient is similar to that seen by Guerin in the aqueous system, i.e. an initial reduction current and the formation of a plateau current, even though the values are larger in his case because he used a much larger working electrode (1 mm diameter Au). The deposition timescale of his experiments, for the same charge density, was almost 500 s.

In the surfactant system, the shape of the deposition transients and the time taken to complete the potential step were found to be less reproducible when compared to the aqueous system. For the same potential step at 0.2 mm diameter Au, Figure 63 shows a selection of typical transients obtained for the deposition of Pd from the hexagonal phase of Brij® 56. For the same charge density of 2.55 C cm^{-2}, the deposition times ranged from about 780 to 2200 s; this wide range, over 1000 s, could be due to the "bubble" problem, as discussed in Chapter 3, although this cannot be confirmed. The transients have quite different plateau shapes with the initial reduction current reaching almost 2 μA.

As mentioned before, the studies by Guerin[35] on the electrodeposition of Pd were restricted to a single set of deposition conditions: that is using one surfactant, at one composition, for one choice of Pd salt composition, at one deposition potential, and at a single deposition temperature. Although carrying out these potential step experiments several times on one type of large planar working electrode (1 mm diameter Au) and one type of pellistor substrate (named as SRL 136, 1.2 mm^2 Au), Guerin did not describe in detail the deposition transients he obtained in the surfactant system of $C_{16}EO_8$; he only mentions that a longer time was required than for the aqueous system; an initial reduction current peak and a plateau were present in the transients. The reduction current initially reached was about –110 μA and after about 100 s, reached a plateau of almost –50 μA. The timescale of the deposition was about 700 s.

Overall, several things can be pointed out. Firstly, the deposition timescales in both the surfactant systems ($C_{16}EO_8$ and Brij® 56) obtained are lower than in the aqueous system (i.e. in the absence of surfactant, using 40 mM $(NH_4)_2PdCl_4$). Since the surfactant mixture used for deposition is rather viscous, very little contribution from convection is expected. Secondly, an initial reduction current peak and a plateau do show up in the transients in both the aqueous and surfactant systems. As expected, the overall reduction currents are observed to be lower in the surfactant system; this makes sense since the aqueous domains are considerably smaller than in the bulk aqueous system, and ion transport, and therefore reduction, can only occur in the aqueous domains.

5.7 Brij® 56 - The Effect of Temperature on Deposition of Pd

5.7.1 The Same Potential Step

This section examines the effect of temperature on the electrodeposition of Pd in the presence of Brij® 56. In all cases, the potential was stepped from 0.4 to 0.16 V using one charge density of 2.55 C cm^{-2}.

Figure 61 shows the current – time transients for temperatures ranging from 25 to 55 ^{0}C for the templating mixture of 60 wt% Brij® 56 and 40 wt% of $(NH_4)_2PdCl_4$. The SCE reference electrode potential was kept the same because only the frit at the end of the body was allowed in the mixture. The hexagonal phase was observed using a polarised light optical microscope from 25 to 35 ^{0}C and the cubic phase at 55 ^{0}C. The transients at 25 and 30 ^{0}C appear to have a similar flat plateau shape, whereas as the temperature increased to 35 ^{0}C, the current plateau appears to drop dramatically after about 1200 s. When the temperature reached 55 ^{0}C, the transient current appears at a high initial current of about -8 μA and then decreases to a plateau at about -5 μA.

It appears that increasing the deposition temperature decreases the deposition time and the specific surface areas, see Table 14. For example, here the longest deposition time (i.e. the slowest deposition rate) and the greatest specific surface area were obtained at 25 ^{0}C in the hexagonal phase. More experiments are needed to determine whether there is a discontinuous change when the phase changes. 55 ^{0}C was chosen in order to be in the middle of the cubic phase.

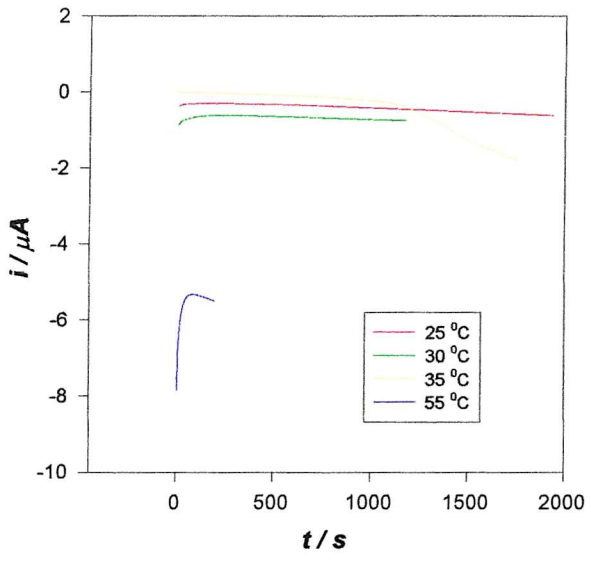

Figure 61 Electrodeposition of Pd film from a templating mixture of 60 wt% Brij® 56 and 40 wt% of $(NH_4)_2PdCl_4$ (aq) at various temperatures: 25, 30 and 35 ^{0}C correspond to the hexagonal phase and 55 ^{0}C to the cubic phase. Using the same charge density of 2.55 C cm^{-2}, the potentials were stepped from +0.4 V vs. SCE. The films were grown on 0.2 mm diameter gold electrodes.

Deposition temperature / ^{0}C	Time of deposition / s	Reduction peak charge / ^{0}C	Number of scans	Pd area/ cm^2	Roughness Factor	Pd specific surface area / m^2 g^{-1}
25	1936	-41.91	54	0.099	315	22.41
30	1180	-39.32	59	0.093	295	21.02
35	1754	-36.10	54	0.085	271	19.30
55	199	-19.13	145	0.045	144	10.23

Table 14 Table of acid characterisation of Pd films deposited by potential step at various temperatures. Using the same charge density of 2.55 C cm^{-2}, all potentials were stepped from 0.4 to 0.16 V vs. SCE. The films were grown on 0.2 mm diameter gold electrodes.

This further confirms the results seen in previous sections that the hexagonal phase required longer deposition times and gave greater surface areas than the cubic phase.

5.7.2 Two Different Potential Steps

The electrodeposition of Pd by two potential steps were compared at two temperatures, 25 and 55 ^{0}C, i.e. in the hexagonal and cubic phases respectively. The potential was stepped from 0.4 to 0.12 and 0.16 V at a charge density of of 2.55 C cm^{-2}. The currents seen in Figure 62 match well with the deposition cyclic voltammograms seen in Figure 59; for example, at 0.12 V, the current reaches -0.8 μA at 25 ^{0}C and –7 μA at 55 ^{0}C.

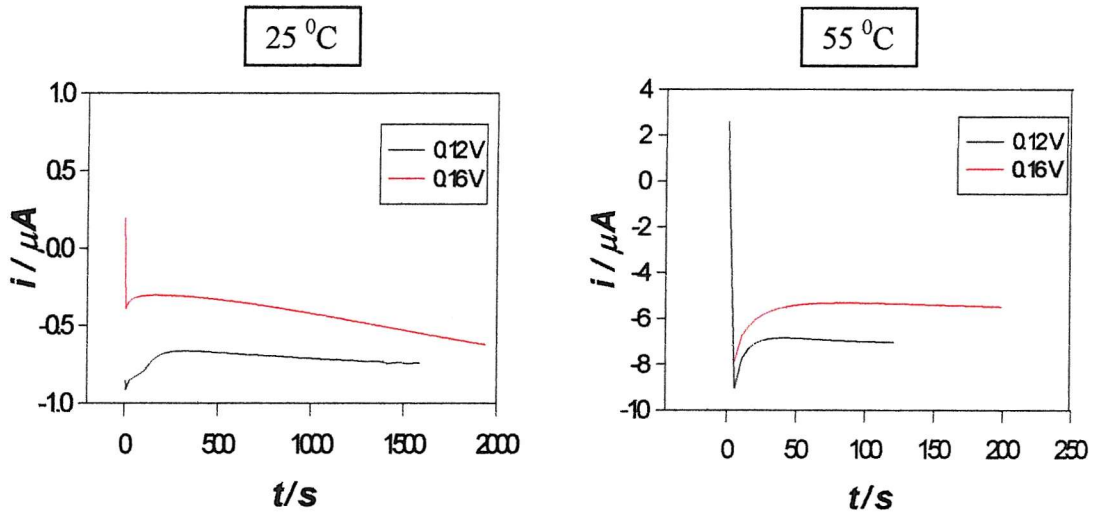

Figure 62 Electrodeposition of Pd film from a templating mixture of 60 wt% Brij® 56 and 40 wt% of $(NH_4)_2PdCl_4$ (aq) at 25 and 55 ^{0}C. Using the same charge density of 2.55 C cm^{-2}, the potentials were stepped from 0.4 to 0.12 and 0.16 V vs. SCE. The films were grown on 0.2 mm diameter gold electrodes.

Figure 62 and Table 15 show several things.

Firstly, at each temperature, the deposition times for both potential steps were similar in terms of the order of magnitude; the deposition at 25 ^{0}C took about ten times longer than at 55 ^{0}C.

Secondly, this similarity in order of magnitude is also seen in the specific surface areas for both potential steps at both temperatures. For instance, the deposition produced at 25 ^{0}C about 29 m^2 g^{-1} at deposition potential of 0.12 V and 22 m^2 g^{-1} at 0.16 V.

Deposition temperature / ^{0}C	Deposition Potential / V	Time of deposition / s	Reduction peak charge / μC	Number of scans	Pd area/ cm^2	Roughness Factor	Pd specific surface area / $m^2 g^{-1}$
25	0.12	1587	-53.26	49	0.126	400	28.5
25	0.16	1936	-41.91	54	0.099	315	22.4
55	0.12	120	-5.17	87	0.012	39	2.8
55	0.16	199	-19.13	145	0.045	144	10.2

Table 15 Table of acid characterisation of Pd films deposited by potential step. Using the same charge density of 2.55 C cm^{-2}, all potentials were stepped from 0.4 V vs. SCE. The films were grown on 0.2 mm diameter gold electrodes.

Thirdly, both potential steps at 55 ^{0}C required shorter deposition times and gave lower surface areas than at 25 ^{0}C, confirming previous results that deposition in the hexagonal phase took longer and produced greater Pd surface areas than in the cubic phase.

Therefore, this appears to be a sensitivity test, where a change in potential does not have much effect and a change in temperature gives a more substantial effect.

5.8 Reproducibility, Repeatability and Sensitivity

In this thesis, the above-mentioned terms are defined as follows:

- reproducibility applies to performing depositions from new mixtures for nominally the same conditions
- repeatability applies to performing repeat depositions in one mixture for nominally the same conditions
- sensitivity applies to performing like depositions in changing conditions.

5.8.1 Replicate Mixtures

To study repeatability and thus reproducibility of the experiments, one set of deposition conditions was applied to the surfactant system, i.e. one composition, deposition potential, temperature and thus phase. Here, Table 16 compares the data acquired for three replicate mixtures of the same composition, i.e. 60 wt% Brij® 56 and 40 wt% of $(NH_4)_2PdCl_4$ solution at 25 ^{0}C. The same batch of Brij® 56 was used. At this temperature, the templating mixture exhibited the hexagonal phase under the polarising light optical microscope. The potential was stepped from 0.4 to 0.1 V at 2.55 C cm^{-2}.

Within one mixture, the deposition times and the specific surface areas appear reasonably repeatable.

This is not clearly seen when comparing three replicate mixtures. Even going from mixtures 1d to 2a, the deposition was slower by a factor of 2.5, which is not reflected in the specific surface area.

Passing the same deposition charge should result in very similar specific surface areas. Comparing the three replicate mixtures, this is not seen here, suggesting that specific surface area is not sensitive to thickness. On the other hand, the thicknesses of electrodeposited Pt films reported by Attard *et al.*[2] varied according to the charge density. The specific surface areas range from about 10 to 16 m^2 g^{-1}.

There is less reproducibility in the deposition times, ranging from about 780 to 2200 s. This wide time range of 1420 s could be due to the "bubble" problem, as discussed in Chapter 3. This cannot be confirmed. Anyway, the current – time transients

in Figure 63 have quite different plateau shapes with the initial reduction current reaching almost 2 μA.

In summary, three potential step experiments on average have been carried out on three different mixtures of the same composition, containing 9 samples in total. An average specific surface area of 12.55 ± 0.76 m^2 g^{-1} was produced, and the average deposition time was 1460 ± 199 s. The average roughness factor was found to be 181 ± 11.

Mixtures	Deposition time / s	Reduction peak charge / μC	Number of scans in acid	Pd surface area / cm^2	Roughness Factor	Pd specific surface area / m^2 g^{-1}
1a	1427	21.03	39	0.0496	158	11.2
1b	2096	27.49	30	0.0648	207	14.7
1c	863	28.72	33	0.0677	216	14.0
1d	776	29.39	30	0.0693	221	15.7
2a	1868	22.01	37	0.0519	165	10.9
2b	2229	19.17	37	0.0452	144	9.7
2c	2011	18.51	38	0.0437	139	9.9
3a	916	22.72	33	0.0536	171	12.2
3b	957	27.53	29	0.0649	207	14.7

Table 16 Table of acid characterisation of Pd films deposited by potential step from a templating mixture of 60 wt% Brij® 56 and 40 wt% of $(NH_4)_2PdCl_4$ (aq) at 25 ^{0}C. Using the same charge density of 2.55 C cm^{-2}, all potentials were stepped from 0.4 to 0.1 V vs. SCE. The films were grown on 0.2 mm diameter gold electrodes.

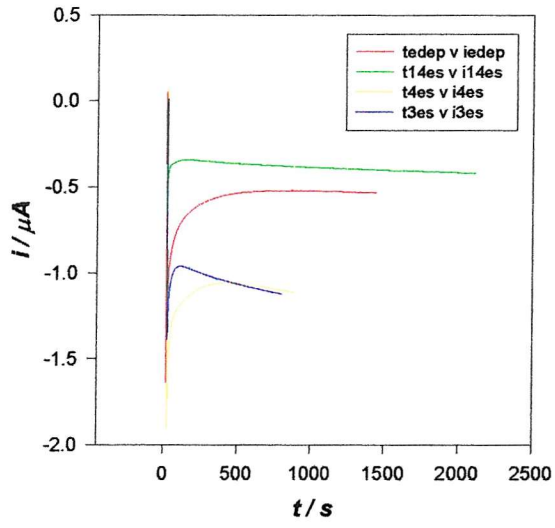

Figure 63 A selection of typical current – time transients showing the electrodeposition of Pd film from a templating mixture of 60 wt% Brij® 56 and 40 wt% of $(NH_4)_2PdCl_4$ (aq) at 25 ^{0}C. Using the same charge density of 2.55 C cm^{-2}, the potentials were stepped from 0.4 to 0.1 V vs. SCE. The films were grown on 0.2 mm diameter gold electrodes.

5.8.2 Different Composition

All electrodepositions of Pd in Brij® 56 described above were carried out in a templating mixture of 60 wt% Brij® 56 and 40 wt% of $(NH_4)_2PdCl_4$(aq). At 25 ^{0}C, the mixture was found to be in the hexagonal phase when examined under the polarising light optical microscope, and at 55 ^{0}C, in the cubic phase. Lower specific surface areas of Pd films were obtained in the latter phase.

The composition is now changed to the templating mixture of 50 wt% Brij® 56 and 50 wt% of $(NH_4)_2PdCl_4$ solution. At 25 ^{0}C, this 1:1 ratio of the Brij® 56 templating mixture was in the hexagonal phase, and using the same charge density of 2.55 C cm^{-2}, Pd was electrodeposited by stepping the potential from 0.4 V to deposition potentials as low as 0.12 V, see Table 17.

Deposition potential / V vs. SCE	Deposition time / s	Reduction peak charge / μC	Number of scans	Pd surface area / cm^2	Roughness Factor	Pd specific surface area / $m^2 g^{-1}$
+0.24	9426	15.61	117	0.0368	117	8.3
+0.22	6885	26.61	97	0.0628	200	11.6
+0.20	2645	31.01	71	0.0731	233	16.6
+0.18	1286	40.22	67	0.0948	302	21.5
+0.16	906	41.00	55	0.0967	308	21.9
+0.14	770	44.82	64	0.1057	337	24.0
+0.12	662	56.29	58	0.1328	423	26.0

Table 17 Table of acid characterisation of Pd films deposited by potential step from a templating mixture of 50 wt% Brij® 56 and 50 wt% of $(NH_4)_2PdCl_4$ (aq) at 25 ^{0}C, i.e. in the hexagonal phase. Using the same charge density of 2.55 C cm^{-2}, all potentials were stepped from 0.4 V vs. SCE. The films were grown on 0.2 mm diameter gold electrodes.

Like the former composition, with more cathodic deposition potentials, Figure 64 shows that the deposition time tended to decrease and the Pd specific surface area to increase. Moreover, the order of magnitude in both the deposition time and surface area does not appear to depend strongly on the ratio of surfactant to aqueous solution, compare also Table 10 and Table 17. For example, the greatest specific surface area here was obtained in both mixtures when the potential was stepped to 0.12 V: 26 $m^2 g^{-1}$ in 50 wt% Brij® 56 and 28 $m^2 g^{-1}$ in 60 wt% Brij® 56 at 25 ^{0}C.

This suggests that changing the templating composition does not appear to affect greatly the electrodeposition of Pd, as long as the phase remains the same.

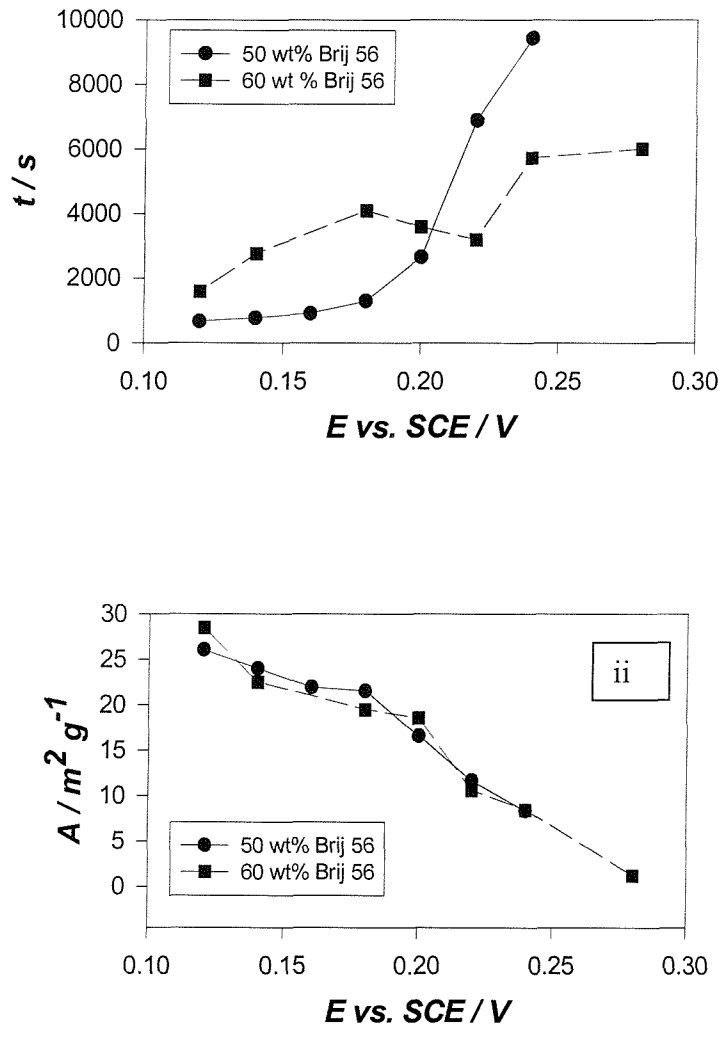

Figure 64 The pair of plots, (i) and (ii), corresponds to the films grown from a templating mixture of Brij 56 and $(NH_4)_2PdCl_4$ (aq) in the ratios 1:1 and 3:2. All potentials were deposition potentials stepped from +0.4 V vs. SCE. Using the same charge density of 2.55 C cm^{-2}, the films were grown on 0.2 mm diameter gold electrodes at 25^{0}C, i.e. in the hexagonal phase. The y-axis is either the deposition time (t) or the Pd specific surface area (A). [error bars for time and for area are about ± 200 s and 1 m^2 g^{-1}]

The same set of experiments was carried out at 55 ^{0}C where the phase of the mixture was cubic.

Deposition potential / V vs. SCE	Deposition time / s	Reduction peak charge / μC	Number of scans	Pd surface area / cm^2	Roughness Factor	Pd specific surface area / $m^2 g^{-1}$
+0.24	949	2.08	252	0.0049	16	0.82
+0.22	672	14.89	12	0.0351	112	5.14
+0.20	515	2.85	90	0.0067	21	1.52
+0.18	305	2.41	83	0.0057	18	1.29
+0.16	134	9.08	54	0.0214	68	4.86
+0.14	139	3.38	56	0.0080	25	1.81
+0.12	134	16.72	71	0.0394	126	8.94

Table 18 Table of acid characterisation of Pd films deposited by potential step from a templating mixture of 50 wt% Brij® 56 and 50 wt% of $(NH_4)_2PdCl_4$ (aq) at 55 ^{0}C, i.e. in the cubic phase. Using the same charge density of 2.55 C cm^{-2}, all potentials were stepped from 0.4 V vs. SCE. The films were grown on 0.2 mm diameter gold electrodes.

Like the hexagonal phase at 25 ^{0}C, Table 18 and Figure 65 show that as the deposition potential became more cathodic at 55 ^{0}C, the deposition time tended to decrease for both templating mixtures.

Figure 65(ii) shows that there is a slight tendency for specific surface area of Pd to increase with more cathodic deposition potentials. However, the increase is not as smooth as in the hexagonal phase, Figure 64(ii).

On the other hand, the order of magnitude in both the deposition time and surface area does not appear to depend strongly on the ratio of surfactant to aqueous solution. For example, for the range of deposition potentials seen here, the shortest deposition time was observed in both mixtures when the potential was stepped from 0.4 to 0.12 V: 134 s in 50 wt% Brij® 56 and 120 s in 60 wt% Brij® 56 at 55 ^{0}C; and the smallest surface area was observed at 0.24 V: 0.8 $m^2 g^{-1}$ in 50 wt% Brij® 56 and 0.7 $m^2 g^{-1}$ in 60 wt% Brij® 56 at 55 ^{0}C. Again, this suggests that changing the templating composition does not appear to affect greatly the electrodeposition of Pd, as long as the phase remains the same.

Furthermore, the results here confirms previous results that deposition in the hexagonal phase took longer and produced greater Pd surface areas than in the cubic phase.

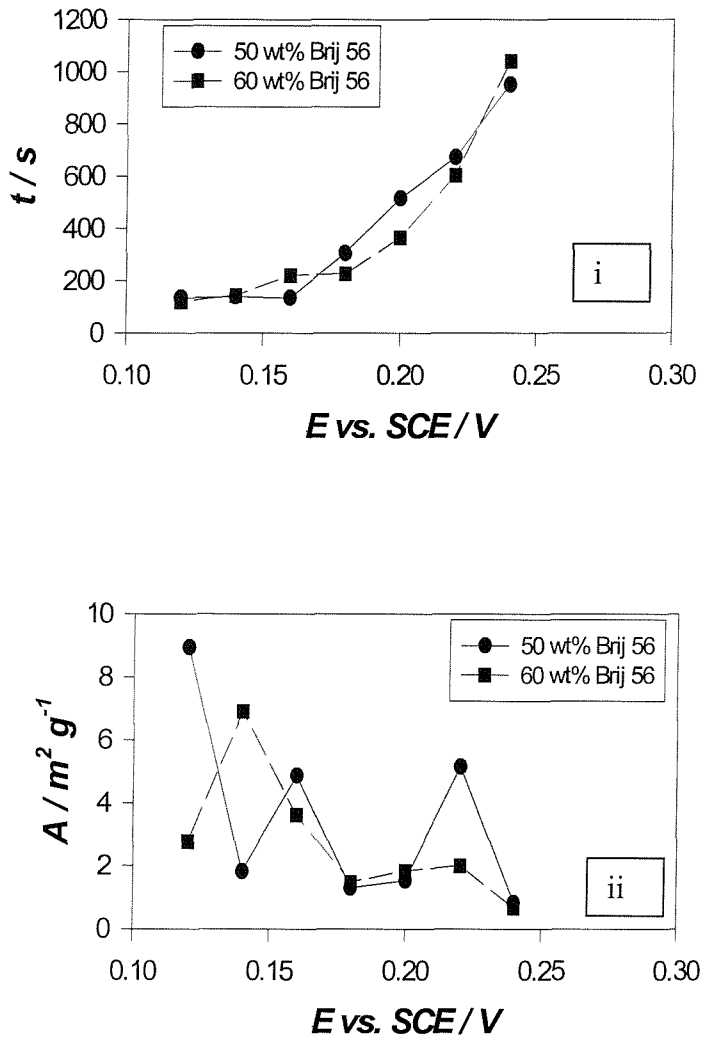

Figure 65 The pair of plots, (i) and (ii), corresponds to the films grown from a templating mixture of Brij 56 and $(NH_4)_2PdCl_4$ (aq) in the ratios 1:1 and 3:2. All potentials were stepped from +0.4 V vs. SCE. Using the same charge density of 2.55 C cm^{-2}, the films were grown on 0.2 mm diameter gold electrodes at 55^0C, i.e. in the cubic phase. The y-axis is either the deposition time (t) or the Pd specific surface area (A), and the x-axis is the deposition potential. [error bars for time and for area are about ± 200 s and 1 m^2 g^{-1}]

5.9 Comparison of Surface Areas

Pd films have been electrodeposited in the presence of Brij® 56 in the hexagonal and cubic phases. The data obtained can be compared with data obtained in $C_{16}EO_8$.[35] For the same charge density of 2.55 C cm^{-2}, the specific surface area of Pd deposited from the hexagonal phase of $C_{16}EO_8$ was 30.3 ± 0.8 m^2 g^{-1} when the film was grown by stepping the potential from 0.4 to 0.1 V at a 1 mm diameter gold electrode. For planar pellistor substrates, SRL 136, 30.4 ± 4.4 m^2 g^{-1} was obtained.

However, both of these values are similar to the values obtained in the hexagonal phase of Brij® 56. For the same charge density, the same potential step in a templating mixture of 60 wt% Brij® 56 and 40 wt% of $(NH_4)_2PdCl_4$ at 25 ^{0}C, where the phase was hexagonal, produced approximately 12.55 ± 0.76 m^2 g^{-1}. This suggested that in the hexagonal phase, electrodeposition of Pd in the presence of Brij® 56 produces a lower specific surface area than in the presence of $C_{16}EO_8$. However, this specific surface area increased to about 28 m^2 g^{-1} when the potential was stepped to 0.12 V.

Specific surface area estimation of electrodeposited Pd has been based on the charge of the reduction peak of PdO during cyclic voltammetry in sulfuric acid, assuming 424 μC cm^{-2} for this process.[179] However, as mentioned previously, this method assumes a (100) plane and Pd is known to contain other planes, which may not have the same charge per unit area.

Surface area estimation of a mesoporous material has also been carried out by BET, Brunauer Emmett Teller method. However, a large amount of material is normally required – a few grams, and this can be difficult to synthesise electrochemically. Differences in surface area have been observed between chemically prepared nanostructured Pt particles and electrochemically prepared nanostructured Pt films.[6] This means that values should only be compared based on one synthesis method.

Although TEM imaging shows some degree of disorder in the Pd samples electrodeposited in $C_{16}EO_8$, it estimates both the pore diameter and wall thickness to be 25 ± 2 Å.[35] Using these, theoretical calculations based on equation 36 give a specific surface area of 39 m^2 g^{-1} assuming a hexagonal geometry.[35]

$$A = \pi\left[\left(1 + {}^{w}/_{d}\right)^{2} \sin 60 - {}^{\pi}/_{4}\right]^{-1} d^{-1}\rho^{-1} \qquad \textbf{Equation 40}$$

where A is the specific surface area ($m^2\ g^{-1}$), w is the thickness (m) of the walls between the nearest pores, d is the pore diameter (m) and ρ is the density ($g\ m^{-3}$) of the material.

This equation is derived from the following equations:

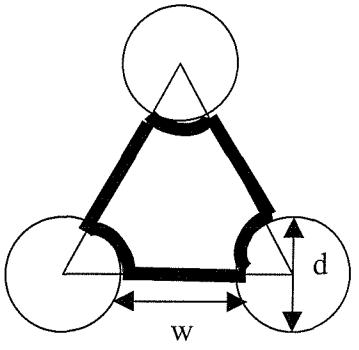

Figure 66 Diagram of circles (representing the pores of the surfactant rods) and triangle (representing the hexagonal geometry) for calculating the area occupied by the water molecules in the pores.

$$area_{triangle} = \frac{1}{2}(base \times height) = \frac{1}{2}\left[(d+w) \times \frac{\sqrt{3}}{2}(d+w)\right] = \frac{\sqrt{3}}{4}(d+w)^2 \qquad \textbf{Equation 41}$$

$$area_{circularoverlap} = \frac{1}{2} \times \pi \frac{d^2}{4} = \frac{1}{8}\pi d^2 \qquad \textbf{Equation 42}$$

$$area_{triangle} - area_{circularoverlap} = \frac{\sqrt{3}}{4}(d+w)^2 - \frac{1}{8}\pi d^2 \qquad \textbf{Equation 43}$$

$$area_{cylinders} = \frac{1}{2}\pi dl \qquad \textbf{Equation 44}$$

$$area_{total} = \frac{1}{2}\pi dl + \frac{\sqrt{3}}{4}(d+w)^2 - \frac{1}{8}\pi d^2 \qquad \textbf{Equation 45}$$

$$mass = volume \times density = \left(\frac{\sqrt{3}}{4}(d+w)^2 - \frac{1}{8}\pi d^2 \right) l\rho$$ **Equation 46**

$$A = area_{total} \div \text{mass} = \frac{\frac{1}{2}\pi dl + \frac{\sqrt{3}}{4}(d+w)^2 - \frac{1}{8}\pi d^2}{\left(\frac{\sqrt{3}}{4}(d+w)^2 - \frac{1}{8}\pi d^2 \right) l\rho}$$

$$\cong \frac{\frac{1}{2}\pi dl}{\left(\frac{\sqrt{3}}{4}(d+w)^2 - \frac{1}{8}\pi d^2 \right) l\rho}$$ **Equation 47**

$$= \frac{4\pi d}{\left(2\sqrt{3}(d+w)^2 - \pi d^2\right)\rho} = \pi \left[\left(1 + {}^{w}/_{d}\right)^2 \sin 60 - {}^{\pi}/_{4} \right]^{-1} d^{-1} \rho^{-1}$$

Therefore, if the Brij® 56 system produces the pore diameter and wall thickness of 25 Å each, then the theoretical calculations based on equation 36 gives a specific surface area of 39 m^2 g^{-1} assuming a hexagonal geometry and assuming 100 % faradaic efficiency.

5.10 Characterisation of Electrodeposited Pd films

5.10.1 Scanning Electron Microscopy (SEM)

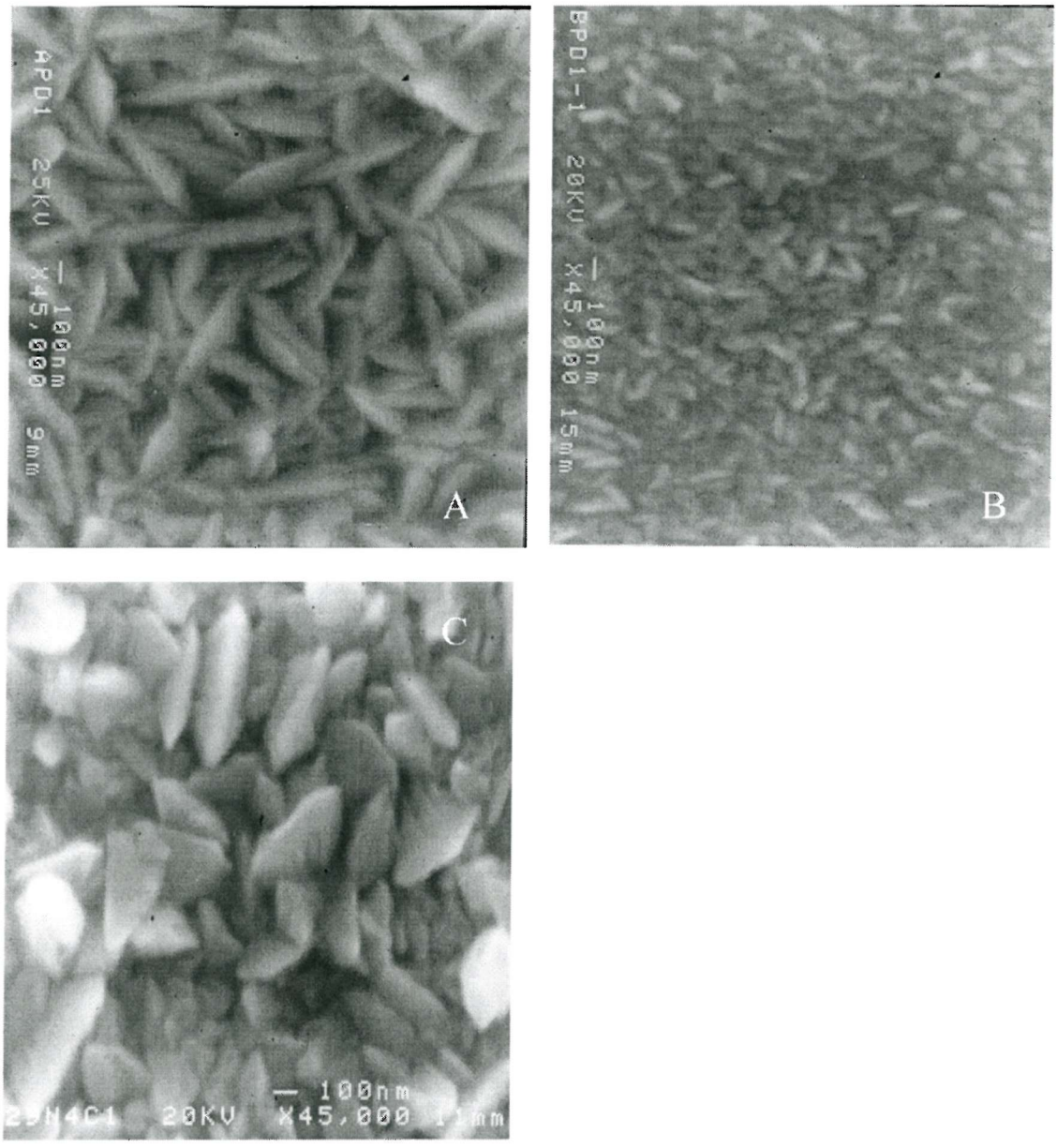

Figure 67 At one magnification of 45 000, SEM photographs of Pd films grown from (A) aqueous $(NH_4)_2PdCl_4$ solution, (B) 60 wt% Brij® 56 and 40 wt% $(NH_4)_2PdCl_4$ solution, i.e. in the hexagonal phase at 25 ^{0}C, and (C) in the cubic phase at 55 ^{0}C. Using one charge density of 2.55 C cm^{-2}, potential step was carried out from +0.4 V vs. SCE to +0.1V.

Pd films were electrodeposited on Au-coated microslides. The construction of these microslides can be found in the experimental section.

In Figure 67, at one magnification of 45 000, the structure of the Pd film formed from aqueous solution adopts a more flake-like structure than that of the Pd film formed from Brij® 56 in the hexagonal phase, for the same charge density of 2.55 C cm^{-2}. The average flake size of the former is estimated at more than 100 nm, whereas it appears to be under 50 nm for the latter film. Figure 67 (C) shows a very different picture, one of Pd film formed from Brij® 56 in the cubic phase, where the average flake size is estimated at about 300 nm.

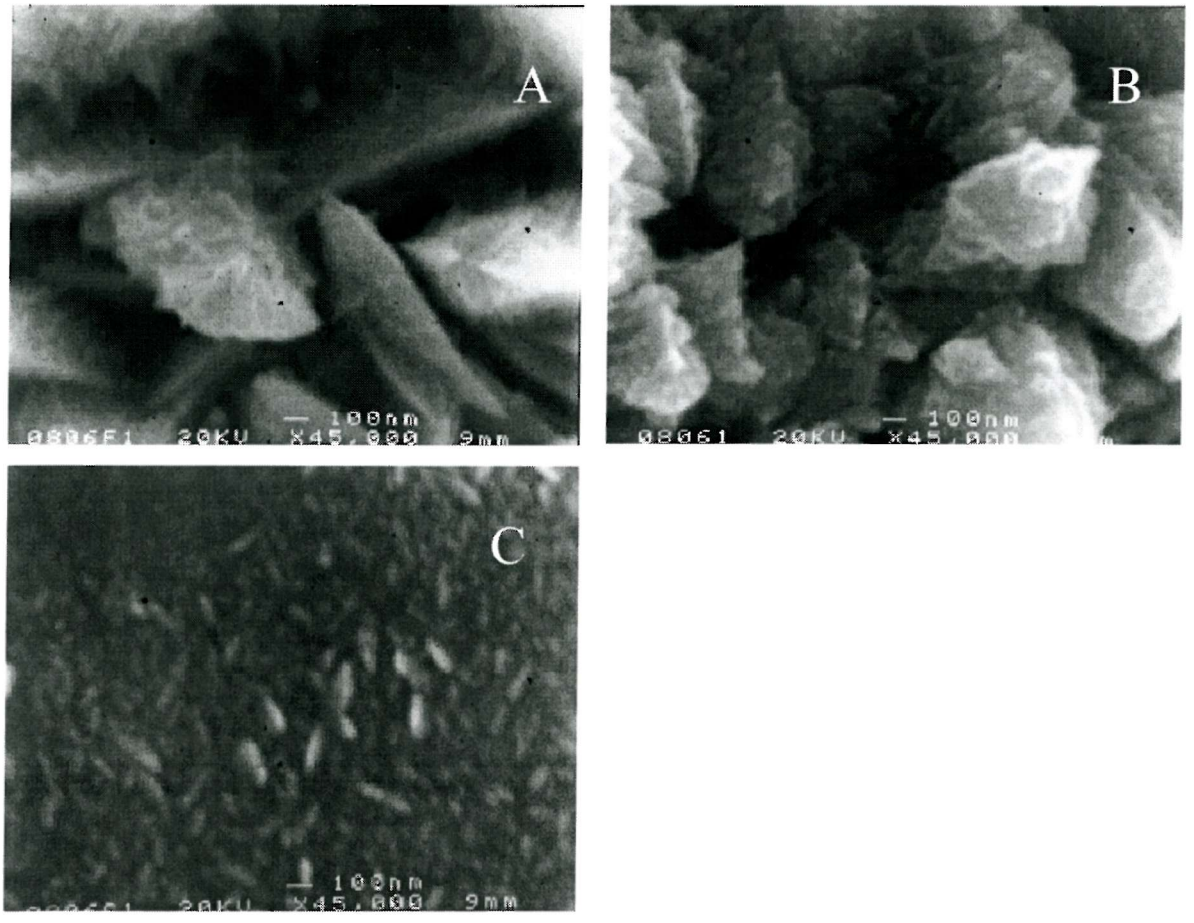

Figure 68 SEM photographs of Pd films grown from 50 wt% Brij® 56 and 50 wt% $(NH_4)_2PdCl_4$ solution at 25 ^{0}C, i.e. in the hexagonal phase. Using the same charge density of 2.55 C cm^{-2}, various potential steps were carried out from +0.4 V vs. SCE to the following potentials: (A) -0.1, (B) -0.15, (C) –0.20.

For Pd films grown from Brij® 56 in the hexagonal phase, Figure 68 shows a collection of Pd films grown as the deposition potential becomes even more cathodic from –0.1 V (A) to –0.2 V (C).

The structures are flake-like as in the previous figure, Figure 67(B). The flake size appears to increase to several hundred nm when the deposition potential became more negative, i.e. –0.1 V (A) and –0.15 V (B). What is also interesting is that the flakes appear to shrink in size at –0.2 V (C). The reason is not clear. What is more important to note is that electrodeposition in the presence of Brij® 56 in the hexagonal phase and in the cubic phase does change the appearance of the Pd film. EDX measurements confirmed all the films prepared from aqueous, hexagonal and cubic systems to be Pd, see Figure 69.

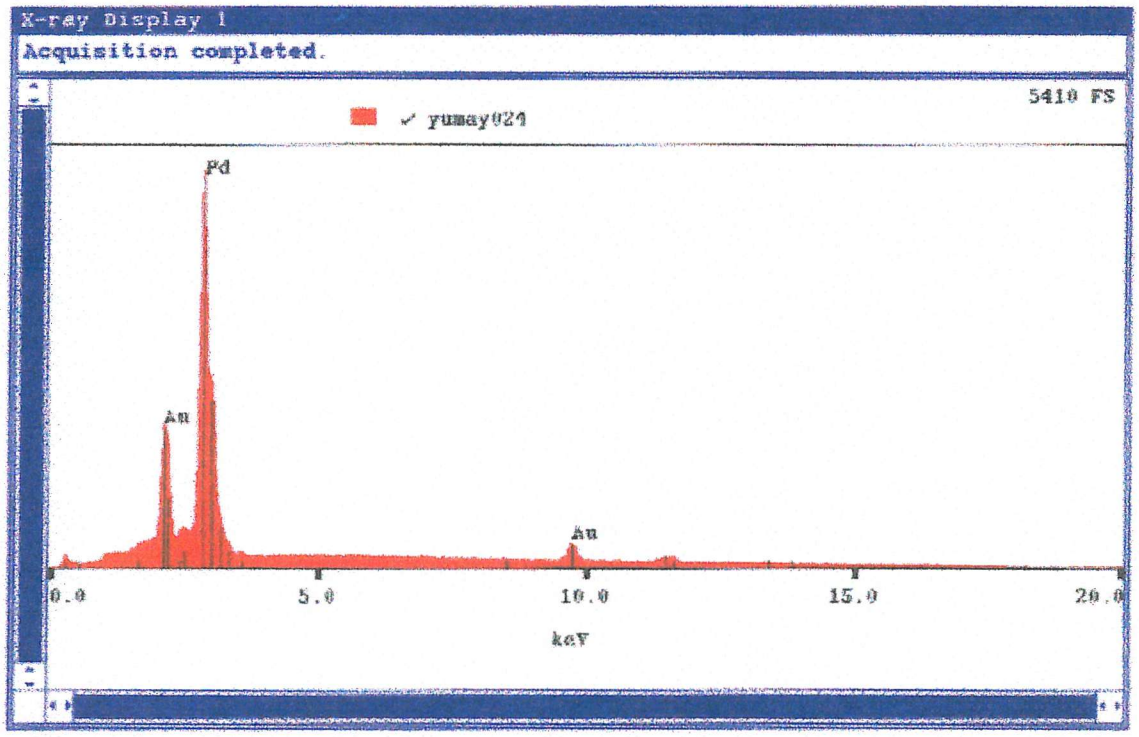

Figure 69 A typical EDX measurement carried out on a Pd sample prepared from 50 wt% Brij® 56 and 50 wt% $(NH_4)_2PdCl_4$ solution at 25 ^{0}C, i.e. in the hexagonal phase. Using the same charge density of 2.55 C cm^{-2}, potential was stepped from +0.4 V to +0.1 V vs. SCE.

5.10.2 Transmission Electron Microscopy (TEM)

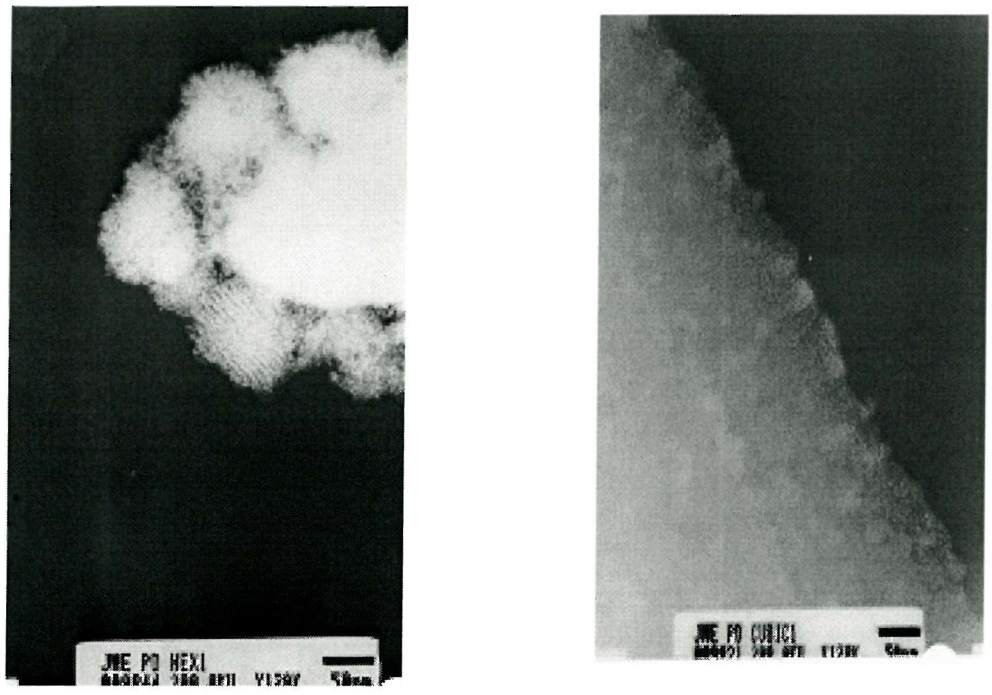

Figure 70 TEM negative on the left is of Pd film electrodeposited from 60 wt% Brij® 56 and 40 wt% $(NH_4)_2PdCl_4$ solution at 25 ^{0}C, i.e. in the hexagonal phase. TEM negative on the right is of Pd electrodeposited in the cubic phase, at 55 ^{0}C. The potential was stepped from +0.4 to +0.1 V vs. SCE.

The mesostructure of Pd films electrodeposited in the lyotropic liquid crystalline phase of a surfactant can be examined by transmission electron microscopy (TEM) imaging. It is a difficult experimental technique, where the loading of the samples can take up to two hours, and once loaded, it takes time to locate porosity, especially mesoporosity. The other drawback is that it takes an experienced eye to distinguish between actual mesostructure and parallel lines which correspond to the crystal orientation known as a Moiré pattern. Thus powder x-ray diffraction tends to be a more favoured method for identifying mesostructure initially, which can then be confirmed by TEM.

Figure 70 shows TEM negatives of Pd films electrodeposited in the hexagonal and cubic phases of Brij® 56. Hexagonal mesostructure is visible whereas in the cubic

phase, there appears to be no ordered structure, only a mesoporous structure. The pictures of the metal films deposited in both the phases seem to confirm hexagonal structure but not cubic structure. The pore diameter was measured to be about 25 Å and the pore wall thickness of the same magnitude. The data match well the pore diameter and wall thickness measured by Guerin in the Pd films electrodeposited in the hexagonal phase of $C_{16}EO_8$.[35]

Figure 71 shows two more TEM negatives, which reveal the hexagonal mesostructure obtained by electrodeposition of Pd from the hexagonal phase of Brij® 56.

Therefore, firstly electrodeposition of Pd can be carried out reproducibly for a lyotropic liquid crystalline phase of surfactant other than $C_{16}EO_8$, i.e. Brij® 56. Secondly, it is possible to obtain hexagonal mesostructure from the Brij® 56, but more experimental work is needed to obtain evidence of transfer of the *Ia3d* cubic mesostructure.

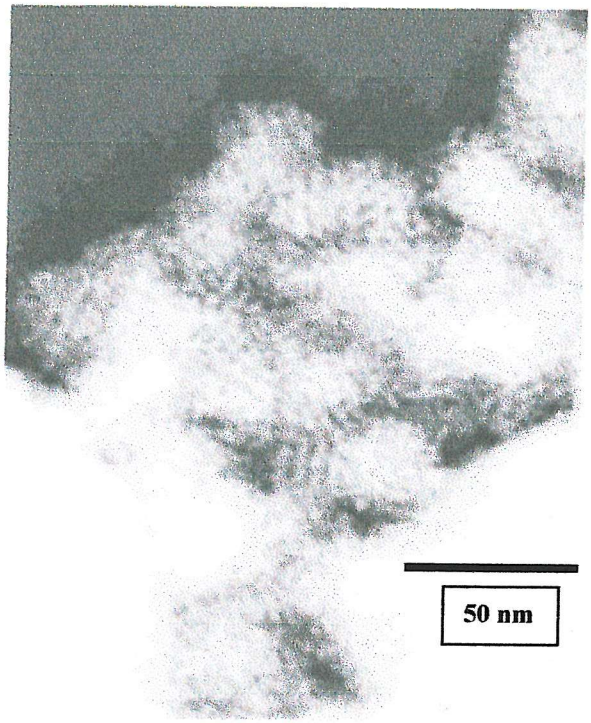

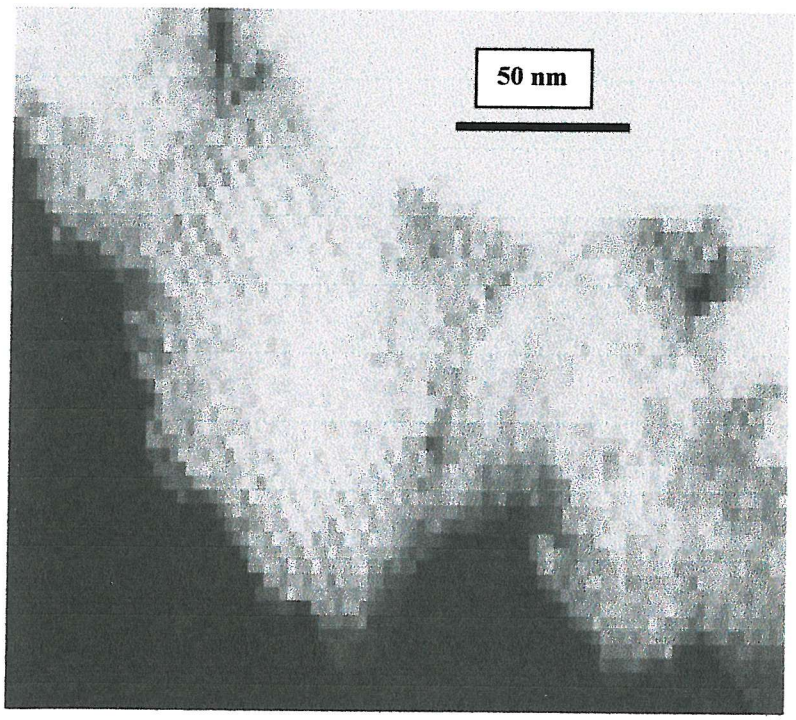

Figure 71 Two TEM negatives of Pd film electrodeposited from 60 wt% Brij® 56 and 40 wt% $(NH_4)_2PdCl_4$ solution at 25 ^{0}C, i.e. in the hexagonal phase. The potential was stepped from +0.4 to +0.1 V vs. SCE.

5.10.3 Powder X-Ray Diffraction

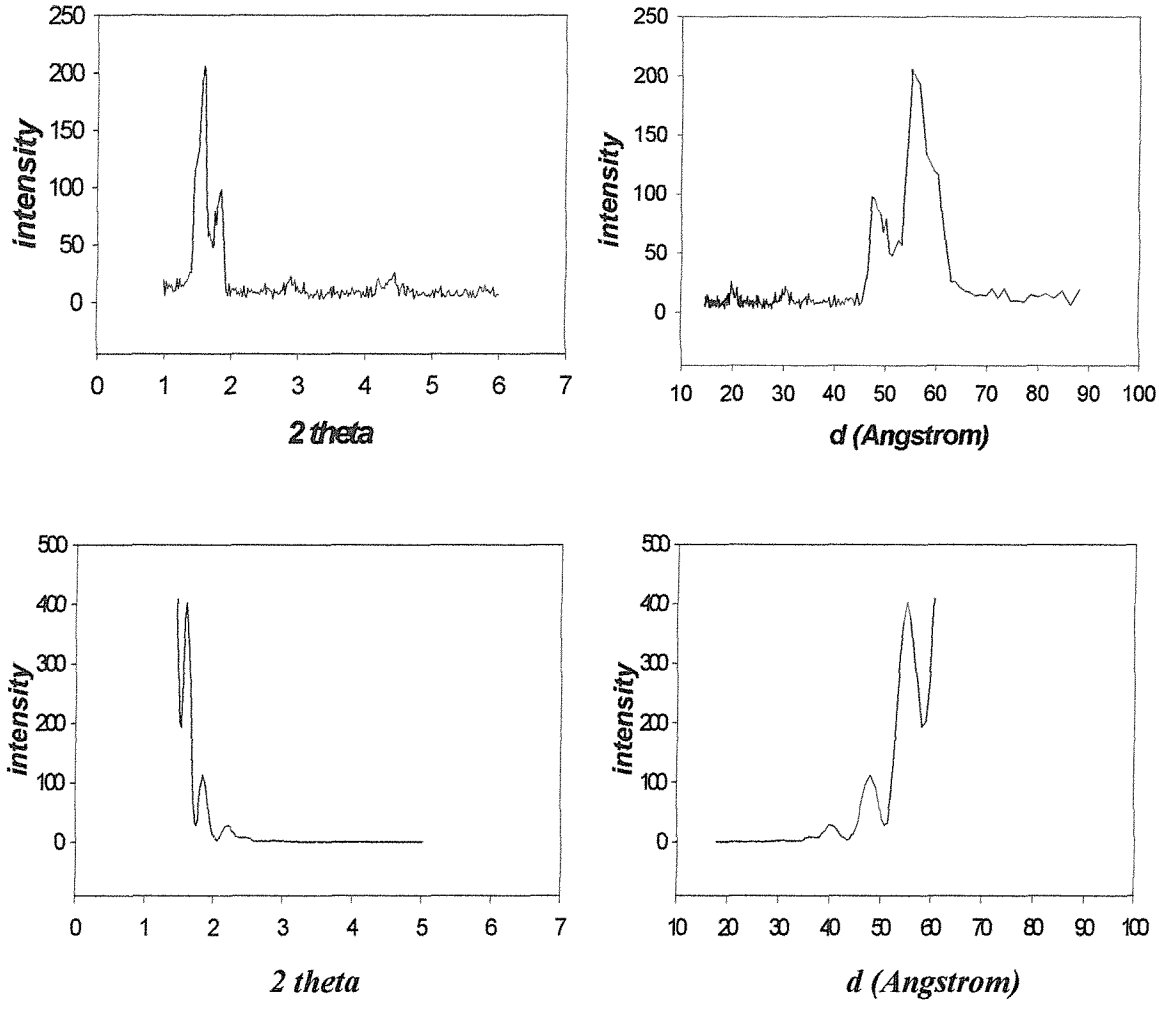

Figure 72 Top and bottom sets of X-ray analysis of Pd film electrodeposited from 50 wt% Brij® 56 and 50 wt% $(NH_4)_2PdCl_4$ solution at 25 ^{0}C, i.e. in the hexagonal phase. The potential was stepped from +0.4 to +0.1 V vs. SCE, based on charge density of 1.36 C cm^{-2}.

Figure 72 is the powder x-ray diffraction analysis of Pd electrodeposited in the hexagonal phase of Brij® 56. Two peaks appear, with the main peak at about 58 Å. This gives further evidence that centre to centre spacing of about 67 Å exist in the Pd film. Therefore, this method can support TEM imaging evidence. This estimates that the pore

diameter and wall thickness are each 33 Å, and theoretical calculations based on these estimate that the maximum specific surface area is 38 $m^2 g^{-1}$.

These values match well the theoretical calculations which give a specific surface area of 39 $m^2 g^{-1}$, when assuming a hexagonal geometry of $C_{16}EO_8$, and assuming both the pore diameter and wall thickness to be 25 ± 2 Å which were estimated by Guerin using TEM technique.[35] Therefore, this supports that Brij® 56 is a suitable alternative for electrodeposition of mesoporous Pd.

When compared to the typical x-ray diffraction pattern in Figure 73 for the hexagonal mesostructure of MCM-41 in the literature,[189] it can be seen that a peak in Figure 72 was obtained near 2-theta value of 2, indicating some evidence of a *100* peak. However, the ratio of peaks is not the same, suggesting some disorder in the Pd films electrodeposited from the hexagonal phase of Brij® 56.

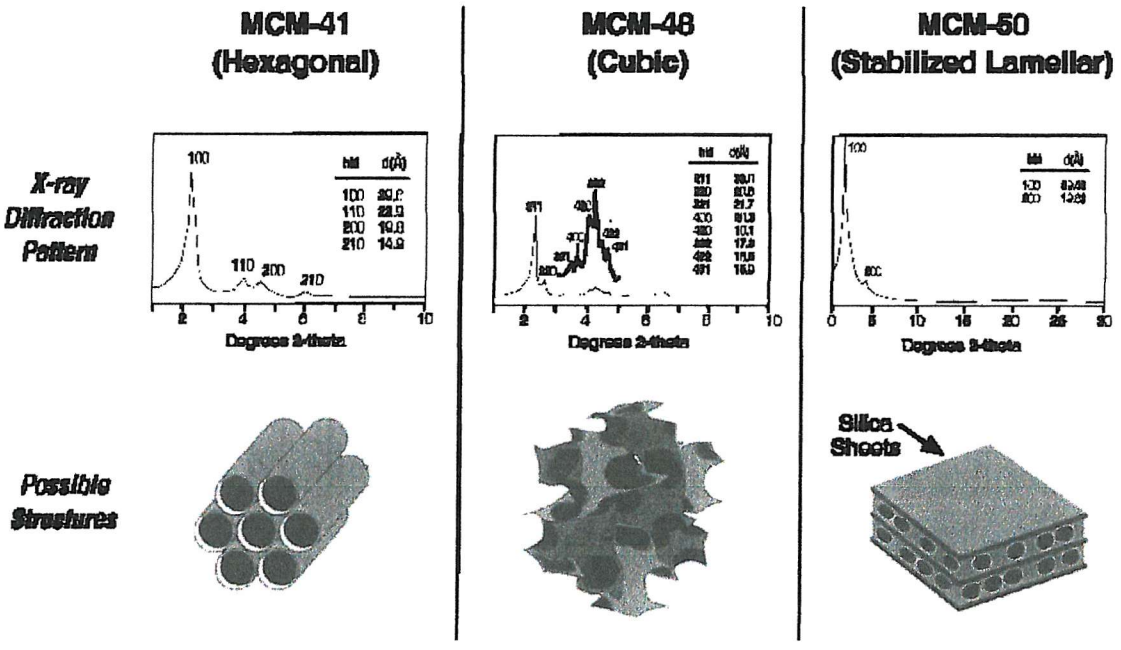

Figure 73 Typical X-ray diffraction pattern for mesoporous MCM silica family, obtained from reference 189.

5.11 Gas Testing

5.11.1 Introduction

Jones described the pellistor as "a miniature calorimeter used to measure the energy liberated on oxidation of a combustible (flammable) gas." [190] In a commercial pellistor, such as those manufactured by City Technology Ltd., a coiled Pt wire is used as a heater and sits embedded in a porous refractory bead (normally alumina) loaded with an active catalyst material made up of precious metals, see Figure 47. The Pt coil heats the bead electrically to its operating temperature, usually about 500 ^{0}C, and is used to detect changes in temperature, i.e. heat, produced by the oxidation of the flammable gas. This changes the resistance of Pt wire, and with enough catalyst, a response can be obtained that is proportional to the amount of the flammable gas in air. For instance, City Technology Ltd. manufactures pellistors with a linear response between 0 and 3 % methane in air.

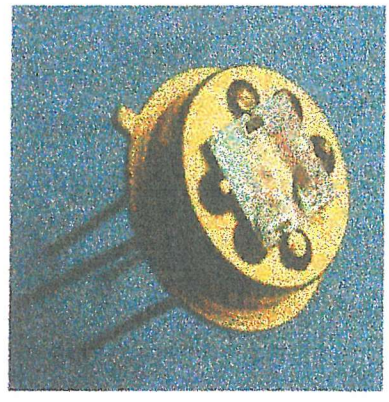

Figure 74 A photograph of the actual SRL 136a pellistor used, where the gold substrate is mounted on a T05 header.[164]

At a certain temperature of about 550 ^{0}C, in the absence of methane, the Pt wire has a certain resistance, which is taken as the reference resistance measurement. In the presence of methane, the catalyst which is Pd, a good catalyst for methane oxidation,[191] will begin to oxidise the methane to water and carbon dioxide, releasing heat. This results in the temperature rise of the pellistor. The resistance of the Pt wire which is embedded in the bead will increases proportionally with temperature. This change in

resistance is measured by a Wheatstone bridge circuit whose output is related to the concentration of the methane in air.

Hence the pellistor is known as a catalytic gas sensor or combustible pellistor gas detectors.

These commercial pellistors consist of a matched pair of elements: the active detector bead containing the catalyst, and a compensating non-active element which is made by treating a plain alumina bead in potassium hydroxide so that oxidation of combustible gas does not occur. The detector bead can detect temperature changes caused by the presence of a flammable gas. The compensator is present only to avoid any false measurement; it helps minimise the baseline drift in the measurement caused by physical changes to pellistors used over several months, since both the detector and compensator should age simultaneously. They are then connected to a Wheatstone bridge circuit in which the bridge supply maintains the detector at the required operating temperature. In addition, the compensator keeps the Wheatstone bridge equilibrated if the temperature, pressure and air flow surrounding the sensors change.

Similarly, in both the SRL 136 and SRL 136a pellistors made by the Department of Engineering, University of Warwick, the microheater is made of Pt and the active catalyst material is the electrodeposited Pd film. The description of both pellistors is below and a photograph of a SRL 136 a pellistor can be seen in Figure 74.

Mesoporous Pd prepared electrochemically from the hexagonal phase of $C_{16}EO_8$ at room temperature appears to improve the performance of pellistors.[35] The Pd films were electrodeposited on SRL 136 substrates, each of which contained a 1 mm^2 Au electrode on top of a Pt micro hotplate or microheater. The electrode was connected to the microheater via a Au strip so that the actual area of electrodeposition is 1.2 mm^2. Au pads linked to the Au strip and the Pt microheater served as electrical connections. Once the films were deposited, the entire SRL 136 substrates plus the films are known as planar pellistors.

Briefly described, they are heatable planar substrates which are low power silicon based devices built by micromachining and photolithographic techniques via a six-mask process.[192] This silicon base is a 380 μm thick Si(100) wafer. Centrally located above this base, a 200 nm thick Pt microheater (heated area of 1x1 mm^2) sits embedded in 500

nm layers of low stress silicon rich silicon nitride (Si_3N_4), which was deposited by low pressure chemical vapour deposition (LPCVD). To alleviate any stress residue in the membrane, 80 nm thermal oxide was deposited before Si_3N_4. Above the Pt microheater is a 300 nm thick Au electrode layer patterned by a lift-off process; the Pt and Au layers were seeded by 10 nm tantalum and titanium layers respectively. A potassium hydroxide anisotropic back-etch helped shape the micromachined membrane (2x2 mm^2), and a special hard-baked photoresist helped protect the interconnects as well as acting as a chemically protective layer. The Au electrode layer served as the working electrode for the electrodeposition of Pd films, which are catalytically active, and the Pt microheater acted obviously as heater and thermometer.

The substrates were glued with epoxy resin onto four-pin Au-plated headers (T05), and electrical connections were made to them by spot welding a 25 μm diameter Au wire between the bond pads and the T05 header contact pads.

5.11.2 The Electrodeposition of Pd on SRL Substrates

5.11.2.1 SRL 136

When the potential was stepped to 0.1 V, Guerin found that the electrodeposition generally took longer in the $C_{16}EO_8$ system than the aqueous system (40 mM $(NH_4)_2PdCl_4$ solution). For example, for a charge density of about 2 C cm^{-2}, the electrodeposition took about 800 ± 250 s in the $C_{16}EO_8$ system, a factor of 3 greater than the aqueous system. Although the shape of the current-time transients was found to be quite reproducible, the small variations observed such as the initial spike in reduction current were attributed to the electrode pretreatment method. Manual polishing with alumina was not possible because of the fragility of the substrates and the thiness of the Au layer; therefore, the cleanliness of the substrates was determined only by cyclic voltammetry in 1 M H_2SO_4 at room temperature.

After depositing Pd films on the SRL 136 substrates, they were soaked in plenty of deionised water for 2 h to remove excess surfactant, i.e. $C_{16}EO_8$. Longer than this would start corroding the headers.

They were then characterised by cyclic voltammetry in 1 M H_2SO_4 at 25 ^{0}C. As mentioned previously, this helped identify the deposited material plus estimate its specific surface area. The same previous experimental conditions were applied (see experimental chapter), and like the 1 mm diameter Au disk electrodes, continuous potential cycling resulted in an increase in the reduction peak; the maximum reduction peak was taken to be the actual specific surface area of Pd. In addition, the voltammograms were reproducible and identical to those corresponding to 0.2 mm diameter Au electrodes, in terms of shape and peak potential. For instance, the reduction peak remained unchanged at 0.5 V, corresponding to Pd deposition.

For a charge density of about 2 C cm^{-2}, the specific surface areas of Pd deposited by stepping the potential to 0.1 V were found to be an average of 30.4 ± 4.4 m^2 g^{-1}. This matched well the average value obtained on the disk electrode, 30.3 ± 0.8 m^2 g^{-1}. Note this assumes a 100 % Faradaic efficiency.

As mentioned earlier in this thesis, the studies carried out by Guerin showed that mesoporous Pd prepared electrochemically from the hexagonal phase of $C_{16}EO_8$ at room temperature appeared to improve the performance of pellistors.[35] The plating salt used was ammonium tetrachloropalladate, $(NH_4)_2PdCl_4$, and was mixed with $C_{16}EO_8$, water and heptane in the correct ratio to produce a dark brown viscous glue-like mixture in the hexagonal phase. However, the studies were restricted to a single set of deposition conditions: that is using one particular surfactant, at one composition, for one choice of Pd salt concentration, at one potential and at a single deposition temperature.

These studies have been expanded in this thesis to examine the effects of variations in the deposition conditions, such as changing the surfactant type and composition, the potential and liquid crystalline phase. Eventually, the obtained conclusions from these results obtained could be applied to the manufacture of better pellistors, i.e. in terms of better sensor performance.

5.11.2.2 SRL 136a

In our work, the same type of Au substrate as SRL 136 was used, and it was known as SRL 136a because these substrates were manufactured from a later production batch which came from mask designs with slight changes. They contained the original micro hotplate design with Au gate, i.e. Au electrode.

These substrates were cleaned in the same way as SRL 136, where manual polishing was not allowed, and the cleanliness of the substrates was determined only by cyclic voltammetry in 1 M H_2SO_4 at room temperature. In addition, like Guerin,[35] the substrates were selected for deposition according to two other factors: there should be no electrical contact between the Au and Pt, and the two contact strips going to the Pt microheater should exhibit room temperature resistances at about and not lower than 100 to 120 Ω.

Here the difference lies in the type of surfactant used, i.e. Brij® 56. Experimental conditions were kept the same. Pd films were electrodeposited in the hexagonal phase of Brij® 56 via the same potential step.

Figure 75 shows a selection of typical deposition current-time transients of SRL 136a, where the potential was stepped to 0.1 V for a charge density of 2.55 C cm^{-2}. The deposition times appear to vary between 1000 and 3000 s, and this is probably due to the "bubble" effect. The initial spike in reduction current can reach between -15 and -35 μA, and the plateau can rise to about -10 μA. This potential step of 0.1V was chosen to compare like data with the data obtain by Guerin.[35]

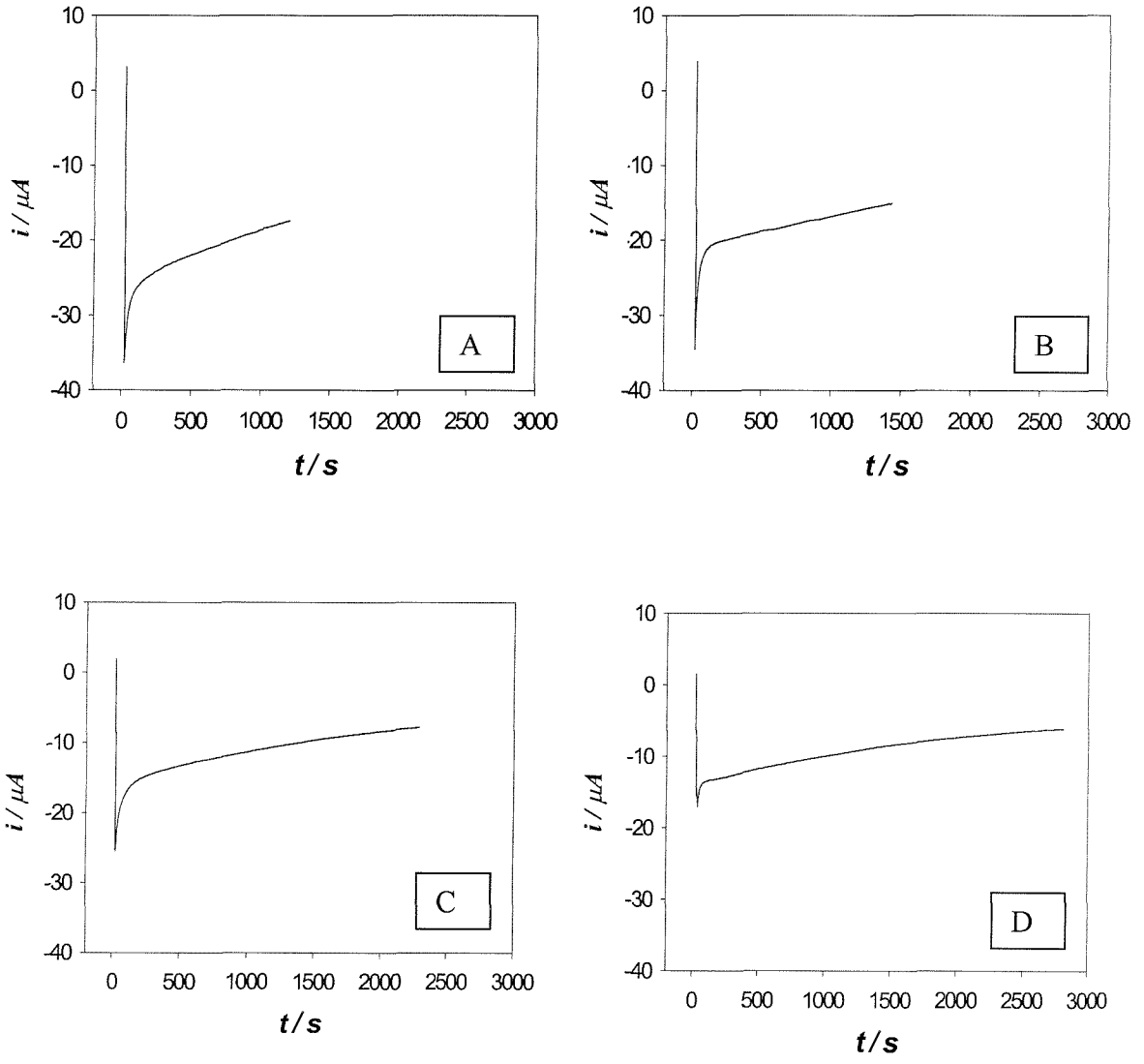

Figure 75 Typical electrodeposition of Pd films from a templating mixture of 50 wt% Brij® 56 and 50 wt% of 1.06 M $(NH_4)_2PdCl_4$ (aq) at 25 ^{0}C. Using the same charge density of 2.55 C cm^{-2}, the potentials were stepped from 0.4 to 0.1 V vs. SCE. The films were grown on SRL136a substrates (1 mm^2 diameter Au electrodes).

Label	Q_{dep} / mC	t_{dep} / s	Reduction peak charge / μC	Number of scans in acid	Pd area / cm^2	Roughness factor	Pd surface area / $m^2\ g^{-1}$
a	25.5	2267	1471	43	3.47	347	24.7
b	25.5	2443	1004	49	2.37	237	16.8
c	25.5	2078	1280	61	3.02	237	21.5
d	21.9	10211	1193	5	2.81	302	20.0
e	25.5	2051	830	51	1.96	196	13.9
f	25.5	5205	1669	73	3.94	196	28.1

Table 19 Summary of data of SRL 136a pellistors *cycled in acid*. These pellistors were later sent for gas testing; this table corresponds to Table 20. Q_{dep} and T_{dep} are the deposition charge and time respectively. The Pd films were electrodeposited from a templating mixture of 50 wt% Brij® 56 and 50 wt% of 1.06 M $(NH_4)_2PdCl_4$ (aq) at 25 ^{0}C. The potentials were stepped from 0.4 to 0.1 V vs. SCE.

Table 19 shows data obtained on SRL 136a pellistors cycled in acid, which were later sent for gas testing, described below. The Pd specific surface areas appear reproducible in terms of order of magnitude, with an average of 20.8 $m^2\ g^{-1}$.

5.11.3 Gas Testing

Two batches of pellistors were prepared for gas testing application: Table 20 summarises the data for the batch characterised in 1 M H_2SO_4 and Table 21 summarises the data for the batch that was not.

The gas testing and analysis were carried out by Stéphane Leclerc at City Technology Ltd. The experimental rig and the procedure are briefly described here.

The rig is made up of the gas handling part which controls the concentration and the flow of the gases, and the Wheatstone bridge along with the electronics. The latter controls the operating temperature of the pellistors and records any changes taking place.

The gases used were compressed air and 2.5 % methane in air, supplied by BOC Special Gases, and work was carried out in the fumehood.

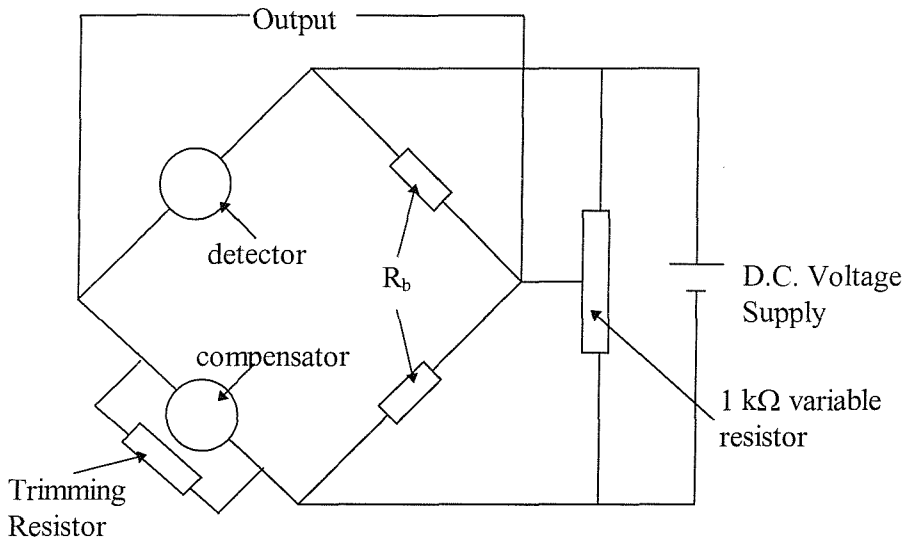

Figure 76 Diagram of the Wheatstone Bridge used.[35]

A typical DC Wheatstone bridge measured the response of the pellistors to the gases. The Wheatstone bridge records the voltage across the detector and the flow of the gases.

The detector was the device, i.e. the pellistor. The Wheatstone bridge also included the active and passive arm resistances. The active arm resistance was made up of two resistors, known as the balance resistors, R_b. In Figure 76, 1 kΩ variable resistor was replaced by a fixed 2 kΩ resistor known as the passive arm resistance. In the case of commercial pellistors, a trimming resistor was put in parallel with the compensator as in Figure 76. In the case of the planar pellistors prepared in our work, the trimming resistor and compensator were replaced by a fixed resistor equal to R_b.

The experimental procedure consisted of the following:

- The cold resistance of each pellistor was initially measured by a voltmeter.
- The Wheatstone bridge was then set at zero mV, so that the active and passive arm resistances were the same
- For each voltage across the pellistor, e.g. 6 V, the gas flow consisted of 5 min air, 5 min 2.5 % methane, and 5 min air.

At a given voltage, sensitivity was measured as change in bridge output (mV per 2.5 % methane). A good Wheatstone bridge should give maximum output sensitivity for minimum power consumption, where most of the power will be consumed by the pellistor and very little is drawn by the resistors.

Pd film was deposited on each SRL 136a substrate via a potential step from 0.4 to 0.1 V, from a templating mixture of 50 wt% Brij® 56 and 50 wt% of 1.06 M $(NH_4)_2PdCl_4$ (aq) at 25 ^{0}C. The deposition charge passed was 25.5 mC, giving a charge density of 2.55 C cm^{-2}. After deposition, these samples are known as SRL 136a pellistors.

Like the work of Guerin,[35] the effect of characterising these pellistors in 1 M H_2SO_4 (i.e. cyclic voltammetry between –0.2 and 1.2 V at 200 mV/s) was studied for gas testing application. Therefore, two batches of pellistors were prepared for gas testing application: Table 20 summarises the data for the batch characterised in 1 M H_2SO_4 and Table 21 summarises the data for the batch that was not.

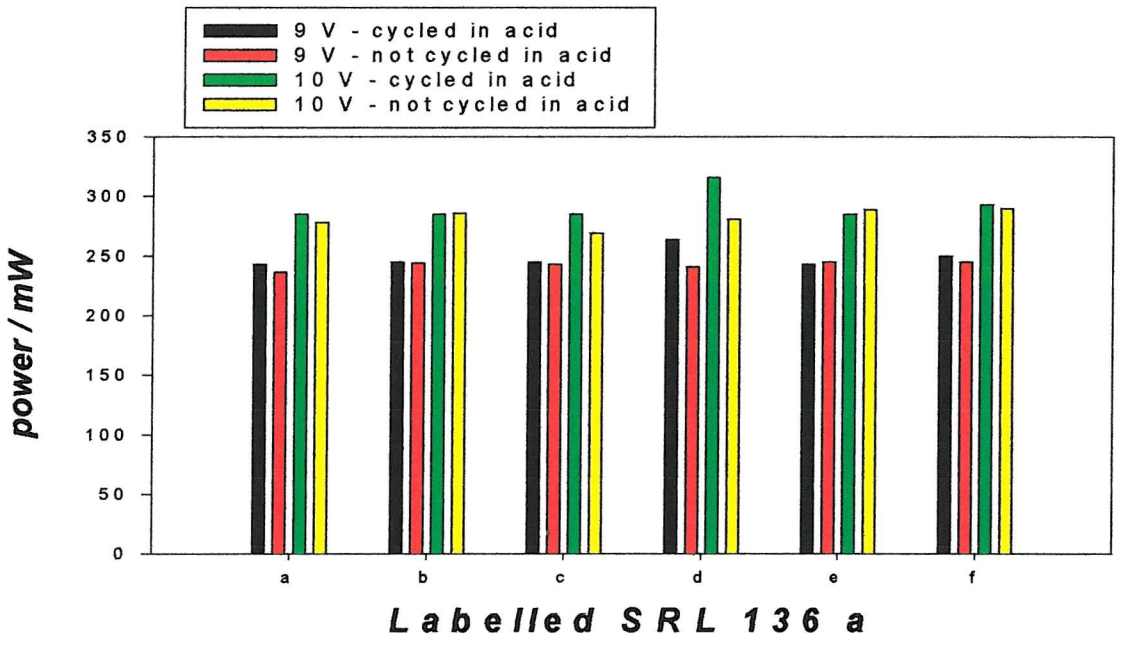

Figure 77 Histograms showing the power consumed at higher applied device voltages of 9 and 10 V by SRL 136a pellistors containing Pd films cycled and not cycled in 1 M H_2SO_4. These data were taken from Table 20 and Table 21.

Label	Q_{dep} / mC	T_{dep}/ s	Cold R / Ω	V_{device}/ V	R_{bal} / Ω	Arm R_{active} / Ω	% I in Arm	Power Supply I / mA	Sensitivity / mV per 2.5% CH_4	Power / mW
a	25.5	2267	171	6	290	580	77.5	27	10	125
				7	292	584	77.4	30	8	162
				8	294	588	77.3	33	17	204
				9	298	596	77.0	35	40	243
				10	300	600	77.0	37	40	285
b	25.5	2443	170	6	288	576	77.6	27	15	126
				7	300	600	77.0	30	21	161
				8	320	640	76.0	32	30	197
				9	285	570	77.8	35	30	245
				10	300	600	77.0	37	27	285
c	25.5	2078	170	6	285	570	77.8	27	10	127
				7	300	600	77.0	30	17	162
				8	290	580	77.5	33	30	204
				9	285	570	77.8	35	29	245
				10	300	600	77.0	37	31	285
d	21.9	10211	128	9	298	496	77.1	38	41	264
				10	300	600	77.0	41	25	316
e	25.5	2051	170	9	298	596	77.0	35	12	243
				10	300	600	77.0	37	9	285
f	25.5	5205	105	9	298	596	77.1	36	54	250
				10	300	600	77.0	38	79	293

Table 20 Summary of data of SRL 136a pellistors *cycled in acid*. Q_{dep} and T_{dep} are the deposition charge and time respectively; cold R is the cold resistance; V_{device} is the voltage across the device; R_{bal} is balance resistance; Arm R_{active} and $R_{passive}$ are the active and passive arm resistances respectively where the latter is 2 kΩ; % I in Arm is the percentage current in active arm, 1 – [R_{bal}/(R_{bal}+1 kΩ)]; and Power Supply I is the power supply current. The Pd films were electrodeposited from a templating mixture of 50 wt% Brij® 56 and 50 wt% of 1.06 M $(NH_4)_2PdCl_4$ (aq) at 25 ^{0}C. The potentials were stepped from 0.4 to 0.1 V vs. SCE.

Label	Q_{dep} / mC	T_{dep}/ s	Cold R / Ω	V_{device}/ V	R_{bal} / Ω	Arm R_{active} / Ω	% I in Arm	Power Supply I / mA	Sensitivity / mV per 2.5% CH_4	Power / mW
a	25.5	1414	171	6	300	600	77.0	27	15	124
				7	310	620	76.3	30	21	158
				8	330	660	75.2	32	30	193
				9	340	680	74.6	35	38	236
				10	360	720	73.5	38	40	278
b	25.5	1185	167	6	296	492	77.2	25	15	116
				7	298	596	77.0	28	20	151
				8	300	600	77.0	33	27	203
				9	300	600	77.0	35	35	244
				10	305	610	76.6	37	40	286
c	25.5	2786	164	9	300	600	77.0	35	27	243
				10	299	598	77.0	35	-	269
d	29.4	2458	105	9	299	598	77.0	35	30	241
				10	300	600	77.0	37	39	281
e	26.0	32	131	9	330	660	75.2	36	25	245
				10	335	670	74.9	39	38	289
f	30.0	104	132	9	329	658	75.3	36	12	245
				10	340	680	74.6	39	33	290
g	30.0	29	157	9	332	664	75.1	36	24	245
				10	340	680	74.6	39	28	290
h	26.2	3042	164	9	298	596	77.1	35	30	243
				10	300	600	77.0	37	34	283
i	26.3	5218	142	9	300	600	77.0	36	10	249
				10	346	692	74.3	38	15	285

Table 21 Summary of data of SRL 136a pellistors *not cycled in acid*. Q_{dep} and T_{dep} are the deposition charge and time respectively; cold R is the cold resistance; V_{device} is the voltage across the device; R_{bal} is balance resistance; Arm R_{active} and $R_{passive}$ are the active and passive arm resistances respectively; % I in Arm is the percentage current in active arm, $1 - [R_{bal}/(R_{bal}+1\ k\Omega)]$; and Power Supply I is the power supply current. The Pd films were electrodeposited from a templating mixture of 50 wt% Brij® 56 and 50 wt% of 1.06 M $(NH_4)_2PdCl_4$ (aq) at 25 ^{0}C. The potentials were stepped from 0.4 to 0.1 V vs. SCE. The labels correpond to each SRL 136a substrate.

For the charge density of 2.55 C cm^{-2}, the data on the substrates can be compared.

The sensor performance of the SRL 136a pellistors can be evaluated based on the power consumed and the sensitivity to exposure of methane gas, where it is more favourable to have as low a power consumption as possible and as high sensitivity to gas exposure as possible. The Pd films were electrodeposited from a templating mixture of 50 wt% Brij® 56 and 50 wt% of 1.06 M $(NH_4)_2PdCl_4$ (aq) at 25 ^{0}C. Using the same charge density of 2.55 C cm^{-2} as on the gold disk electrodes, the potentials were stepped from 0.4 to 0.1 V vs. SCE. The films were grown on SRL136a substrates (1 mm^2 diameter Au electrodes).

When comparing pellistors containing Pd films which have already been characterised by cyclic voltammetry in sulfuric acid, the power consumption appears very reproducible across the range of applied device voltages, see Figure 78. This appears true even at higher applied device voltages, such as 9 and 10 V, as seen in Figure 77. For the range from 6 to 10 V, the power consumption increased from a minimum of about 125 mW to a maximum of approximately 300 mW, as the temperature of the hot plates, and thus the heat losses, increases.

This is also observed for pellistors containing Pd films not characterised in acid. What these results show is that the performance of these SRL 136a pellistors is not visibly affected by dipping in sulfuric acid and by carrying out cyclic voltammetry in the acid. Note, as mentioned previously, this acid characterisation helped identify the deposited material plus estimate its specific surface area.

As expected, the power consumption increased with the applied device voltage by approximately 50 mW per V.

For voltages applied across the substrates, ranging from 6 to 10 V, both tables show a broad scatter, such as the sensitivity measured as output (mV per 2.5 % methane) as at a given voltage for exposure time and the power drain, see Figure 79. Figure 77 shows the scatter more clearly in histograms plotting power consumption for the substrates cycled and not cycled in acid at 9 and 10 V. Based on the same range of applied device voltage, the sensitivity output increased from a minimum of 10 mV to a maximum of 40 mV. This was observed both for pellistors containing Pd films characterised and not characterised in sulfuric acid, again showing that the sulfuric acid

treatment had no significant effect. As for the power consumption, the greater the applied device voltage, the greater the sensitivity to exposure to methane gas.

The power shown in both tables in mW relates to the power consumption of the substrates in 2.5 % methane. It is equivalent to the product of the voltage across the device in volts, the power supply current measured and the % current in the active arm. For instance in Table 20, at 6 V, the substrate labelled a consumed 6 V x 27 mA x 77.5 %, equivalent to about 125 mW. The scatter can be seen when the voltage was applied at 9 V across the pellistors characterised in acid for example: the power ranges from 243 to 264 mW in Table 20.

At 10 V, scatter can also be observed in sensitivity, measured ranging from 9 to 79 mV for SRL 136a pellistors cycled in acid, see Table 20, and from 15 to 40 mV for those *not* cycled in acid, see Table 21.

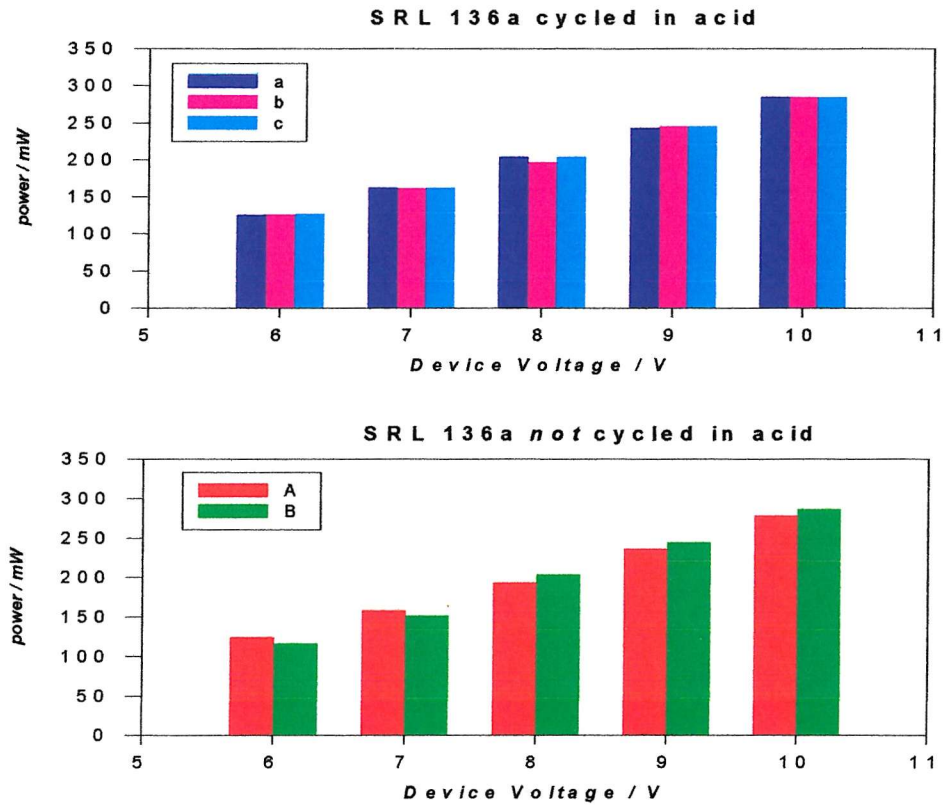

Figure 78 Histograms showing the power consumed by SRL 136a pellistors containing Pd films cycled and not cycled in 1 M H_2SO_4 versus the applied device voltage. These data were taken from Table 20 and Table 21, where a, b, c and A, B refer to different pellistor structures.

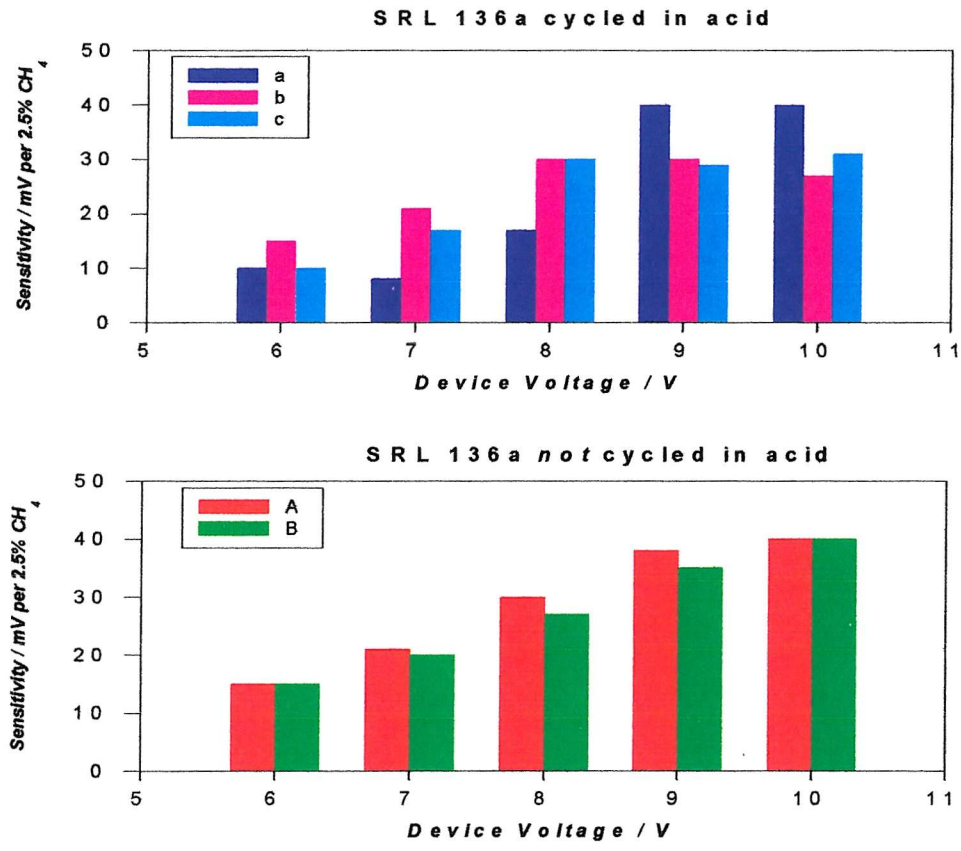

Figure 79 Histograms showing the sensitivity in mV per 2.5% methane by SRL 136a pellistors containing Pd films cycled and not cycled in 1 M H_2SO_4, where a, b, c and A, B refer to different pellistor structures. These data were taken from Table 20 and Table 21.

Hence, a more general and qualitative analysis is more applicable, such as the comparison between these pellistors and the SRL 136 ones studied by Guerin.[35]

Firstly, comparing the effect the of acid characterisation, our pellistors appear to exhibit lower sensitivity than those studied by Guerin. The latter type showed an average sensitivity or output of 138 ± 0.1 mV. This high sensitivity was observed at a lower applied voltage across the device, i.e. 5.5 V. In our case, the maximum seen was 79 mV at 10 V.

Note Guerin has obtained negative sensitivity values, i.e. when the SRL 136 pellistors were not characterised in acid (the applied voltage across the device was 5.5 V). This suggests a drop in the pellistor temperature. This cooling effect was seen in the case of pellistors containing non-mesoporous Pd films (i.e. deposited in the aqueous system). These results seem to imply that acid characterisation promotes good catalytic activity for the oxidation of methane. This was confirmed when the cooling effect occurred in pellistors which were bare of Pd films. The cooling effect was also obtained by Gardner and coworkers at University of Warwick when carrying out tests on the thermal properties of SRL 136 substrates.[35]

The negative sensitivity values suggesting a decrease in pellistor temperature can be explained in the following way. Methane is a better thermal conductor than air: their thermal conductivities are 342 and 260 $\mu J\ s^{-1}\ cm^{-1}\ ^0C$ respectively at 26.7 ^0C, and 374 and 276 $\mu J\ s^{-1}\ cm^{-1}\ ^0C$ respectively at 48.9 ^0C.[193] As the temperature increases, the difference in the thermal conductivities increases. The methane molecule thus removes more heat from the pellistor than the molecules in air, especially at higher temperatures, and the applied voltage of 5.0 V was found by Guerin to correspond to almost 500 ^0C. When air was flowed instead of methane, zero sensitivity was always recorded on both the SRL 136 and 136a pellistors to set calibration. The oxidation of methane to water and carbon dioxide releases heat, giving positive values of sensitivity. Negative values mean that the methane was not oxidised, either enough or at all, i.e. no catalytic activity.

The lower sensitivity seen in our case compared to the SRL 136 pellistors used by Guerin could mean greater power consumption (see Figure 81), but more experiments should be done. In our case, at 6 V, the average power consumed was 126 mW on SRL 136a pellistors characterised by acid and 120 mW on those that were not. At 5.5 V, the SRL 136 pellistors used by Guerin have been measured by City Technology Ltd. at about 165 mW, and by C. Lloyd at University of Warwick at about 117 mW.[35]

The sensor performance of the Pd pellistors is known to depend on the substrate design, e.g. the platinum heater design and the catalyst (the surface area) will both affect the sensitivity of the output in mV per 2.5 % methane gas. There are several complicating factors.

As previously mentioned, both the SRL 136 and SRL 136a pellistors, used by Guerin and the present author respectively, contained the same type of Au substrate. The reason for the slightly different labelling of our pellistors was due to processing, i.e. these SRL 136a substrates were manufactured at a later date and came from the same mask design with slight changes. They contained the original micro hotplate design with Au gate, i.e. Au electrode. In addition, these SRL 136a substrates were cleaned in the same way as SRL 136, where manual polishing was not allowed, and the cleanliness of the substrates was determined only by cyclic voltammetry in 1 M H_2SO_4 at room temperature.

These SRL 136a pellistors contained the same platinum heater design as the SRL 136 pellistors used by Guerin. Therefore, in principle, the heater resistances of the pellistors should be the same, but in practice, the cold resistances were measured to be different for any given device voltage. This in turn contributes to the differences observed in the temperature of the pellistors. Thus, there was evident variation among our SRL 136a substrates, which was also observed by Guerin when studying the SRL 136 pellistors; note his pellistors were from the first batch of production by Warwick University, and Guerin selected the most sensitive pellistors for his early studies.[35]

In addition, during gas testing, when methane gas flows over the Pd catalyst on a pellistor, the oxidation of methane generates heat. The rate of reaction of methane on the catalyst depends on the temperature and on the "quality" of the catalyst. The temperature of the catalyst depends on the applied device voltage and the heat losses over the substrate; i.e. the temperature is determined by the balance of heat input by electrical heating and methane reaction, plus the heat losses by conduction, convection and radiation. This means that the sensitivity of a pellistor to exposure to methane depends on the size of the temperature rise caused by methane reaction, which in turn is determined by the rate of methane reaction (on the catalyst) and the rate of heat conduction (which is determined by substrate design), see Figure 80.

Thus, the sensitivity we measure at any given applied voltage is not just a reflection of the quality of the Pd catalyst but depends on the substrate design. The SRL 136 and SRL 136a pellistors are slightly different as shown by measurement of the cold

resistances. Here a direct comparison of the sensitivities between the two is not simply a comparison of catalytic activity.

Another factor affecting sensitivity is the deposition conditions of the Pd catalyst, which affect the quality of the catalyst, e.g. the surface area.

Therefore, it is always important to measure the cold resistance of a substrate for proper comparison. As seen in the histograms in Figures 77 to 79, the power consumption should not depend on the physical structure of the Pd film, i.e. cycling in acid or not, but depends much more on the substrate design.

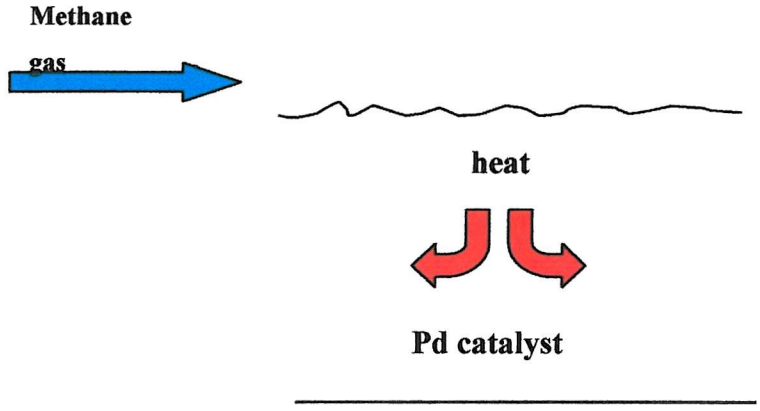

Figure 80 Diagram of the flow of methane gas over the Pd catalyst on a pellistor, showing the heat generated from the oxidation of methane.

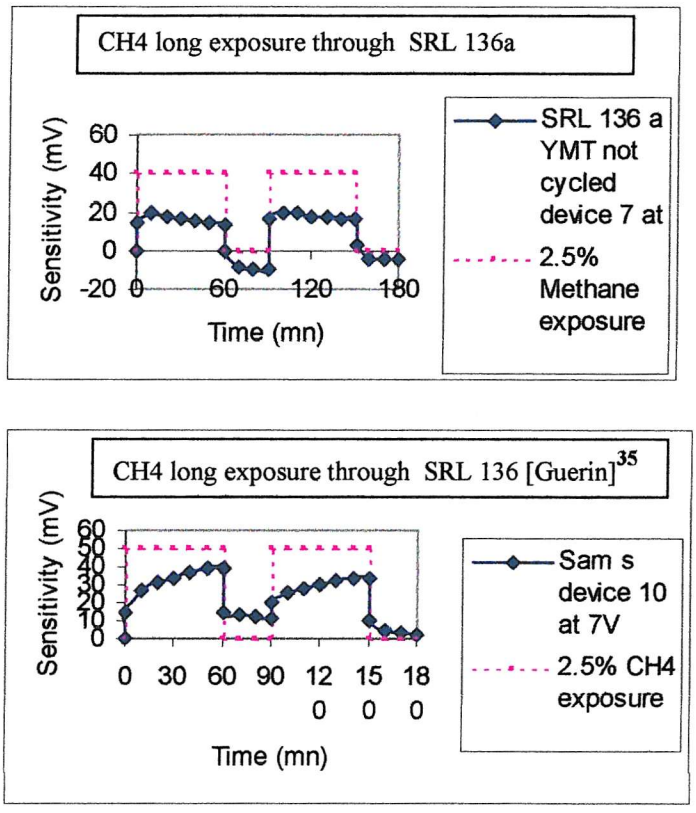

Figure 81 Two samples of the sensitivity responses to 2.5 % methane exposure.[194]

Compared to the commercial pellistors, for a 0.001 inch diameter high-purity Pt wire, operating in a 2 V Wheatstone bridge consumes 175 mA sensor current; thus the power drain is about 350 mW, which is approximately half the value at double the diameter of the Pt wire.[190] Current consumption or power drain of a pellistor decreases when the wire diameter reduces, but further reduction in wire diameter can lead to unreliability because of the lack of wire strength. The power drain values in our case, the SRL 136a pellistors, are lower, thus suggesting greater sensitivities.

As mentioned previously, it is difficult to make quantitative interpretations because of the scatter in the data and more experiments are needed. However, what can be inferred is that electrodeposition of Pd in the hexagonal phase of Brij® 56 was possible on SRL 136a pellistors, and exposing them to methane, whether the pellistors were characterised in acid, showed evidence of sensitivity.

5.12 Overall Summary

The addition of a surfactant, i.e. Brij® 56, gives greater specific surface areas of Pd and longer deposition times than the aqueous system, confirming that electrodeposition in a liquid crystalline phase increases the surface area of a metal.[2] Moreover, there is a significant cathodic shift in potential, with the plateau current only observed in the aqueous system.

Electrodeposition in the hexagonal phase actually required longer deposition times and gave greater surface areas than in the cubic phase, see Table 22. This is surprising because the cubic system is believed to contain a 3-d network, and the cubic pore geometry had been predicted to give the largest surface area of Pd.

System	Time of deposition / s	Pd specific surface area/ $m^2 g^{-1}$
aqueous	189	1.23
hexagonal	1587	28.48
cubic	120	2.76

Table 22 Table of acid characterisation of Pd films deposited by potential step in three systems. Using the same charge density of 2.55 C cm^{-2}, all potentials were stepped from 0.4 to 0.12 V vs. SCE. The films were grown on 0.2 mm diameter gold electrodes.

Similarity in the order of magnitude has been observed in the deposition times and in the specific surface areas of Pd for two different potential steps at two temperatures in the Brij® 56 system. This appears to be a sensitivity test, where a small change in potential and temperature can give a substantial effect. It is not clear whether the effects described are the result of temperature or phase change, but it is clear that they are the result of the presence of a surfactant. More experiments are needed.

Experiments on reproducibility and repeatability showed that within one Brij® 56 mixture at 25 ^{0}C, the deposition times and the specific surface areas appeared reasonably repeatable. This was less clearly seen when comparing three replicate mixtures.

Changing the templating composition does not appear to affect greatly the electrodeposition of Pd, as long as the phase remains the same. This effect is also

observed at 55 ^{0}C, where the phase is cubic. For example, when the potential was stepped to 0.12 V, the specific surface areas obtained were 26 m^2 g^{-1} in 50 wt% Brij® 56 and 28 m^2 g^{-1} in 60 wt% Brij® 56 at 25 ^{0}C.

A fundamental electrochemical study of mesoporous Pd was not the purpose of this chapter; the purpose was to find the conditions suitable to deposit Pd on pellistors for comparison with the data obtained in $C_{16}EO_8$ by Guerin.[35] These pellistors were later sent for gas testing. Comparisons between the two surfactants were made. For the same charge density of 2.55 C cm^{-2}, the specific surface area of Pd deposited from the hexagonal phase of $C_{16}EO_8$ was 30.3 ± 0.8 m^2 g^{-1} when the film was grown by stepping the potential from 0.4 to 0.1 V at a 1 mm diameter gold electrode; for planar pellistor substrates, SRL 136, 30.4 ± 4.4 m^2 g^{-1} was obtained. However, both of these values are similar to the values obtained in the hexagonal phase of Brij® 56. When deposited from the hexagonal phase of Brij® 56, the specific surface area of Pd was 28 ± 0.8 m^2 g^{-1} when the film was grown by stepping the potential from 0.4 to 0.12 V at a 0.2 mm diameter gold electrode; our SRL 136a pellistor substrates produced a slightly lower average of 20.8 m^2 g^{-1}.

These values match well the theoretical calculations which give a specific surface area of 39 m^2 g^{-1}, assuming a hexagonal geometry of $C_{16}EO_8$, and assuming both the pore diameter and wall thickness to be 25 ± 2 Å which were estimated by Guerin using TEM technique.[35] In this thesis, TEM and low-angle powder X-ray studies helped confirm the pore diameter and wall thickness to be 33 Å, and thus, theoretical calculations estimate the ideal specific surface area to be 38 m^2 g^{-1}, assuming a hexagonal geometry of Brij® 56.

As mentioned before, relative values can be used to compare films produced under different conditions with some confidence. Absolute values will be subject to some possible systematic errors, but they are not so great as to invalidate the general conclusions drawn from the studies, i.e. templated versus non-templated films.

EDX measurements helped identify the films as Pd, and SEM studies confirmed that the addition of the surfactant does change the morphology of the Pd films.

Finally, the sensor performance of the Pd pellistors depends on both the substrate design, and the quality of the catalyst, thereby affecting the sensitivity output in mV per 2.5 % methane gas for example. It is also important to bear in mind that the heat generated from the oxidation of methane gas flowing over the Pd catalyst contributes to the temperature of a pellistor. Thus, if the heat loss over the pellistor is large, this will cause a lower temperature change for the same rate of methane reaction, thereby lowering the sensitivity of the pellistor. Another factor affecting the sensitivity is the deposition conditions of the Pd catalyst. In addition, it is always important to measure the cold resistance of a substrate for proper comparison.

As previously mentioned, a fundamental electrochemical study of mesoporous Pd was not the purpose of this chapter; rather the purpose was to find the conditions suitable to deposit Pd on pellistors for comparison with the data obtained in $C_{16}EO_8$ by Guerin.[35] Electrodeposition of Pd in the hexagonal phase of Brij® 56 was possible on SRL 136a pellistors, and exposing them to methane, whether the pellistors were characterised in acid or not, showed good evidence of sensitivity. These gas-testing experiments show that Brij® 56 is a good, and cheap, alternative to $C_{16}EO_8$ in the electrodeposition of Pd on pellistors.

Chapter Six

6 Conclusions and Further Work

Although there is considerable literature on the diffusion of an electrochemical probe in such surfactant media, as described in the introduction of this chapter, diffusion studies of an electrochemical probe in the aqueous domains of different *regular, liquid crystalline structured* phases of a surfactant (formed at sufficiently high surfactant concentrations) have never been carried out until now.

Studies on the diffusion processes of the ferricyanide redox couple in the regular, lyotropic liquid crystalline structures of Brij® 56 can give a clearer picture of carrying out electrochemistry in the presence of a surfactant at sufficiently high concentrations. The effect by the lyotropic liquid-crystalline phase formed by Brij® 56 on the diffusion coefficient of the redox probe could be compared to the aqueous system. The diffusion coefficient of ferricyanide in the surfactant system should be calculated from the maximum reduction limiting currents obtained. A noticeable 10-fold decrease in diffusion coefficient for ferricyanide reduction was observed. Ferricyanide chemistry appeared more reversible in the surfactant system, giving a noticeable cathodic shift in potential, and a timescale appeared to exist for the organisation of the liquid crystalline phase of Brij® 56 into equilibrium. Finally, the diffusion in the aqueous domains of the surfactant system seemed different from the diffusion in the bulk, i.e. the aqueous system.

Electrodeposition of metal films in the presence of lyotropic liquid crystals has shown that nanostructural geometry could be transferred from the liquid crystalline system onto the metal films, thereby enhancing the surface area.[2]

This work is extended to the field of conducting polymers, and the electropolymerisation studies of PANI films in the presence of $C_{16}EO_8$ revealed several things. Firstly, PANI could be electrodeposited in a lyotropic liquid crystalline system. Secondly, although SEM work confirmed that a $C_{16}EO_8$-templated PANI film contained different morphology compared to an untemplated PANI film, it could not prove nanostructure. Unfortunately PANI films were found to be unstable in TEM imaging; and low-angle powder x-ray diffraction studies did not reveal any peaks. Although aniline could electropolymerise in a lyotropic liquid crystalline system, nanostructure could not be proved conclusively.

On the other hand, TEM imaging showed that mesoporous Pd could be obtained in the hexagonal phase of a cheap surfactant, Brij® 56, giving greater specific surface areas than the aqueous system, confirming that electrodeposition in a liquid crystalline phase increases the surface area of a metal. Low-angle powder X-ray diffraction studies helped confirm the pore diameter and wall thickness to be 29 Å. Moreover, like the ferricyanide reduction studies in Brij® 56, there is a significant cathodic shift in potential, with the plateau current only observed in the aqueous system. Electrodeposition in the hexagonal phase actually required longer deposition times and gave greater surface areas than in the cubic phase. This is surprising because the cubic system is believed to contain a 3-d network, and the cubic pore geometry had been predicted to give the largest surface area of Pd.

Experiments on reproducibility and repeatability showed that within one Brij® 56 mixture at 25 ^{0}C, the deposition times and the specific surface areas of Pd appeared reasonably repeatable. This was less clearly seen when comparing three replicate mixtures. Changing the templating composition does not appear to affect greatly the electrodeposition of Pd, as long as the phase remains the same.

A fundamental electrochemical study of mesoporous Pd was not the purpose of this chapter; the purpose was to find the conditions suitable to deposit Pd on pellistors for comparison with the data obtained in $C_{16}EO_8$ by Guerin.[35] Electrodeposition of Pd in the hexagonal phase of Brij® 56 was possible on SRL 136a pellistors, and exposing them to methane, whether the pellistors were characterised in acid, showed evidence of sensitivity. These gas-testing experiments show that Brij® 56 is a good and cheap alternative to $C_{16}EO_8$ in the electrodeposition of Pd on pellistors. EDX measurements helped identify the films as Pd, and SEM studies confirmed that the addition of the surfactant does change the morphology of the Pd films. Acid characterisation studies showed that specific surface areas of Pd were slightly lower in the hexagonal Brij® 56 system than in the $C_{16}EO_8$ system.

As mentioned before, relative values can be used to compare films produced under different conditions with some confidence. Absolute values will be subject to some possible systematic errors, but they are not so great as to invalidate the general conclusions drawn from the studies, i.e. templated versus non-templated films.

Most importantly, the combination of the earlier described work along with the studies of mesoporous Pd show the different facets to electrodeposition in the lyotropic liquid crystalline phases of a surfactant, and that using a cheap and widely available surfactant, i.e. Brij® 56, can be used to construct a gas sensor.

Further work includes examining in greater detail the fundamental study of mesoporous Pd from the lyotropic liquid crystalline phases of Brij® 56 and $C_{16}EO_8$, since the presence of the latter appears to result in greater specific surface areas. Determining whether the result of a small change in potential and temperature can give a substantial effect, and whether the resulting effects are the result of temperature or phase change. The quest for finding the optimum conditions for the construction of mesoporous Pd on a SRL 136a pellistor should be applicable to gas testing experiments, since this can ultimately give a cheaper and better gas sensor.

7 References

[1] G. S. Attard, C. G. Göltner, J. M. Corker, S. Henke and R. H. Templer, Angew. Chem. Int. Ed. Engl., 1997, **36**, p. 1315

[2] G. S. Attard, P. N. Bartlett, N. R. B. Coleman, J. M. Elliott, J. R. Owen and J. H. Wang, Science, 1997, **278**, p. 838

[3] C. T. Kresge, M. E. Leonowicz, W. J. Roth, J. C. Vartuli, J. S. Beck, Nature 1992, **359**, p. 710

[4] G. S. Attard, J. C. Glyde, C. G. Göltner, Nature, 1995, **378**, p. 366

[5] M. E. Raimondi and J. M. Seddon, Liquid Crystals, 1999, **26**, no. 3, p. 305

[6] G. S. Attard, N. R. B. Coleman, J. M. Elliott, Studies in Surface Science and Catalysis, 1998, **117**, p. 89

[7] C.F. Cullis and B.M. Willatt, Journal of Catalysis, 1983. **83**, p. 267

[8] T.A. Jones and P.T. Walsh, *Flammable gas detection.* Platinum Metals Review, 1988, **32**(2), p. 50

[9] M. E. Davies, R. F. Lobo, Chem. Mater. 1992, **4**, p. 756

[10] G. Gottardi and E. Galliv, *Natural Zeolites*, Springer, Berlin, 1985

[11] B. A. Lenner, Chemistry and Industry, 1997, **1**, p. 16

[12] J. S. Beck, J. C. Vartuli, W. J. Roth, M. E. Leonowicz, C. T. Kresge, K. D. Schmitt, C. T-W Chu, D. H. Olson, E. W. Sheppard, S. B. McCullen, J. B. Higgins and J. L. Schlenker, J. Am. Chem. Soc., 1992, **114**, p. 10834

[13] S. Inagaki, Y. Fukishima and K. Kuroda, J. Chem. Soc. Chem. Commun., 1993, p. 680; P. Behrens and G. D. Stucky, Angew. Chem. Int. Edn. Engl., 1993, **32**, p. 696; A. Monnier et al., Science, 1993, 261, p. 1299; P. Behrens, Adv. Mater., 1993, **5**, p. 127; Q. Huo et al, Nature, 1994, **368**, p. 317; V. Alfredsson et al, J. Chem. Soc. Chem. Commun. 1994, p. 921

[14] C. G. Wu and T. Bein, Science, 1994, **264**, p. 1757; C. G. Wu and T. Bein, Science, 1994, **266**, p. 1013; Z. Liu, Y. Sakamoto, T. Ohsuna, K. Hiraga, O. Terasaki, C. H. Ko, H. J. Shin, and R. Ryoo, Angew. Chem. Int. Edn., 2000, **39**, p. 3107; C. R. Martin, Science, 1994, **266**, p. 1013

[15] M. Kruk, M. Jaroniec and A. Sayari, Langmuir, 1997, **13**, p. 6267; K. Morishige and K. Kawano, J. Chem. Phys., 1999, **110**, p. 4867

[16] F. Leroux, B. E. Koene and L. F. Nazar, J. Electrochem. Soc., 1996, **143**, p. L181; W. G. Pell and B. E. Conway, J. Power SOurces, 1996, **63**, p. 255; J. Wang and L. Agnes, Anal. Chem. , 1992, **64**, p. 456

[17] N. Greenwood and A. Earnshaw, *Chemistry of the Elements* (1st ed.), Wiley, New York, 1980, p. 537; K. Othmer, *Encyclopedia of Chemical Technology* (3rd ed.), Wiley, New York, 1980

[18] G. C. Bond, *Catalysis by Metals*, Academic Press, New York, 1962, p. 537

[19] W. Carruthers, *Some Modern Methods of Organic Synthesis* (3rd ed.), Cambridge University Press, 1986

[20] P. N. Rylander, *Catalytic Hydrogenation over Pt Metals*, Academic Press, London, 1967

[21] V. Ponec and T. C. Bond, *Catalysis by Metals and Alloys*, Elsevier, Amsterdam, 1995, **38-41**, p. 238

[22] J. Tsuji, *Innovations in Organic Synthesis*, John Wiley and Sons Ltd., 1995, p. 528

[23] C. F. Cullis and B. M. Willatt, J. Cat., 1983, **83**, p. 267

[24] G. Hoogers and D. Thompsett, Cattech, 2000, **2**, p. 106

[25] P. N. Ross, K. Kinoshita, A. J. Scarpelino and P. Stonehart, J. Electroanal. Interfacial. Electrochem., 1975, **59**, p. 577

[26] G. C. Bond, *Heterogeneous Catalysis: Principles and Applications*, 2nd ed., Clarendon Press, Oxford, 1987

[27] J. T. Woestman and E. M. Logothetis, Industrial Physicist, 1995, p. 20

[28] K. C. Taylor, *The Catalytic Chemistry of Nitrogen Oxides*, R. Klimish & J. G. Latson (Ed.), Plenum, 1975

[29] R. W. McCabe and R. K. Usmen, Studies in Surface Science and Catalysis, 1996, 101, p. 355

[30] T. J. Barton, L. M. Bull, W. G. Klemperer, D. A. Loy, B. McEnaney, M. Misono, P. A. Monson, G. Pez, G. W. Scherer, J. C. Vartuli and O. M. Yaghi, Chem. Mater., 1999, **11**, p. 2633

[31] P.J. Collings, *Liquid Crystals*, IOP Publishing Ltd.: Bristol, 1990

[32] R G Laughlin, *The Aqueous Phase Behaviour of Surfactants*, Academic Press, London, 1994, Appendix 4, p. 521

[33] N.R.B. Coleman, PhD Thesis, Department of Chemistry, University of Southampton, 1998

[34] G. S. Attard, P. N. Bartlett, N. R. B. Coleman, J. M. Elliott and J. R. Owen, Langmuir, 1998, **14**, p. 7340

[35] S. Guerin, PhD Thesis, Department of Chemistry, University of Southampton, 1999

[36] D. J. Mitchell, G. J. Tiddy, L. Waring, T. Bostock and M. P. J. McDonald, J. Chem. Soc., Faraday Trans. 1, 1983, **79**(1), p. 975

[37] T. Yanagisawa, T. Shimizu, K. Kuroda and C. Kato, Bull. Chem. Soc. Jpn., 1990, **63,** p. 988

[38] A. Corma, Chem. Rev., 1997, **97**, p. 2373

[39] N. K. Raman, M. T. Anderson and C. J. Brinker, Chem. Mater., 1996, **8**, p. 1682

[40] M. Kruk, M. Jaroniec and A. Sayari, J. Phys. Chem. B, 1999, **103**, p. 4590

[41] A. Monnier, F. Schuth, Q. Huo, D. Kumar, D. Margolese, R. S. Maxwell, G. D. Stucky, M. Krishnamurty, P. Petroff, A. Firouzi, M. Janicke and B. F. Chimelka, Science, 1993, **261**, p. 1299

[42] C. F. Cheng, Z. H. Luan and J. Klinowski, Langmuir, 1995, **11**, p. 2815

[43] Q. Huo, D. I. Margolez and G. D. Stucky, Chem. Mater., 1996, **8**, p. 1147

[44] A. Sayari, P. Liu, M. Kruk and M. Jaroniec, Chem. Mater., 1997, **9**, p. 2499

[45] M. Kruk, M. Jaroniec, Y. Sakamoto, O. Terasaki, R. Ryoo and C. H. Ko, J. Phys. Chem. B, 2000, 104, p. 292

[46] J. L. Blin, C. Otjacques, G. Herrier and B. L. Su, Langmuir, 2000, **16**, p. 4229

[47] A. Firouzi, D. Kumar, L. M. Bull, T. Besier, P. Sieger, Q. Huo, S. A. Walker, J. A. Zasadzinski, C. Glinka, J. Nicol, D. Margolese, G. D. Stucky and B. F. Chmelka, Science, 1995, **267**, p. 1138

[48] K. Schumacher, P. I. Ravikovitch, A. Du Chesne, A. V. Neimark and K. K. Unger, Langmuir, 2000, **16**, p. 4648

[49] C. F. Cheng, Z. H. Luan and J. Klinowski, Langmuir, 1995, **11**, p. 2815

[50] K. S. W. Sing, D. H. Everett, R. A. W. Haul, L. Moscou, R.A. Pierotti, J. Rouquerol and T. Siemieniewska, Pure Appl. Chem., 1985, **57**, p. 603

[51] C. G. Göltner and M. Antonietti, Adv. Mater., 1997, **9**, p. 431

[52] J. M. Elliott, G. S. Attard, P. N. Bartlett, J. R. Owen, N. Ryan and G. Singh, Journal of New Materials for Electrochemical Systems, 1999, **2** , p. 239

[53] J. M. Elliott, G. S. Attard, P. N. Bartlett, N. R. B. Coleman, D. A. S. Merckel and J. R. Owen, Chem. Mater., 1999, **11**, p. 3602

[54] A. H. Whitehead, J. M. Elliott, J. R. Owen and G. S. Attard, J. Chem. Soc. Chem. Commun., 1999, **331**, p. 14

[55] E. Jones, *Solid State Gas Sensor*, P. T. Moseley (ed.), Adam Hilger, Bristol, England, 1987, p. 17

[56] J. M. Elliott, PhD Thesis, 1994, Department of Chemistry, University of Southampton

[57] P J Goodhew and F J Humphreys, *Electron Microscopy and Analysis*, 2nd edition, Taylor and Humphreys, London, 1988; I M Watt, *The Principles and Practice of Electron microscopy*, 2nd edition, Cambridge University Press, Cambridge, 1997

[58] K. J. Edler, J Dougherty, R Drand, L Iton, G Kirion, G Lockhart, Z Wang, R Withers, J W White, *Colloids and Surfaces A,* 1995, **102**, p. 213

[59] P. C. Hiemenz, *Principles of Surface and Colloid Chemistry*, Marcel Dekker, NewYork, 1986

[60] J. F. Rusling, *Electroanal. Chem.*, A. J. Bard (Ed.), Marcel Dekker, NewYork, 1994, **18**, p.1

[61] A. V. Barzykin, K. Seki, M. Tachiya, Advances in Colloid and Interface Science, 2001, **89**, p.47

[62] M .Kahlweet, Science, 1988, **240**, p.617

[63] S. Papp and I. Dekany, Colloid and Polymer Science, 2001, **279**, p.449

[64] R. P. Bagwe, J. R. Kanicky, B. J. Palla, P. K. Patanjali and D. O. Shah, Critical Reviews in Therapeutic Drug Carrier, 2001, **18**, p.77

[65] E. L. Colichman, J. Am. Chem. Soc., 1950, **72**, p.4036; L. Meites and T. Meites, J. Am. Chem. Soc., 1951, **73**, p.177

[66] J. F. Rusling, C. N. Shi, E. C. Couture and T. F. Kumosinski, *Redox Chemistry and Interfacial Behaviour of Biological Molecules*, G. Dryhurst and K. Niki (Eds.), Plenum, NewYork, 1988, p. 565

[67] E. Pelizzetti and E. Pramauro, Anal. Chim. Acta, 1985, **169**, p.1

[68] H. Hakemi, P. P. Varanasi and N. Tcheurekdjian, J. Phys. Chem., 1987, **91**, p.120

[69] J. F. Rusling, C. N. Shi and T. F. Kumosinski, Anal. Chem., 1988, **60**, p.1260

[70] R. Zana and R. A. Mackay, Langmuir, 1986, **2**, p.109

[71] I. D. Charlton and A. P. Doherty, J. Phys. Chem. B, 2000, **104**, p.8327

[72] D. H. Evans, J. Electroanal. Chem., 1989, **258**, p.451

[73] A. P. Abbott, G. Gounili, J. M. Bobbitt, J. F. Rusling and T. F. Kumosinski, J. Phys. Chem., 1992, **96**, p.11091; J. Georges and S. Desmettre, Electrochim. Acta, 1984, **29**, p.521

[74] J. Georges and S. Desmettre, Electrochim. Acta, 1986, **31**, p.1519

[75] J. F. Rusling, Z. Wang and A. Owlia, Colloids and Surfaces, 1990, **48**, p.173

[76] A. E. Kaifer and A. J. Bard, J. Phys. Chem., 1985, **89**, p.4876; A. E. Kaifer and A. J. Bard, J. Phys. Chem., 1987, **91**, p.2007

[77] A. B. Mandal, B. U. Nair and D. Ramaswamy, Langmuir, 1988, **4**, p.736

[78] A. B. Mandal and B. U. Nair, J. Phys. Chem., 1991, **95**, p.9008; A. B. Mandal, Langmuir, 1993, **9**, p.1932; ; A. B. Mandal and B. Geetha, Langmuir, 1997, **13**, p.2410

[79] C. Hermansky, R. Agarwal and R. A. Mackay, *Colloid and Interface Science*, M. Kerker (Ed.), Academic, New York, 1976, **2**, p.289; R. A. Mackay, *Microemulsions*, I. D. Robb (Ed.), Plenum Press, New York, 1982, p.207

[80] J. Georges and J. W. Chen, Colloid and Polymer Science, 1986, **264**, p.896; E. Dayalan, S. Qutubuddin and J. Texter, J. Colloid Interf. Sci., 1991, **143**, p.423

[81] A. Berthod and J. Georges, J. Colloid Interf. Sci., 1985, **106**, p.194; J. W. Chen, N. Arnaud and J. Georges, Colloid and Polymer Science, 1987, **265**, p.45

[82] S. A. Myers, L. Bobalbhai, A. Bratjer-Toth and R. A. Mackay, Anal. Chem., 1990, **62**, p.1084

[83] S. A. Myers, A. Bratjer-Toth and R. A. Mackay, Electroanal., 1996, **8**, p.759;

[84] J. Santhanalakshmi and G. Vijayalakshmi, Langmuir, 1997, **13**, p.3915; J. F. Rusling and X. L. Zu, Langmuir, 1997, **13**, p.3693; J. F. Rusling and S. P. Zhang, J. Colloid Interf. Sci., 1996, **182**, p.558; J. Santhanalakshmi and K. Anandhi, J. Colloid Interf. Sci., 1995, **176**, p.226; J. W. Chen and J. Georges, J. Electroanal. Chem., 1986, **210**, p.205

[85] A. Ulman, Chem. Rev., 1996, **96**, p.1533

[86] H. C. De Long and D. A. Buttry, Langmuir, 1990, **6**, p.1319; H. C. De Long, J. J. Donohue and D. A. Buttry, Langmuir, 1991, **7**, p.2196

[87] J. M. Pope and D. A. Buttry, J. Electroanal. Chem., 2001, **498**, p.75

[88] J. M. Pope, Z. Tan, S. Kimbrell and D. A. Buttry, J. Am. Chem. Soc., 1992, **114**, p.10085

[89] D. G. Hanken and R. M. Corn, Anal. Chem., 1997, **69**, p.3665

[90] G. E. Poirier, Langmuir, 1997, **13**, p.2019; F. T. Arce, M. E. Vela, R. C. Salvarezza and A. J. Arvia, Langmuir, 1998, **14**, p.7203

[91] S. Imabayashi, D. Hobara and T. Kakiuchi, Langmuir, 2001, **17**, p.2560

[92] F. T. Arce, M. E. Vela, R. C. Salvarezza and A. J. Arvia, Electrochim. Acta, 1998, **44**, p.1053

[93] S. L. Hiley and D. A. Buttry, Colloid Surf. A-Physicochem. Eng. Asp., 1994, **84**, p.129

[94] H. C. De Long and D. A. Buttry, Langmuir, 1992, **8**, p.2491

[95] C. R. Raj and T. Ohsaka, Bioelectrohem., 2001, **53**, p.251

[96] C. A. Goss and M. Majda, J. Electroanal. Chem., 1991, **300**, p.377; E. Torchut, J. M. Laval, C. Bourdillon and M. Majda, Biophysical J., 1994, **66**, p.753

[97] T. A. Postlethwaite, E. T. Samulski and R. W. Murray, Langmuir, 1994, **10**, p.2064

[98] N. Boden, K. J. McMullen, M. C. Holmes and G. J. T. Tiddy, Springer Ser. Chem. Phys., 1980, **11**, p.299

[99] N. Boden, S. A. Corne and K. W. Jolley, Chem. Phys. Lett., 1984, **105**, p. 99; P. J. Photinos and A. Saupe, J. Phys. Chem., 1986, **84**, p.517

[100] P. J. Photino, P. Ukleja and G. Chidichimo, Liq. Cryst.., 1991, **9**, p.359

[101] J. J. Taber, Pure Appl. Chem., 1980, **52**, p.1323; H. Arai, M. Murata and K. Shinoda, J. Coll. Interf. Sci., 1971, **37**, p.223

[102] A. Benkhira and F. J. Franta, J. Coll. Interf. Sci., 1994, **164**, p.428; Y. Wang, D. Lu, H. Yan and R. K. Thomas, J. Phys. Chem. B, 1997, **101**, p.3953

[103] P. Roscigno, L. Paduano, G. D'Errico and V. Vitagliano, Langmuir, 2000, **17**, p.4510

[104] F. M. Menger, A. V. Peresypkin and S. X. Wu, J. Phys. Org. Chem., 2001, **14**, p.392

[105] M. B. Forstner, J. Käs and D. Martin, Langmuir, 2001, **17**, p.567

[106] P. C. Ke and C. A. Naumann, Langmuir, 2001, **17**, p.3727

[107] O. Haas, C. S. Velazquez, Z. Porat and R. W. Murray, J. Phys. Chem., 1995, **99**, p.15279

[108] D. Pletcher, *A First Course in Electrode Processes*, Romsey, England, 1991

[109] C. Beriet, D. Pletcher, J. Electroanal. Chem., 1993, **361**, p. 93; R. N. Adams, *Electrochemistry at Solid Electrodes*, Marcel Dekker, New York, 1969

[110] C. Beriet, *PhD Thesis*, Department of Chemistry, University of Southampton, 1997

[111] J. O'M. Bockris and A. K. N. Reddy, *Modern Electrochemistry*, Plenum Press, New York, 1970, **1**, p. 56

[112] Dr Mark E Light, EPSRC National X-Ray Crystallography Service, Department of Chemistry, University of Southampton

[113] B. E. Conway, *Electrochemical Data*, Elsevier Publishing Company, London, 1952, p. 44

[114] B. L. Ramos, E.A. Blubaughm, T. H. Ridgway, W. R. Heineman, Anal. Chem., 1994, **66**, p.1931

[115] D. T. Sawyer et al., Anal.Chem., 1982, **54**, p. 1720

[116] A. J. Bard, F. R. F. Fan and M. V. Mirkin, *Electroanal. Chem.*, Bard (Ed.), Marcel Dekker, New York, 1994, **18**, p. 244

[117] J. L. Amphlett and G. Denuault, J. Phys. Chem. B, 1998, **102**, p. 9946

[118] R. Mathur-DeVrè, Prog.Biophys.Molec.Biol., 1979, **35**, p. 103

[119] E. W. Lang and L. Piculell, *Water and Aqueous Solutions (Proceedings of the Thirty-Seventh Symposium of the Colston Research Society)*, Neilson and Enderby (Eds.), Adam Hilger, Bristol, 1985, p. 31

[120] A. Firouzi, F. Atef, A. G. Oertli, G. D. Stucky and B. F. Chmelka, J. Am. Chem. Soc., 1997, **119**, p. 3596

[121] G. S. Attard, M. Edgar and C. G. Gőltner, Acta. Mater., 1998, **46**, p. 751

[122] B. J. Forest and L. W. Reeves, Chem. Rev., 1981, **81**, p. 1

[123] A. Rapp, K. Ermolaev and B. M. Fung, J. Phys. Chem. B, 1999, **103**, p. 1705

[124] J. R. Owen and J. M. Elliott, Phys. Chem. Chem. Phys., 2000, **2**, p.5653

[125] P. W. Atkins, *Physical Chemistry – Fourth Edition*, Oxford University Press, Oxford, 1990, p. 691, 765

[126] V. M. M. Lobo, *Handbook of Electrolyte Solutions – Physical Sciences Data 41, Parts A and B*, Elsevier Science Publishers B. V., Amsterdam, 1989, pp. 853, 965, 2235

[127] A. B. Mandal, B. U. Nair and D. Ramaswamy, Langmuir, 1988, **4**, p.736

[128] N. M. Van Os, J. R. Haak and L. A. M. Rupert, *Physico-chemical Properties of Selected Anionic, Cationic and Nonionic Surfactants*, Elsevier Science Publishers, New York, 1993; Sigma Aldrich Product Information Sheet

[129] P. D. T. Huibers, V. S. Lobanov, A. R. Katritzky, D. O. Shah and M. Karelson, Langmuir, 1996, **12**, p.1462

[130] P. H. Elworthy and C. B. MacFarlane, J. Pharm. Pharmacol. Suppl., 1962, **14**, p.100T

[131] G. Inzelt, M. Pineri, J. W. Schultze and M. A. Vorotyntsev, Electrochimica Acta, 2000, **45**, p. 2403

[132] P. Chandrasekhar, Conducting Polymers, Fundamentals and Applications – A Practical Approach, Kluwer Academic Publishers, US, 1999

[133] E. M. Genies, A. R. Boyle, M. Lapkowski and C. Tsintavis, Synthetic Metals, 1990, **36**, p. 139

[134] C. M. Carlin, L. J. Kepley and A. J. Bard, J. Electrochem. Soc., 1985, **132**, p. 353

[135] E. M. Genies and C. Tsintavis, J. Electroanal. Chem., 1985, **195**, p. 109

[136] J. Desilvestro and W. Scheifele, J. Mat. Chem., 1993, **3**, p. 263; E. Sabatini, A. Redondo, J. Rishpon, A. Rudge, I. Rubinstein and S. Gottesfeild, J. Chem. Soc. Faraday Trans., 1993, **89**, p. 287

[137] G. Inzelt, Electroanal. Chem., A. Bard (ed.), Marcel Dekker Inc., New York, 1994, **18**, p. 90

[138] E. M. Genies and C. Tsintavis, J. Electroanal. Chem., 1985, **195**, p. 109

[139] D. E. Stillwell and S. M. Park, J. Electrochem. Soc., 1988, **135**, p. 2497

[140] M. Doriomedoff, F. H. Cristofini, R. De Surville, M. Josefowicz, L. T. Yu and R. Buvet, J. Chim. Phys., 1971, **68**, p. 1055

[141] M. Nechtschein and C. Santier, J. Phys. (Paris), 1986, **47**, p. 935

[142] P. N. Bartlett and Y. Astier, Chem. Commun., 2000, p. 105

[143] C. K. Chiang, C. R. Fincher, Y. W. Park, A. J. Heeger, H. Shirakawa, E. J. Louis, S. C. Gau and A. G. MacDiarmid, Phys. Rev. Lett., 1977, **39**, p. 1089; W. M. Genies, G. Bidan and A. Diaz, J. Electroanal. Chem., 1983, **149**, p. 101; A. F. Diaz, K. K. Kanazawa and G. P. Gardini, J. Chem. Soc. Chem. Commun., 1979, p. 635; J. C, Scott, P. Pfluger, M. T. Krounbi and G. B. Street, Phys. Rev. B., 1983, **28**, p. 2140

[144] A. J. Bard and L. R. Faulkner, *Electrochemical Methods*, John Wiley & Sons, Inc., Canada, 1980

[145] S. W. Feldberg, J. Am. Chem. Soc., 1984, **106**, p. 4671

[146] A. F. Diaz and J. A. Logan, J. Electroanal. Chem., 1980, **111**, p. 111

[147] T. Kobayashi, H. Yoneyama and H. Tamura, J. Electroanal. Chem., 1984, **161**, p. 419; 1984, **177**, p. 281, p. 293

[148] M. Kalaji, L. M. Peter, L. M. Abrantes and J. C. Mesquita, J. Electroanal. Chem., 1989, **274**, p. 289; M. Kalaji, L. Nyholm and L. M. Peter, J. Electroanal. Chem., 1991, **313**, p. 271

[149] C. P. Andrieux, P. Audebert, P. Hapiot, M. Nechtschein and C. Odin, J. Electroanal. Chem., 1991, **305**, p. 153

[150] E. M. Genies and M. Lapowski, J. Electroanal. Chem., 1987, **236**, p. 189

[151] A. A. Syed and K. M. Dinesan, Talanta, 1991, **38**, p. 815

[152] M. C. Miras, K. R. Barbero and O. Haas, J. Electrochem. Soc., 1991, **138**, p. 669

[153] M. Kalaji and L. M. Peter, J. Chem. Soc. Faraday Trans., 1991, **87**, p. 853

[154] J. Tanguy, N. Mermillod and M. Hoclet, J. Electrochem. Soc., 1987, **134**, p. 795

[155] K. Uvdal, M. A. Hasan, J. O. Nillson, W. R. Salaneck, I. Lundstrom, A. G. Macdiarmid, A. Ray and M. Angelopoulos, in H. Kuzmany, M. Mehring and S. Roth (Eds.), *"Electronic Properties of Conjugated Polymers"*, Springer Seires in Solid-State Physics, Springer, Berlin, 1987, **76**, p. 262

[156] M. Doriomedoff, Thesis, University of Paris VI, 1974

[157] A. J. Bard and L. R. Faulkner, *"Electrochemical Methods"*, John Wiley & Sons, Inc., Canada, 1980

[158] I. Kulszewicz-Bajer, M. Zagorska, J. Niziol, A. Pron and W. Luzny, Synthetic Metals, 2000, **114**, p. 125

[159] A. Pron, J. Laska, J. E. Osterholm and P. Smith, Polymer, 1993, **34**, p. 4235

[160] R. K. Paul and C. K. S. Pillai, J. Appl. Polymer Sci., 2001, **80**, p. 1354

[161] N. Furukawa and K. Nishio, *"Applications of Electroactive Polymers"*, B. Scrosati (Ed.), Chapman & Hall, New York, 1993, p. 150

[162] J. K. Avlyanov, J. Y. Josefowicz and A. G. MacDiarmid, Synth. Met., 1995, **73**, p. 205

[163] I. F. Warren, J. A. Walker, D. P. Anderson and C. G. Rhodes, J. Electrochem. Soc., 1989, **136**, p. 2286

[164] S.M. Lee, Department of Engineering, University of Warwick, 2000.

[165] Harrison, J.A., R.P.J. Hill, and J. Thompson, Electroanalytical Chemistry and Interfacial Electrochemistry, 1973, **47**, pp. 431-440; Harrison, J.A., H.B.S. Alcazar, and J. Thompson, Electroanalytical Chemistry and Interfacial Electrochemistry, 1974, **53**, p. 145

[166] L. A. Kibler, M. Kleinert, R. Randler and D. M. Kolb, Surf. Sci., 1999, **443**, p. 19

[167] Penven, R.L., W. Levason, and D. Pletcher, J. Applied Electrochem., 1990, **20**, p. 399

[168] W. M. Latimer, *The Oxidation States of the Elements and Their Potentials in Aqueous Solutions*, 2nd edition, Prentice-Hall inc., New York, 1952, p. 202

[169] H. A. Droll, B. P. Block and W. C. Fernelius, J. Phys. Chem., 1957, **61**, p. 1000

[170] D. H. Templeton, G. W. Watt and C. S. Garner, J. Am. Chem. Soc., 1943, **65**, p. 1608

[171] L. J. Gillespie and F. P. Hall, J. Am. Chem. Soc., 1926, **48**, p. 1207; P. J. Mitchell, N. A. Hampson and A. J. S. McNeil, *Adsorption at solid electrodes* in Electrochemistry, R.S.C. Chemistry, RSC:London, 1985, p. 1

[172] R. Woods, *Chemisorption at electrodes* in Electroanalytical Chemistry, A. J. Bard (Editor), Marcel Dekker Inc.: New York, 1976, p. 109

[173] R. A. Campbell, J. A. Rodriguez and D. W. Goodman, Phys. Rev. B, 1992, **46**, p. 7077

[174] N. M. Marković, B. N. Grgur and P. N. Ross, J. Phys. Chem., 1997, **101**, p. 5405

[175] A. Capon and R. Parsons, J. Electroanal. Chem., 1972, **39**, p. 275

[176] D. A. J. Rand and R. Woods, J.Electroanal. Chem., 1972, **35**, p. 209

[177] K. Sashikata, Y. Matsui, K. Itaya and M. P. Soriaga, J. Phys. Chem., 1996, **100**, p. 20027

[178] T. Solomun, J. Electroanal. Chem., 1987, **217**, p. 435; 1988, **255**, p. 163; 1991, **302**, p. 31

[179] D. A. J. Rand and R. Woods, *The nature of adsorbed oxygen on rhodium, palladium and gold electrodes*, J.Electroanal. Chem., 1971, **31**, pp. 29-38

[180] G. Ertl and P. Rau, Surf. Sci., 1969, **15**, p. 443

[181] D. A. J. Rand and R. Woods, J. Electroanal. Chem., 1972, **36**, p. 57

[182] J. O'M. Bockris and G. A. Razumney, *Fundamental Aspects of Electrocrystallisation*, Plenum Press, New York, 1967, chapter 7

[183] A. R. Blake, J. G. Sunderland and A. T. Kuhn, J. Chem. Soc. A., 1969, p. 3015

[184] A. Goodridge and C. J. H. King, Trans. Faraday Soc., 1970, **66**, p. 2889

[185] N. M. Marković, C. A. Lucas, V. Climent, V. Stamenković and P.N. Ross, Surf. Sci., 2000, **465**, p. 103

[186] Bell, M.F. and J.A. Harrison, *The deposition of palladium.* Electroanalytical Chemistry and Interfacial Electrochemistry, 1973, **41,** p. 15

[187] S. Daniele, M. A. Baldo, C. Bragato, G. Denuault and M. E. Abdelsalam, Anal. Chem., 1999, **71**, p. 811

[188] K. B. Oldham, J. Electroanal. Chem. Interfacial Electrochem., 1992, **337**, p. 91

[189] T. J. Barton, L. M. Bull, W. G. Klemperer, D. A. Loy, B. McEnaney, M. Misono, P. A. Monson, G. Pez, G. W. Scherer, J. C. Vartuli and O. M. Yaghi, Chem. Mater., 1999, **11**, p. 2633

[190] E. Jones, *Solid State Gas Sensor*, P. T. Moseley (ed.), Adam Hilger, Bristol, England, 1987, p. 17

[191] C. F. Cullis and B. M. Willatt, J. Cat., 1983, **83**, p. 267

[192] H. W. Shin and J. W. Gardner, *Instrumentation and Microsensors: Design of Thin Film Pellistor Gas Sensor*, Department of Engineering, University of Warwick, 1996

---

[193] *CRC Handbook of Chemistry and Physics: 1st Student Edition*, R. C. Weast (ed.), CRC Press Inc., Florida, USA, table E-2

[194] S. Leclerc, Personal Communication, City Technology Ltd., 2001.